THE PHYSICS AND CHEMISTRY OF ENVELOPES AND DISKS AROUND YOUNG PROTOSTARS

ELIZABETH ARTUR DE LA VILLARMOIS

DISSERTATION SUBMITTED FOR THE DEGREE OF

PHILOSOPHIÆ DOCTOR

NIELS BOHR INSTITUTE & CENTRE FOR STAR AND PLANET FORMATION
UNIVERSITY OF COPENHAGEN

SUPERVISORS: JES K. JØRGENSEN
LARS E. KRISTENSEN

Copenhagen - Denmark
March - 2019

ABSTRACT

Important clues about the formation of our own Solar System are revealed by studying other young sources that are currently forming. The study of low-mass protostars in different evolutionary stages is, therefore, essential to link their physical and chemical evolution to what we know about the Solar System. In particular, low-mass protostars are associated with disks, where planets form. Very little is known about the initial physical and chemical conditions for planet formation and the relationship between the physical and chemical structures of embedded disks. Therefore, the study of the physics and chemistry at small scales may provide important clues about how the material falls from the envelope to the disk and accretes from the disk into the protostar and what is the physico-chemical link between deeply embedded stages and the onset of planet formation.

The goal of this thesis is to study the physics and chemistry at play at small scales (disk scales) towards low-mass protostars in order to constrain the mass flow and identify the physical and chemical processes that dominate at these scales. The study of the formation and evolution of disks is challenging since they are embedded in the parental cloud and are relatively small in size ($\lesssim 700$ AU), requiring observations with high sensitivity and angular resolution. For this, we observe a sample of Class I protostars using the Atacama Large Millimeter/submillimeter Array (ALMA) and the Submillimeter Array (SMA) to characterise their physical and chemical structures. Class I sources have been chosen since disks are expected to have been formed at this stage and because they serve as a link between the deeply embedded Class 0 sources and the emergence of protoplanetary disks.

The results from these studies are presented in three papers (published in or submitted to international journals). We find an empirical linear correlation between the bolometric luminosity and the mass accretion rate, suggesting that more massive protostars accrete material with a higher accretion rate. The mean mass accretion estimated for a sample of 13 Class I sources is 2.4×10^{-7} M$_\odot$ yr^{-1}. This value is lower than the expected if the accretion is constant in time and rather points to a sce-

nario of accretion occurring in bursts. In addition, this low mass accretion rate provides observational evidence that a typical protostar will spend most of its lifetime in a quiescent state of accretion.

The formation and evolution of the disk is reflected on the chemical structure of the envelope, from large to small scales. The disk shields material beyond its extent where cold temperature tracers are detected, such as DCO^+. Furthermore, the non detection of CH_3OH suggests that material from the inner envelope follows the flattened structure of the disk and, since less material is exposed to high temperatures, desorption of complex-organic molecules is not efficient. In addition, compact emission and large line widths of warm SO_2 emission are consistent with the presence of accretion shocks produced at the interface between the inner envelope and the disk surface.

Class I sources show a physical and chemical link between deeply embedded Class 0 sources and more evolved Class II sources. The gas column density decreases as the system evolves, which is reflected on the emission of high density tracers such as CO isotopologues. The formation and evolution of the disk, together with the increase of the outflow-opening angle as the system evolves, allow the UV radiation from the central protostar to reach the surface layers of the disk, promoting the photodissociation of molecules and enhancing the abundance of others, for example, CN. On the other hand, the chemistry of Class 0 sources can be preserved, to some extent, in Class II sources mainly towards the disk midplane and beyond its extension, where the shielding is efficient.

DANSK RESUME

Gennem studiet af unge stjerner i vores interstellare nabolag, kan vi få vigtig ny indsigt i dannelsen af Solsystemet. Studiet af unge protostjerner i forskellige stadier af stjernedannelsesprocessen er derfor essentielt for vores forståelse af fysikken og kemien i det tidlige solsystem. Lav-masse proto-stjerner ses ofte omkranset af protoplanetariske skiver hvor planeter forventes at blive dannet. Vores forståelse af de fysiske og kemiske initialbetingelser for planetdannelse er på nuværende tidspunkt meget begrænset. Det er derfor vigtigt at studere fysikken og kemien i disse skiver med høj opløsning så processerne i skiverne kan kortægges. Herved kan vigtige detaljer omkring fx massetransport fra molekyleskyer til protoplanetariske skiver og fra disse skiver til protostjerner og protoplaneter analyseres.

Formålet med denne afhandling er at studere fysikken og kemien omkring protostjerner på små skalaer, dvs. ved tilstrækkelig høj rummelig opløsning til at identificere og analysere den protoplanetariske skive, med det formål at undersøge massetransporten under stjerne- og planetdannelsen samt identificere de dominerende fysiske og kemiske processer. Det er en udfordring at observere og studere formationen og udviklingen af disse skiver idet de er omgivet af en tæt sky af støv og gas. Ydermere er skiverne relativt små (< 700 AU) og der kræves derfor en høj følsomhed og en høj rummelig opløsning for at identificere disse skiver. Vi betragter her et udvalg af "Klasse-I" protostjerner som er observeret med Atacama Large Millimeter/submillimeter Array (ALMA) og Submillimeter Array (SMA) teleskoperne for at karakterisere deres fysiske og kemiske strukturer. Vi har udvalgt Klasse-I protostjerner idet protoplanetariske skiver forventes at være tilstede omkring disse objekter, hvorfor disse objekter er bindeleddet mellem den tidligste fase af stjernedannelsesprocessen ("Klasse-0") og dannelsen af protoplanetariske skiver.

Resultaterne af disse studier er præsenteret i tre videnskabelige artikler (udgivet eller indsendt til udgivelse i internationale tidsskrifter). Vi finder en empirisk lineær korrelation mellem den bolometriske

iv

luminositet og massetilvæksten, hvilket antyder at tungere protostjerner dannes med en højere tilvækstrate. Den gennemsnitlige massetilvt estimeret på baggrund af 13 Klasse-I objekter er 2.4×10^{-7} $M_\odot$ yr^{-1}. Denne værdi er lavere end forventet hvis massetilvæksten er konstant over tid og antyder derfor at massetilvæksten er episodisk, med såkaldte "udbrud" med højere massetilvækst. Ydermere betyder den lave gennemsnitslige massetilvækst at protostjerner tilbringer mest tid i en stille fase, med lav massetilvækst.

Dannelsen og den efterfølgende evolution af disse protoplanetariske skiver er reflekteret i den kemiske struktur i den omkringliggende gas-sky. Skiven skærmer for protostjernens stråling og danner et reservoir af kold gas udenfor skivens udstrækning. Dette reservoir er identificeret ved DCO^+, et molekyle der kendetegner kolde regioner. Materiale fra den omkringliggende gas-sky samles i skivens midtplan, hvor en stor del af materialet er afskærmet fra stråling og derfor forbliver adsorberet på støvkorn. Dette afsløres idet metanol (CH_3OH) ikke er detekteret i gasfasen, på trods af store forekomster af metanol i stjernedannende skyer. Kompakt linjeemission og stor linjebredde fra varm SO_2 gas er i overensstemmelse med tilstedeværelsen af et "accretion shock" hvor gas fra den omkringliggende gas-sky rammer skiven og varmes op idet kinetisk energi omdannes til termisk energi.

Klasse-I objekterne afslører en fysisk og kemisk sammenhæng mellem den tidligere Klasse-0 fase og den mere udviklede Klasse-II fase. Gas søjledensiteten falder i takt med at systemet dannes, hvilket er reflekteret i emission fra molekyler der kendetegner høje gasdensiteter så som CO isotoper. Skivens dannelse og evolution, koblet med en ændring af vinklen på det molekylære outflow betyder at UV-stråling fra protostjernen kan ramme det øverste lag af den protoplanetariske skive, hvorved nogle molekyler i denne region fotodissocieres hvilket ændrer den kemiske komposition og resultere i en højere forekomst af fx CN. I andre områder, så som i skivens midtplan, forbliver kemien nogenlunde uændret mellem Klasse-0 og Klasse-II objekter, idet molekylerne her er skærmet fra protostjernens stråling og derfor ikke oplever en betydelig ændring af de fysiske forhold.

Contents

List of Figures

List of Tables

ACKNOWLEDGEMENTS

This thesis is the product of, not only scientific results but also the support and guidance of a lot of people that somehow were involved and helped me during the hole "PhD process" and to arrive where I am now. These three years were full of new experiences for me and I have discovered a new world, from the whole process of writing a paper to live in another continent.

First I would like to thank my supervisors Jes Jørgensen and Lars Kristensen. I am very grateful to work with people like you, always willing to help, teach and discuss about science. Thank you for the infinite patience, guidance, and for giving me this chance. I feel lucky for having both of you as supervisors and you are my example to follow, from a scientific and human point of view.

To my old friends, distributed all over the world but still in contact. Sharing good and bad moments, infinite chats, trips, or maybe just a coffee per year to see how many new grey hairs had appeared. Maru Zamar and Gabi Zambrano, friends for more than 20 years that are still present even when our paths have separated a long time ago. Thank you to Euge Ardiles, Leila Saker, Antonela Taverna, Leti (Lechuga) Ferrero, and Cris Quinteroz, without you my university life would have been a boring way to become nerdier and you always support me and pushed me further. To my Argento/Brazilian friends, Cinchu Martínez, Ximena Saad-Olivera, Matias García (El Tucu), and Merce Arana. You made me feel at home in a new country, with another language and culture, and helped me to "survive" the beaches, carnivals, and 40 degrees of inhuman weather.

To my new friends that I met in Copenhagen. The ones that for different reasons are not in Denmark anymore, Jorge Colmenar (Jorgelito), Mirek Groen, Elishevah van Kooten, Michael Kuffmeier, and Hanna Mary Calcutt. Those first months, being in another continent to the other side of the "lake" and in the other hemisphere, would have been so desolated without you guys, my buddies. The ones that are still here since the beginning, Mafalda Costa, Lene Bentzen, and Lars Kristensen, and the ones that arrived later to my life, Bettina Livermore, Mattia Tagliavento, Giulia Perotti, Laura Clau-

1 INTRODUCTION

One of the main questions that we would like to answer nowadays is, where do we come from? This question is related with a broad range of topics, from biology to astrophysics. For the latter, understanding how our Solar System formed can give us clues and provide pieces of the puzzle. Nevertheless, how can we trace the past and investigate the formation of our Sun and planet Earth? It is a complex and challenging task, however, some clues are provided by the study of other solar-type protostars that are currently forming. These are young sources which are expected to be part of a Solar System like ours. Therefore, the comparison between protostars in different evolutionary stages sheds light on the physical and chemical processes that could have been involved in the formation of our Solar System. It is, then, essential to observe and study these young stages.

This thesis is focussed in getting a better understanding of the low-mass star-formation process and it is outlined as follows. Chapter 1 presents an introduction to the low-mass star-formation process, describing our current knowledge and important caveats about the physical and chemical processes. It starts with a focus on the physics, the observable characteristics that constrain the different evolutionary stages, and a widely discussed topic on how the protostar gains its mass: the luminosity problem. It is followed by an introduction to molecular spectroscopy and the chemistry of star-forming regions, where ice-surface chemistry, complex organic molecules, warm carbon-chain chemistry, and the disk chemistry are discussed in more detail. The chapter ends with a description of a particular star-forming region, the Ophiuchus molecular cloud. The observations presented in the papers that compose this thesis are carried out towards this star-forming region.

Chapter 2 presents the methods, explaining our choice to observe at radio wavelengths and introducing the fundamentals of radio interferometry, describing briefly the telescopes that were used. It is followed by an explanation of how the data are calibrated and a description of the approach taken to interpret the observations, in particular what we measure with the telescope and how to decode this information in order to assess the physics and chemistry of the studied regions.

A summary of the papers that constitute this thesis is presented in Chapter 3, with the main conclusions and future prospects. Here I discuss the results of this thesis in the big picture of low-mass star formation and state my own contributions to the individual papers.

Finally, Chapters 4, 5, and 6 gather papers I, II, and III, respectively.

1.1   Star formation

This section states our current understanding of the low-mass star-formation processes based on models and theoretical constrains, followed by a classification of protostars that depends on observational parameters, and a more detail discussion of the luminosity problem and mass-accretion process.

Low-mass stars, similar to our Sun, forms within giant molecular clouds, when dense regions of molecular gas and dust collapse due to gravity (e.g., Ward-Thompson 2005). Because of the high extinction, star-forming regions are seen as dark structures at optical wavelengths, since the dust absorbs the more energetic photons and re-emits them at longer wavelengths. Therefore, infrared and radio observations are suitable for studying the internal structures of molecular clouds and the star-formation process. Figure 1.1 shows the star forming region NGC 1333 seen in different wavelengths. The region is observed as a dark cloud in the optical regime, while the dust becomes transparent at longer wavelengths and emits at infrared (IR) and radio frequencies.

The classical description of the star-formation process starts with the contraction of a core, where gravity overcomes the local pressure (Fig. 1.2a; Shu et al. 1993). The collapse begins with an isothermal sphere (Larson 1969), where the internal regions present higher densities and a shorter collapsing time. When material is concentrated in the centre, the pressure support is reduced on the external layers and they also collapse due to gravity. The collapse information reaches the external layers through waves that propagate at the sound speed (c_s) and the mass of the isothermal sphere (protostar) grows linearly with the radius $r = c_s t$. The so-called *inside-out collapse* model for formation of solar-type stars (Shu 1977) follows this collapse starting from an isothermal sphere with a density profile $\rho \propto r^{-2}$, and within the collapse radius determined by the sound speed, the density profile flattens, i.e., $\rho \propto r^{-1.5}$ (see Fig. 1.3).

If the initial core has an angular velocity Ω, the angular momentum of a single particle depends on the angle θ between its trajectory and the rotation axis. Therefore, material with different directions is associated with different quantities of angular momentum and reaches the midplane (plane perpendicular to the rotation axis) at different radii (Fig. 1.4; Terebey et al. 1984). The material close to the rotation axis reaches the central source, due to the low angular momentum, while the particles with trajectories $\theta \sim \pi/2$ are deposited in the midplane at a radius r_c, known as *centrifugal radius*. If the collapse is symmetric above and under the equatorial plane, the particles from the upper region will collide with the ones coming from the lower region, dissipating kinetic energy in the direction
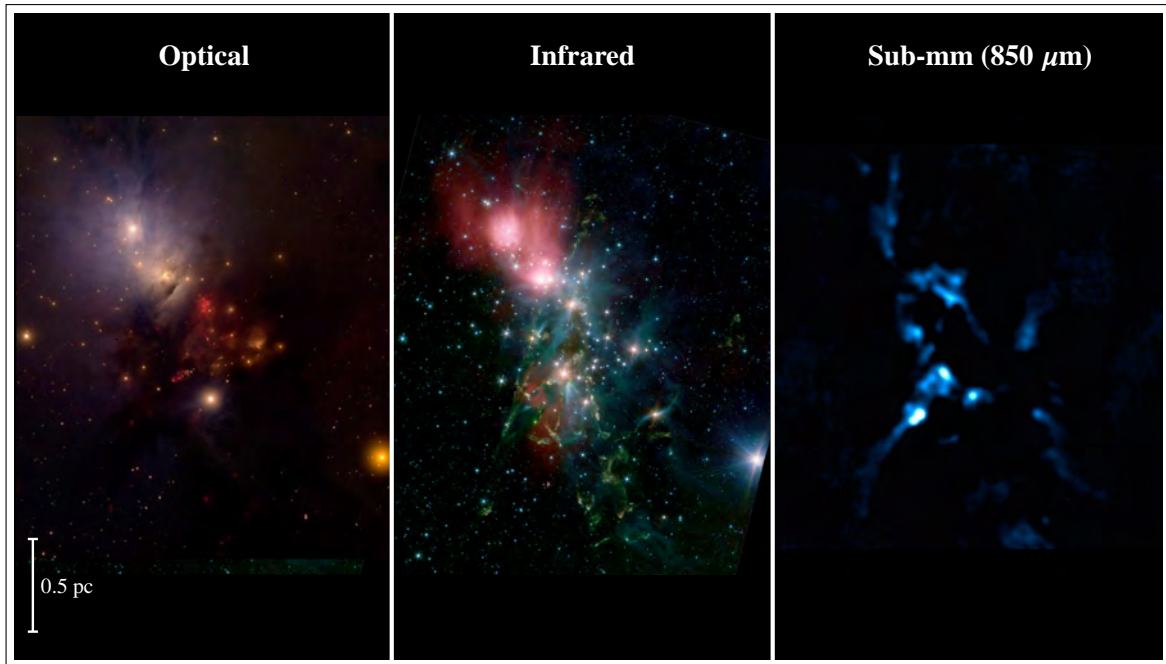
Figure 1.1: The NGC 1333 star forming region at different wavelengths. Credit: T.A. Rector/University of Alaska Anchorage, H. Schweiker/WIYN and NOAO/AURA/NSF; Jørgensen et al. (2006); Kirk et al. (2006).

perpendicular to the midplane and cool down (Hartmann 1998). These particles accumulate in the equatorial plane, retaining the velocity component parallel to the equatorial plane and mixing with the existing material. This process dissipates energy and transfer angular momentum, ending with a rotating disk (Yorke et al. 1993; Canto et al. 1995; Hartmann 1998).

Disk formation was originally thought to be a straight consequence of conservation of angular momentum during the core collapse, however, magnetic fields have important consequences in their formation (e.g., Li et al. 2014). If ideal magnetohydrodynamic (MHD) is assumed, the disk formation is suppressed and this is known as the *magnetic braking catastrophe* (Galli et al. 2006). This is inconsistent with observations, where rotationally-supported disks are detected (e.g., Jørgensen et al. 2009; Harsono et al. 2014; Yen et al. 2015). Some scenarios were proposed in order to avoid the magnetic braking catastrophe, such as non-ideal MHD (e.g., Machida & Matsumoto 2011), misalignment of the magnetic field orientation with the rotational axis (e.g., Joos et al. 2012; Krumholz et al. 2013), or turbulence inherited from large-scales dynamics (e.g., Seifried et al. 2013; Kuffmeier et al. 2017). While disks must form at some point, how early they form and how quickly they grow in mass and size remain key open questions.

To allow the flow of material from the disk into the central protostar, the disk angular momentum needs to be transported away. Friction between adjacent annuli have been proposed to transfer angular
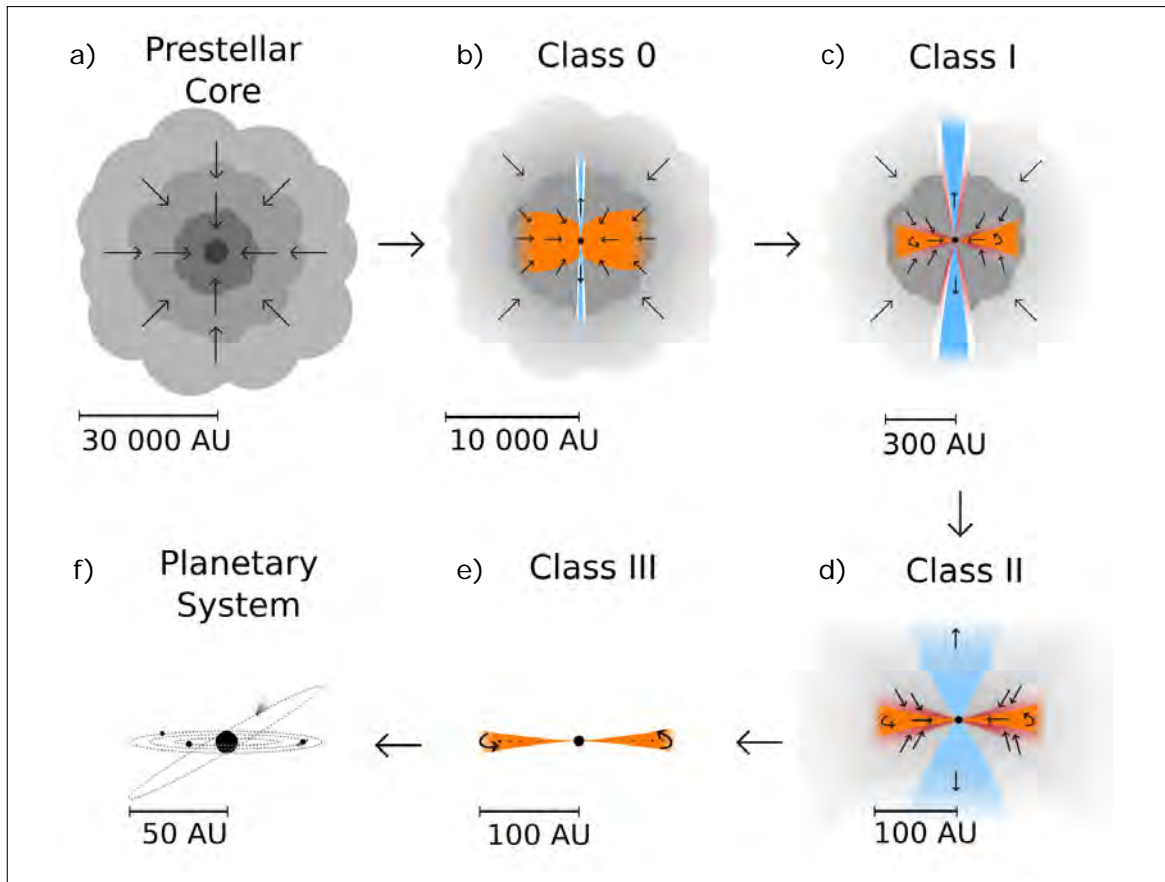
Figure 1.2: Schematic representation of the low-mass star-formation process. *a)* A prestellar core contracts due to gravity. *b)* Class 0: a disk is formed in the equatorial plane, energetic outflows are expelled through the rotational axis, and envelope material infalls into the disk-protostar system. *c)* Class I: a Keplerian disk is formed, the outflow opening angle increases, and material infalls from the envelope to the disk and is accreted from the disk to the potostar. *d)* Class II: dust particles settle into the disk midplane and grow in size, the outflows are very weak, and the envelope material is almost entirely dissipated. *e)* Class III: dust particles grow to planetesimal sizes and the gas content of the disk is dispersed by stellar winds or by accretion into giant planets. *f)* The system ends up with a star surrounded by planets. Credit: M. Persson.

momentum from the inner regions of the disk to the outer parts (Ward-Thompson 2005), while bipolar jets and a strong MHD disk wind have been shown to carry off the disk angular momentum very efficiently (e.g., Fendt & Camenzind 1996; Ouyed & Pudritz 1997; Pudritz et al. 2007). In particular, the jet interacts with the envelope, dissipating and transferring angular momentum to more quiescent material, and producing a low-velocity component known as the *outflow* (Fig. 1.2b). These jets and outflows are observed during the first stages of star formation and are linked to very energetic ejection processes (e.g., Cabrit et al. 1997; Reipurth & Bally 2001).

Accretion and ejection are linked to each other and it is estimated that between 1 and 10% of the accreted mass is being ejected (Cabrit et al. 2010). The jets show high collimation[1] and are

---

[1]The collimation factor R_{coll} is defined as the ratio of the major axis and the minor axis of the jet. Jets with $R_{coll} \geq 10$
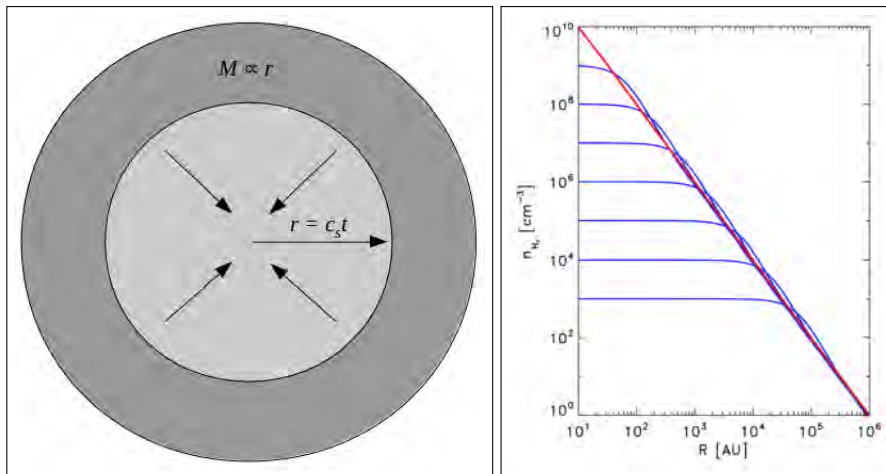
Figure 1.3: Schematic representation of the *inside-out collapse* of an isothermal sphere. *Left*: the collapse starts in the internal regions and the information propagates at the sound speed c_s. *Right*: density distribution as a function of the distance for different values of the central density (blue curves) and the solution for the collapse of a singular isothermal sphere (red curve). Credit: Hartmann (1998) and J. K. Jørgensen.
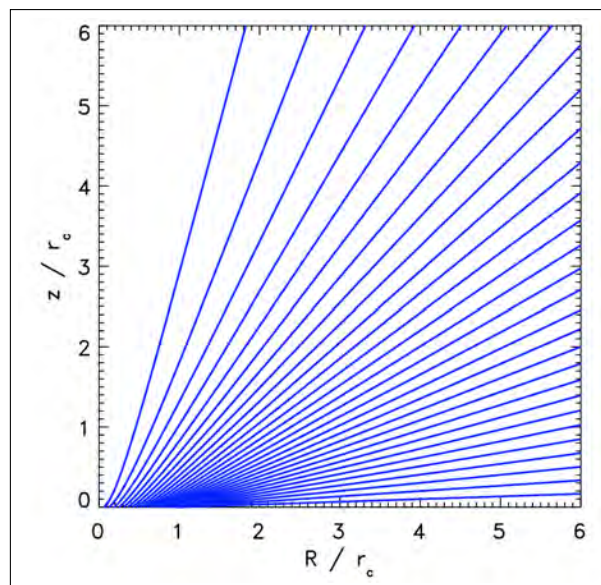
Figure 1.4: Particle trajectories for different values of θ. The material tends to accumulate towards the equatorial plane. Credit: J. K. Jørgensen.

associated with shocked regions. Once the protostar has reached most of its final mass, the accretion rate decreases as well as the ejection rate, and the outflow collimation is reduced. At this stage, the source is surrounded by a disk of gas and dust and becomes visible at optical wavelengths. This phase is named after the prototypical object which defines it, the T Tauri source or stage (Fig. 1.2d; Bertout 1989).

Towards the disk midplane the density is relatively high ($10^5 - 10^{13}$ cm^{-3}) and dust grains grow

---

are classified as highly collimated.
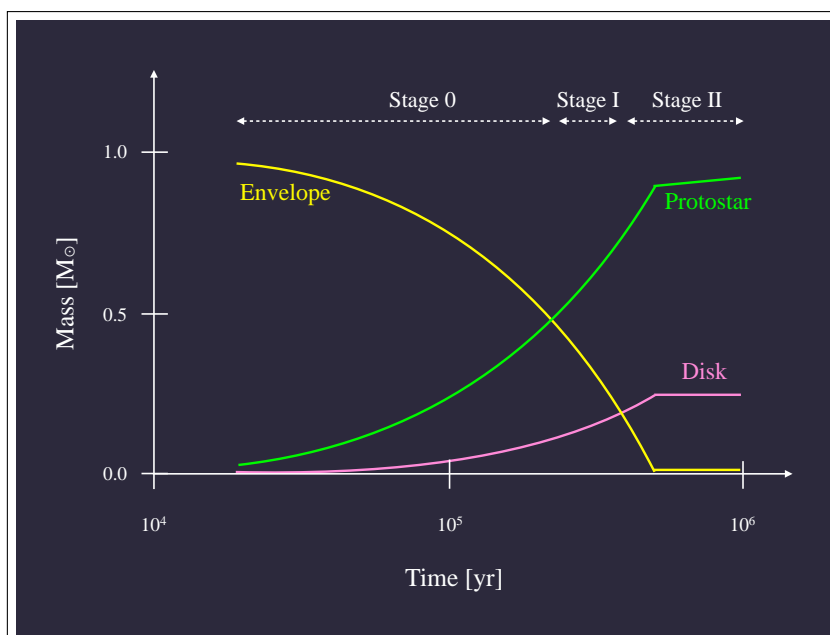
Figure 1.5: Mass evolution as a function of time for the envelope, protostar, and disk components, normalised to the envelope mass. The Stages for the embedded phase are indicated and where taken from Robitaille et al. (2006). Figure adapted from the results from Terebey et al. (1984); Shu et al. (1993) and Hartmann (1998).

through collisions and agglomeration, forming larger particles that can reach planetesimal, proto-planet, and planet sizes (e.g., Birnstiel et al. 2016). The gas in the disk can be accreted by giant planets (Fig. 1.2e), photo-evaporated by the UV radiation from the central source, or dissipated through stellar winds (Muzerolle 2010; Andrews et al. 2011).

When the whole disk is dissipated, the planets that have formed will be visible around the protostar (Fig. 1.2f). The protostar continues to contract until a temperature of $\sim 10^7$ K is reached in the core and hydrogen fusion starts. At this point, the protostar reaches the *zero age main sequence* (ZAMS).

Depending on the mass content between the envelope, disk, and protostar, three physical *Stages* are defined for the embedded phase (Robitaille et al. 2006): Stages 0, I, and II. These Stages should not be confused with the Classes (see Sect. 1.1.1), defined from observations. Figure 1.5 shows the mass evolution as a function of time for the envelope, protostar, and disk components. At Stage 0, the envelope dominates the mass content of the system ($M_{env} > M_\star, M_{disk}$). As material infalls from the envelope onto the disk and accretes from the disk to the protostar, the latter is the dominant component ($M_\star > M_{env}$) at Stage I. Nevertheless, the envelope contribution is still important, i.e., $M_{env} > M_{disk}$. At Stage II, the protostar has almost reached its final mass, the disk grows in mass and size, and the envelope material has been dissipated or incorporated into the system ($M_\star > M_{disk} > M_{env}$).

The physical evolutionary stages discussed above are based on models of young stellar objects

and their associated spectral energy distribution (Robitaille et al. 2006). The analysis of the later, however, historically divided the protostars into four observational Classes, and are discusses in the following section.

1.1.1 Spectral energy distribution

From the collapse until reaching the ZAMS, the protostars are called *young stellar objects* (YSOs; Strom 1972). Since YSOs are deeply embedded in molecular clouds and their mass and luminosity change with time, it is difficult to assign a single temperature and other physical parameters are used in order to classify them. These physical parameters are defined from the *spectral energy distribution* (SED) and the most commonly used to indicate the evolutionary stage of the source are: *(i)* the *infrared spectral index ($\alpha_{\rm IR}$)*, defined from the logarithmic inclination of the SED between 2 and 20 μm (Lada 1987), *(ii)* the *bolometric temperature* ($T_{\rm bol}$), defined as the temperature of a black body having the same mean frequency as the observed continuum spectrum (Myers & Ladd 1993), and *(iii)* the ratio between the submillimetre and bolometric luminosity ($L_{\rm smm}/L_{\rm bol}$), where $L_{\rm smm}$ is calculated for $\lambda \geq 350$ μm (Dunham et al. 2014a). From the shape of the SED, four observational *Classes* are defined: Class 0, I, II, and III, corresponding to the stages illustrated in the cartoon in Fig. 1.2 (see Fig. 1.6; Lada & Wilking 1984; Lada 1987; André et al. 1993).

1.1.1.1 Class 0

Identified by André et al. (1993), these sources have $T_{\rm bol} \leq 70$ K and a ratio of submillimeter to bolometric luminosity ($L_{\rm smm}/L_{\rm bol}$) greater than 0.5%. Their emission usually peaks at sub-millimetre wavelengths with typically undetectable near- to mid- infrared emission (e.g., André et al. 1993; Barsony 1994), reflecting the large quantities of gas and dust in their cold envelopes. Jørgensen et al. (2009) found that the continuum emission excess on small scales (≤ 150 AU), towards a sample of 10 Class 0 sources, can be explained by a disk component, and Maury et al. (2010) found no evidence for large disks with sizes grater than $\sim$100 AU. From gas kinematic studies, only a few Keplerian[2] disks have been identified towards Class 0 sources (e.g., Tobin et al. 2012; Murillo et al. 2013; Lee et al. 2014).

Class 0 sources tend to exhibit massive and powerful outflows, and have been associated with *Herbig Haro* (HH) objects in the near infrared (Herbig 1950; Haro 1952). HH objects are small

---

[2]Keplerian rotation takes place when the specific angular momentum increases as the radius increases, i.e., $v_{\rm rot} \propto r^{-0.5}$
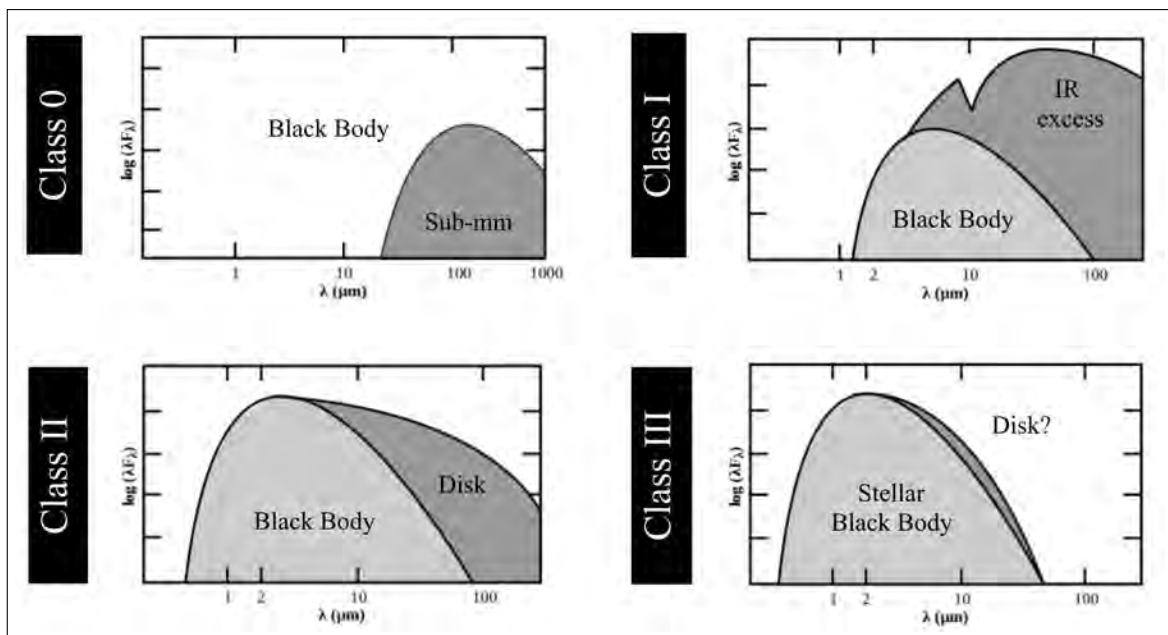
Figure 1.6: Spectral energy distribution (SED) for the different Classes. Figure adapted from and André et al. (1993) and Lada (1999).

nebular-like regions (~0.01 pc) associated with shocked gas, and are detected towards the jet direction. These object reach high velocities ($100 - 500$ km s^{-1}) and reflect the presence of highly energetic jets and, as a consequence, powerful outflows and a high mass accretion rate (e.g., Bontemps et al. 1996).

1.1.1.2   Class I

For Class I sources, the SED peaks between the mid and far infrared with $\alpha_{IR} > 0.3$ (Greene et al. 1994), and is associated with a large infrared excess with a particular absorption feature at 9.7 μm, due to the presence of interstellar silicate in the disk (e.g., Boogert et al. 2015). Their ratio of sub-millimeter to bolometric luminosity is lower than 0.5%, and bolometric temperatures range between 70 and 650 K. Class I sources are also associated with outflows, however, they are less energetic than those of Class 0 sources, reflecting a corresponding decay in the mass accretion rate (Bontemps et al. 1996).

Class I sources are also associated with disks, and the disk radii are expected to grow as the central protostellar masses grow (Aso et al. 2015). Disks radii between 25 and 700 AU have been associated with Class I sources (e.g., Harsono et al. 2014; Sheehan & Eisner 2017; Yen et al. 2017), in agreement with the growth in size as the system evolves (Terebey et al. 1984; Basu 1998). The mass evolution is less clear, however: Jørgensen et al. (2009) for example found no evidence for a disk mass increase

from the Class 0 to I stages.

1.1.1.3 Class II

Class II sources are also know as T Tauri sources, protostars that are observed in the optical regime and show strong emission of chromospheric lines and irregular variability in their intensity (Bertout 1989). The SED of Class II sources can be modelled by adding the contribution of the star, at near infrared wavelengths, and the circumstellar disk, between the near and far infrared (Dullemond & Monnier 2010). They have been associated with $-1.6 < \alpha_{IR} < -0.3$ and $650 < T_{bol} < 1880$ K. The disks associated with Class II sources are known as protoplanetary disks and positive correlations have been found between the dust mass and the protostellar mass (e.g., Ansdell et al. 2016, 2018). In addition, Class II disks show intricate dust structures (e.g., Andrews et al. 2018), where some of them may be the consequence of planet formation (e.g., ALMA Partnership et al. 2015; Bae et al. 2017; Meru et al. 2017). The formation of planets, however, may begin at earlier stages, around Class I sources (e.g., Harsono et al. 2018).

1.1.1.4 Class III

At this stage, the SED can be represented by the emission of a stellar black body with very little (or zero) contribution from the disk and $\alpha_{IR} < -1.6$. In addition, the bolometric temperatures are > 2880 K. Class III sources show similar characteristics than weak T Tauri stars and they represent the last step of the low-mass star-formation process, before arriving at the ZAMS.

Although the general picture of low-mass star formation and the evolution of young stellar objects is relatively well stablished, there are still significant puzzles concerning the details of the physical processes at smaller scales, i.e., when and how quickly the envelope dissipates? How early do disks form and how quickly do they grow in mass and size? How does material accrete from the disk onto the protostar? The following section describes a problem that arises when observations and theory do not match.

1.1.2 The luminosity problem and episodic accretion

One example of a puzzling observational evidence is the so-called *luminosity problem*. The bolometric luminosity at earlier stages results mainly from the gravitational energy released by the material

accreted onto the surface of the protostar (Kenyon & Hartmann 1995). The *mass accretion rate* ($\dot{M}_{\mathrm{acc}}$ = M/t) is related with L_{bol} by

$$\dot{M}_{\mathrm{acc}} = \frac{L_{\mathrm{bol}} R_\star}{G M_\star} , \qquad (1.1)$$

where $R_\star$ is the protostellar radius and G the gravitational constant. The big unknowns from Equation 1.1 are the mass accretion rate and the protostellar mass, however, $\dot{M}_{\mathrm{acc}}$ can be estimated from observations and by taking some assumptions. For a typical Class I protostar, where $R_\star = 3$ R$_\odot$, $M_\star = 1$ M$_\odot$, and $L_{\mathrm{bol}} = 1$ L$_\odot$ can be assumed (Stahler et al. 1980), a mass accretion rate of $\sim 1 \times 10^{-7}$ M$_\odot$ yr^{-1} is estimated, implying a lifetime of ~ 10 Myr. Nevertheless, this lifetime is inconsistent with derived values for Class I sources (≤ 0.78 Myr Dunham et al. 2015; Kristensen & Dunham 2018).

Another approach is to calculate the mass accretion rate by assuming a lifetime of 0.78 Myr. This results in $\dot{M}_{\mathrm{acc}} = 1.3 \times 10^{-6}$ M$_\odot$ yr^{-1} for a 1 M$_\star$ protostar and, employing Eq. 1.1, a bolometric luminosity ≥ 13 L$_\odot$ is found. Again, this value is inconsistent with observations, where typical bolometric luminosities are ~ 1 L$_\odot$. This inconsistency is know as the *luminosity problem* (Kenyon & Hartmann 1995; Dunham et al. 2014a; Audard et al. 2014).

In order to reconcile theory with observations, a time-variable accretion rate onto the protostar is proposed (Kenyon & Hartmann 1995; White et al. 2007; Evans et al. 2009; Vorobyov & Basu 2010; Dunham & Vorobyov 2012; Audard et al. 2014; Dunham et al. 2014a). Material infalling from the envelope accumulates in the disk and increases the disk local density. This generates an instability in the disk (Frank et al. 1992), which later promotes a higher accretion rate of material from the disk to the protostar. In this time-variable or *episodic accretion* scenario the protostar spends most of its lifetime in a low state ($10^3 - 10^4$ yr), with low mass accretion rate ($\dot{M}_{\mathrm{acc}} \leq 10^{-6}$ M$_\odot$ yr^{-1}), and accretes a significant quantity of mass (a few 10^{-5} M$_\odot$ yr^{-1}) in short bursts ($\leq 100-200$ yr; Vorobyov & Basu 2010; Dunham et al. 2014a).

The episodic accretion scenario explains the low average L_{bol} of protostars, the presence of knots or bullets in outflows (e.g., Reipurth 1989; Arce et al. 2013), and the observed change in the visual magnitude of some T Tauri stars. For the latter, when the protostar shows a change of magnitude is it said to be experiencing a FU Ori[3] event (Bertout 1989; Reipurth 1990; Hartmann & Kenyon 1996). Historically, FU Ori events have been associated with T Tauri stars, since their visual magnitudes

---

[3]Named after the prototype FU Orionis

could be observed (e.g., Kenyon 1999). For more deeply embedded objects, the chemistry plays an important role: the high luminosity during the accretion burst heats up more material and moves the evaporation radii of molecules, such as CO, to larger distances from the protostar (Visser 2013; Audard et al. 2014). Therefore, the comparison between the observed and expected radial distribution of molecular transitions provides clues to the accretion history of the source (e.g., Jørgensen et al. 2013, 2015; Frimann et al. 2016a).

The luminosity problem and the episodic-accretion scenario are discussed in more detail in paper II (Chapter 5), where the improvement in sensitivity and angular resolution allows us to estimate protostellar masses. Therefore, one less assumption is employed in Eq. 1.1, providing more empirical results.

The chemistry of low-mass star-forming regions is discussed in the following section, where an introduction to molecular spectroscopy is presented and the chemistry towards different evolutionary stages is analysed.

1.2 Chemistry

As discussed in the previous Section, the physical parameters of protostars (e.g., α_{IR}, T_{bol}, L_{bol}) can be estimated by analysing the SED, which provides information about the dust distribution and properties. Nevertheless, the gas content cannot be assessed by this approach and the observations of molecular transitions are suitable for this purpose. Molecules are excellent diagnostics of the physical conditions and processes from a wide range of astronomical environments, such as the interstellar chemical evolution (Herbst & van Dishoeck 2009) and the formation of planets (Öberg et al. 2011a). The following section discuss the theory of molecular spectroscopy and what to expect from observations.

1.2.1 Molecular spectroscopy

The energy levels of a given molecule are a complex combination of *electronic* states E_{elec}, *vibrational* states E_{vib}, and *rotational* states E_{rot}, where the total energy E_{total} is the sum of each component, i.e.,

$$E_{total} = E_{elec} + E_{vib} + E_{rot}. \tag{1.2}$$

Different transitions are associated to different wavelength ranges of the spectrum, depending on

the amount of energy needed to excite a given level. Rotational, vibrational, and electronic transitions are commonly observed at radio, infrared, and optical wavelengths, respectively. Cold environments, such as star-forming regions, present ideal conditions to populate the rotational levels of a molecule (e.g., CO; Ungerechts & Thaddeus 1987). For a diatomic molecule (composed of two atoms), its configuration is seen as a rigid rotor and the energy needed to excite a rotational state is given by

$$E_{\mathrm{rot}} = \frac{\hbar^2}{2I} J(J+1), \tag{1.3}$$

where $\hbar$ is the reduced Planck constant, I the moment of inertia of the molecule, and J the rotational quantum number.

In order to excite vibrational states, higher energies are needed, commonly found at infrared wavelengths. This regime is crucial for the detection of molecules condensed into interstellar ices, where the lines are seen in absorption towards, for example, inner warm disks of Class II sources (Pontoppidan et al. 2005; Honda et al. 2009). In addition, shocked regions are exposed to high energetic processes and show distinctive signatures at NIR (e.g., the H_2 transition at 2.12 μm; Wilking et al. 1990). The vibration of a molecule can be represented by a simple harmonic oscillator of natural frequency ν_0, i.e.,

$$E_{\mathrm{vib}} = 2\pi\nu_0\hbar(v + 1/2), \tag{1.4}$$

where v is the vibrational quantum number. The transition at infrared wavelengths can be *pure vibrational*, when only the vibrational quantum number changes, or *ro-vibrational*, when both the vibrational and rotational quantum numbers change.

Electronic transitions within a molecule require higher energies and they are commonly observed in optical or UV wavelengths. One example is the detection of N_2 towards the reddened star HD 124314 at 958.6 Å(Knauth et al. 2004). As for ro-vibrational transitions, within different electronic states the vibrational and rotational quantum numbers can also change. Figure 1.2.1 shows a representation of rotational and vibrational levels in two different electronic states of a diatomic molecule.

For molecules with nuclear spin (I)[4] different from zero, or the presence of an unpaired electron with spin $s = 1/2$, the rotational levels can be divided into sub-levels and the allowed transitions between the sub-levels are called hyperfine or fine splitting. The effect of this splitting is the separation

---
[4]Note that the same letter I is used for the momentum of inertia and the nuclear spin.
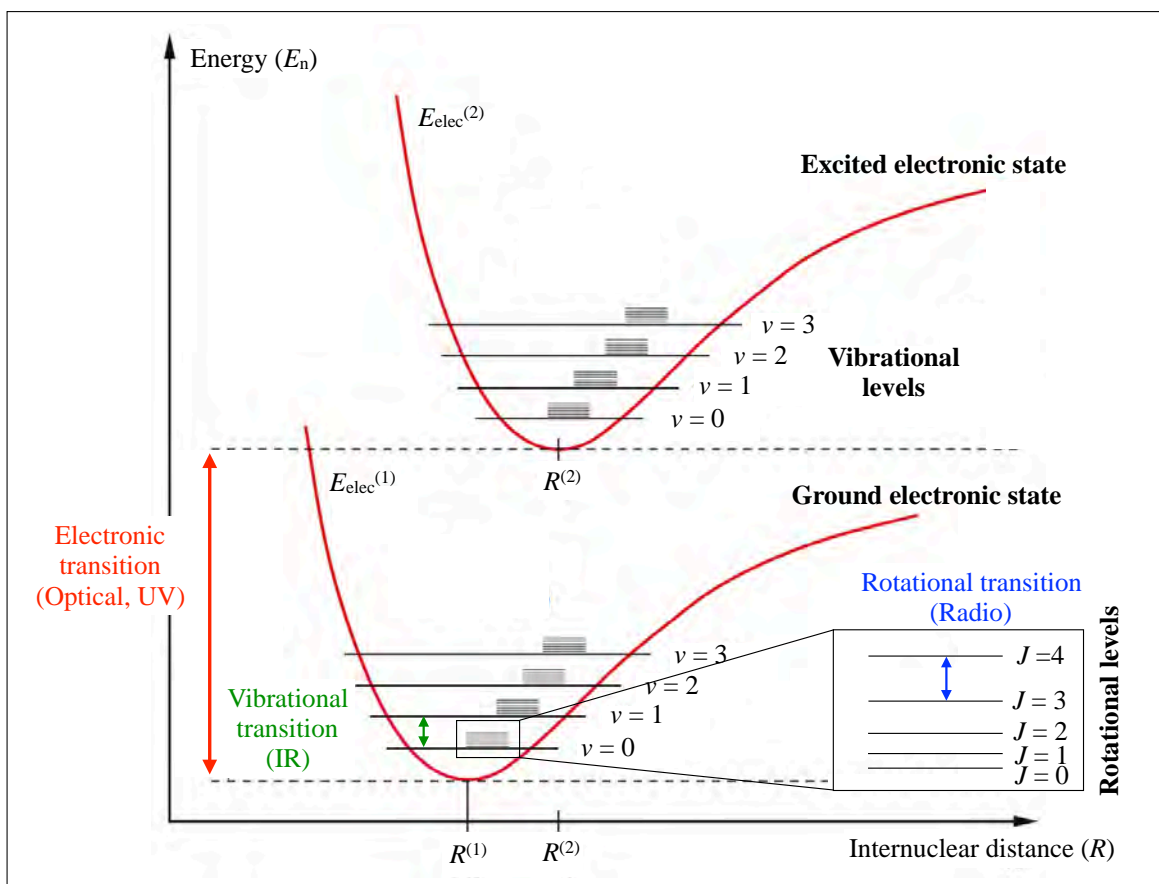
Figure 1.7: Schematic representation of electronic, vibrational, and rotational levels of a diatomic molecule, indicating the spectral range were each transition is expected to be detected. Figure adapted from Demtroderet al. (2006).

of the line profile (usually fitted with a Gaussian distribution) into two or more components relatively close to each other. The separation between the hyperfine components depends mainly on the value of F, the quantum number associated with the hyperfine splitting and defined as: $F = I + J$, where J is the sum of the rotational angular momentum N, the electronic angular momentum L, and the total electronic spin $S = \sum s$. For most of the pure rotational transitions observed at radio wavelengths, the molecule resides in the ground electronic state, i.e., $L = 0$, therefore, $J = N + S$. For the particular case where the electrons are paired ($S = 0$), $J = N$ and the hyperfine splitting arise solely from the fact the the nuclear spins are not zero. Figure 1.8 shows the example of the hyperfine splitting associated with the CN molecule for transitions between the rotational levels 2 and 1. These CN hyperfine transitions are detected towards the Class I source, Oph-IRS 67, and form part of the third paper, discussed in Sect. 6.

The cold and dense environment associated with star-forming regions promotes the detection of the rotational transitions of molecules at long wavelengths (sub-mm, mm, and cm; McGuire 2018).
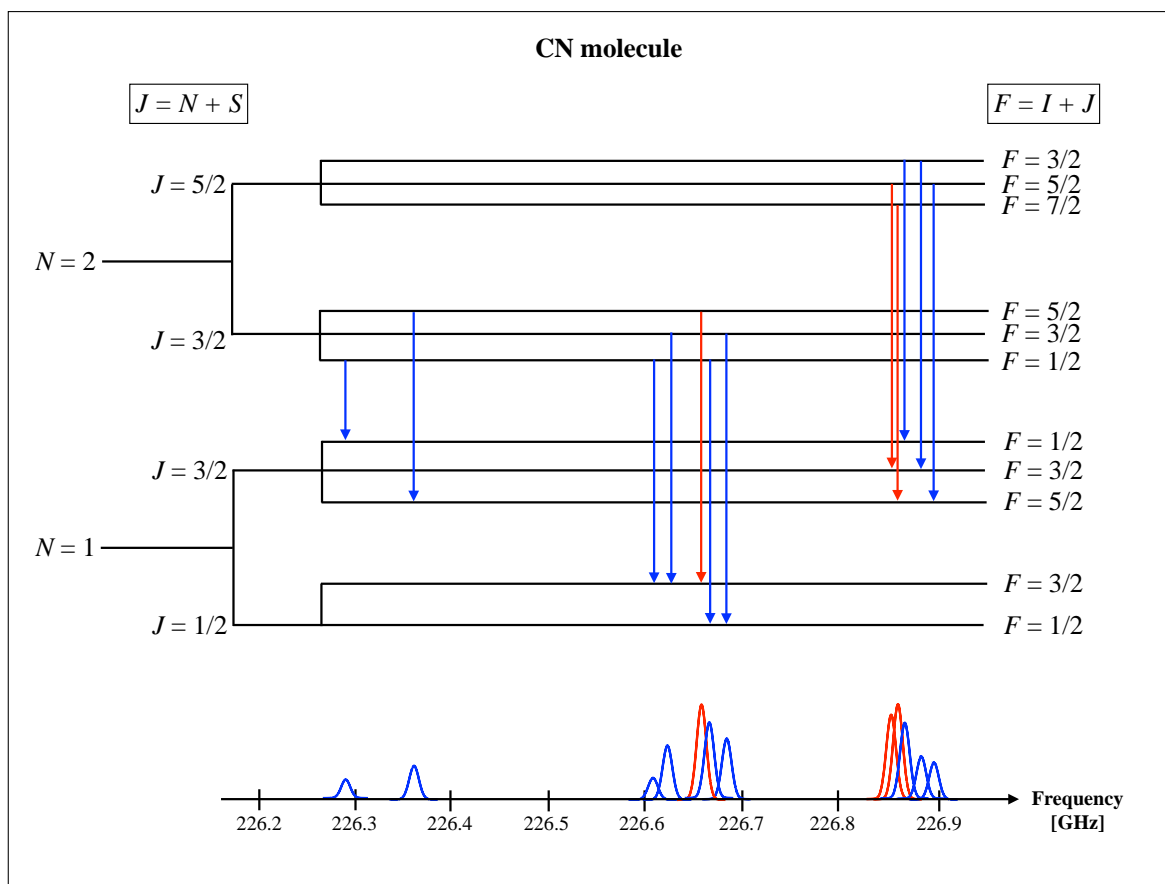
Figure 1.8: Hyperfine transitions of CN between the rotational levels $N = 2-1$, and their frequency on the spectrum. The red lines represent the three most probable transitions.

Figure 1.9 shows that most of the first molecular detections towards star-forming regions were done at these long wavelengths. The most abundant molecule in the interstellar medium is H_2, however, it is not observed at radio wavelength. It is composed of two equal H nuclei, therefore it lacks an electric dipole and this prevents allowed rotational transitions to occur. In addition, due to its small moment of inertia (see Eq 1.3), the rotational levels are widely spaced requiring high energies to be excited (~ 500 K). Consequently, its first allowed rotational transition ($J = 2-0$) occurs at 28.2 μm, tracing warmer environments. Therefore, in order to trace the cold molecular content of the interstellar medium, other molecules have to be studied.

The second most common molecule in molecular clouds is carbon monoxide, CO, with a canonical abundance with respect to H_2 of $\sim 10^{-4}$ (van Dishoeck et al. 1992). CO has a permanent dipole moment, promoting rotational transitions and excitation at low temperatures ($\gtrsim 5.5$ K), and requires high energies to dissociate (11.09 eV), thus it remains molecular. CO is, therefore, a common tracer of the mass content in molecular clouds.
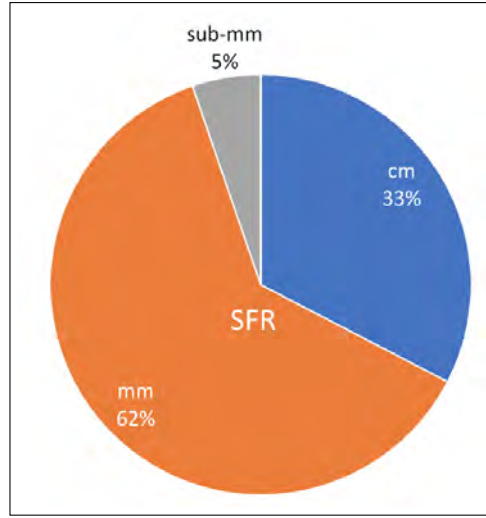
Figure 1.9: Percentage of first molecular detections towards star-forming regions. Figure adapted from McGuire (2018).

The excitation of a molecule can be radiative (absorption of a photon) or collisional (mainly with H_2). In particular, the dense environments of molecular clouds promote the collisional excitation. Once the molecule is excited, it de-excites and goes back to the ground level (where the energy is minimum). De-excitation can also be radiative or collisional. For radiative (or spontaneous) de-excitation, a photon is emitted at a particular energy and wavelength (line emission). The emission is spontaneous and occurs at a rate that is determined by the Einstein A_{ul} coefficient, from the upper state u to the lower state l. If a collisional de-excitation occurs, no radiation is emitted and the excess of energy is converted into kinetic energy.

All molecular transitions are associated with a *critical density*, n_{crit}, at which the rate of excitation by collisions is equal to the rate of spontaneous decay, i.e.,

$$n_{\mathrm{crit}} = \frac{A_{ul}}{C_{lu}},\tag{1.5}$$

where C_{lu} is the collisional rate coefficient. At densities higher than n_{crit}, the excitation is dominated by collisions and the level populations are said to be in *local thermodynamic equilibrium* (LTE), and the upper-state populations are thermalised. At densities lower than n_{crit} the population in the upper state is not highly populated, the level populations are *sub-thermal*, and LTE is not applicable.

The huge diversity of molecular species (from diatomic to molecules with 70 atoms) detected in the interstellar and circumstellar medium reflects the different physical conditions found in the space (McGuire 2018). In particular, low-mass star-forming regions are line-rich and the chemistry

observed towards these regions is discussed in the following chapter.

1.2.2 The chemistry through the star formation history

The process of low-mass-star and planet formation involves a wide range of spatial scales (up to $\sim 10^4$ AU), temperatures (up to ~ 1000 K), and densities (up to $\sim 10^{13}$ cm^{-3}; van Dishoeck 2018). Therefore, different molecular transitions are excellent diagnostics of the physical conditions and processes involved from the very young stages (Class 0 sources) up to the formation of a planetary system (Class III sources). Observations have shown the diversity of molecular transitions tracing different physics, such as CO isotopologues probing high gas-column densities (e.g., Bally et al. 1987; Heyer et al. 1987), sulphur-bearing species tracing shocked regions (e.g., Charnley 1997; Tabone et al. 2017), and deuterated species probing cold regions (e.g., Jørgensen et al. 2011; Öberg et al. 2015; Aikawa et al. 2018), among others (for a recent review of molecular detections, see McGuire 2018).

It is still an open question how the chemical diversity of Class 0 sources can be transferred towards more evolved stages, to the disk content and to future planetesimals. Two scenarios exist: *inheritance* or *reset*. In the inheritance scenario, the molecules are preserved through the entire star-formation process, while, on the other hand, multiple physical processes can promote a chemical reset, i.e., processing of material strong enough to destroy its memory of past chemistry (Pontoppidan et al. 2014). For this to be better understood, it is essential to compare the chemical composition of sources within different evolutionary stages.

1.2.2.1 Grain surfaces

Freeze-out of molecules on the surfaces of dust grains, and subsequent chemical reactions, promote the formation of new species that cannot readily be formed in the gas phase (Tielens & Hagen 1982; Herbst & van Dishoeck 2009). Surface chemistry thus controls the composition not only of the icy mantles in dense clouds and cold disk midplanes, but also of the molecular gas desorbed from the grains in the vicinity of cloud edges, shocks, and the radiation fields of young stellar objects (e.g., Boogert et al. 2015). Water ice is the dominant ice species and is produced on the grain surface by sequential hydrogenation of oxygen atoms, as well as via the more complex hydrogenation of O_2 and O_3 (Tielens & Hagen 1982). When CO freeze-out onto dust mantles at temperatures below 20 K (Cuppen et al. 2009), successive hydrogenation of CO will form CH_3OH and more complex species (e.g., Watanabe & Kouchi 2002; Öberg et al. 2009; Garrod et al. 2007). Molecules that form on dust

mantles can, later on, desorb and enrich the gas-phase chemistry. Possible desorption mechanisms are photodesorption (e.g., Öberg et al. 2009), reactive desorption (e.g., Drozdovskaya et al. 2015), sputtering (e.g., Jones et al. 1996), and thermal desorption such as elevated dust temperatures (e.g., Herbst & van Dishoeck 2009).

Towards star-forming regions, molecules desorbe from dust mantles at specific radii from the protostar, according to their surface binding energies. Figure 1.10 shows a cartoon representing the evolution of material from the prestellar core stage through the collapsing envelope into the proto-planetary disk. In the prestellar core stage the grains are covered in water ice, and CO freeze-out, promoting the formation of more complex species by hydrogenation of CO. As the density and temperature increase, weakly bound ices evaporate from the grains and, when the envelope temperature reaches ~100 K, even more strongly bound ices start to evaporate. Once material enters the disk, it will rapidly move to the cold midplane where additional freeze-out and grain surface chemistry occur (Herbst & van Dishoeck 2009).

1.2.2.2 Hot corinos

In cold regions (~10 K), the *complex organic molecules* (COMs; defined as molecules with 6 or more atoms) formed on ice-covered dust-grain surfaces are called the *first generation* complex molecules (Garrod et al. 2006; Herbst & van Dishoeck 2009; Chuang et al. 2016; Walsh et al. 2016). The freeze-out of CO onto dust grains is followed by hydrogenation and formation of more complex species. Close to the protostar where the dust temperature is $\gtrsim$ 100 K, COMs sublimate from the dust surface and enrich the gas-phase. This $\gtrsim$ 100 K region is called the *hot core*[5] (Ceccarelli 2004). The sublimated molecules thus provide an important input for gas-phase reactions and formation of *second generation* of complex organic molecules (Charnley et al. 1992; Herbst & van Dishoeck 2009).

The hot-corino chemistry has been observed mainly towards Class 0 sources (e.g., Jørgensen et al. 2012; Maury et al. 2014; Taquet et al. 2015; Codella et al. 2016), where the number of detected COMs can be as high as 100 (Jørgensen et al. 2016). Figure 1.11 shows an example of the line-rich spectrum towards the hot-corino source IRAS 16293−2422. Meanwhile, faint CH_3OH emission is seen towards Class I sources (e.g., Lindberg et al. 2014) and only two complex molecules, CH_3CN and CH_3OH, have been detected so far towards Class II sources, and only barely (e.g., Öberg et al. 2015; Walsh

---

[5]*Hot corinos* is the term used for low-mass hot cores
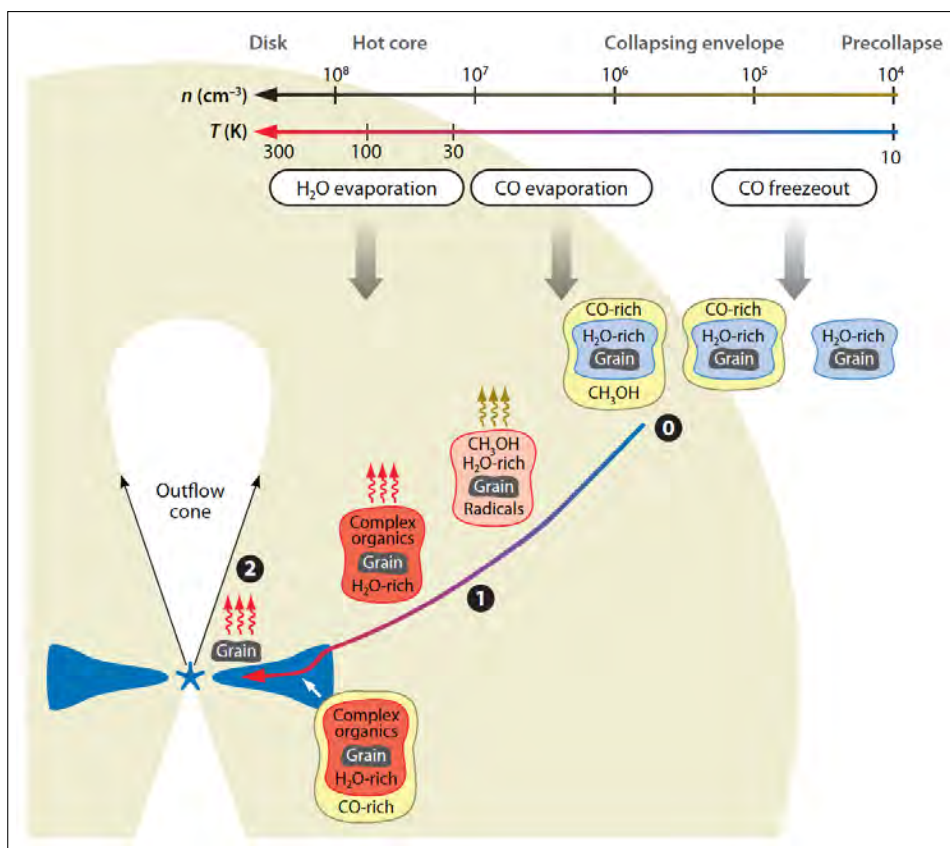
Figure 1.10: Cartoon representation of the evolution of material from the prestellar core stage through the collapsing envelope into a protoplanetary disk. The temperature and density scales of the envelope are shown, together with the regions where freeze-out and evaporation dominate. The indexes 0, and 1 represent the formation of zeroth- and first- generation molecules, respectively, while the index 2 stands for regions where complex species are expected to be present in the gas phase. Figure from Herbst & van Dishoeck (2009).

et al. 2016). This suggest that the amount of material in the inner 100 K zone towards Class 0 sources is much higher than towards more evolved sources.

1.2.2.3 Warm-carbon-chain chemistry

The warm-carbon-chain chemistry (WCCC) has been invoked to explain the large amount of carbon-chain molecules detected towards some Class 0 sources (e.g., Sakai et al. 2008, 2009). Sakai & Yamamoto (2013) propose that if the collapsing time is short ($<10^6$ yr), the atomic carbon is not efficiently locked up in gas-phase CO, instead, carbon is mainly depleted onto dust grains. This atomic carbon forms CH_4 on the grain surfaces through hydrogenation reactions, and CH_4 sublimates from dust mantles at a temperature of 30 K. The presence of CH_4 in the gas-phase is, therefore, decisive for the subsequent formation of carbon-chain molecules. Since CH_4 sublimates at 30 K, carbon-chain molecules are expected to be found on larger spatial scales than complex organic molecules which
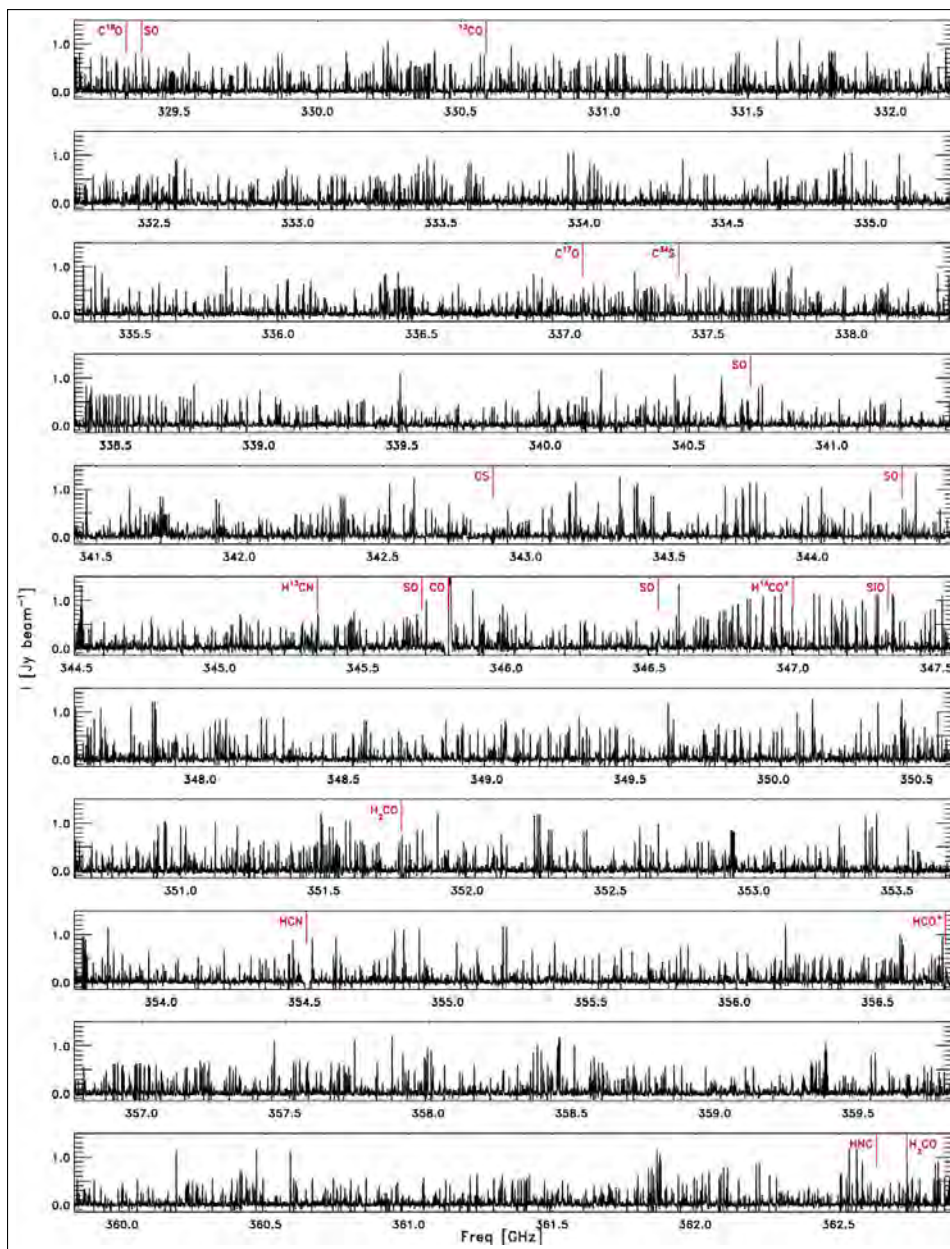
Figure 1.11: Spectrum towards the Class 0 hot-corino source, IRAS 16293−2422. The vertical red lines show the frequencies of a few key species. Figure from Jørgensen et al. (2016).

sublimate at ∼100 K.

A consequence of the warm-carbon-chain chemistry is the inhibition of complex organic molecule formation: since atomic carbon is depleted onto dust grains, there is less carbon available to form CO in the gas-phase, therefore, less CO available for the formation of more complex species on the surface of dust grains. Figure 1.12 shows a schematic representation of both hot corino and WCCC sources. The prototypical WCCC sources are L1527 (Sakai et al. 2008) and IRAS 15398-3359 (Sakai et al. 2009), where species as complex as HC$_9$N have been detected. To the present, only Class 0 and Class
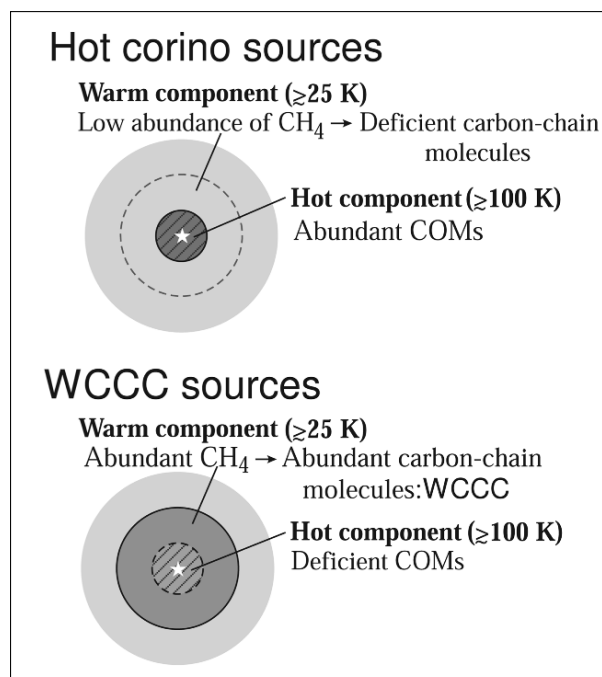
Figure 1.12: Schematic representation of the hot-corino and WCCC sources, indicating the regions where COMs and carbon-chain molecules are expected to be seen. Figure from Sakai & Yamamoto (2013).

0/I sources have been associated with the WCCC (Higuchi et al. 2018; Law et al. 2018).

1.2.2.4 Class I sources

From a chemical point of view, there is a huge gap between the chemically rich Class 0 sources (Jørgensen et al. 2009; Sakai & Yamamoto 2013; Jørgensen et al. 2016), and Class II sources, where molecular transitions are hardly detected (Öberg et al. 2011b; Walsh et al. 2016). Therefore, the observation and study of the chemical content towards Class I sources is essential to understand the chemical evolution across the embedded stages and, at the same time, the physical processes involved in such evolution.

Circumstellar disks provide the initial chemical conditions for planet formation and are associated with complex morphologies, where the density, temperature, and dust grain sizes change not only in the radial, but also in the vertical direction. The temperature can vary from >1000 K in the inner disk and upper layers, to ≤10 K in the outer midplane, while the density can be as high as 10^{13} cm^{-3} in the inner midplane down to 10^5 cm^{-3} in the upper outer layers (e.g., van Dishoeck 2018; Kamp 2019). In addition, due to the flared structure, the UV radiation from the central source can reach the upper layers of the disk, setting up a *photon dominated region* (PDR) structure in the vertical direction. Dust grains settle to the midplane and grow in size, forming larger particles and future planetesimals
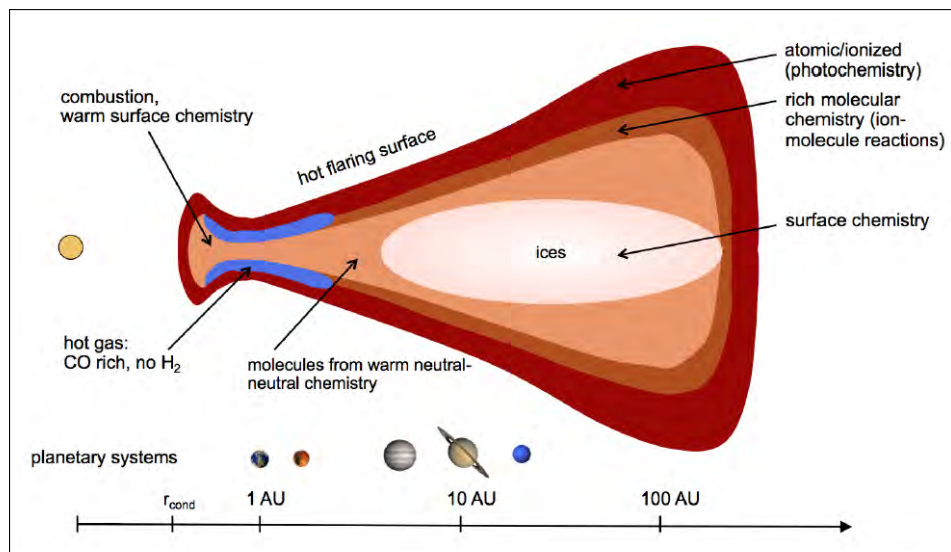
Figure 1.13: Chemical structure of a planet forming disk showing the different layers associated with different chemistry. Figure from Kamp (2019).

(for a review, see Henning & Semenov 2013; Dutrey et al. 2014; Kamp 2019). Figure 1.13 shows a schematic representation of a typical disk. Theoretically, the disk can be divided in three main layers:

- a hot ionized/atomic layer in which photochemistry is particularly important and depends strongly on the strength and shape of the radiation field,

- a warm molecular layer (30−70 K) in which ion-molecule chemistry dominates. This region is partly shielded from stellar and interstellar UV/X-ray radiation, allowing a rich molecular chemistry, and

- a cold icy midplane in which cosmic ray ionization and reactions on grain surfaces dominate.

Recent studies focused on characterising the gas kinematics towards Class I sources have detected some of the most abundant species, i.e., ^{13}CO, $C^{18}O$ (Harsono et al. 2014; Yen et al. 2015), HCO^+, and HCN (Jørgensen et al. 2009). The main purpose of those studies was to identify Keplerian motions and, thus, infer the presence of circumstellar disks. Consequently, the chemistry towards Class I sources has not been investigated in great detail.

For more evolved systems (Class II sources), the chemistry is difficult to constrain observationally, since they are associated with a low gas column density (e.g., Ansdell et al. 2016; Walsh et al. 2016). Nevertheless, a chemical trend can be established by analysing the chemistry of earlier stages, such as Class I sources, thereby linking the line-rich Class 0 sources with emerging Class II disks.
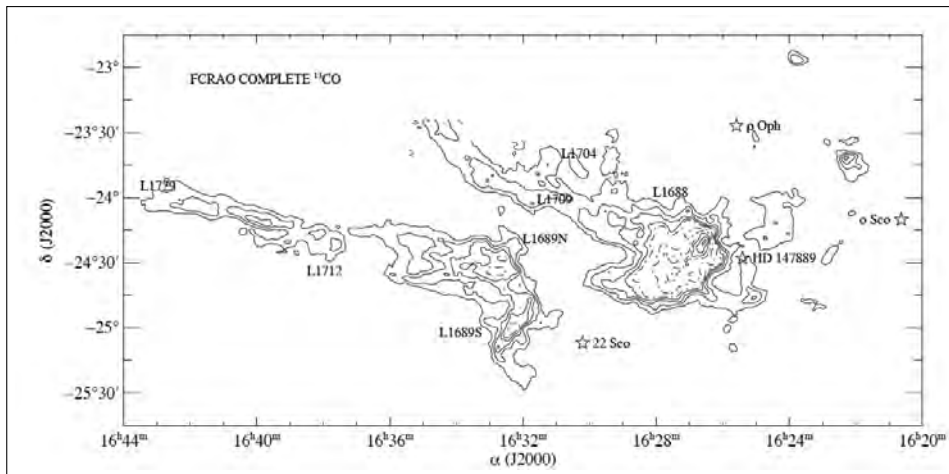
Figure 1.14: A ^{13}CO map of the Ophiuchus cloud complex, where the major clouds are labeled with their Lynds designations. Figure from Wilking et al. (2008).

1.3 The Ophiuchus star-forming region

The focus of this thesis is the observational study of Class I young stellar objects in the Ophiuchus molecular cloud, where the targeted sources are all well-characterised through mid-infrared and sub-millimeter surveys (Jørgensen et al. 2008).

Ophiuchus is one of the closest low-mass star-forming regions, with a distance (*d*) of 139 ± 6 pc (Mamajek 2008), mass of $\sim 10^4$ M$_\odot$, and extent of $\sim$20 pc (de Geus et al. 1990; Loren et al. 1990). It is distinguished for its high density of YSOs ($\sim$300; Wilking et al. 2008), which have been studied through a broad spectral range: in radio (André et al. 1987; Leous et al. 1991; Mezger et al. 1992; Bontemps et al. 1996), millimetre (André et al. 1990), infrared (Young et al. 1986; Greene & Young 1992; Barsony et al. 1997; Luhman & Rieke 1999; Bontemps et al. 2001; Wilking et al. 2001; Allen et al. 2002; Padgett et al. 2008), optical wavelengths (Wilking et al. 1987, 2005), and X-rays (Montmerle 1983; Casanova et al. 1995; Grosso et al. 2000; Imanishi et al. 2001; Ozawa et al. 2005). Within the protostars detected towards Ophiuchus, 27 YSOs have been classified between Class 0 and I sources, 44 between Class I and II sources, 179 as Class II sources, and 42 as Class III sources (Zhang & Wang 2009).

The main cloud of Ophiuchus has been divided into sub-clouds, where the richest one in star formation is L1688 (named from the Lynds catalogue of dark nebulae; Lynds 1962). Figure 1.14 shows a ^{13}CO map of the Ophiuchus molecular cloud, distinguishing each sub-cloud (Loren 1989). Meanwhile, L1688 has been divided in smaller regions from Oph-A through Oph-F (see Fig. 1.15). The sources presented in this thesis (Chapters 4, 5, and 6) are part of the L1688 and L1689S sub-
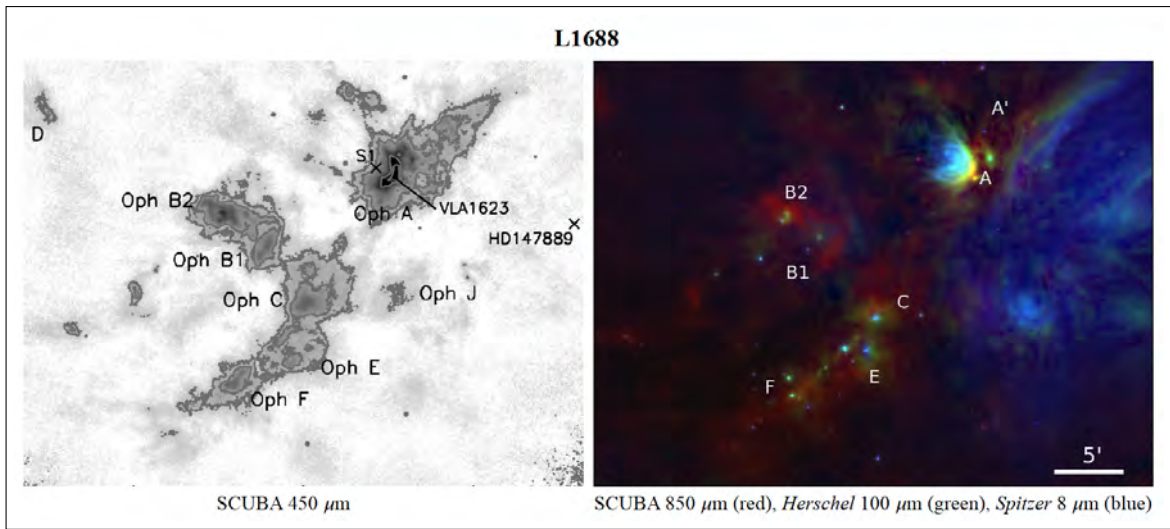
Figure 1.15: Zoom in of the L1688 cloud. Emission at 450 μm (*left*) and three-colour image combining near-infrared, far-infrared, and sub-millimeter observations (*right*). Figure adapted from Pattle et al. (2015).

clouds.

1.4   Goal

The main goal of this thesis is to link the physical and chemical evolution between deeply embedded Class 0 sources and the initial conditions of emerging circumstellar disks, by studying the chemical content and its correlation with the physical parameters of Class I sources. For this, we compare the chemistry within a sample of Class I sources, and between other evolutionary stages.

In order to reach our goals, we use interferometric observations in the submillimeter regime towards a sample of Class I sources located in the Ophiuchus molecular cloud, to analyse the dust and gas emission from continuum and molecular transitions, respectively. The use of interferometers allow us to probe disk scales and filter-out more extended emission related to envelope scales. The next chapter describes the basis of interferometric observations, the data calibration process, and the interpretation of the observations.

2 METHODS

Our atmosphere (mainly H_2O, O_2, N_2, and CO_2) absorbs radiation from space within a broad range of the electromagnetic spectrum. Figure 2.1 shows the fraction of radiation blocked by the atmosphere as a function of wavelength, highlighting the spectral windows where ground-based observations are suitable. If the blocked fraction is too high, observations from space telescopes have to be carried out. The fact that the atmosphere is completely transparent at radio wavelengths facilitates radio observations and telescopes can range from single-dish antennas to kilometer-size interferometer arrays.

As described in Sect. 1.1 and 1.2, the study of low-mass star-forming regions is best done at long wavelengths (IR, sub-mm, and radio), since these regions are related with cold environments. In addition, the rotational spectra of multiple species lie within the sub-mm, mm, and cm regime. Radio astronomy is, therefore, a powerful tool for understanding the low-mass star-formation process and for exploring the chemical richness of multiple astronomical sources.

In the next section we discuss the basis of interferometry and explain how we do the observations, what is the output of the telescope, and how we interpret the data in order to achieve a scientific knowledge.

2.1 Fundamentals of Interferometry

Following the criteria of Rayleigh, the angular resolution (θ) of a telescope is proportional to the wavelength (λ) and inversely proportional to the diameter of the telescope (D), i.e., $\theta \sim \lambda/D$. Therefore, the longer the wavelength, the larger the diameter of the telescope has to be, in order to keep a certain angular resolution. The construction and maintenance of big telescopes provide considerable engineering challenges. Figure 2.2 shows two of the biggest radio telescopes: Arecibo, located in Puerto Rico, with a diameter of 305 m, and the Five-hundred-meter Aperture Spherical radio Telescope (FAST), located in China. Despite the large dimensions, these telescopes reach angular resolutions of $\sim 10''$ for observations at centimeter wavelengths, while optical telescopes easily reach $\sim 1''$ of angular resolution with a diameter of 1 m. The optimal way of improving the angular resolution, without the need for building kilometer-sized structures, is through interferometry.

Radio interferometry is a technique that combines the collected power of individual antennas in
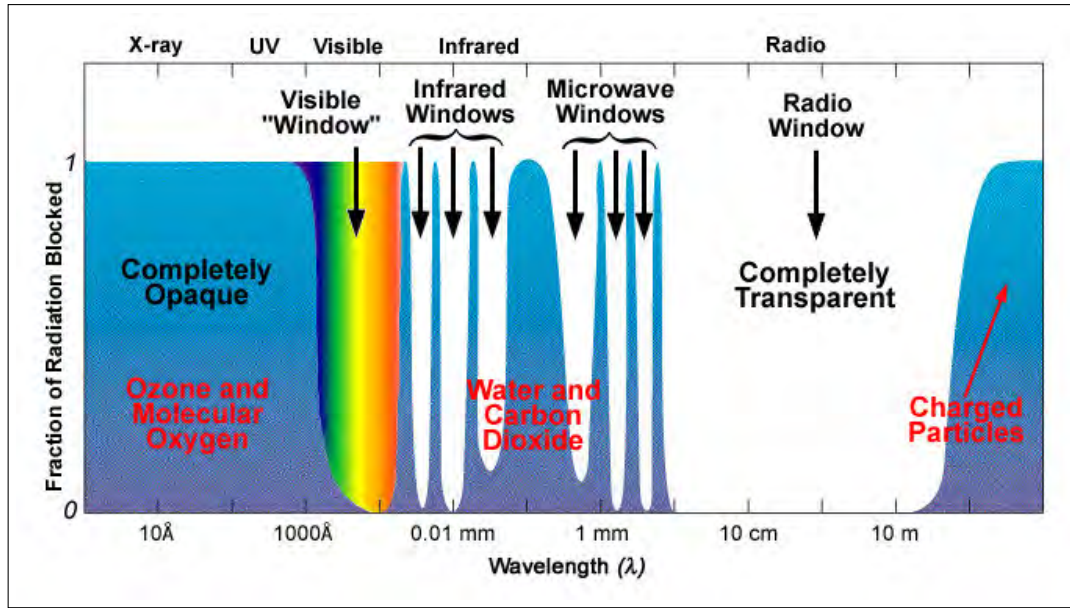
Figure 2.1: Fraction of radiation blocked by the Earth atmosphere as a function of wavelength, indicating the main molecules that block the radiation and the spectral windows where the atmosphere is transparent. Credit: https://christinatang1992.wordpress.com/2013/10/25/blog-2/

Figure 2.2: *Left:* Arecibo radio telescope in Puerto Rico with a diameter of 305 m. *Right:* Five-hundred-meter Aperture Spherical radio Telescope (FAST) located in China.

order to attain the highest angular resolutions. The angular resolution of an array of N antennas is now inversely proportional to the largest distance between two antennas (B), i.e., $\theta \approx \lambda/B$. The distance between two antennas is called the *baseline*, and an array of N antennas consists of *N(N-1)/2* baselines.

For an array of two antennas, A_1 and A_2, separated by a distance B (see Fig. 2.3), a plane electromagnetic wave with amplitude E induces a power U_1 at the entrance of antenna A_1:

$$U_1 \propto E \, e^{i\omega t}, \tag{2.1}$$

where ω is the angular frequency. After a time-delay (τ), the electromagnetic wave induces a power
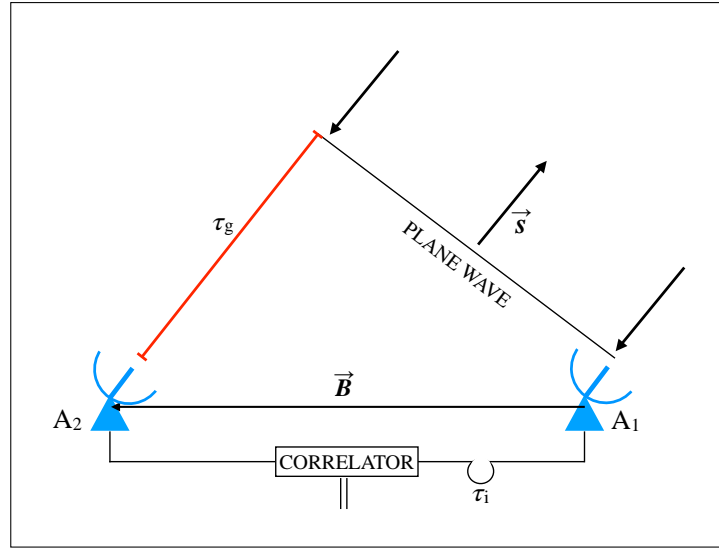
Figure 2.3: Geometry of an interferometer of two antennas, A_1 and A_2 separated by a distance B. A plane wave with direction s intercepts first antenna A_1 and, after a time τ_g, antenna A_1. The received power of each antenna and an additional delay τ_i reach the correlator.

U_2 at the exit of antenna A_2:

$$U_2 \propto E \, e^{i\omega(t-\tau)}. \tag{2.2}$$

τ is defined as the difference between the geometric delay τ_g and an additional delay τ_i added in the circuit. The geometric delay is caused by the orientation of the baseline B relative to the propagation direction of the wave s, defined as

$$\tau_g = \frac{\vec{\mathbf{B}} \cdot \vec{\mathbf{s}}}{c} \,, \tag{2.3}$$

where c is the light speed. Therefore

$$\tau = \tau_g - \tau_i = \frac{1}{c}\mathbf{B} \cdot \mathbf{s} - \tau_i \,. \tag{2.4}$$

The received power from each antenna, together with τ_i, are mixed in the correlator. The correlation type used in interferometry is called *cross correlation*. Assuming that the power U_1 and U_2 of each antenna is given by

$$U_1 = U_S + U_{R_1} \quad and \quad U_2 = U_S + U_{R_2} \,, \tag{2.5}$$

where U_S is the power associated with the source of interest and U_{R_i} represents the noise introduced by each receptor, the cross correlation is defined as

$$\langle (U_1 \cdot U_2) \rangle = \left\langle U_{R_1} \cdot U_S + U_{R_1} \cdot U_{R_2} + U_{R_2} \cdot U_S + U_S^2 \right\rangle . \tag{2.6}$$

The brackets $\langle \ \rangle$ denote time average and, since the terms are independent, the first three terms of the right side of Eq. 2.6 are zero. Thus, $U_1 \cdot U_2 = U_S{}^2$. Replacing Eqs. 2.1 and 2.2 into Eq. 2.6, the output of the correlator $R(\tau)$ is

$$R(\tau) \propto E^2 \, e^{i\omega\tau} . \tag{2.7}$$

From Eq. 2.7 it is seen that the response of the correlator varies periodically with τ. If the relative orientation between the baseline and the direction of the wave propagation is invariable, $R(\tau)$ is constant with time. However, due to the rotation of the Earth, the relative orientation between B and s is always changing and interferometric patterns are generated as a function of time.

The next step is to relate the response of the interferometer with measurable quantities. If the brightness distribution associated with the source is given by $I_\nu(s)$, the received power from the element $d\Omega$ per frequency range $d\nu$ towards a collecting effective area in the direction of propagation $A(s)$, is $A(s)I_\nu(s)d\Omega d\nu$. Therefore,

$$R(\tau) = A(\mathbf{s})I_\nu(\mathbf{s})e^{i\omega\tau}d\Omega d\nu . \tag{2.8}$$

Integrating over the solid angle and employing Eq. 2.4, we obtain

$$R(\mathbf{B}) = \iint_\Omega A(\mathbf{s}) \, I_\nu(\mathbf{s}) \exp\left[i2\pi\nu \left(\frac{1}{c}\mathbf{B} \cdot \mathbf{s} - \tau_i \right) \right] d\Omega d\nu . \tag{2.9}$$

$R(\mathbf{B})$ is known as the visibility function and the challenge of interferometry is to represent I_ν through $R(\mathbf{B})$.

In order to solve Eq. 2.9, a new coordinate system is introduced for the two vectorial quantities, s and B (see Fig. 2.4). The unity vector s points to the studied region, satisfying

$$\mathbf{s} = \mathbf{s}_0 + \sigma , \quad |\sigma| = 1 , \tag{2.10}$$
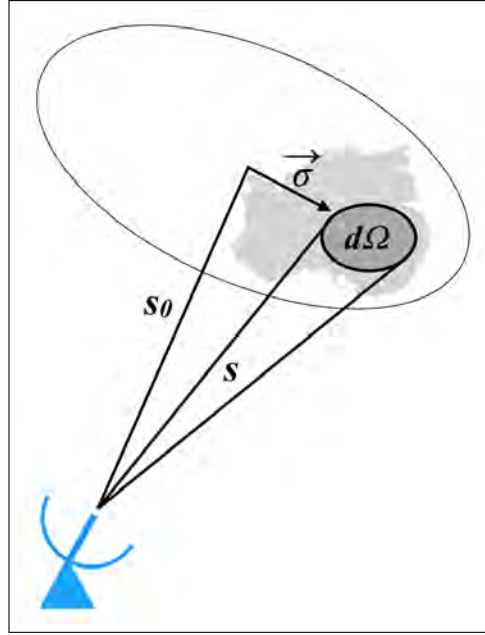
Figure 2.4: Geometry of the coordinate system introduced for the vectorial quantities s and $\mathbf{B}$. s points to the studied region $d\Omega$ and s_0 represents a reference direction. σ is the difference between s_0 s and belongs to the plane of the source.

where s_0 is a reference direction and σ represents the displacement between s and s_0 in the plane of the source. Replacing Eq. 2.10 into Eq. 2.9,

$$R(\mathbf{B}) = \exp\left[i\omega\left(\frac{1}{c}\mathbf{B}\cdot\mathbf{s}_0 - \tau_i\right)\right] d\nu \iint\limits_{\Omega} A(\sigma)I(\sigma)\exp\left(i\frac{\omega}{c}\mathbf{B}\cdot\sigma\right)d\sigma . \qquad (2.11)$$

The first exponential factor describes the plane wave, defining the phase of $R(\mathbf{B})$ towards the centre of the image. The visibility V is the Fourier transform of the intensity distribution $I(\sigma)$, i.e.,

$$V(\mathbf{B}) = \iint\limits_{\Omega} A(\sigma)I(\sigma)\exp\left(i\frac{\omega}{c}\mathbf{B}\cdot\sigma\right)d\sigma . \qquad (2.12)$$

The visibility function is referenced from the centre of the image, since the phase of the correlated signals are adjusted in order to have a zero delay at this position. For the vector B, a new coordinate system is defined as

$$\frac{\omega}{2\pi c}\mathbf{B} = (u, v, w) , \qquad (2.13)$$

where u,v,w are measured in units of wavelength $\lambda = 2\pi c/\omega$. The direction of w is parallel to s_0, while u points to the east and v to the north (see Fig. 2.5). The vector $\sigma = (x,y,z)$ is defined such that x and y
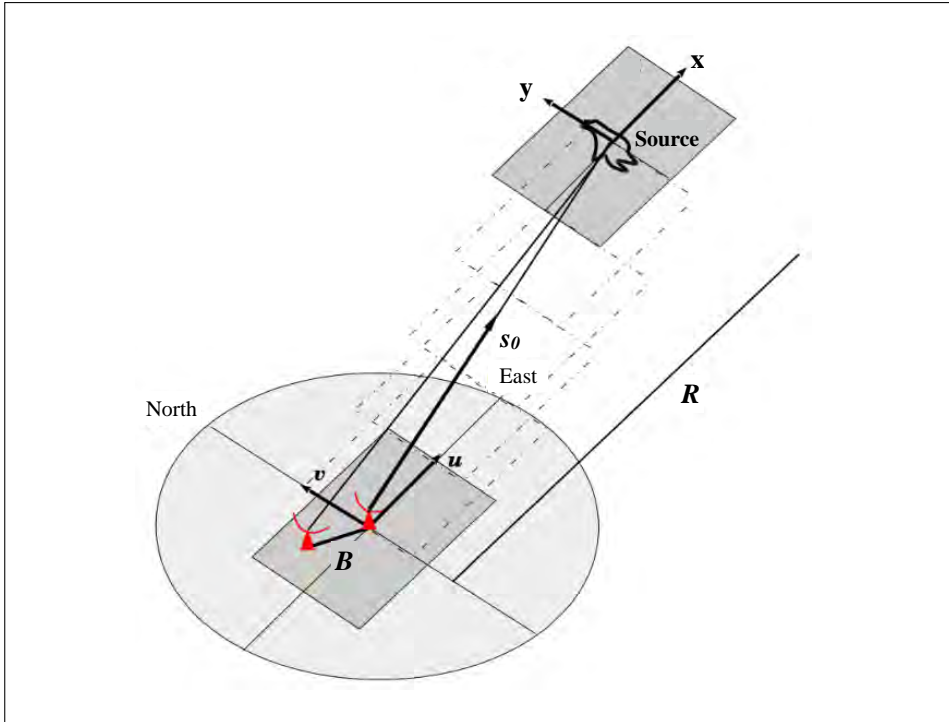
Figure 2.5: Geometric relationship between the x,y plane and the u,v plane. The x,y plane is located at a distance R and contains the source of interest. The u,v plane is parallel to the x,y plane and contains the baseline B. The u and v vectors point to the East and North directions, respectively.

are the directional cosines of the axes u and v. In this way, the uv plane is parallel to the xy plane and contains the baseline B. In u,v,w coordinates,

$$V(u, v, w) = \int_{-\infty}^{\infty} \int_{-\infty}^{\infty} A(x, y) I(x, y) \exp[i2\pi(ux + vy + w\sqrt{1 - x^2 - y^2})] \frac{\mathrm{d}x\mathrm{d}y}{\sqrt{1 - x^2 - y^2}} . \qquad (2.14)$$

The integration limits can be extended to $\pm \infty$ since $A(x,y) = 0$ for $x^2 + y^2 > l^2$, where l is the length of the main lobe. If the observed region is small, $(1 - x^2 - y^2)^{1/2} \cong 1$ and

$$V(u, v, w)e^{-i2\pi w} = \int_{-\infty}^{\infty} \int_{-\infty}^{\infty} A(x, y) I(x, y) \exp^{i2\pi(ux+vy)} \mathrm{d}x\mathrm{d}y . \qquad (2.15)$$

The term $e^{-i2\pi w}$ is a conversion factor, such that

$$V(u, v, w)e^{-i2\pi w} \cong V(u, v, 0) . \qquad (2.16)$$

Replacing Eq 2.16 into Eq 2.15 and applying the inverse Fourier transform, the intensity $I'(x,y)$

can be expressed as

$$I'(x, y) = A(x, y)I(x, y) = \int\limits_{-\infty}^{\infty} \int\limits_{-\infty}^{\infty} V(u, v, 0)e^{-i2\pi(ux+vy)}\mathrm{d}u\mathrm{d}v. \tag{2.17}$$

$I'(x,y)$ is the intensity $I(x,y)$ modified by the shape of the main lobe $A(x,y)$.

The u,v values are expressed as a function of the wavelength and have units of spatial frequencies. The antennas in an array should be located such that they give the maximum coverage of the u,v plane, since empty spaces imply a loss of the Fourier components in the synthesised image and, thus, a loss of flux. The u,v plane is filled by the baselines B, and it is important to observe with the maximum possible number of antennas and for a long period of time. The largest spatial frequency, associated with the longest baseline, provides the smallest spatial scale that can be observed with the interferometer, i.e., the angular resolution. On the other hand, the smallest baseline gives the largest angular scale that can be mapped and emission from larger scales is filtered-out by the interferometer.

If the visibility function $V(u,v)$ is known for the complete u,v plane, the modified intensity distribution $I'(x,y)$ can be obtained through the Fourier transform (Eq. 2.17). However, in a realistic situation $V(u,v)$ is sampled in discrete points, following elliptic trajectories and not covering the entire u,v plane. Therefore, the visibilities are weighted with the function $g(u,v)$, known as the *weight function*. In this way, a summation can be applied and an image is obtained through a discrete Fourier transform (DFT):

$$I_D(x, y) = \sum_{k} g(u_k, v_k)V(u_k, v_k)e^{-i2\pi(u_k x + v_k y)} , \tag{2.18}$$

where I_D is known as the *dirty image*. There are two widely used weighting functions: uniform and natural. Data which are naturally weighted result in lower angular resolution, but give a better signal-to-noise ratio than uniform weighting. Between these two extreme cases, there exist intermediate weighting schemes such as the Briggs weighting given by

$$w_i = \frac{\omega_i}{1 + W_k f^2} , \tag{2.19}$$

where w_i is the weight of the i-th sample, W_k the gridded weight of the relevant cell and f^2 is defined as

$$f^2 = \frac{\left(5 \times 10^{-R}\right)^2}{\frac{\sum\limits_i W_k^2}{\sum\limits_i \omega_i}} \,, \tag{2.20}$$

where R is the robustness parameter and can take values from -2.0 (close to uniform weighting) to 2.0 (close to natural weighting). A robustness value of 0 gives a good compromise between sensitivity and resolution (Briggs et al. 1999).

The dirty image I_D is also related to I through

$$I_D(x, y) = P_D(x, y) * I(x, y) \,, \tag{2.21}$$

where $*$ means convolution and P_D is the response to a point source, i.e.,

$$P_D = \sum_k g(u_k, v_k) e^{-i2\pi(u_k x + v_k y)} \tag{2.22}$$

also known as the *point spread function* (PSF) for the dirty beam. In order to remove the effects introduced by the PSF, deconvolution methods are needed. The most common deconvolution method used nowadays is called CLEAN (Högbom 1974). This is an algorithm with an iterative process that executes the following steps:

(i) Find the position of the brightest peak in the dirty image.

(ii) Subtract from the dirty image a fraction γ with the PSF shape.

(iii) Fill a map with the intensity and position of the subtracted point source. This map is known as the *CLEAN component map*.

(iv) Repeat n times steps **(i)**, **(ii)**, and **(iii)**, until the intensities of the remaining peaks are below a specific limit. After the subtraction, the dirty image is called the *residual image*.

(iv) The components in the CLEAN map are convolved with a 2D elliptic Gaussian function, known as the *CLEAN beam*, and create a model map.

(iv) The residuals are added to the model map, resulting in the *CLEAN image*.

After deconvolution, two images are created: the residual image and the CLEAN image, which has information about the intensity distribution of the studied region.

The radio telescopes that were used to collect the data for this thesis are briefly introduced below.

Figure 2.6: The eight SMA antennas of 6 m each located on the top of Mauna Kea, in Hawaii, USA. Credit: Harvard-Smithsonian Center for Astrophysics (CfA).

2.1.1 The Submillimeter Array

The Submillimeter Array (SMA; Ho et al. 2004) is a joint project between the Smithsonian Astrophysical Observatory and the Academia Sinica Institute of Astronomy and Astrophysics. It is located on top of of Mauna Kea in Hawaii, USA, at an altitude of 4100 m. It consists of a total of 8 antennas of 6 m each and operate in a frequency range from 180 to ~400 GHz. Figure 2.6 shows a view of the 8 SMA antennas.

2.1.2 The Atacama Large Millimeter/submillimeter Array

The Atacama Large Millimeter/submillimeter Array (ALMA) is a joint project between Europe, North America, East Asia, and Chile. It consists of 66 antennas, where 54 have 12 m and 12 have 7 m. It is located on the Chajnantor Plateau, in Chile, at an altitude of 5060 m. ALMA is nowadays the largest millimeter/submillimeter observatory in the world, reaching baselines up to 16 km. The ALMA antennas are shown in Fig 2.7.

Once the observations are finished, the raw data has to be inspected to account for undesirable points and subtract the system and atmospheric components, i.e., a calibration procedure needs to be done to achieve the information from the science target.
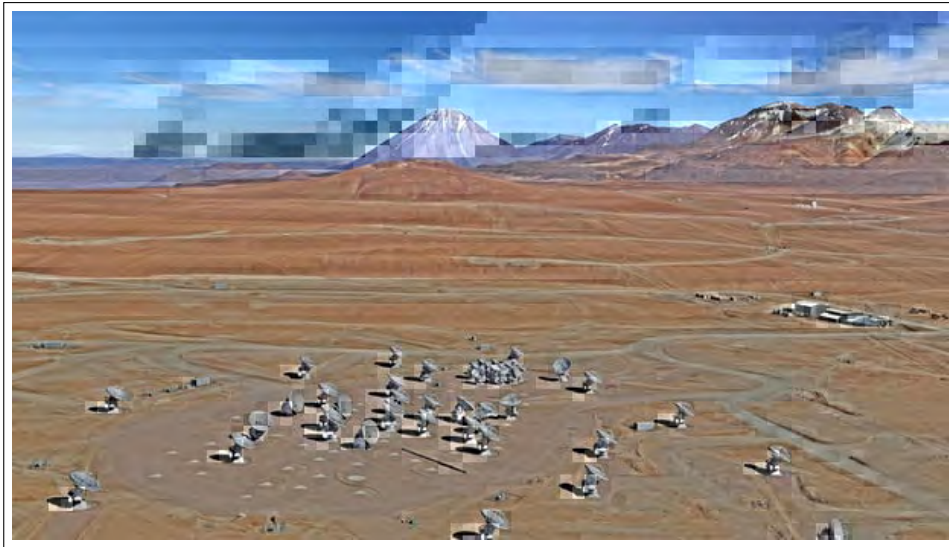
Figure 2.7: ALMA antennas located on the Chajnantor Plateau, in Chile. Credit: European South Observatory (ESO).

2.2 Data calibration

The response of an array contains information not only about the source of interest, but also from other components such as the atmosphere and the array components (antennas, receivers, etc). In order to subtract the undesirable components, a calibration process is implemented. There are three types of calibrators: flux calibrator, bandpass calibrator, and gain calibrator. These calibrators are objects whose flux and position are well known.

The flux calibrator adjusts the observations to an adequate flux scale, and the flux density should be known as a function of frequency. Common flux calibrators are planets, moons, asteroids or quasars. The bandpass calibrator accounts for the receiver response, providing information about how the signal varies as a function of frequency. In order to achieve signal in every frequency interval, the bandpass calibrator should be a bright and line-free object, as quasars. The gain calibrator removes the atmospheric distortion contribution, determining a time-dependent solution for each frequency interval. This calibrator should be close to the source of interest in the plane of the sky in order to cover the same portion of atmosphere. The gain calibrator requires a good signal-to-noise in a short period of time. Therefore, quasars are ideal gain calibrators.

The inspection, calibration, imaging, analysis, and visualisation of data from radio telescopes can be done with the Common Astronomy Software Applications (CASA) package (McMullin et al.

2007)[1], including tools and tasks that are executed in a Python interface. The calibration and imaging of the ALMA and SMA data presented in the three papers of this thesis were all done in CASA.

The main differences between the calibration of both ALMA and SMA datasets are the observed calibrators and the choice of the robustness parameter in the imaging process. The observed calibrators depend mainly on the observing date and their position with respect to the source of interest. The robustness parameter, on the other hand, depends on a compromise between resolution and sensitivity, and the purpose of the project itself. The ALMA data presented in papers 1 and 2 have been imaged with a robustness parameter of 0.5, since a high angular resolution is sought in order to probe small scales (disks scales) but, at the same time, weak lines are intended to be detected. On the other hand, the goal of the SMA observations presented in paper 3 is focused on the chemistry, therefore, high sensitivity is essential and a robustness parameter of 1.0 is used.

The following chapter describes the interpretation of the data, once the observation and calibration processes are done. It explains which are the observed physical quantities and how the physical and chemical structures are constrain from them.

2.3   Radiative Transfer

The flux density (F_ν) received by the telescope is defined as the amount of energy (dE) that arrives to the collecting area (dA), per unit of time (dt) and frequency ($d\nu$), i.e.,

$$F_\nu = \frac{dE}{dA d\nu dt}. \tag{2.23}$$

The flux density at radio wavelengths is commonly expressed in units of Jansky (1 Jy = 1×10^{-23} erg s^{-1} cm^{-2} Hz^{-1}) and the flux (F) is given by

$$F = \int F_\nu d\nu. \tag{2.24}$$

The specific intensity (I_ν) is defined as the flux per solid angle (Ω), per unit of frequency, and depends on the angle (θ) between the source of interest and the observer, i.e.,

$$I_\nu = \frac{dE}{d\nu dA dt d\Omega cos\theta}. \tag{2.25}$$

---

[1] http://casa.nrao.edu.

The general radiative transfer equation tells us how the specific intensity varies along a path s when absorption and emission are taking into account. This is,

$$\frac{\mathrm{d}I_\nu}{\mathrm{d}s} = -\alpha_\nu I_\nu + j_\nu, \tag{2.26}$$

where α_ν is the absorption coefficient and j_ν the emission coefficient of the medium. α_ν is related to the opacity κ_ν and the mass density ρ through

$$\alpha_\nu = \rho\kappa_\nu. \tag{2.27}$$

Equation 2.26 can be studied for three different cases: **(i)** if there is no absorption, $\mathrm{d}I_\nu/\mathrm{d}s = j_\nu$, **(ii)** if there is no emission, $\mathrm{d}I_\nu/\mathrm{d}s = -\alpha_\nu I_\nu$, or **(iii)** if the medium is in radiative equilibrium, $\mathrm{d}I_\nu/\mathrm{d}s = 0$ and, as a consequence, $I_\nu = j_\nu/\alpha_\nu$.

The absorption and emission coefficients can be written as

$$j_\nu = \frac{h\nu}{4\pi} n_u A_{ul} \phi(\nu), \tag{2.28}$$

$$\alpha_\nu = \frac{h\nu}{4\pi}(n_l B_{lu} - n_u B_{ul})\phi(\nu), \tag{2.29}$$

where n_u and n_l are the level populations, h is Planck's constant, $\phi(\nu)$ is known as the *profile function* and depends on the shape of the spectral line, and A_{ul}, B_{ul}, and B_{lu} are the Einstein coefficients for spontaneous emission, induced emission, and induced absorption, respectively.

For a stationary situation, the population of a given level n_i is determined by the *equation of statistical equilibrium*:

$$n_i \left[\sum_{k<l} A_{lk} + \sum_{k \neq l}(B_{lk}J_\nu + C_{lk}) \right] = \sum_{k>l} n_k A_{kl} + \sum_{k \neq l} n_k (B_{kl}J_\nu + C_{kl}) \, , \tag{2.30}$$

where C_{lk} and C_{kl} are the collisional rates and J_ν is the local mean intensity of the radiation field. The collisional rates depend on the density, temperature, and the collisional rate coefficient for each interaction between the molecule and its collisional partner. The left side of Eq. 2.30 indicates the processes that depopulate the level i, while the right side shows how to populate it. In non-LTE, the ratio between level populations can be obtained through the Boltzmann equation, i.e.,

$$\frac{n_l}{n_u} = \frac{g_l}{g_u} \exp\left[-\left(h\nu\right)/\left(kT_{\text{ex}}\right)\right].\tag{2.31}$$

When collisions dominate, T_{ex} approaches the kinetic temperature T_{kin} and LTE can be assumed.

2.3.1   RADEX - a non-LTE radiative transfer code

The RADEX code (van der Tak et al. 2007) is commonly used to constrain column densities and physical conditions from observations. RADEX assumes homogeneous medium and, using the basic equations of radiative transfer (see Sect. 2.3), it calculates the resulting spectral line intensities for a given kinetic temperature, column density, broadening parameter, and H_2 number density. The intensity of the line is then compared to the observed intensity by the telescope. RADEX is a powerful tool for comparing intensity ratios of different molecular transitions that trace the same physical component, since the geometry is not specified. We make use of the RADEX code in the first and second papers of this thesis (Chapters 4 and 5).

The next chapter summarises the main results of the papers included in this thesis, where observations of protostellar sources were carried out by radio interferometers, the calibration process was done in CASA, and the physics and chemistry were analysed, interpreted, and discussed.

3 THE RESEARCH

The following sections present an introduction to the main questions address in this thesis, a summary of the three papers presented in Chapters 4, 5, and 6, the future prospects, and my own contributions to each paper.

3.1 Short description

The study of the physics and chemistry of the low-mass star-formation process is closely linked to our understanding of the origins of our own Solar System. In particular, the formation and evolution of protoplanetary disks is strongly linked to the physical processes taking place at small scales, that in turn potentially affects the chemistry and thus, the initial conditions for planet formation. Very little is known about the initial physical and chemical conditions for planet formation and the relationship between the physical and chemical structures of embedded disks. How is gas and dust accreted from the envelope to the disk? Does the presence of the disk reflect the chemical structure of the inner envelope? Which are the physical and chemical processes that dominate on disk scales scales? How do the physics and chemistry evolve from deeply embedded stages to the onset of planet formation?

In order to address these questions, we observe a sample of Class I protostars using the Atacama Large Millimeter/submillimeter Array (ALMA) and the Submillimeter Array (SMA) to characterised their physical and chemical structures. This early stage of star formation has been chosen since some Class I protostars reveal the presence of Keplerian disks while still embedded in significant envelopes of gas and dust (e.g., Brinch et al. 2007; Jørgensen et al. 2009; Harsono et al. 2014; Yen et al. 2015). The Class I objects therefore serve as the link between the properties of the parental molecular cloud and the initial conditions of the emerging circumstellar disks. In addition, the chemistry observed towards Class I sources will fill the observed gap between the line-rich Class 0 sources (e.g., Sakai & Yamamoto 2013; Jørgensen et al. 2016) and Class II disks (e.g., Andrews et al. 2018). The chemistry of Class II disks is difficult to constrain observationally, since they are associated with a low gas column density (e.g., Ansdell et al. 2016; Walsh et al. 2016), however, a chemical trend can be established by analysing the chemistry of earlier stages, such as Class I sources. The physical and chemical evolution between Class 0 and Class II sources can then be linked.

3.1.1   Publications

The results of this thesis are presented in three papers included in Chapters 4, 5, and 6. The papers are:

1. **Artur de la Villarmois, E.**, Kristensen, L. E., Jørgensen, J. K., Bergin, E. A., Brinch, C., Frimann, S., Harsono, D., Sakai, N. & Yamamoto, S. 2018, A&A, 614, A26. "Chemistry of a newly detected circumbinary disk in Ophiuchus";

2. **Artur de la Villarmois, E.**, Jørgensen, J. K., Kristensen, L. E., Bergin, E. A., Harsono, D., Sakai, N., van Dishoeck, E. F. & Yamamoto, S. 2019, A&A, submitted. "The physical and chemical fingerprint of protostellar disk formation";

3. **Artur de la Villarmois, E.**, Kristensen, L. E. & Jørgensen, J. K. 2019, A&A, submitted. "Revealing the chemical structure of the Class I disk Oph IRS 67".

A summary of each paper is presented in the following.

3.1.1.1   Paper I: Chemistry of a newly detected circumbinary disk in Ophiuchus

Chapter 4 presents high-angular-resolution ($0.4''$, ~60 AU) ALMA observations towards the Class I protobinary system, Oph-IRS 67. A Keplerian circumbinary disk towards this source is detected for the first time from the continuum emission at 0.87 mm and the velocity profile in emission of $C^{17}O$ and $H^{13}CO^+$. From the Keplerian fit, a mass of 2.2 $M_\odot$ is estimated for the binary system. The dust and gas masses are estimated from the continuum and the $C^{17}O$ emission, respectively. CO abundances with respect to H_2 are calculated for different temperatures, where the results are comparable with the canonical value of 2.7×10^{-4}. This suggests that there is no significant CO freeze-out in the midplane, possibly due to a non-effective shielding of the disk. A region rich in carbon-chain molecules (C_2H and c-C_3H_2) is identified beyond the extent of the circumbinary disk. The possible physical scenarios for the nature of this region, such as a centrifugal barrier, the outflow cavity irradiated by the sources, spiral-arm features, or envelope material infalling into the disk, are discussed. The observations favour the scenario where envelope material infalls into the disk but more work will be needed to address this.

3.1.1.2   Paper II: The physical and chemical fingerprint of protostellar disk formation

Chapter 5 builds on the initial pilot study of IRS 67 and presents high-angular-resolution (0.4″, ~60 AU) ALMA observations towards a representative sample of 12 Class I protostars located in the Ophiuchus star forming region. The purpose of this work is to explore and compare the physical and chemical structures of Class I sources on disk scales with a representative sample. Disk masses are estimated from the continuum emission at 0.87 mm, while stellar masses are determined from Keplerian fits of optically thin isotopologues, when possible. We observe an empirical linear correlation between the stellar mass and the bolometric luminosity for a sample of 13 Class I sources (5 from our dataset and 8 taken from the literature), and one outlier, providing a mass accretion rate of $(2.4 \pm 0.6) \times 10^{-7}$ M$_\odot$ yr^{-1}. The lifetime and bolometric luminosity of a typical Class I source are incompatible with a constant mass accretion rate, favouring the episodic-accretion scenario, i.e., accretion occurring in bursts. Consequently, the discussed sources may be in a quiescent phase with one exception, a source that has been associated with FU Ori events. In addition, it is found that the accretion bursts may have important effects on the chemistry.

A comparison between molecular line detection and the physical properties of the sources (bolometric temperature and bolometric luminosity) shows a chemical differentiation between C^{17}O and SO$_2$: C^{17}O is detected towards the less evolved and less luminous sources, while SO$_2$ is detected towards the most evolved sources with high luminosities. In addition, no molecular lines are detected towards the more evolved sources with low bolometric luminosity, and these sources are proposed to be at the edge of the Class I/II stage. The decrease of C^{17}O emission as the system evolves is expected, since the gas column density also decreases, however, the SO$_2$ emission is compact (consistent with the extent of the continuum emission), is tracing warm material (~200 K), and presents broad line widths (more than 10 km s^{-1}). This implies that C^{17}O and SO$_2$ are tracing different physical components and SO$_2$ seems to be related with high accretion rates and, therefore, may be tracing accretion shocks. Moreover, we can exclude that SO$_2$ is tracing a hot-corino region, since no CH$_3$OH is detected towards any of the sources. The non-detection of methanol furthermore suggests that the presence of the disk dominates the mass budget of the inner envelope, generating a flat density profile and thus, less material exposed to higher temperatures ($\gtrsim$100 K).

Overall, the work presented in this chapter is a demonstration of how the gas column density decreases as the system evolves and that the formation of circumstellar disks results in characteristic

chemical imprints.

3.1.1.3   Paper III: Revealing the chemical structure of the Class I disk Oph IRS 67

Chapter 6 presents SMA observations towards the protobinary source Oph-IRS 67, where a combination of compact and extended configurations were employed. The resulting angular resolution is $\sim 1.5''$ ($\sim$200 AU), enough to separate the sources and the region rich in carbon-chain molecules (see paper I). The use of the SWARM correlator allowed us to detect multiple molecular transitions in a broad frequency range ($\sim$30 GHz), providing information about the physical and chemical structure of the system. Three main regions are identified: (*i*) a cold zone beyond the extent of the circumbinary disk, traced by DCO^+, (*ii*) the circumbinary disk structure, traced by CO isotopologues and sulphur-bearing species, and (*iii*) a photon-dominated region likely related with the surface layers of the circumbinary disk, traced by CN, DCN, and carbon-chain molecules. A temperature structure is provided by the ratio between two H_2CO transitions and is consistent with the location of the different components, i.e., warmer temperatures are seen towards the outflow direction, while lukewarm and colder temperatures are consistent with the photon-dominated region and the circumbinary disk structure, respectively. IRS 67 shows chemical similarities with Class 0 sources, such as the detection of sulphur-bearing species and carbon-chain molecules, and also with Class II sources, such as the CN emission. IRS 67 seems to be a chemical link between Class 0 and II sources, where the gas column density is still significant and the UV radiation from the protostars can photodissociate the surface layers of the disk. Finally, the physico-chemical structure of IRS 67 highlights the importance of the presence of the disk in order to shield and preserve molecular species in cold regions and, on the other hand, reset the chemistry on the surface layers of the disk.

3.1.1.4   Research summary

In terms of the bigger picture of low-mass star formation, the key contributions of this thesis can be summarised as follows:

1. With the high sensitivity and angular resolution of ALMA it was possible to resolve disk scales and estimate protostellar masses for a sample of Class I sources. We found an empirical linear correlation between the bolometric luminosity and the mass accretion rate, suggesting that more massive protostars accrete material with a higher accretion rate. In addition, the accretion rate

varies with time and a significant amount of mass is accreted in episodic bursts. The fact that 13 of 14 Class I sources show low mass accretion rates provides observational evidence that a typical protostar will spend most of its lifetime in a quiescent state of accretion.

2. The formation and evolution of the disk is reflected on the chemical structure of the envelope, from large to small scales: the disk shields material beyond its extent where a cold chemistry is seen, while material from the inner envelope follows the flattened structure of the disk and, since less material is exposed to high temperatures, desorption of complex-organic molecules is not efficient. In addition, accretion shocks are produced at the interface between the inner envelope and the disk surface, promoting a more violent chemical reset.

3. Class I sources show a physical and chemical link between deeply embedded Class 0 sources and more evolved Class II sources. The gas column density decreases as the system evolves, which is reflected on the emission of high density tracers such as CO isotopologues. The formation and evolution of the disk, together with the increase of the outflow-opening angle as the system evolves, allow the UV radiation from the central protostar to reach the surface layers of the disk, promoting the photodissociation of molecules. On the other hand, the chemistry of Class 0 sources can be preserved, to some extent, in Class II sources mainly towards the disk midplane and beyond its extent, where the shielding is efficient.

3.1.2 Outlook

The observations and results presented in Chapters 4, 5, and 6 open up a new set of questions and directions for future projects.

Similar observations for a larger sample will allow us to confirm (or not) the observed trends, such as the linear correlation between stellar mass and bolometric luminosity, the low column density of complex organic molecules due to the presence of the disk, and the link between the physico-chemical structure of Class 0, I, and II sources. New observations will provide a more statistical sample for understanding the physics and chemistry of these earlier stages of low-mass star formation.

For protobinary systems, higher angular resolution observations may resolve the individual circumbinary disks around each source. This will allow us to constrain the dynamics at small scales and link circumstellar with circumbinary disks, investigating how the mass flow between the individual components and how each of the sources grow in mass. In addition, the chemistry towards each of

the protostars can be investigated and understand how the physics at these small scales affects the chemistry.

Finally, higher-angular resolution will provide a velocity profile of accretion shocks tracers and yield strong evidence for the presence (or absence) of accretion shocks, a physical process that is commonly invoked but not yet fully understood. If future observations confirm the existence of accretion shocks, this will have important consequences for the chemical content of the disk. Since accretion shocks are more violent than the gradual heating of material from the radiation of the central source, molecules can desorb from dust grains and/or other species can dissociate in the gas phase, altering the chemistry and reseting the initial chemical condition for planet formation.

3.1.3   Own contributions versus contributions of collaborators

This section states my own contributions to the papers and the contributions of the co-authors, respectively.

Paper I. The analysis of the data and the paper were carried out and written by myself, respectively. Lars Kristensen and Jes Jørgensen gave substantial input and suggestions in the analysis, interpretation, and writing processes. Christian Brinch, Edwin Bergin, Søren Frimann, Daniel Harsono, Nami Sakai, and Satoshi Yamamoto provided extra comments and suggestions that helped improve the whole paper.

Paper II. The analysis of the data and the paper were carried out and written by myself, respectively. Lars Kristensen and Jes Jørgensen gave substantial input and suggestions in the analysis, interpretation, and writing processes. Edwin Bergin, Daniel Harsono, Nami Sakai, Ewine F. van Dishoeck, and Satoshi Yamamoto provided with extra comments and suggestions that helped to improve the whole paper.

Paper III. The analysis of the data and the paper were carried out and written by myself, respectively. Lars Kristensen and Jes Jørgensen gave substantial input and suggestions in the analysis, interpretation, and writing processes. Johan Lindberg provided us with extra data and valuable discussion.

4   PAPER I: Chemistry of a newly detected circumbinary disk in Ophiuchus

Elizabeth Artur de la Villarmois[1], Lars E. Kristensen[1], Jes K. Jørgensen[1], Edwin A. Bergin[2], Christian Brinch[3], Søren Frimann[4], Daniel Harsono[5], Nami Sakai[6] & Satoshi Yamamoto[7]

[1] Centre for Star and Planet Formation, Niels Bohr Institute and Natural History Museum of Denmark, University of Copenhagen, Øster Voldgade 5-7, DK-1350 Copenhagen K, Denmark

[2] Department of Astronomy, University of Michigan, 311 West Hall, 1085 S. University Ave, Ann Arbor, MI 48109, USA

[3] Niels Bohr International Academy, The Niels Bohr Institute, University of Copenhagen, Blegdamsvej 17, DK-2100 Copenhagen Ø. Denmark

[4] ICREA and Institut de Ciències del Cosmos, Universitat de Barcelona, IEEC-UB, Martí Franquès 1, 08028 Barcelona, Spain

[5] Leiden Observatory, Leiden University, PO Box 9513, NL-2300 RA Leiden, the Netherlands

[6] The Institute of Physical and Chemical Research (RIKEN), 2-1 Hirosawa, Wako-shi, Saitama 351-0198, Japan

[7] Department of Physics, The University of Tokyo, Bunkyo-ku, Tokyo 113-0033, Japan

4.1   Abstract

Context: Astronomers recently started discovering exoplanets around binary systems. Therefore, understanding the formation and evolution of circumbinary disks and their environment is crucial for a complete scenario of planet formation.

Aims: The purpose of this paper is to present the detection of a circumbinary disk around the system Oph-IRS67 and analyse its chemical and physical structure.

Methods: We present high-angular-resolution (0.″4, ~60 AU) observations of $C^{17}O$, $H^{13}CO^{+}$, $C^{34}S$, SO_2, C_2H and $c-C_3H_2$ molecular transitions with the Atacama Large Millimeter/submillimeter Array (ALMA) at wavelengths of 0.8 mm. The spectrally and spatially resolved maps reveal the kinematics of the circumbinary disk as well as its chemistry. Molecular abundances are estimated using the non-local thermodynamic equilibrium (LTE) radiative-transfer tool RADEX.

Results: The continuum emission agrees with the position of Oph-IRS67 A and B, and reveals the

presence of a circumbinary disk around the two sources. The circumbinary disk has a diameter of ~620 AU and is well traced by $C^{17}O$ and $H^{13}CO^+$ emission. Two further molecular species, C_2H and c-C_3H_2, trace a higher-density region which is spatially offset from the sources (~430 AU). Finally, SO_2 shows compact and broad emission around only one of the sources, Oph-IRS67 B. The molecular transitions which trace the circumbinary disk are consistent with a Keplerian profile on smaller disk scales ($\lesssim$ 200 AU) and an infalling profile for larger envelope scales ($\gtrsim$ 200 AU). The Keplerian fit leads to an enclosed mass of 2.2 $M_\odot$. Inferred CO abundances with respect to H_2 are comparable to the canonical ISM value of 2.7×10^{-4}, reflecting that freeze-out of CO in the disk midplane is not significant.

Conclusions: Molecular emission and kinematic studies prove the existence and first detection of the circumbinary disk associated with the system Oph-IRS67. The high-density region shows a different chemistry than the disk, being enriched in carbon chain molecules. The lack of methanol emission agrees with the scenario where the extended disk dominates the mass budget in the innermost regions of the protostellar envelope, generating a flat density profile where less material is exposed to high temperatures, and thus, complex organic molecules would be associated with lower column densities. Finally, Oph-IRS67 is a promising candidate for proper motion studies and the detection of both circumstellar disks with higher-angular-resolution observations.

4.2 Introduction

Low-mass star formation takes place within dense cold molecular clouds, where individual cores collapse due to gravity. Because of the initial core rotation, conservation of angular momentum will lead to the formation of a circumstellar disk around the young stars. The angular momentum is transferred to the outer regions of the disk and moved outward by energetic outflows, sweeping away material from the envelope. In the earliest stages, the young source is deeply embedded in its infalling envelope of cold gas and dust, obscuring the radiation from the central star. As the system evolves, the envelope dissipates, revealing the pre-main sequence star and the circumstellar disk. The properties and evolution of these disks are crucial for the final mass of the host star and the initial conditions of planetary systems.

Within the envelope, the large variations in temperature (tens to hundreds of K) and density (10^5–10^9 cm^{-3}) leave strong chemical signatures that can potentially be observed directly, thus making

these systems interesting laboratories for astrochemical studies (e.g. Jørgensen et al. 2004). Since individual molecular transitions are enhanced at specific temperatures and densities, their emission (and/or absorption) reveals the peculiarities and characteristics of the gas and can be used to reveal the physical structure and evolution of the young protostar (when the chemistry is taken into account).

While the overall framework of low-mass star formation is well accepted nowadays, the details are significantly more complex, particularly when the formation of binary and/or multiple systems is considered (e.g. Tobin et al. 2016). Circumstellar disks have been detected around individual binary components, as well as a circumbinary disk surrounding the system for Class I sources. Some cases show an alignment between the disks (e.g. Dutrey 2015), while other systems consist of misaligned components (e.g. Brinch et al. 2016; Takakuwa et al. 2017). For more evolved systems, discrepancies are reported between disk sizes inferred from observations in multiple systems and predictions from tidal interaction models (e.g. Harris et al. 2012). Apart from the physical structure, the chemical differentiation between the younger Class 0 and the more evolved Class I multiple systems provides information about the evolution of important parameters, such as temperature and density. Consequently, more observations are needed in order to understand the complexity of binary and multiple systems.

With the high angular resolution of the Atacama Large Millimeter/submillimeter array (ALMA), smaller scales ($\lesssim$10–50 AU) can be resolved towards nearby star-forming regions, providing very detailed observations of the environments in which stars form. One of the closest star-forming regions is the Ophiuchus molecular cloud (Wilking et al. 2008), characterised by a high visual extinction (A_V) of between 50 and 100 magnitudes, and a high number of solar-type young stellar objects (YSOs) in different evolutionary stages (Wilking et al. 2008). Ophiuchus is therefore one of the most important regions for studies of the star formation process and early evolution of young stars.

One of the particularly interesting YSOs in Ophiuchus is the proto-binary system IRS67AB, located in the L1689 part of the cloud. This source is also known as L1689SAB and WLY2-67. The distance to IRS67AB and L1689 were recently determined through proper motion and trigonometric parallax measurements by Ortiz-León et al. (2017). The distance was determined to be 147.3 ± 3.4 pc to L1689 as a whole and 151.2 ± 2.0 pc to IRS67AB specifically; in this paper, we adopt the latter.

IRS67AB was associated with a large-scale outflow structure ($\gtrsim$ 1000 AU), detected in CO J=2−1 emission by Bontemps et al. (1996), and was also surveyed at infrared and other wavelengths as part of the *Spitzer* Space Telescope c2d legacy program (Evans et al. 2009). In that survey, the source

was associated with a bolometric temperature (T_{bol}) of 130 K, bolometric luminosity (L_{bol}) of 4.0 L$_{\odot}$, infrared spectral index (α_{IR}) of 1.39 and visual extinction of 9.8 magnitudes, all characteristics of embedded Class I young stellar objects. Later, McClure et al. (2010) proved the binary nature of the system (L1689S-A and L1689S-B in their work), through infrared observations, calculated a separation of 0.6″ (∼90 AU) between the two sources, and identified sources A and B as a disk and envelope candidate, respectively.

In this paper, we present ALMA observations of Oph-IRS67AB. The study of this binary system demonstrates the complexity of protoplanetary disk formation and evolution (both circumstellar and circumbinary), from an observational point of view. Section 2 describes the observational procedure, data calibration, and covered molecular transitions. In Sect. 3, we present the results, highlighting the detection of the circumbinary disk and the chemical diversity of the system. Section 4 is dedicated to the analysis of the data, where dust and gas masses are calculated, and different velocity profiles are considered for the circumbinary disk. In addition, relative molecular abundances are estimated in order to compare them with values associated with a younger system. We discuss the structure and kinematics of the whole system, and the temperature profile of the circumbinary disk in Sect. 5. Finally, we end the paper with a summary in Sect. 6.

4.3 Observations

IRS67 was observed with ALMA on four occasions between 2015 May 21 and June 5 as part of a larger program to survey the line and continuum emission towards 12 Class I protostars in Ophiuchus (program code: 2013.1.00955.S; PI: Jes Jørgensen). At the time of the observations, 36 antennas were available in the array (37 for the June 5 observations) providing baselines between 21 and 556 metres (784 metres for the June 5 observations). Each of the four sessions provided an on-source time of 43 minutes in total for the 12 different sources (i.e. each source was observed for approximately 15 minutes in total)

The observations targeted five different spectral windows and the choice of species has been made specifically to trace different aspects of the structure of protostars. For example, the lines of $C^{17}O$, $H^{13}CO^{+}$ and $C^{34}S$ are optically thin tracers of the kinematics of disk formation, while SO_2 and CH_3OH are expected to trace the warm chemistry in the inner envelope or disk. Two spectral windows consist of 960 channels, each with 122.07 kHz (0.11 km s^{-1}) spectral resolution

centred on C^{17}O J=3$-$2 and C^{34}S J=7$-$6, while the other three contain 1920 channels each with 244.14 kHz (0.22 km s^{-1}) spectral resolution centred on H^{13}CO$^+$ J=4$-$3, the CH$_3$OH J_k=7$_k$$-6_k$ branch at 338.4 GHz and the CH$_3$CN 14$-$13 branch at 349.1 GHz. The latter two organic molecules are not detected towards IRS67, but instead the two settings pick up SO$_2$, C$_2$H, and c-C$_3$H$_2$ transitions. The spectral setup and covered molecular transitions are summarised in Table 6.1.

The calibration and imaging were done in CASA[1] (McMullin et al. 2007): the complex gains were calibrated through observations of the quasars J1517-2422 and J1625-2527, passband calibration on J1924-2914 and flux calibration on Titan. The resulting dataset has a beam size of 0.″44 × 0.″33, a continuum *rms* level of 0.4 mJy beam^{-1} and a spectral *rms* level of 10 mJy beam^{-1} per channel. The channel width can be 0.11 or 0.22 km s^{-1}, depending on the spectral window (see Table 6.1).

4.4   Results

4.4.1   Continuum emission

Figure 4.1 shows the submillimetre continuum emission toward Oph-IRS67, where two peaks are detected toward the A and B sources plus a fainter disk-like structure. Oph-IRS67B is brighter than Oph-IRS67A (155 vs. 30 mJy) and was identified by McClure et al. (2010) as a binary companion at infrared wavelengths. The disk-like structure has a deconvolved continuum size of (4.″1 ± 0.″2) × (0.″82 ± 0.″05) or (620 ± 20 AU) × (124 ± 7 AU), and a position angle (PA) of 54° ± 1°, measured from north to east. Assuming a toy model for a thin and circular structure, an inclination of ∼ 80° (i = 0° for face-on and i = 90° for edge-on) is found by fixing the major and minor axis values of the deconvolved continuum size.

The position and integrated flux of each source are obtained by fitting two-dimensional (2D) Gaussians to both peaks and are listed in Table 5.3. The position of the geometric centre is also calculated, by taking the middle point between both sources. The separation between sources A and B is 0.″71 ± 0.″01 (107 ± 2 AU). All the figures and calculations in this work are shown relative to the geometric centre, and relative to the system velocity (V_{LSR}) of 4.2 km s^{-1} (Lindberg et al. 2017). The red diamond in Fig. 4.1 represents the position of an offset region, that may be associated with a high-density region, and is discussed in more detail in Sect. 3.2.1.

---

[1]http://casa.nrao.edu/

Table 4.1: Spectral setup and parameters of the detected molecular transitions.

Spectral window	Frequency range [GHz]	Spectral resolution [km s^{-1}]	Molecular transition	A_{ij} [a] [s^{-1}]	E_u [a] [K]	$n_{\rm crit}$ [b] [cm^{-3}]
spw 1a	337.002–337.119	0.11	C^{17}O J=3–2	2.3×10^{-6}	32.3	3.5×10^{4}
spw 1b	337.337–337.454	0.11	C^{34}S J=7–6	8.4×10^{-4}	50.2	1.3×10^{7}
spw 2	338.165–338.634	0.22	c-C$_3$H$_2$ $5_{5,1}$–$4_{4,0}$ (para)	1.6×10^{-3}	48.8	1.2×10^{8}
			SO$_2$ $18_{4,14}$–$18_{3,15}$	3.3×10^{-4}	196.8	5.9×10^{7}
			SO$_2$ $20_{1,19}$–$19_{2,18}$	2.9×10^{-4}	198.9	3.8×10^{7}
spw 3	346.880–347.115	0.11	H^{13}CO$^+$ J=4–3	3.3×10^{-3}	41.6	8.5×10^{6}
spw 4	349.165–349.634	0.22	c-C$_3$H$_2$ $5_{5,0}$–$4_{4,1}$ (ortho)	1.6×10^{-3}	49.0	1.3×10^{8}
			C$_2$H N=4–3, J=9/2–7/2, F=5–4	1.3×10^{-4}	41.9	2.2×10^{7}
			C$_2$H N=4–3, J=9/2–7/2, F=4–3	1.3×10^{-4}	41.9	2.3×10^{7}
			C$_2$H N=4–3, J=7/2–5/2, F=4–3	1.2×10^{-4}	41.9	1.7×10^{7}
			C$_2$H N=4–3, J=7/2–5/2, F=3–2	1.2×10^{-4}	41.9	1.8×10^{7}

[a] Values from the CDMS database (Müller et al. 2001). [b] Calculated values for a collisional temperature of 30 K and collisional rates from the Leiden Atomic and Molecular Database (LAMDA; Schöier et al. 2005). The collisional rates of specific species were taken from the following works: C^{17}O from Yang et al. (2010), C^{34}S from Lique et al. (2006), c-C$_3$H$_2$ from Chandra & Kegel (2000), SO$_2$ from Balança et al. (2016), H^{13}CO$^+$ from Flower (1999) and C$_2$H from Spielfiedel et al. (2012).

Table 4.2: Position and continuum fluxes of the system.

	α_{J2000}	δ_{J2000}	Integrated flux [mJy]
Oph-IRS67A	$16^h32^m00.989^s \pm 0.001^s$	$-24°56'42.75'' \pm 0.01''$	30 ± 3
Oph-IRS67B	$16^h32^m00.978^s \pm 0.001^s$	$-24°56'43.44'' \pm 0.01''$	155 ± 4
Geometric center	$16^h32^m00.983^s \pm 0.001^s$	$-24°56'43.09'' \pm 0.01''$	—
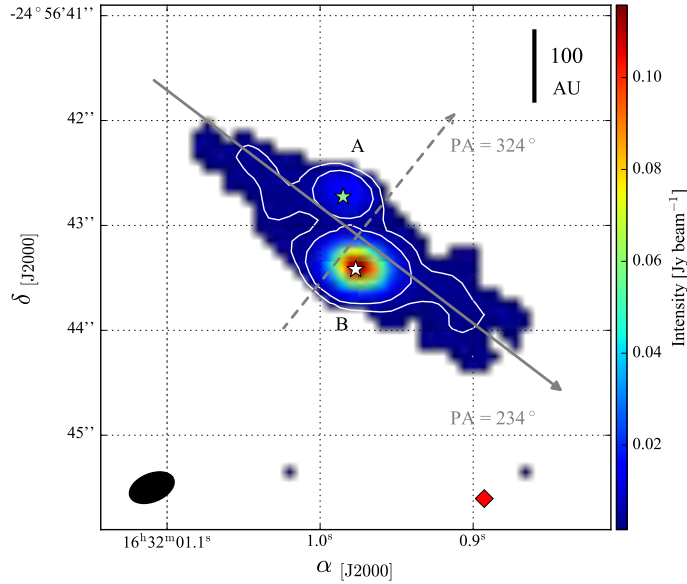
Figure 4.1: Continuum emission above 4σ ($\sigma = 0.4$ mJy beam^{-1}) in colour scale and specific values of 7 and 15σ in white contours. The synthesised beam is represented by the black filled ellipse. The grey solid and dashed arrows cross at the geometric centre and they represent the direction of and perpendicular to the disk-like structure, respectively. The green and white stars show the positions of Oph-IRS67A and Oph-IRS67B, respectively. The red diamond denotes the location of the offset region.

4.4.2   Molecular emission

Table 6.1 contains the parameters of the detected molecular transitions. The original proposal aimed at detecting the CH_3OH $J_k=7_k-6_k$ branch, but no significant emission above 3σ is observed. In the case of C_2H, the four lines compose two pairs of hyperfine splittings of two rotational levels. Since both hyperfine transitions in each pair are very close to one another, the C_2H transitions are labelled as $N=4-3$, $J=9/2-7/2$ and $N=4-3$, $J=7/2-5/2$. All the listed species are detected towards at least one of the following regions: source A, source B, the disk-like structure or a region spatially offset from the system ($\sim$430 AU from the geometrical center), located South-West from the continuum emission (red diamond in Fig. 4.1).

4.4.2.1 Moment maps

Figures 4.2 and 4.3 present the integrated emission (moment 0) and the velocity field (moment 1) for $C^{17}O$, $H^{13}CO^+$, $C^{34}S$, the two doublets of C_2H, both transitions of c-C_3H_2, and SO_2. In moment 0 maps, the continuum emission from Fig. 4.1 corresponding to 4 and 15σ contours is also plotted. $C^{17}O$ is tracing the disk-like structure, with a strong correlation with the continuum emission and its integrated intensity peaks at the position of source B. The $H^{13}CO^+$ emission is very intense in the proximity of both sources, showing an S-shape correlated with the continuum emission, and is enhanced in the offset region. $C^{34}S$ peaks in isolated regions away from both sources and part of the emission lies beyond the continuum emission. The lines of C_2H display the most extended emission and their integrated intensity dominates in the offset region. The North-East emission presents a curved shape beyond the continuum emission, while the South-West region is almost completely dominated by C_2H emission. Close to the protostars, the C_2H integrated intensity is below 5σ. Both c-C_3H_2 transitions show extended emission only in the vicinity of the offset region and are anti-correlated with the continuum emission. SO_2 shows compact emission only toward source B, where the continuum emission peaks. The velocity ranges in Figs. 4.2 and 4.3 are chosen to bring forward the disk-like structure. For a detailed comparison of the more quiescent gas associated with the individual protostars, see the channel maps in Figs. A.1, A.2 and A.3 in Appendix A.

The offset region shows strong emission of the two c-C_3H_2 transitions. Since these two transitions are associated with high critical densities ($n_{crit} = 1.2 \times 10^8$ and 1.4×10^8 cm^{-3}; see Table 6.1), the offset region is henceforth referred to as the *high density region*.

The moment 1 maps in Figs. 4.2 and 4.3 show the existence of a velocity gradient and suggest an approximately edge-on and flat morphology for the disk-like structure, with the blue-shifted emission arising from the South-West region and the red-shifted emission emerging from the North-East area. In addition, the high-density region only shows blue-shifted emission with no red-shifted counterpart, and its emission peaks around 2 km s^{-1}. SO_2 emission shows a velocity gradient toward source B (PA $\approx 30°$), misaligned with the gradient seen for the other detected lines (PA $\approx 54°$). This orientation difference may reveal that a possible circumstellar disk around source B is misaligned with respect to the disk-like structure, if SO_2 is tracing circumstellar disk material, or SO_2 may be tracing accretion shocks and thus, related with infalling motion.
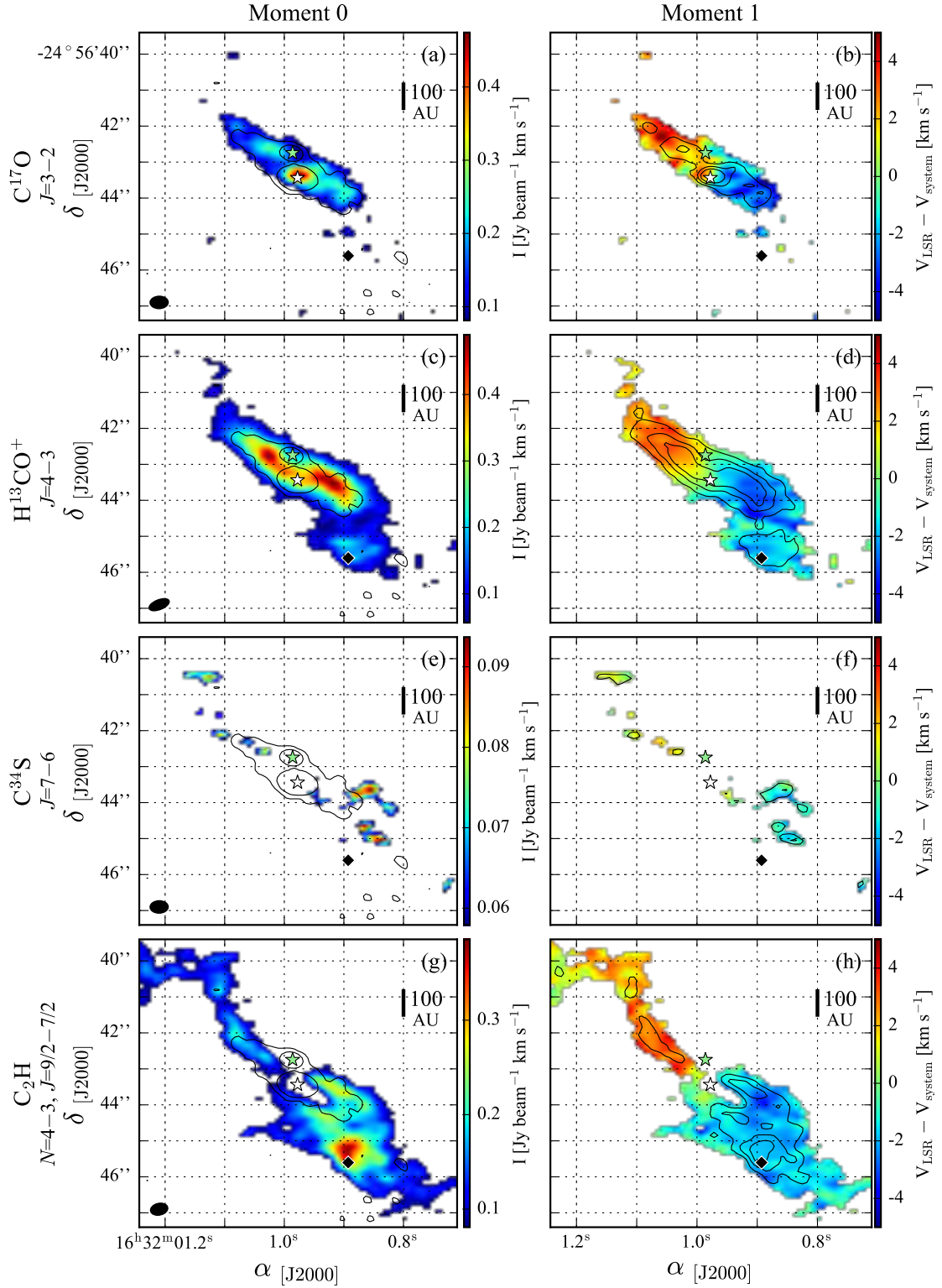
Figure 4.2: Moments 0 (*left column*) and 1 (*right column*) for $C^{17}O$, $H^{13}CO^+$, $C^{34}S$ and the C_2H $N=4-3$, $J=9/2-7/2$ doublet, above 5σ ($\sigma_{C^{17}O}$ =15 mJy beam^{-1} km s^{-1}, $\sigma_{H^{13}CO^+}$ = 10 mJy beam^{-1} km s^{-1}, $\sigma_{C^{34}S}$ = 10 mJy beam^{-1} km s^{-1} and σ_{C_2H} = 15 mJy beam^{-1} km s^{-1}). Each σ was calculated using the following formula: $\sigma = rms \times \Delta N \times (N)^{0.5}$, where ΔN and N are the channel width and number of channels, respectively. Black contours in moment 0 maps represent the continuum emission from Fig. 4.1, for values of 4 and 15σ. Black contours in moment 1 maps show σ values of their respective moment 0 maps, being 10, 15 and 20σ for $C^{17}O$ and C_2H, 10, 20 and 30σ for $H^{13}CO^+$, and 6 and 8σ for $C^{34}S$. The green and white stars indicate the position of Oph-IRS67A and B, respectively. The black diamond denotes the location of the offset region. The synthesised beam for each species is represented by a black filled ellipse.
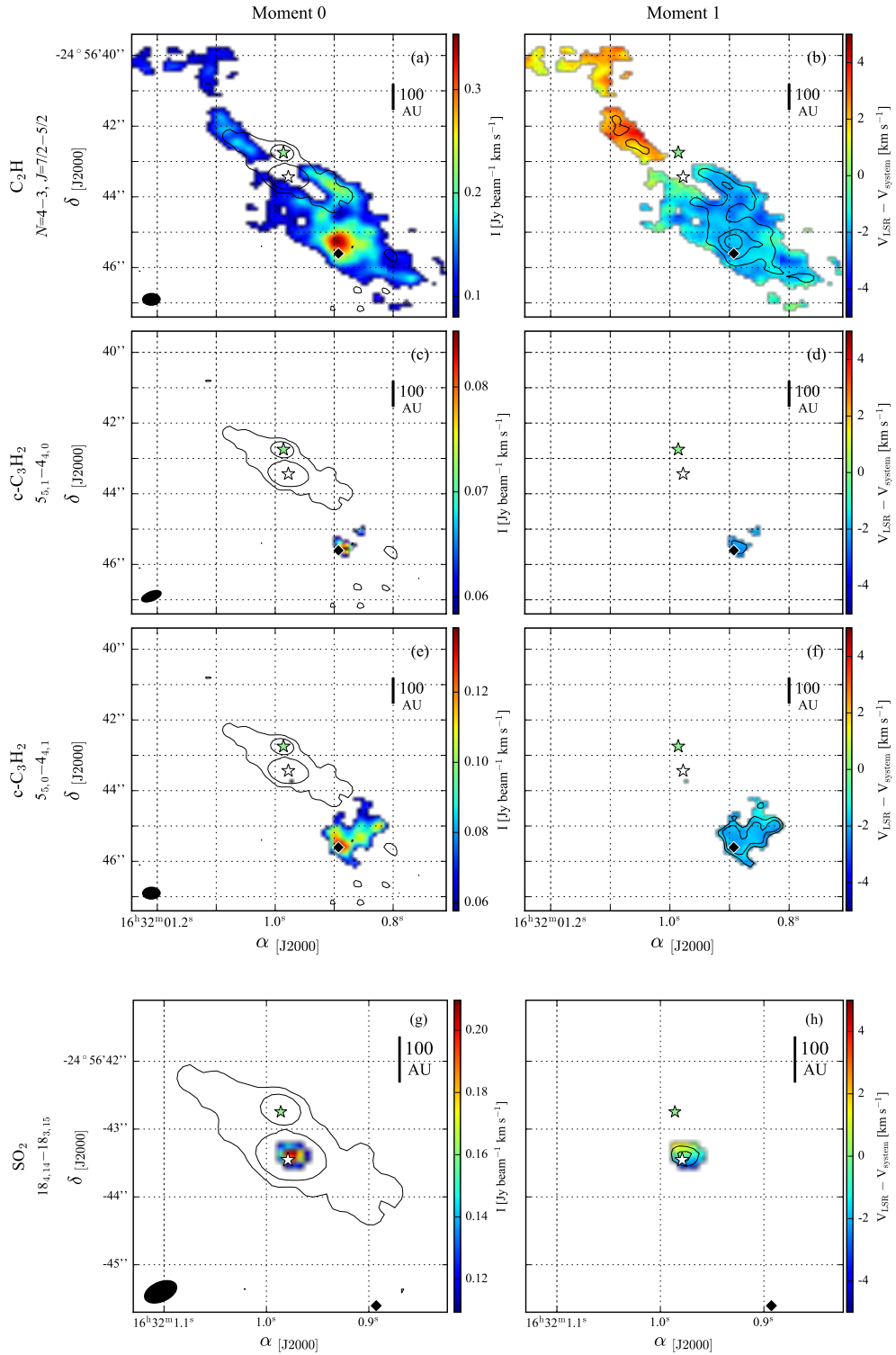
Figure 4.3: As in Fig. 4.2 but for the C$_2$H N=4−3, J=7/2−5/2 doublet, both c-C$_3$H$_2$ transitions and SO$_2$ $18_{4,14}$−$18_{3,15}$ ($\sigma_{\text{c−C}_3\text{H}_2}$ = 11 mJy beam^{-1} km s^{-1} and σ_{SO_2} = 25 mJy beam^{-1} km s^{-1}). For SO$_2$, the emission is above 4σ. Black contours in moment 1 maps represent 10, 15 and 20σ for C$_2$H, 6 and 8σ for c-C$_3$H$_2$, and 5 and 7σ for SO$_2$. Panels *g* and *h* represent a zoomed-in region.

4.4.2.2   Spectra

Figure 4.4 shows the spectra of $C^{17}O$, $H^{13}CO^+$, $C^{34}S$, C_2H and both c-C_3H_2 transitions towards the positions of source B, source A, and the high density region. Each spectrum was extracted over 1 pixel, that is, $0.''1 \times 0.''1$. At the position of source B, $C^{17}O$ shows a central component with two clear peaks at higher velocities (between -8 and -4 km s^{-1} and $+4$ and $+8$ km s^{-1}), $H^{13}CO^+$ peaks near V_{LSR} with a wing morphology that extends over positive velocities, and both C_2H doublets present two peaks, related with each hyperfine transition. $C^{34}S$ and both c-C_3H_2 transitions are not detected towards source B. Source A is associated with narrower lines from $C^{17}O$ and $H^{13}CO^+$, showing only a central component, and a weaker contribution from C_2H. As for source B, $C^{34}S$ and c-C_3H_2 are not detected towards source A. The high-density region presents weaker emission of $C^{17}O$ and $H^{13}CO^+$, where both lines peak at -1.7 km s^{-1}. The two C_2H doublets show intense and broader lines, and both c-C_3H_2 transitions are enhanced in this region. Observing the emission of $C^{17}O$ and $H^{13}CO^+$ over both sources, the peak in the spectra associated with Oph-IRS67B appears slightly blue-shifted (Fig. 4.4a and d) with respect to V_{LSR}, while Oph-IRS67A shows a red-shifted displacement (Fig. 4.4b and e).

Figure 4.5 shows part of the spectral window number 2 toward the position of source B and source A, where the rest frequencies of SO_2 and CH_3OH are indicated. SO_2 transitions are only seen towards source B and show broad emission (from -8 to 10 km s^{-1}), with an intense blue-shifted component and a weaker red-shifted one. One of the CH_3OH $J_k=7_k-6_k$ transitions falls close to a SO_2 line (Fig. 4.5a), but since no other lines in the CH_3OH branch are seen, including the lower excitation transitions, the line can clearly be attributed to SO_2.

4.4.2.3   Channel maps

Contour maps for $C^{17}O$ integrated over five different velocity ranges are shown in Fig. 4.6. The panels are divided into low velocities (-1 to 1 km s^{-1}), intermediate velocities (-5 to -1 km s^{-1} and 1 to 5 km s^{-1}) and high velocities (-10 to -5 km s^{-1} and 5 to 10 km s^{-1}). $H^{13}CO^+$, $C^{34}S$, C_2H and c-C_3H_2 only show intermediate- and low-velocity components, thus, contour maps associated with these species are taken for three ranges of velocities (Fig. 4.7). SO_2 shows a broad and double-peaked spectrum associated with blue- and red-shifted components (see Fig. 4.5a), therefore, the spectrum is fitted by a two-component Gaussian and the velocity ranges used for the channel maps of Fig. 4.8 are
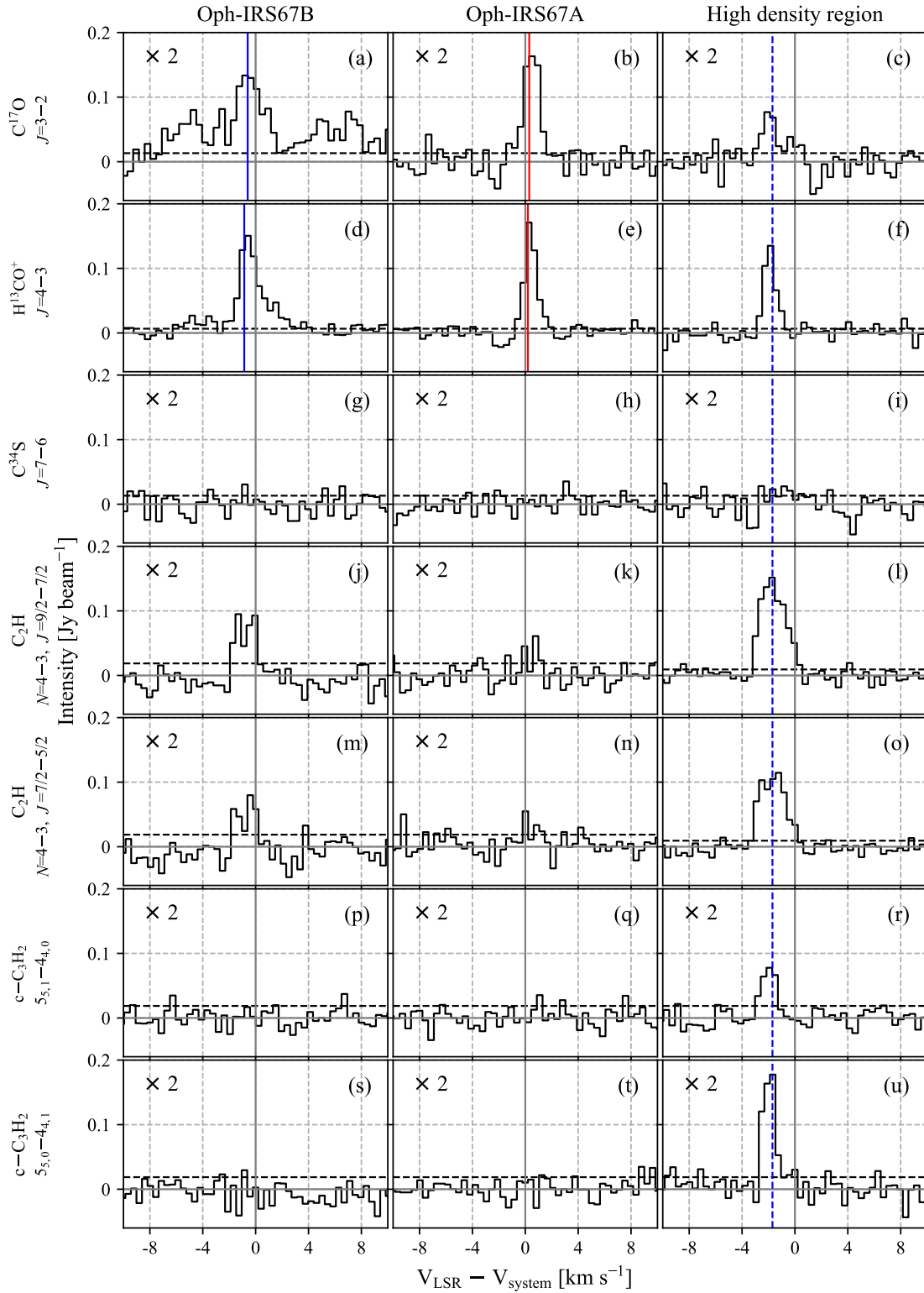
Figure 4.4: Spectra of $C^{17}O$, $H^{13}CO^{+}$, $C^{34}S$, both C_2H doublets and both c-C_3H_2 transitions for three different regions: the position of Oph-IRS67B (*left column*), the position of Oph-IRS67A (*middle column*) and the high-density region (*right column*). Spectra from panels *(a)* to *(i)* are rebinned spectrally by a factor of 4, while panels from *(j)* to *(u)* are rebinned spectrally by a factor of 2, so that all spectra have the same spectral resolution (0.43 km s^{-1}). The dashed black horizontal line shows the value of 3σ ($\sigma = 3$ mJy beam^{-1} km s^{-1}). All spectra have been shifted to the systemic velocity (4.2 km s^{-1}; grey vertical line). The solid blue and red lines indicate the offset of the peak velocity determined from a Gaussian fit (see Table 4.4). The dashed blue line in the right column represents a velocity of -1.7 km s^{-1}. Some spectra have been multiplied by a scaling factor as indicated in the top left corner.
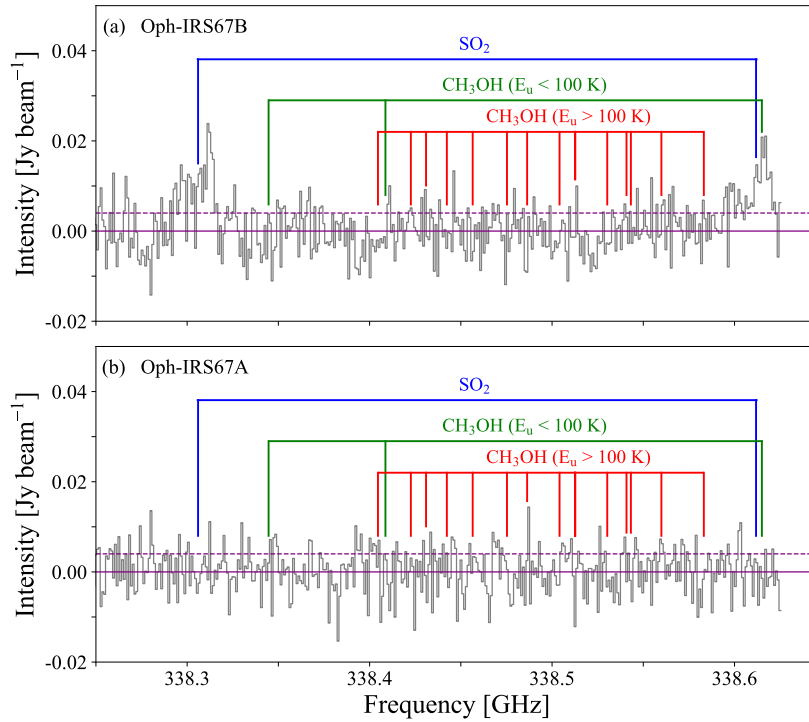
Figure 4.5: Spectra from spectral window number 2, taken at the position of Oph-IRS67B (*top*) and Oph-IRS67A (*bottom*), and rebinned by a factor of 4. Blue lines show the rest frequency of SO_2 transitions. Green and red lines indicate the rest frequency of CH_3OH transitions with upper energy levels (E_u) below and above 100 K, respectively. The purple dashed line shows the value of 1σ ($\sigma = 4$ mJy beam^{-1} per channel).

associated with the FWHM of the blue- and red-shifted components.

At low velocities, $C^{17}O$ and $H^{13}CO^+$ appear to be centred around both sources. $C^{34}S$ presents isolated peaks closer to source B, while C_2H dominates the central and Southern regions. A lack of emission at low velocities is seen for both c-C_3H_2 transitions.

At intermediate velocities, $C^{17}O$ and $H^{13}CO^+$ show some symmetry with respect to Oph-IRS67B. $C^{34}S$ presents an S-type morphology and enhanced emission far away from the binary system, while C_2H shows the most extended emission and the blue-shifted emission dominates over a wider region than the red-shifted one. Both c-C_3H_2 transitions show the same behaviour, with intermediate blue-shifted velocities tracing the high-density region and no red-shifted counterpart.

High velocities are associated with $C^{17}O$ and SO_2, showing compact emission only around Oph-IRS67B. $C^{17}O$ blue- and red-shifted emission are strongly symmetric around the source, while the blue component associated with SO_2 stands out over the red one and is concentrated around the source.
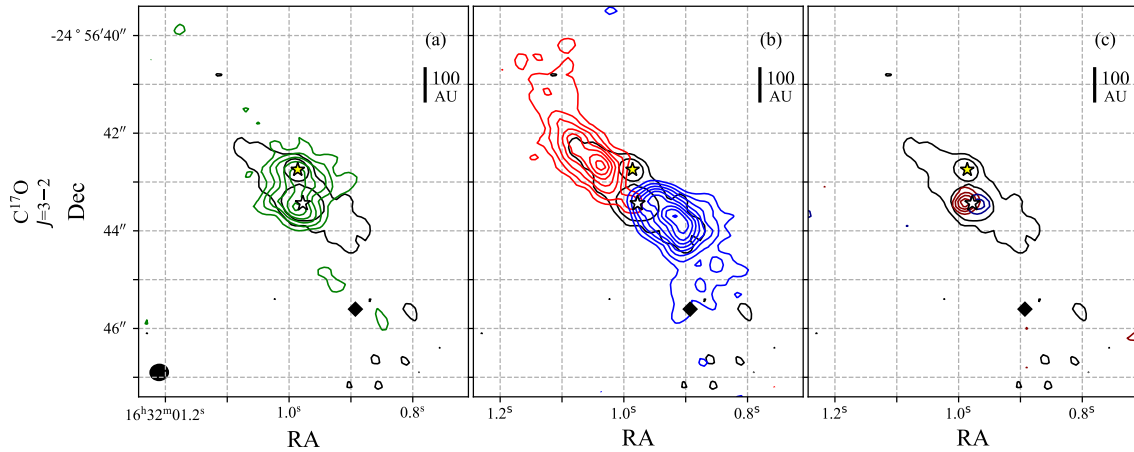
Figure 4.6: Contour maps for C^{17}O, starting at 5σ (σ = 6 mJy beam^{-1} km s^{-1}) and following a step of 4σ. Green contours represent low velocities emission, from -1 to 1 km s^{-1} (*left*). Blue and red contours indicate intermediate velocities, from -1 to -5 km s^{-1} and from 1 to 5 km s^{-1}, respectively (*middle*). Dark-red and dark-blue contours show high-velocity emission, from -5 to -10 km s^{-1} and from 5 to 10 km s^{-1}, respectively (*right*). The black contours represent the continuum emission of Fig. 4.1 for values of 4 and 15σ (σ = 0.4mJy beam^{-1}). The yellow and white stars indicate the position of Oph-IRS67A and B, respectively. The black diamond denotes the location of the high density region. The synthesised beam is represented by a black filled ellipse.

4.5 Analysis

4.5.1 Velocity profiles

C^{17}O and H^{13}CO$^+$ are the best candidates for studying the velocity profile of the disk-like structure through position-velocity (PV) diagrams, since they are correlated with the continuum emission. The other species are not suitable for studying the velocity profile of the disk-like structure, as they seem to be tracing different material. C$_2$H has an important contribution beyond $2''$ and may be tracing envelope material, while C^{34}S is tracing smaller regions from the outer parts of the disk-like structure, and SO$_2$ emission is unresolved within the beam size. On the other hand, c-C$_3$H$_2$ is tracing the high-density region; its velocity profile is discussed in Sect. 4.1.2.

In order to obtain the velocity profiles, the peak emission for each channel is obtained through the CASA task `imfit`. Two fits are considered for high-velocity points (>1.7 km s^{-1}): (i) a Keplerian fit where $v \propto r^{-0.5}$ and (ii) an infalling fit where $v \propto r^{-1}$ (i.e. infalling motion where the angular momentum is conserved). In all cases, the central (0,0) position corresponds to the location of the geometric centre and the distance increase toward the disk-like structure direction (PA = 234°; grey solid arrow in Fig. 4.1), assuming an inclination of 80°.
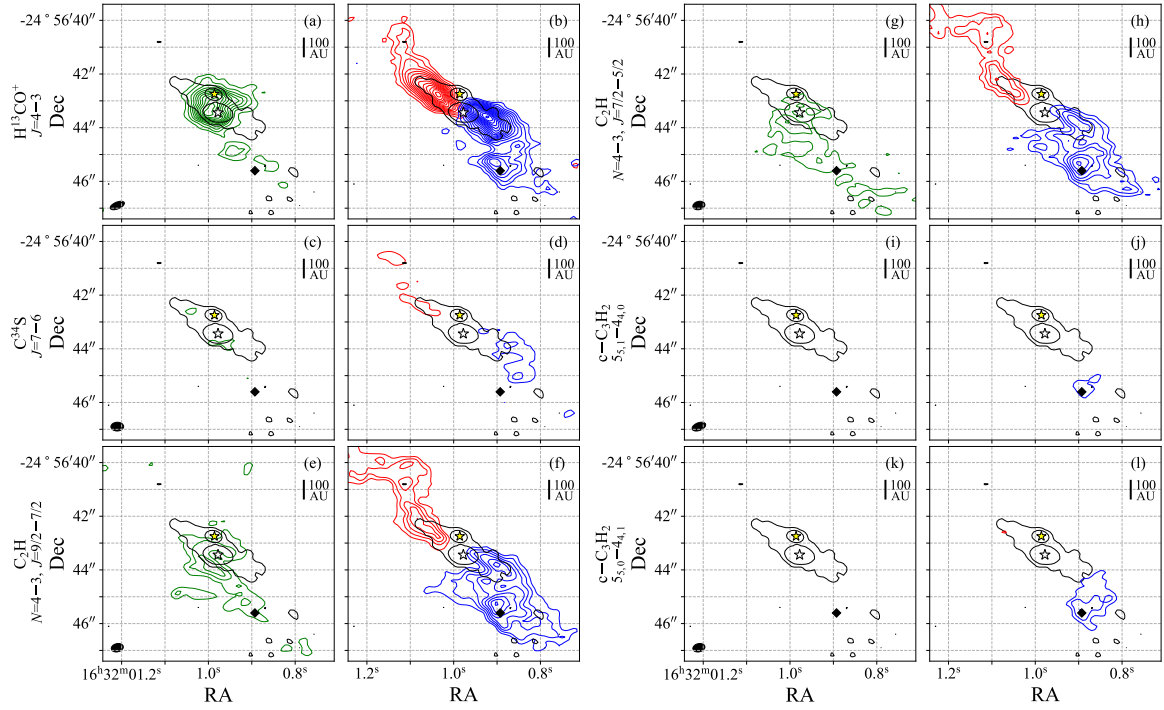
Figure 4.7: Contour maps for $H^{13}CO^+$, $C^{34}S$, both C_2H doublets and both c-C_3H_2 transitions, starting at 5σ and following a step of 4σ ($\sigma_{H^{13}CO^+}$ and $\sigma_{C^{34}S}$ are 6 mJy beam^{-1} km s^{-1}, while σ_{C_2H} and $\sigma_{c-C_3H_2}$ are 9 mJy beam^{-1} km s^{-1}). Green contours represent low-velocity emission, from -1 to 1 km s^{-1}. Blue and red contours indicate intermediate velocities, from -1 to -5 km s^{-1} and from 1 to 5 km s^{-1}, respectively. The black contours represent the continuum emission of Fig. 4.1 for a value of 4 and 15σ ($\sigma = 0.4$ mJy beam^{-1}). The yellow and white stars indicate the position of Oph-IRS67A and B, respectively. The black diamond denotes the location of the high-density region. The synthesised beam for each species is represented by a black filled ellipse.
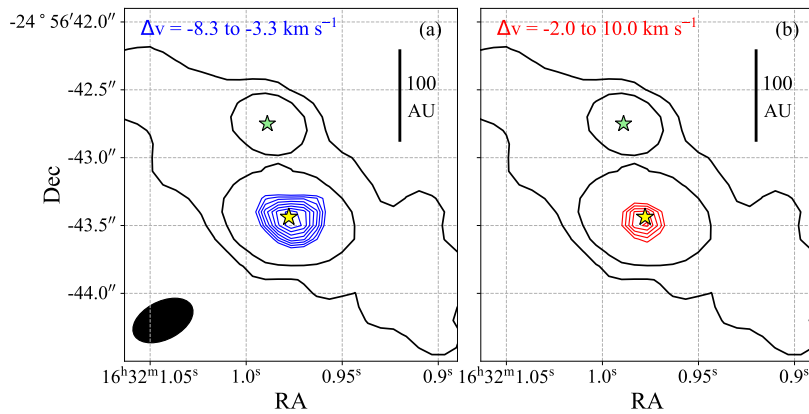
Figure 4.8: Contour maps for SO_2 $18_{4,14}-18_{3,15}$ for two ranges of velocities. The contours start at 4σ, following a step of 0.5σ. The black contours represent the continuum emission of Fig. 4.1 for a value of 4 and 15σ ($\sigma = 0.4$ mJy beam^{-1}). The green and white stars indicate the position of Oph-IRS67A and B, respectively. The synthesised beam is represented by a black filled ellipse.

4.5.1.1   Disk-like structure

The PV diagrams for $C^{17}O$ and $H^{13}CO^+$ are shown in Fig. 4.9. Neither the Keplerian nor the infalling fit is representative of the data, where the points with velocities greater than 3 km s^{-1} seem to follow the Keplerian curve, while points with velocities between $\sim$ 2 and 3 km s^{-1} tend to follow the infalling curve. This fact is highlighted by their reduced χ^2 values, listed in Table 4.3. For $C^{17}O$ both fits are associated with the same χ^2_{red}, while for $H^{13}CO^+$ the Keplerian fit has a lower χ^2_{red} value than the infalling one. This means that the goodness of the Keplerian fit is better than the infalling fit, but neither of them can be discarded by this PV analysis. However, the presence of low-velocity points (< 1.7 km s^{-1}) that appear to follow a linear distribution is expected for a Keplerian disk with finite radius (Lindberg et al. 2014). This emission arises from the edge of the disk and is an unlikely effect in the infall scenario, since the infalling material should not have a sharp edge.

The Keplerian and infalling fits were also tested for the scenario where the position of source B is used as the centre, resulting in χ^2_{red} values higher than 10 for both fits. Therefore, the material from the disk-like structure is not moving with respect to either source, but with respect to some position between the two.

The PV diagrams taken towards the direction perpendicular to the disk-like structure (PA = 324°; grey dashed arrow in Fig. 4.1) did not show significant emission beyond 1″ (150 AU) and no infall signatures were detected. This lack of emission towards a perpendicular direction is consistent with Keplerian rotation around the binary system at small scales.

The presence of a linear velocity profile for low velocities in Fig. 4.9 and the lack of infalling signatures towards a perpendicular direction suggests that *circumbinary disk* is a reasonable label for the disk-like structure. Based on the Keplerian fit, the circumbinary disk is associated with a central mass of 2.2 ± 0.2 M$_\odot$.

4.5.1.2   High-density region

The PV diagram for c-C_3H_2 is shown in Fig. 4.10. In this case, the goodness of the infalling fit is better than the Keplerian one, with χ^2_{red} values of 2.4 and 4.6, respectively (Table 4.3). However, the central mass associated with the infalling fit is 3.6 ± 0.3 M$_\odot$, which is not consistent with the central mass of 2.2 ± 0.2 M$_\odot$ found from the Keplerian fit of $C^{17}O$ and $H^{13}CO^+$. This implies that the c-C_3H_2 gas may not be following an infalling motion around the geometric centre and another velocity profile

Table 4.3: Central mass and χ^2_{red} values for the Keplerian and infalling fits employed in Figs. 4.9 and 4.10.

Species	Fit	Central mass [$M_\odot$]	χ^2_{red}
		Disk-like structure	
$C^{17}O$	Keplerian	2.2 ± 0.2	3.3
	Infalling	1.5 ± 0.2	3.3
$H^{13}CO^+$	Keplerian	2.2 ± 0.2	6.5
	Infalling	1.5 ± 0.2	15.1
		High-density region	
$c\text{-}C_3H_2$	Keplerian	2.2 ± 0.2	4.6
	Infalling	3.6 ± 0.3	2.4
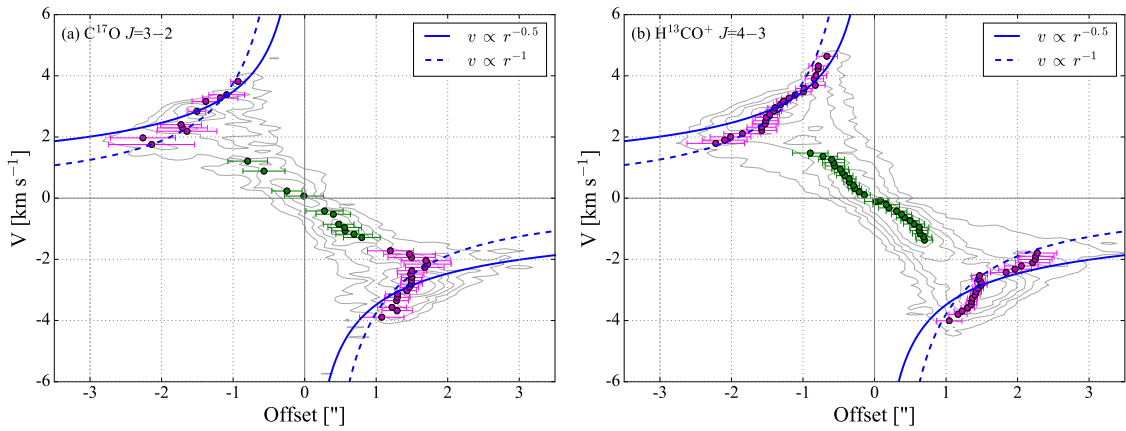
Figure 4.9: Position-velocity diagrams for $C^{17}O$ and $H^{13}CO^+$ towards the disk-like structure direction (PA = 234°) and centred at the position of the geometric centre. Green and magenta dots represent low- (< 1.7 km s^{-1}) and high-velocity (> 1.7 km s^{-1}) emission peaks, respectively. Blue solid and dashed lines show the best fit for a Keplerian and an infalling velocity profile, respectively. The cut taken from the image data is shown in grey contours, ranging from 3σ ($1\sigma = 10$ mJy beam^{-1}) to the maximum value of each transition. Each adjacent contour represents an increment of the 20% of the maximum value.

has to be considered for this molecular transition.

The high-density region may also be a separate object with a different centre; however, if this were the case, we would expect compact continuum emission toward this region, contrary to what we see. Thus, it is more likely that the high-density region is related to the inner envelope or ambient cloud, and not to a third object.

4.5.2 Disk mass

The dust and gas masses are calculated from the continuum emission (Fig. 4.1) and from the integrated intensity of $C^{17}O$ $J=3-2$ (Fig. 4.2a), respectively. For both cases, the calculated mass represents the entire system, i.e. both sources and the circumbinary disk contribution.

If the emission is optically thin, the total mass is
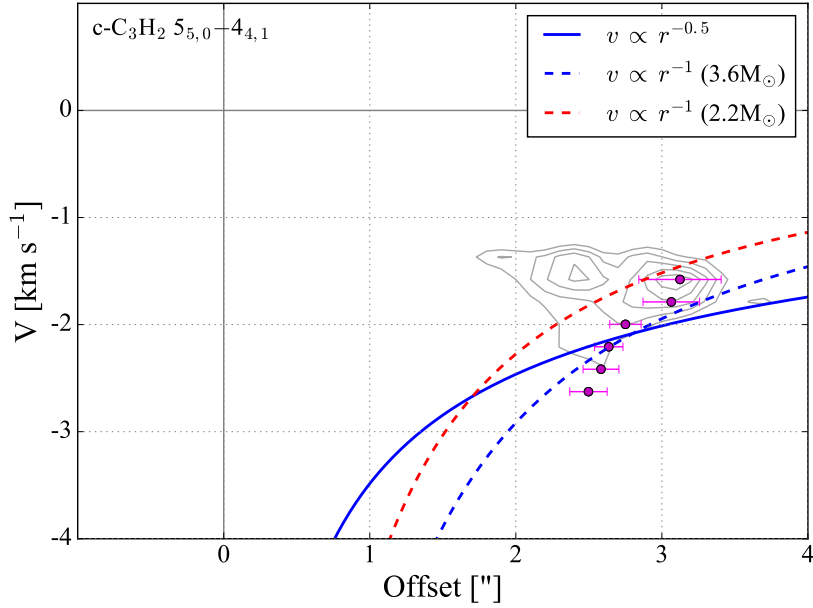
Figure 4.10: Position-velocity diagram for c-C$_3$H$_2$ $5_{5,0}-4_{4,1}$ towards the disk-like structure direction (PA = 234°) and centred at the position of the geometric centre. The magenta dots represent high-velocity (> 1.7 km s^{-1}) emission peaks. Blue solid and dashed lines show the best fit for a Keplerian and an infalling velocity profile, respectively, while the red dashed line represents an infalling profile for a central mass of 2.2 M$_\odot$. The cut taken from the image data is shown in grey contours, ranging from 3σ ($1\sigma = 10$ mJy beam^{-1}) to the maximum value. Each adjacent contour represents an increment of the 20% of the maximum value.

$$M = \frac{S_\nu d^2}{\kappa_\nu B_\nu(T)} , \tag{4.1}$$

where S_ν is the surface brightness, d the distance to the source, κ_ν the dust opacity and $B_\nu(T)$ the Planck function for a single temperature. For typical parameters of the dust temperature (30 K) and opacity at 0.87 mm (0.0175 cm^2 per gram of gas; Ossenkopf & Henning 1994), commonly used for dust in protostellar envelopes and young disks in the millimetre regime (e.g. Shirley et al. 2011), the mass can be estimated as:

$$M_{0.87\text{mm}} = 0.18 \, M_\odot \left(\frac{F_{0.87\text{mm}}}{1 \text{ Jy}}\right)\left(\frac{d}{200 \text{ pc}}\right)^2 \left\{\exp\left[0.55\left(\frac{30 \text{ K}}{T}\right)\right] - 1\right\}, \tag{4.2}$$

where $M_{0.87\text{mm}}$ is the total (dust + gas) mass at 0.87 mm and $F_{0.87\text{mm}}$ is the flux at 0.87 mm.

For the gas mass calculation, the intensity of C^{17}O J=3−2 is integrated over a velocity range of 20 km s^{-1}, obtaining a value of 5.31 ± 0.01 Jy km s^{-1} for S_ν times the velocity interval (dν), for emission above 5σ. Assuming a Boltzmann distribution with temperature T, the total column density of C^{17}O, N_{total}(C^{17}O), is

$$N_{\text{total}}(\text{C}^{17}\text{O}) = \frac{4\pi S_v dv}{\Omega A_{32} hc} \, Q(T) \exp\left(\frac{E_3}{k_B T}\right), \tag{4.3}$$

where Ω is the beam solid angle, A_{32} the Einstein coefficient for the transition $J=3-2$, h the Plank constant, c the light speed, $Q(T)$ the partition function and E_3/k_B the upper level energy. Finally, the gas mass (M_{gas}) is

$$M_{\text{gas}} = N_{\text{total}}(\text{C}^{17}\text{O}) \left[\frac{\text{CO}}{\text{C}^{17}\text{O}}\right]\left[\frac{\text{H}_2}{\text{CO}}\right] 2.8 m_H \mathcal{A}, \tag{4.4}$$

where $[\text{CO}/\text{C}^{17}\text{O}]$ and $[\text{H}_2/\text{CO}]$ are relative abundances, $2.8\,m_H$ is the mean molecular weight (Kauffmann et al. 2008), m_H the hydrogen mass and $\mathcal{A}$ the beam area. By assuming a C^{17}O abundance with respect to CO of 4.5×10^{-4} (Penzias 1981) and a CO abundance with respect to H_2 of 2.7×10^{-4} (Lacy et al. 1994), gas masses are found for different temperatures.

Figure 4.11 shows the dust mass, gas mass, and CO abundances with respect to H_2 for different temperatures. The dust and gas masses are calculated using Eqs. 4.2 and 4.4, respectively, while the CO abundances are calculated by isolating $[\text{CO}/\text{H}_2]$ from Eq. 4.4 and assuming a gas-to-dust ratio of 100. The CO abundances are specifically inferred to test if a significant fraction of this molecule is frozen out in the cold midplane of the circumbinary disk, as would normally be expected. For comparison, the purple line shows the typical value of 2.7×10^{-4} for the abundance of CO with respect to H_2. Dust and gas masses increase as the temperature decreases, following an exponential behaviour, while a raise in the CO abundance is observed for higher temperatures. For a typical dust temperature of 30 K, a value of $1.1 \times 10^{-2}\ M_\odot$ is obtained for the total mass and, by taking a gas-to-dust ratio of 100, a dust mass of $1.1 \times 10^{-4}\ M_\odot$ is derived. We note that for all of the temperatures used in the calculations, CO abundances are comparable to the canonical value of 2.7×10^{-4}.

4.5.3 Fits and abundances

Towards the position of source B and source A, the central components from C^{17}O and H^{13}CO^+ show a slightly blue-shifted emission in the case of source B and a red-shifted emission for source A (Fig. 4.4a, b, d and e). This shift between both sources can be related to their proper motion, relative to the geometric centre. In order to obtain an accurate value of this shift, the central component of the spectra of both species is fitted with a Gaussian and the values are listed in Table 4.4. By comparing the velocity centroid for the same species, a difference of ~ 1 km s^{-1} is seen between the
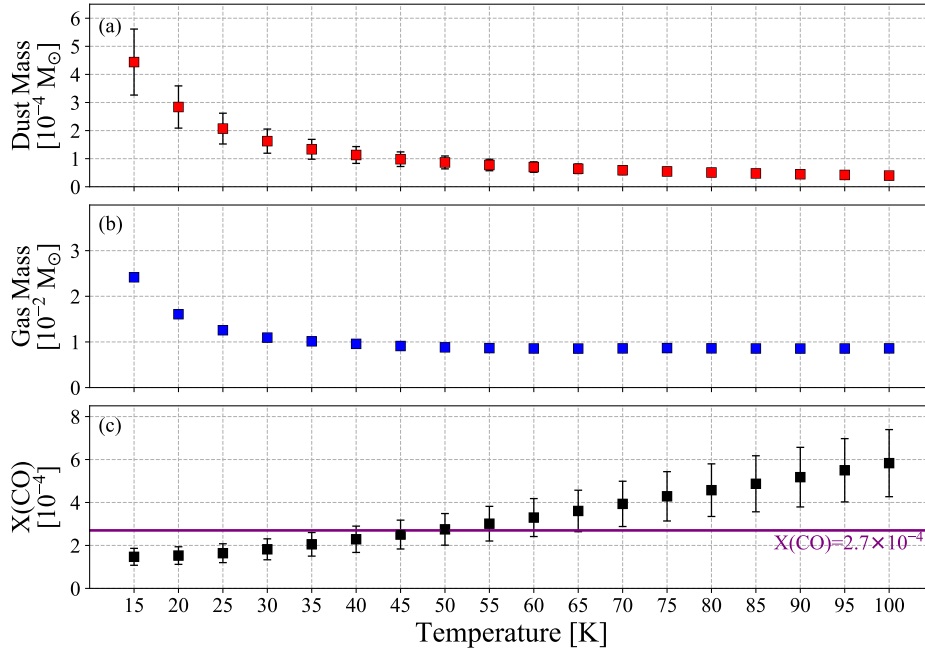
Figure 4.11: Dust mass, gas mass, and values of CO abundances, for different temperatures and taken for the entire system (both sources and the circumbinary disk). The CO abundances are calculated by assuming a gas-to-dust ratio of 100. For gas masses (blue squares), the uncertainties are ~0.3 % of the value and are imperceptible on the plot. The purple horizontal line shows the value of 2.7×10^{-4} for the abundance of CO with respect to H_2.

sources. Apart form $C^{17}O$ and $H^{13}CO^+$, SO_2 also shows emission towards source B and its emission is compact. The spectrum of SO_2 does not show a central component but presents blue- and red-shifted emission, thus, a two component Gaussian fit was employed. The blue component is more intense than the red one (20 vs. 9 mJy beam^{-1}), however, the red-shifted emission presents a broader component (12 vs. 5 km s^{-1}).

The statistical equilibrium radiative transfer code (RADEX; van der Tak et al. 2007) is used to estimate the optical depth (τ) and column densities of $C^{17}O$, $H^{13}CO^+$, and SO_2, towards the position of source B. An upper limit for the CH_3OH column density is also determined by taking an intensity of 10 mJy beam^{-1} (1σ) and a *FWHM* of 2.4 km $^{-1}$ (same value as the *FWHM* of the central component of $C^{17}O$; Table 4.4). The calculated values for τ and column density are listed in Table 4.5, and are obtained by assuming a H_2 number density of 1×10^7 cm^{-3} (collision partner), two kinetic temperatures ($T_{\rm kin}$) of 30 and 100 K, and a broadening parameter (*b*) corresponding to the *FWHM* value of each transition (see Table 4.4). The chosen value for the H_2 number density is related to the average value for the critical densities of the observed transitions (see Table 6.1). If we change the H_2 density by a factor of 10, the $C^{17}O$ column density remains constant since its level populations

Table 4.4: Gaussian fit values over the position of Oph-IRS67 A and B.

Transition	Source	Component	Intensity [mJy beam^{-1}]	Centre [km s^{-1}]	*FWHM* [km s^{-1}]
C^{17}O J=3−2	Oph-IRS67B	Central	63 ± 5	-0.6 ± 0.1	2.4 ± 0.3
	Oph-IRS67A	Central	90 ± 20	0.3 ± 0.2	1.4 ± 0.4
H^{13}CO$^+$ J=4−3	Oph-IRS67B	Central	120 ± 10	-0.9 ± 0.1	1.3 ± 0.1
	Oph-IRS67A	Central	160 ± 20	0.2 ± 0.1	1.1 ± 0.2
SO$_2$ $18_{4,14}$−$18_{3,15}$	Oph-IRS67B	Blue	20 ± 4	-5.8 ± 0.4	5 ± 1
		Red	9 ± 2	4 ± 2	12 ± 5
CH$_3$OH $7_{-1,7}$−$6_{-1,6}$ E [a]	—	—	< 11 [b]	—	2.4 [c]

Reported uncertainties are all 1σ. [a] Expected brightest transition at 100 K. [b] Value of 1σ. [c] Same value as C^{17}O.

are thermalized (the critical density for this transition is 3.5×10^4 cm^{-3}; see Table 6.1). In the case of H^{13}CO$^+$, its abundance remains constant for an increasing H$_2$ density but may increase by a factor of 3 for a decreasing density (depending on the kinetic temperature). On the other hand, the SO$_2$ column density varies from 5×10^{15} to 1×10^{18} cm^{-2} for an increasing density. Thus, the abundances presented in Table 4.5 are lower limits for H^{13}CO$^+$ and approximate values for SO$_2$. The kinetic temperature of 30 K represents the lower limit for a rich molecular layer of the disk, warm enough that most molecules are in the gas phase, and that the chemistry is dominated by ion-neutral reactions (Henning & Semenov 2013). In addition, the kinetic temperature of 100 K represents the inner regions around the source, where a hot corino chemistry is expected. The optical thickness of C^{17}O and H^{13}CO$^+$ are close to 1 for a gas temperature of 30 K. For warmer gas (100 K), C^{17}O, H^{13}CO$^+$, and CH$_3$OH emission are optically thin (τ<1), while SO$_2$ shows optically thick emission (τ>1). In the case of SO$_2$, a value of ~16 K is obtained for the calculated excitation temperature ($T_{\rm ex}$) of the model, suggesting that the line is sub-thermally excited.

The calculated relative abundances of HCO$^+$, SO$_2$, and CH$_3$OH with respect to CO are shown in Table 4.6, employing standard isotope ratios (Wilson 1999). The obtained values are compared with abundance ratios observed for the prototypical Class 0 source, IRAS 16293-2422, taken from Schöier et al. (2002). IRAS 16293-2422 is deeply embedded ($M_{\rm env}$ ~ 4 M$_\odot$; Jacobsen et al. 2018) and more luminous ($L = 21 \pm 5$ L$_\odot$; Jørgensen et al. 2016) than IRS 67, but it was chosen for the comparison since molecules such as CH$_3$OH and SO$_2$ were detected towards the system. Schöier et al. (2002) calculated molecular abundances for two different scenarios: (i) using a constant molecular abundance relative to H$_2$, and (ii) applying a jump in the fractional abundance at a temperature of 90 K. For scenario (ii), they present the abundances for the inner, dense, hot part of the envelope

Table 4.5: Retrieved parameters from RADEX by assuming a kinetic temperature ($T_{\rm kin}$) and a broadening parameter (b), for Oph-IRS67 B.

Transition	Component	$T_{\rm kin}$ [K]	b [km s^{-1}]	τ	$N(X)$ [cm^{-2}]
C^{17}O J=3$-$2	Central	30	2.4	0.76	2.0×10^{16}
		100	2.4	0.14	2.3×10^{16}
H^{13}CO$^+$ J=4$-$3	Central	30	1.3	1.02	$\geq 1.3 \times 10^{13}$
		100	1.3	0.14	$\geq 8.3 \times 10^{12}$
SO$_2$ $18_{4,14}-18_{3,15}$	Blue	100	5	1.97	$\sim 2.0 \times 10^{17}$
	Red	100	12	2.04	$\sim 4.9 \times 10^{17}$
CH$_3$OH $7_{-1,7}-6_{-1,6}$ E	—	100	2.4	0.02	$< 1.6 \times 10^{14}$

Reported values are for a fixed H$_2$ density of 1×10^7 cm^{-3}.

Table 4.6: Comparison between calculated relative abundances with respect to CO for Oph-IRS67 B and values taken from Schöier et al. (2002) for the Class 0 protostar IRAS 16293$-$2422.

Species	This work	Schöier et al. (2002)		
		Constant abundance [a]	Jump ($T > 90$ K) [b]	Jump ($T < 90$ K) [c]
HCO$^+$ [d]	$[4.8 \times 10^{-6} - 2.2 \times 10^{-5}]$ [e]	**3.9×10^{-5}**	—	—
SO$_2$	$[4.3 \times 10^{-3} - 1.1 \times 10^{-2}]$ [f]	1.7×10^{-5}	**2.8×10^{-3}**	1.3×10^{-5}
CH$_3$OH	$< 3.5 \times 10^{-6}$	4.8×10^{-5}	2.8×10^{-3}	9.8×10^{-6}

[a] Value using a constant molecular abundance relative to H$_2$. [b] Value using a jump in the fractional abundance and obtained for the hot part of the envelope ($T > 90$ K). [c] Value using a jump in the fractional abundance and obtained for the cooler part of the envelope ($T < 90$ K). Highlighted values are closer to our calculations. [d] Assuming standard isotope ratios for C^{17}O (^{16}O/^{17}O = 2005) and H^{13}CO$^+$ (^{12}C/^{13}C = 69) from Wilson (1999). [e] For a range of temperatures, between 30 and 100 K. [f] For blue and red components.

($T > 90$ K), and for the cooler, less dense, outer part of the envelope ($T < 90$ K). Comparing our relative abundances with those from Schöier et al. (2002), the [HCO$^+$]/[CO] abundance ratio agrees with a model with constant molecular abundance, the [SO$_2$]/[CO] abundance ratio is consistent with a relative abundance in the hot part of the envelope for a jump model, and the upper limit for the [CH$_3$OH]/[CO] abundance ratio is, at least, two orders of magnitude smaller than the obtained values for each model.

4.6 Discussion

4.6.1 Structure of Oph-IRS67

The continuum emission (Fig. 4.1) shows the binary system, separated by 0.″71 $\pm$ 0.″01 (107 $\pm$ 2 AU), previously detected by McClure et al. (2010) at infrared wavelengths. They estimated a separation of 0.6″ ($\sim$ 90 AU) between the two sources and found that Oph-IRS67A (L1689S-A) is brighter than Oph-IRS67B (L1689S-B), while the opposite situation is observed in the sub-millimetre regime. The contrast between the sources at different wavelengths could be due to, (i) different

evolutionary stages, i.e. Oph-IRS67A is more evolved than Oph-IRS67B, (ii) different dust grain sizes, (iii) different orientation of possible circumstellar disks, where the one associated with source A may be more face-on and the one related to source B more edge-on, (iv) different temperatures if the sources present distinct masses or one of them displays ongoing accretion bursts or, (v) the two sources lie differently in the circumbinary disk, where source B is more obscured than source A.

Since close binaries are expected to be coeval systems, options (i) and (ii) are less likely. Option (iii) is supported by SO_2 and $C^{17}O$ emission, where both species show compact morphology around source B at high velocities. Such behaviour would be expected for an edge-on circumstellar disk, however this emission can also be related to accretion shocks (Podio et al. 2015). On the other hand, source A is associated with $C^{17}O$ emission at low velocities but no SO_2 emission is observed towards this source. This supports the scenario where a possible circumstellar disk associated with source A is more face-on, where the shift in velocities is not as perceptible as in the edge-on case. Although a perpendicular misalignment between the two sources is statistically unlikely ($\sim 2\%$; Murillo et al. 2016), this scenario will be consistent with source A being brighter than source B at infrared wavelengths, where the warm dust in the line of sight is not obscured by the cold dust. Option (iv) is plausible if the sources have different masses, however if one of the sources presents higher temperatures due to accretion bursts, we would expect to detect gas-phase CH_3OH around it. The arrangement proposed in option (v) agrees with the scenario suggested for IRS 43 (Brinch et al. 2016), where one of the sources lies behind the circumbinary disk and, therefore, is more obscured by the material along the line of sight. In the case of IRS 43, the two continuum sources have the same mass but differ in intensity by a factor of $5-10$. For Oph-IRS67 AB, the intensity of the two sources differs by a factor of 5, however there are no constraints on the individual masses.

The velocity difference between the two sources seen in $C^{17}O$ and $H^{13}CO^+$ (Fig. 4.4 and Table 4.4) is more consistent with emission arising from different regions than radial motion of both sources. If $C^{17}O$ and $H^{13}CO^+$ trace radial motions, a better correlation between the parameters of their Gaussian fits is expected. This does not exclude that both sources are rotating around the centre of mass: indeed, such rotation is expected, but proper motion measurements are necessary to support this interpretation (see, e.g. Brinch et al. 2016).

At first glance, the weaker emission associated with the disk-like structure could be thought to be associated with a circumbinary disk, an inner infalling envelope or an outflow. However, the latter is ruled out since the system is already associated with an outflow perpendicular to the disk-like structure

(Bontemps et al. 1996). On the other hand, neither the Keplerian nor the infalling fit can be ruled out from the PV diagrams of $C^{17}O$ and $H^{13}CO^+$. A combination of both fits is more consistent with the data, where the large-scale structure is dominated by infalling motion and gas from inner regions follows a Keplerian profile (e.g. Harsono et al. 2014). The presence of low-velocity points that seem to follow a linear distribution is expected for a Keplerian disk with finite radius. In addition, the lack of infalling signatures towards the perpendicular direction at small scales, agrees with the existence of a circumbinary disk associated with Keplerian motion around a central mass of 2.2 ± 0.2 $M_\odot$. Assuming that the major axes of the deconvolved continuum size represents the circumbinary disk diameter, its value of 620 AU is three times larger than the typical size of circumstellar disks around Class I sources, which is about 200 AU (Harsono et al. 2014). However, other detected circumbinary disks around Class I sources, such as IRS 43 (Brinch et al. 2016) and L1551 NE (Takakuwa et al. 2017), show comparable sizes to that of Oph-IRS67 (diameters of $\sim$ 650 and $\sim$ 600 AU for IRS 43 and L1551 NE, respectively).

Given the low mass of the ambient core estimated from larger-scale SCUBA maps (0.08 $M_\odot$; Jørgensen et al. 2008), the two protostars can only accrete a small amount of additional material from here on. Assuming that both sources have similar masses, each of them would have a final mass of about 1 $M_\odot$, which is consistent with the total luminosity of the system (4.0 $L_\odot$; Evans et al. 2009).

The high-density region is enhanced in c-C_3H_2 and lies beyond the extension of the circumbinary disk; it stands out in intermediate blue-shifted velocities and there is a lack of red-shifted counterpart. This region also shows bright C_2H emission, but since this molecule also traces material from the vicinity of the protostars and is associated with red-shifted emission, its chemistry is not exclusively associated with the high-density region. The mentioned region could be related to, (i) a centrifugal barrier (a transition zone within the disk where the kinetic energy of the infalling gas is converted into rotational energy; Sakai et al. 2014), (ii) a region from the outflow cavity that is being irradiated by the sources, (iii) spiral-arm features formed by gravitational torques from the binary system or, (iv) ambient gas cloud or envelope that is infalling into the disk.

Option (i) was proposed by Sakai et al. (2014), where they observe a drastic change in the chemistry (between c-C_3H_2 and SO) and argue that c-C_3H_2 follows an infalling motion, while SO shows a Keplerian profile. Therefore, the centrifugal barrier will be located in the discontinuous region between both molecular emission. In our case, a spatial difference is seen between $C^{17}O$ and c-C_3H_2, however there is no evidence of a discontinuous change in the motion of the gas. The infalling fit

for c-C_3H_2 is associated with a central mass that is not consistent with the value obtained from the Keplerian fit of $C^{17}O$, thus a centrifugal barrier cannot explain the presence of the high-density region in Oph-IRS67. Option (ii) was proposed by Murillo et al. (2018) for the Class 0 source VLA 1623. They observed a correlation between c-C_3H_2 and C_2H in a region located ~300 AU from the source, and interpret that this emission is arising from the outflow cavity, where material is being irradiated by the star. Oph-IRS67 is associated with a large-scale outflow (Bontemps et al. 1996) and it has been shown that the outflow opening angle widens with time (Arce & Sargent 2006). If the high-density region is related to the outflow cavity, an opening angle of ~ 60° is needed for the radiation of the two stars to reach the region where c-C_3H_2 and C_2H are abundant. However, there is no evidence for red-shifted emission associated with c-C_3H_2 and a symmetric blue-shifted counterpart on the other side of the postulated outflow cavity. Option (iii) was observed for the protobinary system L1551 NE (Takakuwa et al. 2017), where velocity gradients suggest the presence of expanding gas motions in the arms. This was observed in $C^{18}O$ emission and the velocity gradient was found between blue- and red-shifted emission from transverse directions with respect to the circumbinary disk. For IRS 67, the search for a velocity gradient will be incomplete without the red-shifted counterpart, however, this possibility cannot be ruled out. Finally, option (iv) was predicted by circumstellar disk formation simulations (e.g. Harsono et al. 2015b): Shocks are generated when the infalling material from the ambient gas or envelope reaches the disk, and may induce the enhancement of some species, such as c-C_3H_2 and C_2H in the case of IRS 67. The presence of a red-shifted counterpart is expected for this scenario, however, the red-shifted emission may be obscured by the circumbinary disk material. Further modeling efforts and observations of multiple species would be required to clarify the nature of the high-density region.

$C^{17}O$ and SO_2 show compact and high-velocity emission only around source B. This emission arises from a region with a diameter of ~60 AU and could be related to a circumstellar disk or to accretion shocks. If circumstellar disks are present around the sources, they are unresolved in our data and observations with better resolution are necessary. Resolving possible circumstellar disks will be necessary to evaluate whether or not they are perpendicularly misaligned and to estimate individual masses.

4.6.2 Methanol abundances

The rest frequencies of methanol transitions $J_k = 7_k - 6_k$ are covered by one of the spectral windows (see Table 6.1) but not detected. The lack of emission indicates an absence of methanol in the gas phase, or a low abundance with respect to H_2 ($< 10^{-10} - 10^{-9}$; see Table 4.6). The stringent upper limit is similar to what was found towards R CrA IRS7B in ALMA Cycle 0 observations by Lindberg et al. (2014), where they found relatively low CH_3OH abundances ($< 10^{-10} - 10^{-8}$) compared to what is seen in the innermost $T > 90 - 100$ K regions of some Class 0 sources, where the abundances are $10^{-8} - 10^{-7}$ (Jørgensen et al. 2005a). Lindberg et al. (2014) suggest either that methanol formation is suppressed by the high temperature in the cloud, preventing significant CO to freeze-out, or the presence of an extended circumstellar disk. The extended disk would dominate the mass budget in the innermost regions ($\lesssim 100$ AU) of the protostellar envelope and generate a flattened density profile, that is, $n \propto r^{-1.5}$ for $r \gtrsim 100$ AU and $n = $ constant for $r \lesssim 100$ AU (Lindberg et al. 2014). For a flat profile, a lower column density of material with high temperatures is expected. Since CH_3OH desorbs from dust grains at a temperature of ~ 100 K, less material at high temperatures would imply a lower column density for gas-phase CH_3OH. Therefore, the flattened profile associated with the disk evolution would explain the low methanol column density seen toward circumstellar disks around Class I sources (e.g. Lindberg et al. 2014). These observations thus point to a scenario in which gas-phase methanol column densities are low in the Class I stage, as opposed to the younger Class 0 stage where methanol is often present and detected (e.g. Jørgensen et al. 2005b; Maret et al. 2005; Kristensen et al. 2010).

4.6.3 Disk mass and temperature structure

Independent from temperature, the CO abundance is found to be comparable with the canonical value of 2.7×10^{-4}. This implies that freeze-out of $C^{17}O$ onto dust grains in the disk midplane or conversion of CO into other species (e.g. Anderl et al. 2016) is not significant, assuming thin dust and $C^{17}O$ emission. Figure 4.1 shows that the continuum emission arises mainly from source B and presents a minor contribution from source A and the circumbinary disk. On the other hand, the gas emission from $C^{17}O$ (Fig. 4.2a) stands out toward source B and has an important contribution from the circumbinary disk, adding more surface area with significant contribution to the total gas mass. A similar case was seen for the proto-binary system IRS 43 (Brinch & Jørgensen 2013), where HCO^+

shows strong lines and extended emission while the continuum is relatively weak and compact. They also studied the case of IRS 63 that shows a brighter continuum and weak HCO$^+$ emission, the opposite situation to IRS 43. The disk associated to IRS 63 is more massive than that of IRS 43 (0.053 vs. 0.0081 M$_\odot$; Jørgensen et al. 2009) and could explain the difference seen in HCO$^+$. The more massive the disk, the stronger the shielding would be, and thus, the colder the midplane where molecules can effectively freeze-out. Oph-IRS67 and IRS 43 may present the same situation, where the disk mass is not enough to provide an efficient shielding and C^{17}O (for the case of Oph-IRS67) is hardly affected by freeze-out. This means that most of the C^{17}O is in the gas phase and a significant fraction of the disk has temperatures $\geq$ 30 K (temperature at which CO sublimates from dust grains). In addition to the radiation field of both sources, the presence of an envelope can be regarded as an extra heating source, where the envelope serves as a blanket and the circumbinary disk remains warm (e.g. Harsono et al. 2015a).

From C^{17}O emission and lack of methanol emission, a range of temperatures between 30 and 100 K is suggested for the circumbinary disk gas content. This is a wide range, however other molecular transitions with sublimation temperatures between 30 and 100 K are needed in order to constrain the temperature profile. In particular, the detection of formaldehyde (H$_2$CO) towards IRS 67 (Lindberg et al. 2017) agrees with this range of temperatures, since H$_2$CO can be formed in the gas-phase or via grain surface chemistry. In the gas phase, CO reacts with H$_2$ to form H$_2$CO, and temperatures above 30 K are needed in order to prevent CO freeze-out, while a temperature of ~50 K is required for H$_2$CO to sublimate from the grain mantles.

4.7 Summary

This work presents high-angular-resolution (0.″4, ~60 AU) ALMA observations of the proto-binary system Oph-IRS67AB and its associated circumbinary disk. The continuum emission is analysed, together with molecular species such as C^{17}O, C^{34}S, H^{13}CO$^+$, SO$_2$, C$_2$H, c-C$_3$H$_2$ and CH$_3$OH. The main results of this paper are provided below.

The flattened structure seen in the continuum proves the existence of a circumbinary disk around sources A and B, for which a diameter of ~620 AU is estimated, assuming an inclination of ~80°. The kinematic analysis supports a scenario where a Keplerian profile is associated with the gas motion of the circumbinary disk around a 2.2 $M_\odot$ central mass, however other velocity profiles cannot be ruled

out from this analysis.

The contrast between sources A and B at different wavelengths is more likely to be a consequence of different temperatures between both sources or the position of the two sources within the circumbinary disk.

The high-density region shows strong emission from carbon chain molecules (C_2H and $c\text{-}C_3H_2$) and may be related to the inner envelope material (i.e. outflow cavity, spiral-arm structures or infalling material from the envelope to the circumbinary disk).

The SO_2 transition is optically thick ($\tau \approx 2$), shows compact emission, and is detected only around source B. The emission arises from a region of ~60 AU in diameter, which is comparable with the beam size (~45 AU $\times$ 60 AU). The width of the line (~20 km s^{-1}) may be related with the presence of an edge-on circumstellar disk or with accretion shocks. The absence of SO_2 emission towards source A is an intriguing fact and observations with better resolution are needed.

The lack of methanol emission suggests an upper limit between 10^{-10} and 10^{-9} for the abundance of CH_3OH. This can be explained by the presence of the disk, where the bulk of the material is dominated by the flattened structure in the inner regions and less material is subjected to high temperatures (~100 K), preventing CH_3OH sublimation from dust grains.

For different temperatures, calculated CO abundances are comparable to the canonical value of 2.7×10^{-4}, suggesting a non-effective shielding of the dust and, thus, no significant freeze-out of CO in the midplane. Considering that CO sublimates from dust grains at ~30 K, and the lack of methanol detection, a temperature between 30 and 100 K characterises the bulk of the circumbinary disk.

The main conclusions of this work are the detection of the circumbinary disk and the clear difference seen by the chemistry between the high-density region and the circumbinary disk, where different physical processes are taking place in each of them. The high-angular-resolution observations make it possible to distinguish and differentiate the two regions. Future observation of other molecules and more transition from $c\text{-}C_3H_2$ will provide more information about the high-density region, while higher-angular-resolution observations are needed in order to resolve the cimcumstellar disks around each source and explain the chemical differences seen between them. Finally, Oph-IRS67AB is an ideal candidate for proper motion studies and planet formation, not only around circumstellar disks, but also around circumbinary disks.

Acknowledgements

4.8   Appendix

4.8.1   Channel maps of individual molecular transitions

For a more detailed inspection, channel maps for $C^{17}O$, $H^{13}CO^+$, $C^{34}S$, the doublet C_2H $N=4-3$, $J=9/2-7/2$ and c-C_3H_2 $5_{5,0}-4_{4,1}$ are shown in Figs. 4.12, 4.13 and 4.14. The main differences between these channel maps and Figs. 4.2 and 4.3 are, (i) the $C^{17}O$ emission appears more extended than the continuum emission around $\pm$ 2 km s^{-1}, (ii) $C^{17}O$ and $H^{13}CO^+$ have significant emission around sources A and B for low velocities (between -1 and 1 km s^{-1}) and, (iii) there is no C_2H emission at the positions of either sources.
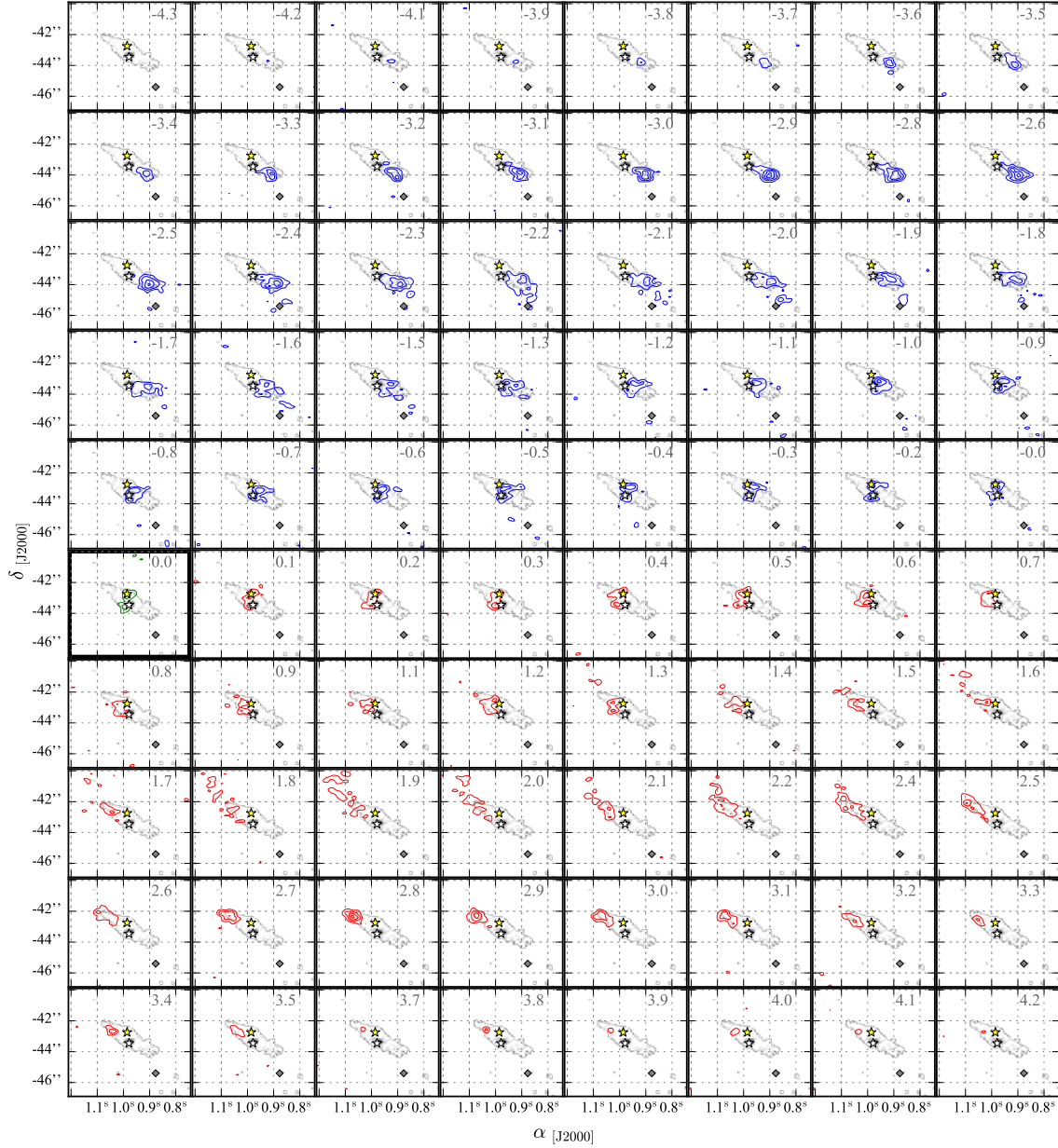
Figure 4.12: Velocity channel maps for C^{17}O J=3−2 (contours), superposed on the 0.87 mm continuum image (grey-scale; Fig. 4.1). The highlighted panel with green contours represents the systemic velocity of 4.2 km s^{-1}. Blue and red contours indicate blue- and red-shifted emission with respect to the systemic velocity, respectively. In each panel, the contours start at 4σ (σ = 10 mJy beam^{-1} per channel), following a step of 3σ, and the mean velocity of each channel is also presented in units of km s^{-1}. The yellow and white stars show the positions of Oph-IRS67A and B, respectively. The grey diamond denotes the location of the high-density region.
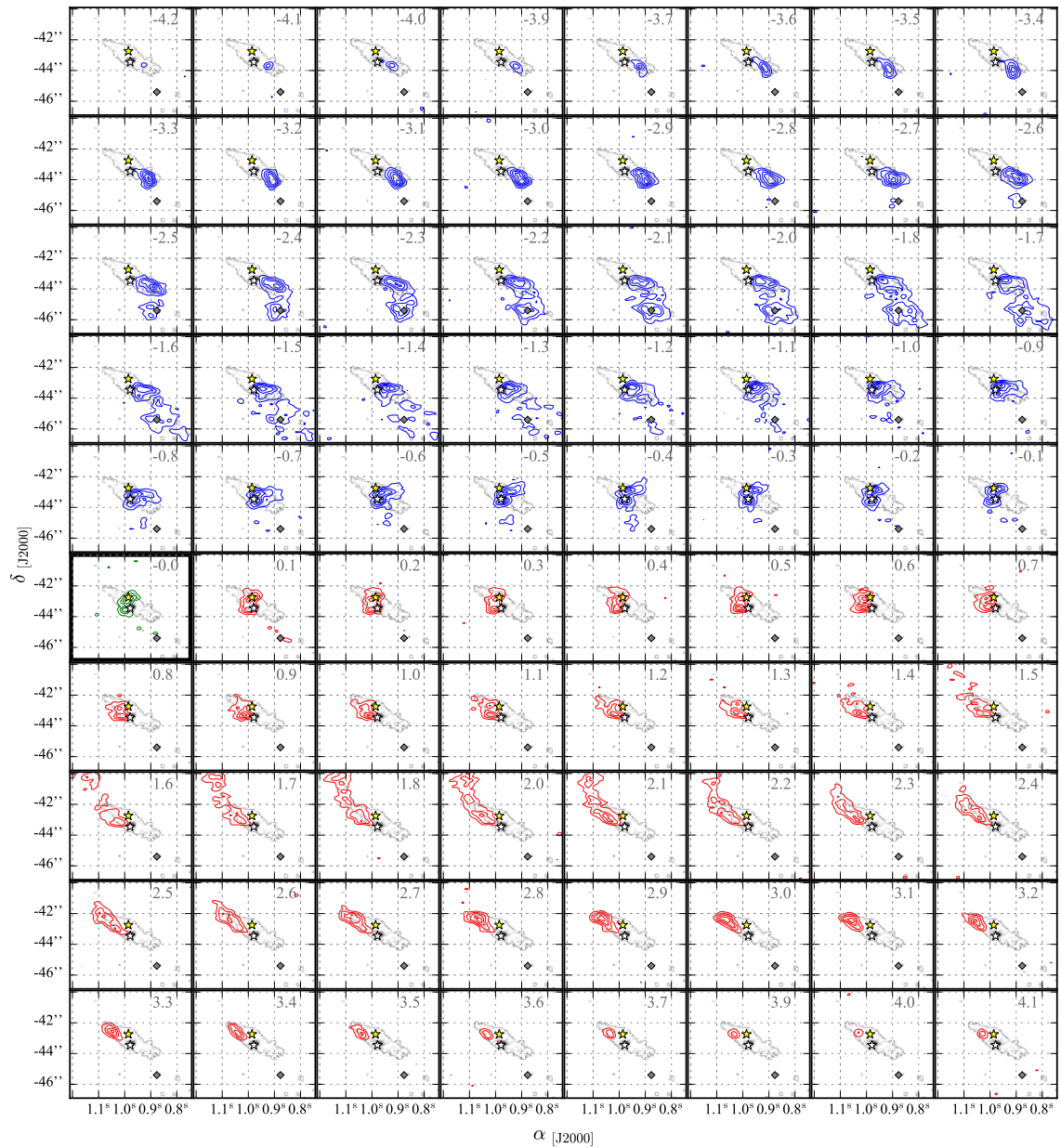
Figure 4.13: As in Fig. 4.12 but for H^{13}CO$^+$ J=4−3, where contours start at 4σ and follow a step of 4σ.
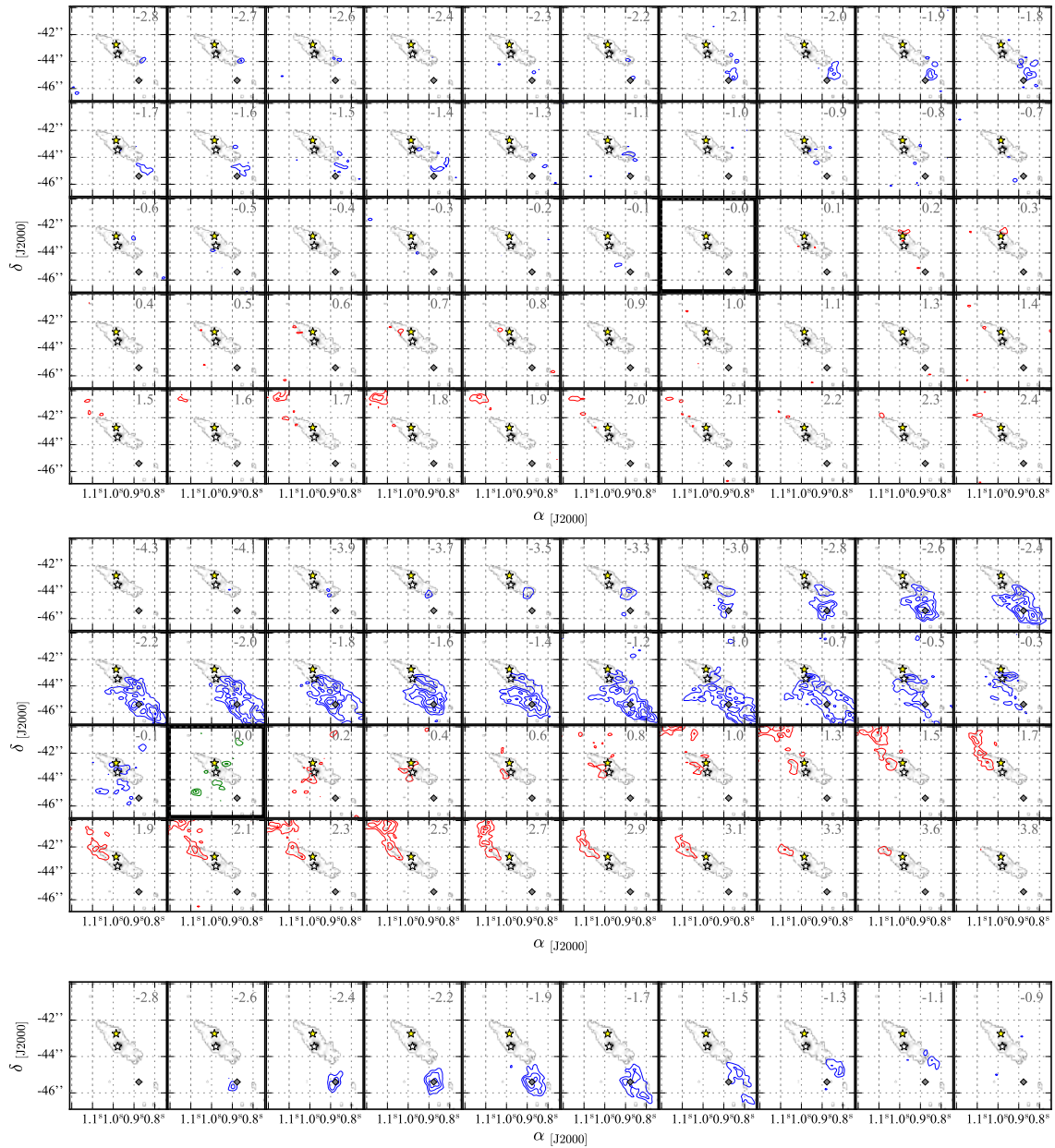
Figure 4.14: As in Fig. 4.12 but for C^{34}S J=7−6 (*upper frame*), the doublet C$_2$H N=4−3, J=9/2−7/2 (*central frame*) and c-C$_3$H$_2$ 5$_{5,0}$−4$_{4,1}$ (*lower frame*).

5 PAPER II: The physical and chemical fingerprint of protostellar disk formation

Elizabeth Artur de la Villarmois[1], Jes K. Jørgensen[1], Lars E. Kristensen[1], Edwin A. Bergin[2], Daniel Harsono[3], Nami Sakai[4], Ewine F. van Dishoeck[3,5] & Satoshi Yamamoto[6]

[1] Centre for Star and Planet Formation, Niels Bohr Institute and Natural History Museum of Denmark, University of Copenhagen, Øster Voldgade 5-7, DK-1350 Copenhagen K, Denmark

[2] Department of Astronomy, University of Michigan, 311 West Hall, 1085 S. University Ave, Ann Arbor, MI 48109, USA

[3] Leiden Observatory, Leiden University, PO Box 9513, NL-2300 RA Leiden, the Netherlands

[4] The Institute of Physical and Chemical Research (RIKEN), 2-1 Hirosawa, Wako-shi, Saitama 351-0198, Japan

[5] Max-Planck-Institut für extraterrestrische Physik, Giessenbachstraße 1, 85748, Garching bei München, Germany

[6] Department of Physics, The University of Tokyo, Bunkyo-ku, Tokyo 113-0033, Japan

5.1 Abstract

Context: The structure and composition of emerging planetary systems are likely strongly influenced by their natal environment within the protoplanetary disk at the time when the star is still gaining mass. Therefore, it is essential to identify and study the physical processes at play in the gas and dust close to young protostars and the chemical composition of the material inherited from the parental cloud.

Aims: The purpose of this paper is to explore and compare the physical and chemical structure of Class I low-mass protostellar sources on protoplanetary disk scales.

Methods: We present a study of the dust and gas emission towards a representative sample of 12 Class I protostars from the Ophiuchus molecular cloud with the Atacama Large Millimeter/submillimeter Array (ALMA). The continuum at 0.87 mm and molecular transitions from $C^{17}O$, $C^{34}S$, $H^{13}CO^+$, CH_3OH, SO_2 and C_2H were observed at high angular resolution ($0.''4$, ~60 au diameter) towards each source. The spectrally and spatially resolved maps reveal the kinematics and the spatial distribution of each species. Moreover, disk and stellar masses are estimated from the continuum flux and position-velocity diagrams, respectively.

Results: Six of the sources show disk-like structures in $C^{17}O$, $C^{34}S$ or $H^{13}CO^+$ emission. Towards the more luminous sources, compact emission and large line widths are seen for transitions of SO_2 probing warm gas ($E_u \sim 200$ K). In contrast $C^{17}O$ emission is detected towards the least evolved and less luminous systems. No emission of CH_3OH is detected towards any of the continuum peaks indicating an absence of warm CH_3OH gas towards these sources.

Conclusions: A trend of increasing stellar mass is observed as the envelope mass decreases. In addition, a power-law relation is seen between the stellar mass and the bolometric luminosity, corresponding to a mass accretion rate of $(2.4 \pm 0.6) \times 10^{-7}$ $M_\odot$ year^{-1} for the Class I sources, with a minimum and maximum value of 7.5×10^{-8} and 7.6×10^{-7} $M_\odot$ year^{-1}, respectively. This mass accretion rate is lower than the expected value if the accretion is constant in time and rather points to a scenario of accretion occurring in bursts. The differentiation between $C^{17}O$ and SO_2 suggests that they trace different physical components: $C^{17}O$ traces the densest and colder regions of the disk-envelope system, while SO_2 may be associated with elevated temperature regions, such as accretion shocks. The lack of warm CH_3OH emission suggests that there is no hot-core like region around any of the sources and the CH_3OH column density averaged over the disk is low. Finally, the combination of bolometric temperature and luminosity may indicate an evolutionary trend of chemical composition during these early stages.

5.2   Introduction

The formation and evolution of protoplanetary disks are fundamental in the process of low-mass star formation and to understand how our own Solar System formed. The chemical complexity of the protoplanetary disk is established either by the material that is inherited from the envelope or from processed material within the disk, or a combination (e.g., Pontoppidan et al. 2014; Drozdovskaya et al. 2018), providing the initial chemical conditions for planet formation. However, the physical and chemical processes at play on small scales (≤ 500 au) in low-mass protostars are still not well understood.

The dynamical evolution of the system affects the mass distribution, where material from the inner envelope falls towards the disk, the disk accretes material onto the central protostar, and part of this material is ejected through outflows (Terebey et al. 1984; Shu et al. 1993; Hartmann 1998). Class I sources are associated with the formation and evolution of circumstellar disks (e.g., Sheehan & Eisner

2017; Yoo et al. 2017) and still have an important contribution from the envelope material (Robitaille et al. 2006). Therefore, Class I sources act as a bridge between the deeply embedded Class 0 sources and the protoplanetary disks, associated with Class II sources. The evolutionary sequence, Class 0 - Class I - Class II, still has puzzling questions such as, when and how quickly the envelope dissipates? How early do disks form and how quickly do they grow in mass and size? How does material accrete from the disk onto the protostar? The presence of knots or bullets in outflows (e.g., Reipurth 1989; Arce et al. 2013) and the low luminosity of protostars compared to models (Kenyon & Hartmann 1995; Evans et al. 2009; Dunham & Vorobyov 2012) suggest that the mass accretion rates may vary with time. Direct measurement of the mass accretion rate is extremely challenging for embedded protostars, however, an approximate estimate can be obtained from the accretion luminosity equation (e.g., Kenyon & Hartmann 1995; White et al. 2007; Dunham et al. 2014a; Mottram et al. 2017). The changes in accretion, and thus in luminosity, may have important consequences in the chemistry and further evolution of the system (e.g., Jørgensen et al. 2013, 2015; Frimann et al. 2016b).

The complex environment in which protoplanetary disks form and evolve is exposed to large variations in temperature (tens to hundreds of K) and density (10^5-10^{13} cm^{-3}), leaving strong chemical signatures and making molecules excellent diagnostics of the physical conditions and processes. Observed different molecular species that trace different physics, such as disk tracers (like ^{13}CO and C^{18}O; e.g., Harsono et al. 2014), warm gas tracers (such as CH$_3$OH; e.g., Jørgensen et al. 2013), and shock tracers (like SO; e.g., Sakai et al. 2014), are essential in order to understand the different physical and chemical processes involved at disk scales. Previous studies of molecular line emission towards Class I sources were focused on characterising the gas kinematics, or the chemistry of single sources, or a few sources, (e.g., Jørgensen et al. 2009; Harsono et al. 2014), making it difficult to compare them. In addition, little is known about the evolution of the molecular content as a function of physics in these stages.

With the high sensitivity and angular resolution of the Atacama Large Millimeter/submillimeter Array (ALMA), it is becoming possible to resolve disk scales ($10-50$ au towards nearby star forming regions) and study the physics and chemistry of these environments. Disk rotation, when detectable, is a strong tool to determine protostellar masses (e.g., Jørgensen et al. 2009; Harsono et al. 2014; Yen et al. 2014, 2015). Therefore, a comparison between the chemistry and the physical parameters of protostars at disk scales and in a more statistical way is now becoming possible.

One of the closest low-mass star-forming regions is the Ophiuchus molecular cloud (Wilking

et al. 2008), with a distance (d) of 139 ± 6 pc (Mamajek 2008), associated with protostellar sources at different evolutionary stages. Therefore, this star-forming region is an excellent laboratory for the study of low-mass star formation and their disks.

In this paper, we present ALMA observations of a representative sample of 12 Class I sources in the Ophiuchus molecular cloud, where the observations include continuum emission at 0.87 mm and molecular lines that trace different components of the star-forming environment: $C^{17}O$, $C^{34}S$, $H^{13}CO^+$, CH_3OH, SO_2, and C_2H. Section 2 describes the observational procedure, data calibration, the source properties, and the covered molecular transitions. The results are presented in Sect. 3, where moment 0 and 1 maps are shown for each molecular transition. Section 4 presents an analysis of the mass evolution, with a comparison between disk masses, stellar masses, envelope masses, and bolometric luminosities, following an estimate of the mass accretion rate. Section 5 describes the chemical evolution, focusing on the lack of warm CH_3OH detection, the compact and broad SO_2 emission and the chemical trend observed within the sources. Finally, Sect. 6 summarises the main findings of the paper.

5.3 Observations

In order to address the physical and chemical properties of disks in their earliest stages, a sample of 12 Class I protostars in Ophiuchus was observed. The sources are all well-characterised through large-scale mid-infrared (*Spitzer*) and submillimetre (SCUBA) surveys (Jørgensen et al. 2008), and were selected in order to include protostars with bolometric temperatures (T_{bol}) below 400 K. In addition, the sample covers a wide range of bolometric luminosities (L_{bol}), from 0.03 to 18 $L_\odot$, and envelope masses from about 0.05 $M_\odot$ up to 0.3 $M_\odot$ (Table 5.1). With this approach, the sample is a representative set for exploring the physical and chemical structures of Class I sources.

The 12 sources were observed with ALMA on 4 occasions, between 2015 May 21 and June 5 (program code: 2013.1.00955.S; PI: Jes Jørgensen). At the time of the observations, 36 antennas were available in the array (37 for the June 5 observations) providing baselines between 21 and 556 metres (784 metres for the June 5 observations) and a maximum angular scale of ~18″. Each of the four sessions provided an on-source time of 43 minutes in total for the 12 different sources (i.e. each source was observed for approximately 15 minutes in total). The observed sources are listed in Table 5.1, with their physical properties and other common identifiers.

Table 5.1: Properties of the observed sources: infrared position, bolometric temperature (T_{bol}), bolometric luminosity (L_{bol}), envelope mass (M_{env}), and other common identifiers of the targeted Class I sources.

Source	Infrared position[a]		T_{bol}[b]	L_{bol}[b]	M_{env}[c]	Other Common Identifiers
	RA [J2000.0]	Dec [J2000.0]	[K]	[$L_\odot$]	[$M_\odot$]	
J162614.6	16 26 14.63	–24 25 07.5	7	0.03	0.095	[EDJ2009] 800
GSS30-IRS1	16 26 21.35	–24 23 04.3	250	11.00	0.15	Oph-emb 8, [GY92] 6, Elias 21
[GY92] 30	16 26 25.46	–24 23 01.3	200	0.12	0.27	Oph-emb 9
WL 12	16 26 44.19	–24 34 48.4	380	1.40	0.076	VSSG 30, [GY92] 111
IRAS 16238-2428	16 26 59.10	–24 35 03.3	120	1.70	0.045	[EDJ2009] 856
[GY92] 197	16 27 05.24	–24 36 29.6	120	0.18	0.16	Oph-emb 6, LFAM 26
Elias 29	16 27 09.40	–24 37 18.6	420	18.00	0.045	Oph-emb 16, [GY92] 214
IRS 43[d]	16 27 26.91	–24 40 50.7	300	3.30	0.13	Oph-emb 14, [GY92] 265, YLW 15
IRS 44	16 27 27.98	–24 39 33.4	280	7.10	0.057	Oph-emb 13, [GY92] 269, YLW 16
IRAS 16253-2429	16 28 21.61	–24 36 23.4	36	0.24	0.15	Oph-emb 1, MMS 126
ISO-Oph 203	16 31 52.45	–24 55 36.2	330	0.15	0.072	Oph-emb 15
IRS 67[d]	16 32 00.99	–24 56 42.6	180	2.80	0.078	Oph-emb 10, L1689S1 3

[a] Position of *Spitzer* sources from the c2d catalog (Evans et al. 2009). [b] From Dunham et al. (2015). [c] Envelope mass from models of sub-mm and IR data following description in Jørgensen et al. (2009). [d] Binary system.

Table 5.2: Spectral setup and parameters of the detected molecular transitions.

Molecular transition	Frequency [a] [GHz]	A_{ij} [a] [s^{-1}]	E_u [a] [K]	n_{crit} [b] [cm^{-3}]
C^{17}O J=3−2	337.06110	2.3×10^{-6}	32	3.5×10^4
C^{34}S J=7−6	337.39646	8.4×10^{-4}	50	1.3×10^7
SO$_2$ $J_{K_A K_C}$=18$_{4,14}$−18$_{3,15}$	338.30599	3.3×10^{-4}	197	5.9×10^7
CH$_3$OH J_K=7$_{-1}$−6$_{-1}$ E	338.34463	1.7×10^{-4}	70	2.0×10^6
CH$_3$OH J_K=7$_0$−6$_0$ A$^+$	338.40868	1.7×10^{-4}	65	2.8×10^7
H^{13}CO$^+$ J=4−3	346.99835	3.3×10^{-3}	42	8.5×10^6
C$_2$H N=4−3, J=9/2−7/2, F=5−4	349.33774	1.3×10^{-4}	42	2.2×10^7
C$_2$H N=4−3, J=9/2−7/2, F=4−3	349.39934	1.3×10^{-4}	42	2.3×10^7

[a] Values from the CDMS database (Müller et al. 2001). [b] Calculated values for a kinetic temperature of 30 K and collisional rates from the Leiden Atomic and Molecular Database (LAMDA; Schöier et al. 2005). The collisional rates of specific species were taken from the following sources: C^{17}O from Yang et al. (2010), C^{34}S from Lique et al. (2006), SO$_2$ from Balança et al. (2016), CH$_3$OH from Rabli & Flower (2010), H^{13}CO$^+$ from Flower (1999), and C$_2$H from Spielfiedel et al. (2012).

The observations covered five different lines setting and the choice of species was made specifically to trace different aspects of the structure of protostars. Lines of C^{17}O, H^{13}CO$^+$ and C^{34}S were targeted as tracers of disk kinematics, while SO$_2$ and CH$_3$OH are expected to trace the warm chemistry in the inner envelope or disk, and C$_2$H is commonly associated with outer-envelope regions. Two spectral windows consist of 960 channels each with 122.07 kHz (0.11 km s^{-1}) spectral resolution centered on C^{17}O J=3−2 and C^{34}S J=7−6, while the other three contain 1920 channels each with 244.14 kHz (0.22 km s^{-1}) spectral resolution centered on H^{13}CO$^+$ J=4−3, the CH$_3$OH J_k=7$_k$−6$_k$ branch at 338.4 GHz and the CH$_3$CN 14−13 branch at 349.1 GHz. The latter two settings also pick up SO$_2$ and C$_2$H transitions. The observed molecular transitions and their parameters are summarised in Table 6.1.

The calibration and imaging were done in CASA[1] (McMullin et al. 2007): the complex gains were calibrated through observations of the quasars J1517-2422 and J1625-2527, passband calibration on J1924-2914 and flux calibration on Titan. A robust weighting with the Briggs parameter set to 0.5 was applied to the visibilities, and the resulting dataset has a typical beam size of 0.″43 × 0.″32 (∼60 × 40 au), a continuum *rms* level of 0.3 mJy beam^{-1} and a spectral *rms* level of 13 and 9 mJy beam^{-1} per 0.11 and 0.22 km s^{-1}, respectively.

---

[1]`http://casa.nrao.edu/`

Table 5.3: Results of 2D Gaussian fits towards the continuum peak of our Oph surces.

Source	RA [J2000.0]	Dec [J2000.0]	Size[a] ["]	PA [°]	$F_{0.87mm}$ [mJy]	$S_{0.87mm}$ (0."4)[b] [mJy beam^{-1}]
GSS30-IRS1	16 26 21.358	-24 23 04.85	0.19 ± 0.02 × 0.12 ± 0.01	96 ± 9	35.3 ± 0.7	30.0 ± 0.3
[GY92] 30	16 26 25.475	-24 23 01.81	0.25 ± 0.01 × 0.12 ± 0.01	28 ± 1	105.0 ± 0.5	80.2 ± 0.2
WL 12	16 26 44.203	-24 34 48.86	0.14 ± 0.01 × 0.11 ± 0.01	60 ± 11	160.4 ± 1.0	142.4 ± 0.5
LFAM 23[c]	16 26 59.166	-24 34 59.07	0.09 ± 0.02 × 0.05 ± 0.04	38 ± 45	17.6 ± 0.3	16.9 ± 0.2
[GY92] 197	16 27 05.252	-24 36 30.14	0.44 ± 0.01 × 0.13 ± 0.01	169 ± 1	128.3 ± 0.6	71.1 ± 0.2
Elias 29	16 27 09.416	-24 37 19.20	0.17 ± 0.02 × 0.16 ± 0.02	61 ± 90	41.2 ± 0.6	34.1 ± 0.3
IRS 43 VLA 1	16 27 26.908	-24 40 50.67	0.21 ± 0.03 × 0.13 ± 0.02	96 ± 17	41.6 ± 1.9	32.1 ± 0.9
IRS 43 VLA 2	16 27 26.917	-24 40 51.18	0.36 ± 0.09 × 0.2 ± 0.1	150 ± 37	7.5 ± 1.0	3.7 ± 0.4
IRS 44	16 27 27.988	-24 39 33.93	0.24 ± 0.03 × 0.18 ± 0.03	124 ± 19	38.6 ± 1.2	29.1 ± 0.6
IRAS 16253-2429	16 28 21.620	-24 36 24.17	0.23 ± 0.02 × 0.13 ± 0.02	111 ± 6	39.8 ± 0.7	31.9 ± 0.4
ISO-Oph 203	16 31 52.445	-24 55 36.48	0.14 ± 0.03 × 0.05 ± 0.03	107 ± 18	11.3 ± 0.3	10.6 ± 0.2
IRS 67 A	16 32 00.989	-24 56 42.78	0.5 ± 0.1 × 0.3 ± 0.2	46 ± 17	35.7 ± 7.0	16.2 ± 2.3
IRS 67 B	16 32 00.978	-24 56 43.44	0.22 ± 0.02 × 0.14 ± 0.01	88 ± 9	155.5 ± 4.0	125.1 ± 2.0

[a] Deconvolved size (FWHM). [b] Brightness at the continuum peak. [c] Class II T Tauri source located in the same field as IRAS 16238-2428.
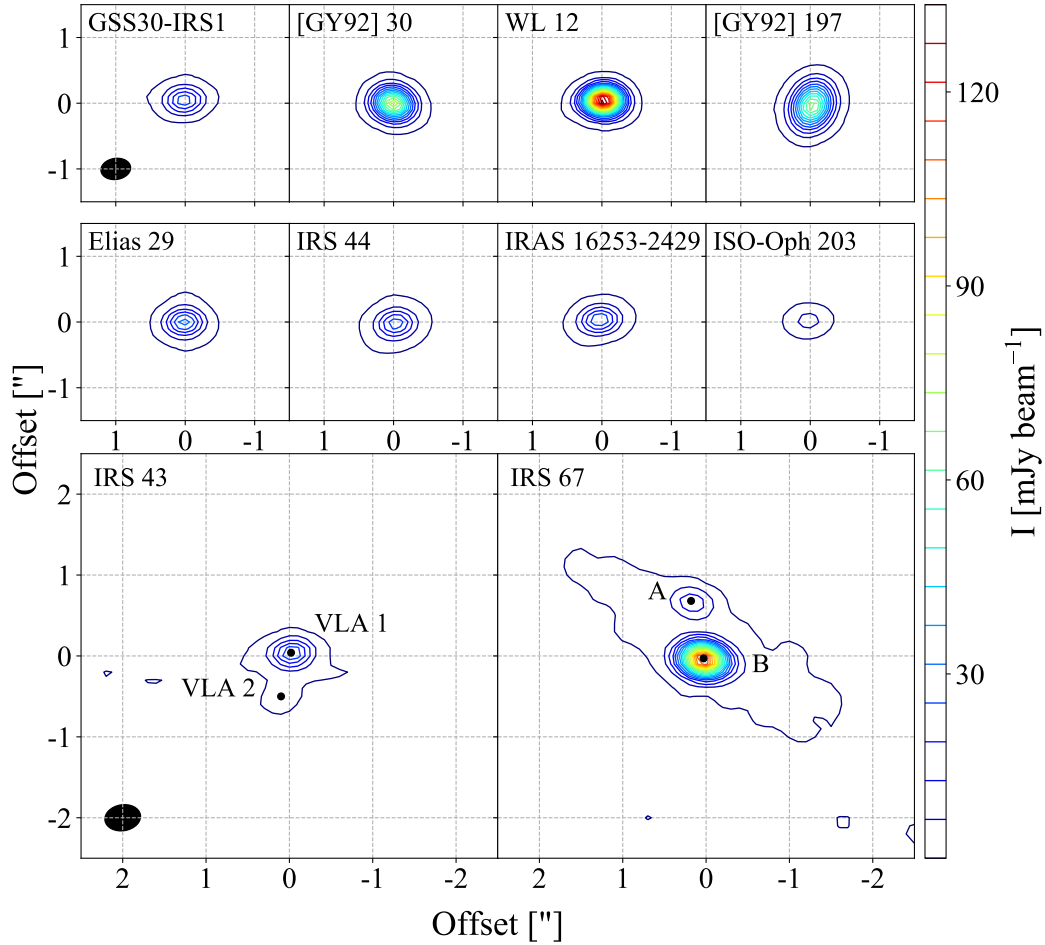
Figure 5.1: Continuum emission of the detected sources above 5σ (σ = 0.3 mJy beam^{-1}). The contours start at 5σ and follow a step of 20σ. The typical synthesised beam is represented by the black filled ellipse in the upper- and lower-left panels. The (0,0) position represents the position fitted with a 2D Gaussian (see Table 5.3). The lower panels show the binary systems with the common identifiers of both components.

5.4 Results

5.4.1 Continuum

The sources that show continuum emission at 0.87 mm are listed in Table 5.3, with the sub-mm coordinates, deconvolved sizes, and fluxes calculated by fitting two-dimensional (2D) Gaussians in the image plane. Two of the sources, IRS 43 (Girart et al. 2000) and IRS 67 (McClure et al. 2010), are known binary systems and their components are separated by ~70 au (0.″53) and ~90 au (0.″68) for IRS 43 and IRS 67, respectively. The sources associated with a single continuum peak have diameters from ~20 au (0.″14 for ISO-Oph 203) to ~60 au (0.″44 for [GY92] 197) and fluxes from 11.3 mJy (ISO-Oph 203) to 160.4 mJy (WL 12). The deconvolved sizes show that most of the sources are marginally resolved, with the exception of LFAM 23, IRS 43 VLA 2, and IRS 67 A, which are

unresolved.

J162614.6 and IRAS 16238-2428 show neither continuum nor molecular line emission; the upper limit is 0.9 mJy beam^{-1} (3σ) for the continuum emission. J162614.6 shows faint emission at 24 μm and a low concentrated SCUBA[2] core (Jørgensen et al. 2008), suggesting that this source is more likely related with a prestellar core than with a protostar. For IRAS 16238-2428, the separation between its *Spitzer* position and SCUBA core is 38.″6 (Jørgensen et al. 2008), where the last one lies beyond the ALMA primary beam ($\sim$18″). However, the continuum emission detected in the same field of view as IRAS 16238-2428 may correspond to a T Tauri source (LFAM 23) located $\sim$4″ offset from the *Spitzer* position associated with IRAS 16238-2428. Table 5.3 presents results from a 2D Gaussians fit for LFAM 23, revealing that it is a point source. However, this source does not show molecular line emission and is therefore not included in the discussion in this paper.

Figure 5.1 shows the continuum emission of the remaining 10 sources. For the binary systems, the continuum also traces the circumbinary material, which is remarkably extended for IRS 67 ($\sim$550 au; for a detailed analysis of IRS 67, see Artur de la Villarmois et al. 2018). It is worth mentioning that IRS 43 VLA 1 and IRS 67 B are brighter than IRS 43 VLA 2 and IRS 67 A at 0.87 mm, while the opposite situation is observed at infrared wavelengths (Haisch et al. 2002; McClure et al. 2010).

5.4.2 Molecular lines

The molecular transitions trace different components and are related with different morphologies. Some of them are detected towards the source position, while others peak offset from the source, and the emission may present compact or extended structures. Table 5.4 summarises the regions where the individual molecular transitions are detected, specifying if the emission is compact or extended (with respect to the extent of the continuum emission), and the source velocity (V_{source}). The latter is estimated by visual inspection of $C^{17}O$ emission, or SO_2 emission when $C^{17}O$ is not detected. For sources where no molecular line emission is detected, V_{source} is taken from the literature (see Table 5.4). Both C_2H lines listed in Table 6.1 are hyperfine transitions, and the C_2H emission arises from a blended doublet, C_2H N=4−3, J=9/2−7/2, F=5−4 plus C_2H N=4−3, J=9/2−7/2, F=4−3. Emission of at least one molecular transition is detected towards 8 of the 10 sources. WL 12 (the brightest continuum source) and ISO-Oph 203 (the weakest continuum source), are the only sources where no line emission is detected within the spectral setting shown in Table 6.1.

---

[2]The Submillimeter Common-User Bolometer Array (SCUBA) on the James Clerk Maxwell Telescope (JCMT)
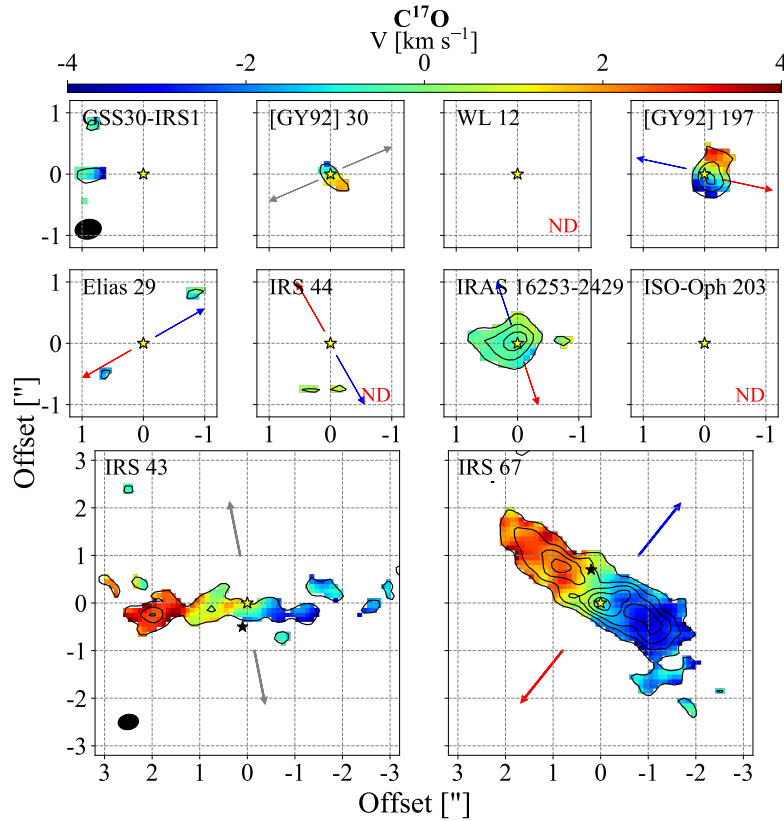
Figure 5.2: Moment 0 (black contours) and moment 1 (colour scale) maps for $C^{17}O$ J=3-2 above 5σ and integrated over a velocity range of 8 km s^{-1}. The contours start at 5σ and follow a step of 4σ (σ = 4 mJy beam^{-1} km s^{-1}). The yellow star indicates the position from a 2D Gaussian fit and the black stars in the lower panels represent the position of the binary components. The arrows show the outflow direction from the literature, where the blue and red represent blue- and red-shifted emission, respectively, and the grey represents infrared observations. The typical synthesized beam is shown by the black filled ellipse in the upper- and lower-left panels. The ND label marks a Non-Detection.

5.4.2.1 Optically thin tracers: $C^{17}O$, $H^{13}CO^+$ and $C^{34}S$

$C^{17}O$, $H^{13}CO^+$ and $C^{34}S$ are less abundant isotopologues and they are expected to be optically thin tracers associated with the disk kinematics. For example, a Keplerian disk was detected towards the Class 0/I source R CrA in similar $C^{17}O$ observations with ALMA (Lindberg et al. 2014).

Figure 5.2 shows moment 0 and 1 maps for $C^{17}O$, indicating the outflow direction, if available, from the literature (Bontemps et al. 1996; Allen et al. 2002; van der Marel et al. 2013; Zhang et al. 2013; White et al. 2015; Yen et al. 2017). Five of the sources, [GY92] 30, [GY92] 197, IRAS 16253-2429, IRS 43, and IRS 67, show on-source $C^{17}O$ emission and, with the exception of IRAS 16253-2429, are associated with a rotational profile perpendicular to the outflow direction, consistent with a disk-like structure (Sect. 4.2). In addition, the binary systems (IRS 43 and IRS 67) show $C^{17}O$ emission much more extended than towards the other sources: 6.″1 diameter for IRS 43, 5.″4 for
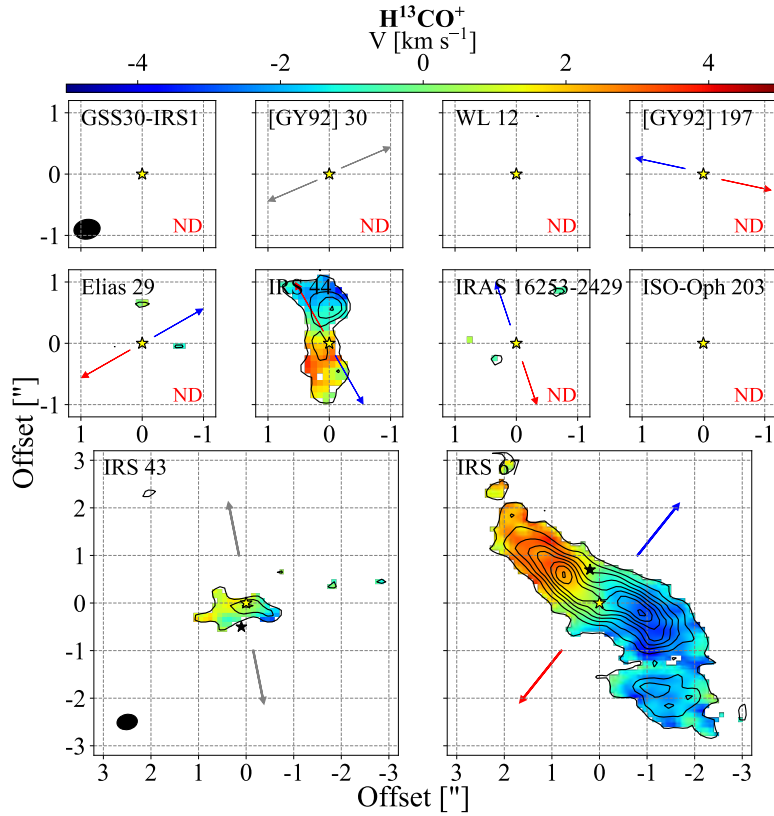
Figure 5.3: Same as Fig. 5.2 for H^{13}CO$^+$ $J=4-3$, integrated over a velocity range of 10 km s^{-1}. The contours start at 5σ and follow a step of 3σ with the exception of IRS 67, that follows a step of 6σ.

IRS 67, 1."3 for IRAS 16253-2429, 0."9 for [GY92] 197, and 0."7 for [GY92] 30. The emission towards IRAS 16253-2429 is slightly elongated in the direction perpendicular to the outflow axis and associated with low velocities ($< \pm 2$ km s^{-1}). This low velocity component may be tracing infalling material from the inner envelope (see detailed discussion in Sect. 4.2).

Figures 5.3 and 5.4 show images of the H^{13}CO$^+$ and C^{34}S emission. H^{13}CO$^+$ is detected towards only 3 of the 10 sources: IRS 44 and both binary systems, IRS 43 and IRS 67. IRS 44 shows a velocity gradient with two components, one consistent with the outflow direction, and another one rotated by ~45°. The peak of emission (moment 0), however, is related with more quiescent material. For the binary systems, the more massive one (IRS 67) shows more extended emission with a velocity profile perpendicular to the outflow direction, while the emission towards IRS 43 is concentrated in the inner regions ($\leq 1''$) and a tentative velocity gradient is detected. In addition, C^{34}S is solely seen towards the binary systems. IRS 43 shows a velocity gradient perpendicular to the infrared jet direction and the emission peaks spatially offset from the system ($\sim 2''$), where the red-shifted emission stands out. A different situation is observed for IRS 67, with no clear velocity gradient and isolated peaks of
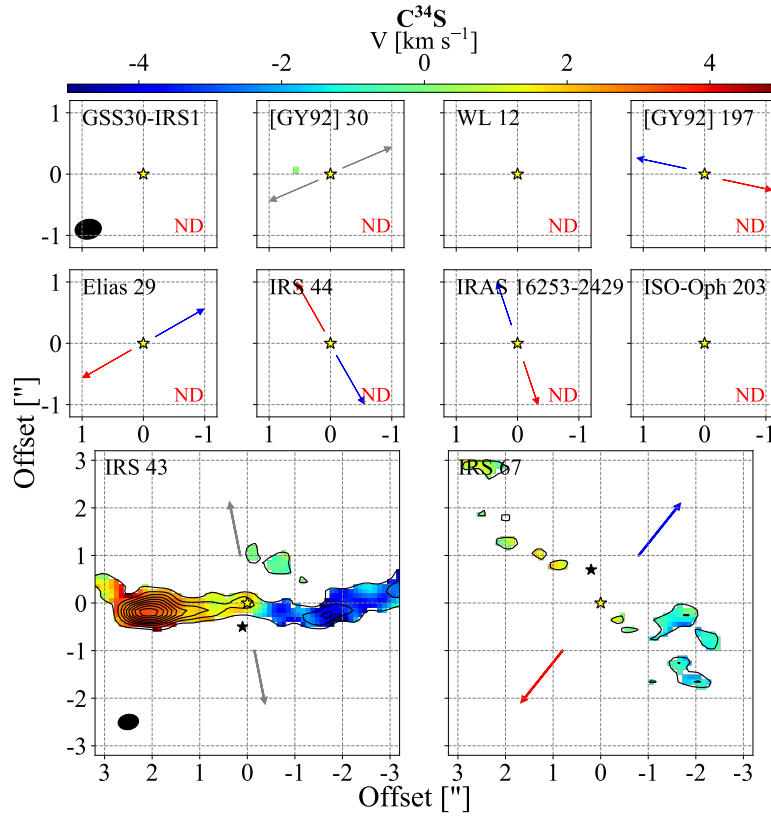
Figure 5.4: Same as Fig. 5.2 for C^{34}S J=7−6, integrated over a velocity range of 10 km s^{-1}. The contours start at 5σ and follow a step of 3σ with the exception of IRS 43, that follows a step of 6σ.

emission spatially offset from the system.

5.4.2.2 Warm chemistry tracers: CH$_3$OH and SO$_2$

CH$_3$OH forms exclusively on ice-covered dust grain surfaces, since gas-phase reactions produce negligible CH$_3$OH abundances (Garrod et al. 2006; Chuang et al. 2016; Walsh et al. 2016). When the temperature reaches ~90 K, CH$_3$OH thermally desorbs from the grain mantles and its gas-phase abundance is enhanced close to the protostar (Brown & Bolina 2007). Therefore, CH$_3$OH transitions associated with high rotational levels, such as J=7$_k$−6$_k$, are expected to trace the warm gas close to the protostar.

The observed CH$_3$OH J=7$_k$−6$_k$ branch includes transitions with E_u from 65 to 376 K, however, no significant emission is detected towards the continuum position from a 2D Gaussian fit of any source (see Table 5.3). This is highlighted in Fig. 5.5, where the observed and predicted spectrum are plotted together. The predicted spectrum is obtained by using the statistical equilibrium radiative transfer code (RADEX; van der Tak et al. 2007) and assuming local thermodynamic equilibrium

Table 5.4: Regions where the individual molecular transitions are detected above 3σ towards each source and the estimated source velocity (V_{source}).

Source	Molecular transitions						V_{source} [a] [km s^{-1}]
	C^{17}O	H^{13}CO$^+$	C^{34}S	SO$_2$	CH$_3$OH	C$_2$H	
GSS30-IRS1	Offset	-	-	On source [C]	-	-	3.4
[GY92] 30	On source [C]	-	-	-	Offset	Offset	3.1
WL 12	-	-	-	-	-	-	4.0 [b]
[GY92] 197	On source	-	-	-	-	On source [C]	3.1
Elias 29	Offset	-	-	On source [C]	-	-	3.6
IRS 43	On source [E]	On source	On source [E]	On source B [C]	-	Offset	4.0
IRS 44	-	On source [E]	-	On source [C]	-	-	2.3
IRAS 16253-2429	On source [E]	-	-	-	-	On source [E]	4.0
ISO-Oph 203	-	-	-	-	-	-	4.5 [b]
IRS 67	On source [E]	On source [E]	Offset	On source B [C]	-	On source [E]	4.2

[a] Estimated from visual inspection of the C^{17}O spectrum, or SO$_2$ when C^{17}O is not detected. [b] Values taken from Lindberg et al. (2017). The [C] and [E] labels refer to compact or extended emission (with respect to the extension of the continuum emission).
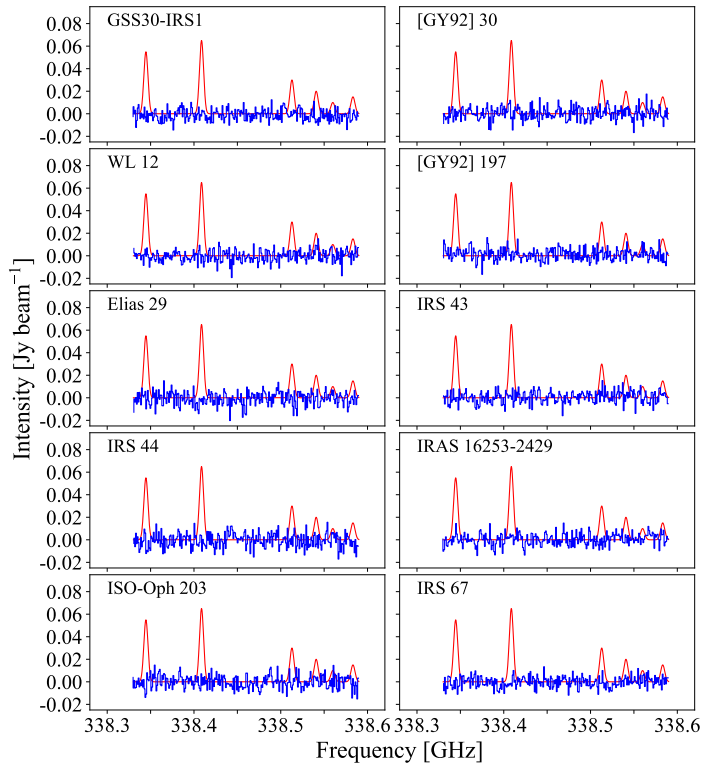
Figure 5.5: Observed CH_3OH spectra *(blue)* towards the 10 sources that show continuum emission, superimposed with the predicted CH_3OH spectrum *(red)* for a column density of 2.5×10^{15} cm^{-2}, ~4 orders of magnitude below the value from the Class 0 source IRAS 16293-2422 (Jørgensen et al. 2016).

(LTE), a CH_3OH column density of 2.5×10^{15} cm^{-2} (~4 orders of magnitude below the CH_3OH column density measured towards the Class 0 source IRAS 16293-2422; Jørgensen et al. 2016), and a kinetic temperature (T_{kin}) of 100 K. Clearly, no CH_3OH lines are seen even at this level.

Nevertheless, a peculiar case is seen for [GY92] 30 (the least luminous source of the sample, $L_{bol} = 0.12\ L_\odot$, and the one associated with the more massive envelope, $M_{env} = 0.27\ M_\odot$), where two CH_3OH transitions are detected offset from the source, beyond the 25σ continuum contour (Figs. 5.14 and 5.15 in the Appendix). These transitions are associated with the lowest E_u levels (65 and 70 K) and the emission is related with low velocities, between -0.5 and 0.5 km s^{-1} from the source velocity. Thus, the CH_3OH emission towards [GY92] 30 is likely related with extended envelope material. In addition, there is no clear association between the CH_3OH emission and the direction of the infrared jet.

SO_2 is commonly associated with outflows and shocked regions (e.g., Jørgensen et al. 2004; Persson et al. 2012; Podio et al. 2015; Tabone et al. 2017). In addition, the highly excited rotational transitions (E_u ~200 K) may be tracing warm shocked gas. The observed SO_2 transition, listed in
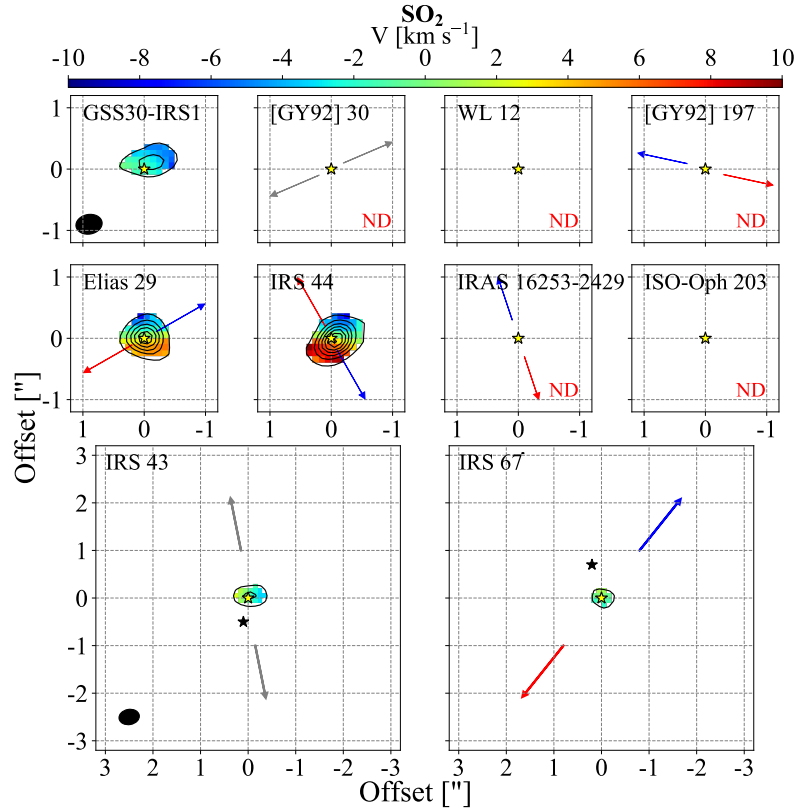
Figure 5.6: Same as Fig. 5.2 for SO$_2$ $J_{K_A K_C}=18_{4,14}-18_{3,15}$, integrated over a velocity range of 20 km s^{-1}. The contours start at 5σ and follow a step of 20σ.

Table 6.1, is associated with a high rotational level (E_u = 197 K) and is detected towards five of the sources, showing compact emission (Fig. 5.6). A rotational profile is seen for Elias 29 and IRS 44, associated with high velocities (up to ±10 km s^{-1} with respect to the source velocity), and almost perpendicular to the outflow direction. Towards the binary systems, the SO$_2$ emission is relatively weak and detected around one of the sources, IRS 43 VLA1 and IRS 67 B, that correspond to the brightest components at 0.87 mm. In addition, GSS30-IRS1 shows only a blue-shifted component, without a clear velocity profile. The SO$_2$ emission towards Elias 29 and IRS 44 may be consistent with a disk-like structure, however, the broad line profile suggests that SO$_2$ is tracing a different component associated with warm-shocked gas.

5.4.2.3   Outer envelope tracer: C$_2$H

The emission of C$_2$H has been associated with dense regions exposed to UV radiation (e.g., Nagy et al. 2015; Murillo et al. 2018). Its emission is shown in Fig. 5.7 and is detected towards five of the sources. Two of the them, [GY92] 197 and IRAS 16253-2429, show on-source emission related
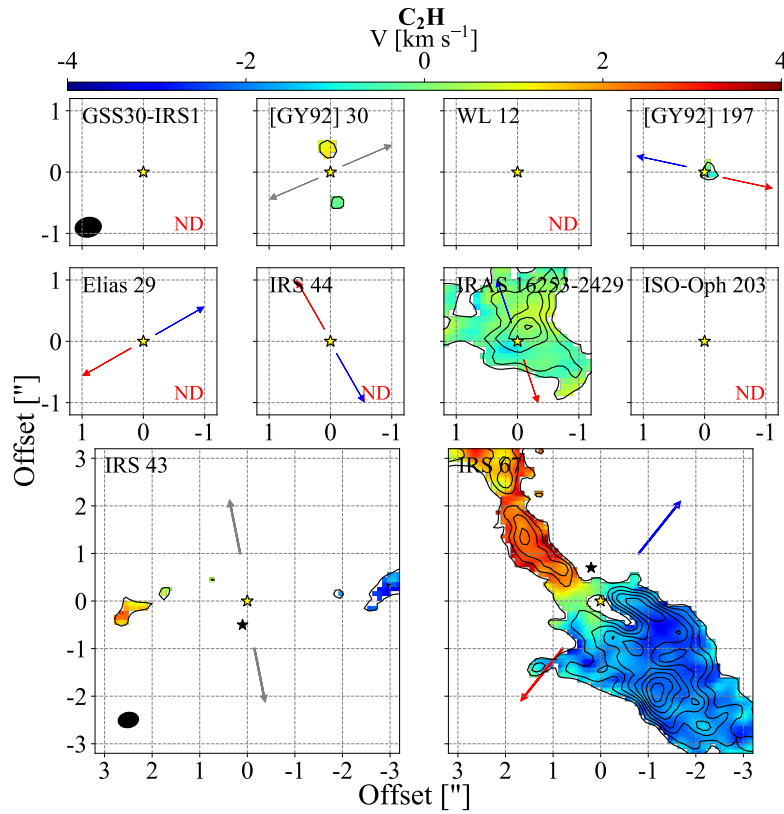
Figure 5.7: Same as Fig. 5.2 for the doublet C_2H $N=4-3$, $J=9/2-7/2$.

with low velocities, showing a compact morphology for [GY92] 197 and an extended structure for IRAS 16253-2429. Towards [GY92] 30, IRS 43, and IRS 67 there is no C_2H emission (above 5σ) at the positions of the sources, however, a velocity gradient is seen for the circumbinary material, with a remarkable extended emission for IRS 67 ($\sim 9''$). Since IRAS 16253-2429 has one of the most massive envelopes ($M_{env} = 0.15$ $M_\odot$) and circumbinary disks are usually related with a higher mass content and extension than circumstellar disks, C_2H is likely tracing more dense regions.

5.5   Mass evolution

The final mass of a protostar and the amount of material available in the disk to form planets depend on the mass evolution of the whole system (envelope, disk, protostar and outflow). Determining when and how quickly the envelope dissipates and the disk grows in mass and size, the rate at which the protostar gains mass, and the amount of material expelled through the outflows, are all linked to each other and are crucial components in the mass evolution. In this section, we estimate the disk masses from the continuum emission (Sect. 4.1) and the stellar masses from molecular lines that show

Keplerian profiles (Sect. 4.2). Later on, a comparison between envelope mass, disk mass, stellar mass, and bolometric luminosity is presented (Sect. 4.3). Finally, the mass accretion rate is estimated from a relationship between the stellar mass and the bolometric luminosity, and this is compared with the bolometric temperature.

5.5.1 Disk mass

The disk masses (M_{disk}) are calculated from the continuum fluxes ($F_{0.87\mathrm{mm}}$), listed in Table 5.3, and

$$M_{\mathrm{disk}} = \frac{S_\nu d^2}{\kappa_\nu B_\nu(T)} \ , \tag{5.1}$$

where S_ν is the surface brightness, d is the distance to the source, κ_ν is the dust opacity, and $B_\nu(T)$ is the Planck function for a single temperature. A distance of 139 ± 6 pc (Mamajek 2008) and $\kappa_{0.87\mathrm{mm}}$ of 0.0175 cm^2 g^{-1} (Ossenkopf & Henning 1994), commonly used for dust in protostellar envelopes and young disks in the millimetre regime (e.g., Shirley et al. 2011), are adopted for the calculations (Artur de la Villarmois et al. 2018). A value of 15 K is adopted for the dust temperature (T_{dust}) following the analysis by Dunham et al. (2014b). The calculated disk masses (gas + dust, assuming a gas-to-dust ratio of 100) are listed in Table 5.5, together with values from the literature. Errors in T_{dust} are not considered in Table 5.5, however, the disk masses will decrease by a factor of ∼3 if a dust temperature of 30 K is assumed instead (found to be appropriate for Class 0 sources in the study by Dunham et al. 2014b). For WL 12, Elias 29 and IRS 43, disk masses are available from other studies (see Table 5.5). For Elias 29 and IRS 43 the values from this work are comparable with the literature, and the difference seen for WL 12 appears to be due to the choice of dust temperature (15 vs. 30 K). Assuming T_{dust} = 30 K, a value of (10.3 ± 2.4) × 10^{-3} M$_\odot$ is found for M_{disk} associated with WL 12.

5.5.2 Stellar mass

In order to investigate if the optically thin tracers are associated with Keplerian motions and to estimate the stellar masses ($M_\star$), Position-Velocity (PV) diagrams were created for those sources that show disk-like structures in C^{17}O, H^{13}CO$^+$ or C^{34}S. The peak emission for each channel is obtained through the CASA task `imfit` and the offset position is calculated by projecting the peak emission onto the disk position angle (Table 5.3). Next, a Keplerian profile ($v \propto r^{-0.5}$) is employed to fit the points with velocities above ±2 km s^{-1}. This velocity range was chosen in order to avoid the envelope

Table 5.5: Calculated disk masses for $T_{\text{dust}} = 15$ K and values from the literature.

Source	M_{disk} [10^{-3} M$_\odot$]	
	This work	Literature
GSS30-IRS1	6.2 ± 0.6	
[GY92] 30	18.5 ± 1.6	
WL 12	28.3 ± 2.4	11 [a]
LFAM 23	3.1 ± 0.3	
[GY92] 197	22.6 ± 2.0	
Elias 29	7.3 ± 0.6	11 [a]
		< 7 [b]
IRS 43 VLA 1	7.3 ± 0.7	8 [a]
IRS 43 VLA 2	1.3 ± 0.2	
IRS 44	6.8 ± 0.6	
IRAS 16253-2429	7.0 ± 0.6	
ISO-Oph 203	2.0 ± 0.2	
IRS 67 A	6.3 ± 1.3	
IRS 67 B	27.4 ± 2.5	

The errors in the second column do not include uncertainties in the assumed dust temperature ($T_{\text{dust}} = 15$ K), however, the disk masses will decrease by a factor of ~3 if a dust temperature of 30 K is assumed. [a] From Jørgensen et al. (2009) at 1.1 mm, with $T_{\text{dust}} = 30$ K. [b] From Lommen et al. (2008) at 1.1 mm, with $T_{\text{dust}} = 30$ K.

contribution (e.g., van 't Hoff et al. 2018). The PV diagrams and peak points are shown in Figs. 5.8 and 5.9, overlapped with the resulting Keplerian curve from the fit. Figure 5.8a shows a robust Keplerian profile for [GY92] 197, while the PV diagram for IRS 44 is noisy (Fig. 5.8b), with an unclear Keplerian profile. IRAS 16253-2429 shows low-velocity emission (≤ 2 km s^{-1}) and both negative and positive velocities for the same distance to the source (see Fig. 5.8c), a characteristic feature of infalling material (e.g., Tobin et al. 2012). Therefore, these points are fitted with an infalling profile under the conservation of angular momentum ($v \propto r^{-1}$; e.g., Lin et al. 1994; Harsono et al. 2014). The resulting stellar masses are listed in Table 5.6, adopting an inclination (i) of 70° from the plane of the sky. This value is adopted from the mean value of the inclination of the sample, calculated from the deconvolved continuum sizes (Table 5.3) and assuming a circular structure. In addition, 70° is consistent with values from the literature: 70° for IRS 43 (Brinch et al. 2016) and 60° for IRAS 16253-2429 (Yen et al. 2017). The stellar mass will change less than 14% if the inclination varies with ±10°.

IRS 43 shows extended emission in C^{17}O and C^{34}S, with PV diagrams and Keplerian fits shown in Fig. 5.9 for both molecular transitions. The blue-shifted C^{34}S emission is well fitted with a Keplerian profile, however, the red-shifted emission shows an enhancement around 2″ and a vertical velocity structure, from ~2 to ~4 km s^{-1}. PV diagrams for IRS 67 from C^{17}O and H^{13}CO$^+$ emission are
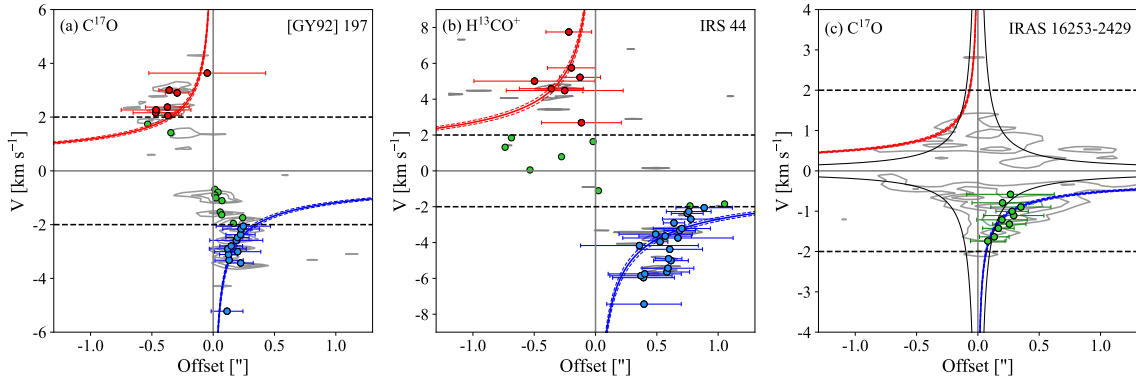
Figure 5.8: Position-velocity diagrams towards [GY92] 197, IRS 44 and IRAS 16253-2429. Blue and red dots represent blue- and red-shifted emission peaks above ± 2 km s^{-1}, respectively, while green dots indicate velocities below ± 2 km s^{-1}. Blue and red solid lines show the best fit for a Keplerian velocity profile with their respective errors, shown in dashed blue and red lines. The cut taken from the image data is shown in grey contours, ranging from 3σ ($\sigma = 13$ mJy beam^{-1}) to the maximum value of each transition. Each adjacent contour represents an increment of 30% of the maximum value for panels *(a)* and *(c)*, and an increment of 50% for panel *(b)*. The black dashed lines indicate the velocity above which the Keplerian profile was fitted. The solid black curves in panel *(c)* show the best fit for an infalling velocity profile.

Table 5.6: Protostellar masses obtained from the velocity profile fits and values from the literature.

Source	This work		Literature	
	$M_\star$ [M$_\odot$] [a]	Molecule	$M_\star$ [M$_\odot$]	Method
[GY92] 197	0.23 ± 0.02	C^{17}O		
Elias 29			2.5 ± 0.6 [b]	HCO$^+$ $J=3-2$ emission
IRS 43	4.0 ± 0.3	C^{34}S	1.80 ± 0.42 [c]	HCN $J=3-2$ emission
	3.9 ± 0.7	C^{17}O		
IRS 44	1.2 ± 0.1	H^{13}CO$^+$		
IRAS 16253-2429	0.03 ± 0.02	C^{17}O (Infalling)	0.03 ± 0.01 [d]	C^{18}O $J=2-1$ emission
IRS 67 [e]	2.2 ± 0.2	C^{17}O		

[a] The stellar masses were calculated assuming an inclination of 70°. [b] From Lommen et al. (2008). [c] From Brinch et al. (2016), for the binary system. [d] From Yen et al. (2017). [e] A more detailed analysis of IRS 67 is presented in Artur de la Villarmois et al. (2018).

presented in Artur de la Villarmois et al. (2018).

Table 5.6 lists the stellar masses obtained from PV diagrams and values from the literature. For IRS 43, the stellar masses inferred from a Keplerian fit from C^{17}O and C^{34}S emission are a factor of 2 higher than the 1.80 M$_\odot$ from Brinch et al. (2016). To be consistent within the sample, the stellar mass of 4.0 M$_\odot$ is used for the IRS 43 system hereinafter. For IRAS 16253-2429, the stellar mass from Yen et al. (2017) is consistent with our value from the fit for the infalling gas.

5.5.3 Mass evolution

Figure 5.10 compares the envelope masses ($M_{\rm env}$; Table 5.1), disk masses ($M_{\rm disk}$; Table 5.5), and stellar masses ($M_\star$; Table 5.6). The uncertainties in $M_{\rm env}$ are assumed to be 20%. There is no clear
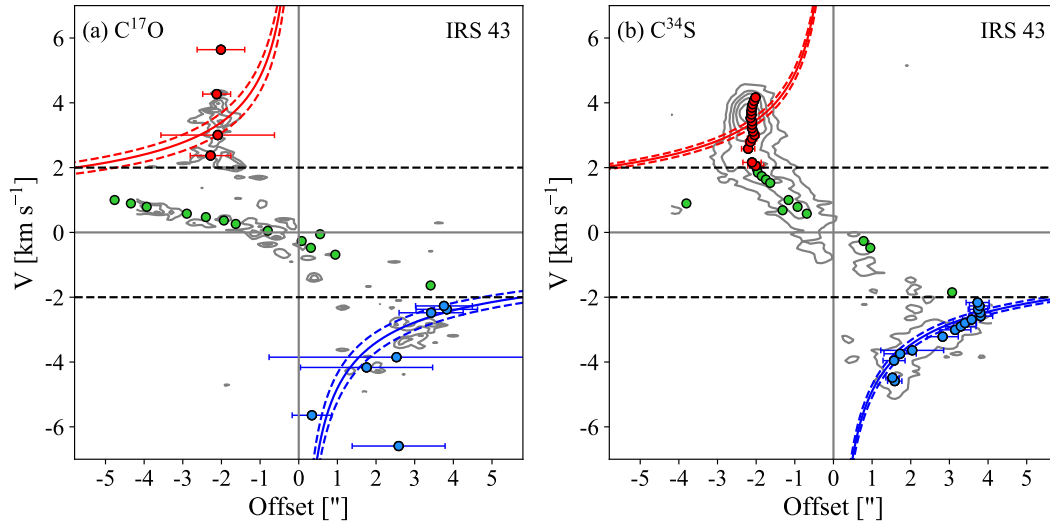
Figure 5.9: Position-velocity diagrams for $C^{17}O$ and $C^{34}S$ towards IRS 43. Blue and red dots represent blue- and red-shifted emission peaks above ± 2 km s^{-1}, respectively, while green dots indicate velocities below ± 2 km s^{-1}. Blue and red solid lines show the best fit for a Keplerian velocity profile with their respective errors, shown in dashed blue and red lines. The cut taken from the image data is shown in grey contours, ranging from 3σ ($\sigma = 13$ mJy beam^{-1}) to the maximum value of each transition. Each adjacent contour represents an increment of 30 and 20% of the maximum value for $C^{17}O$ and $C^{34}S$, respectively. The black dashed lines indicate the velocity above which the Keplerian profile was fitted.

trend between M_{disk} and $M_\star$ or M_{env}, however, all the points satisfy the condition $M_\star > M_{\text{disk}}$ and $M_{\text{env}} > M_{\text{disk}}$, characteristic of Class I stages (Robitaille et al. 2006). For $M_\star$ as a function of M_{env}, there is an increase of the stellar mass as the mass of the envelope decreases, and only one of the sources (IRAS 16253-2429) satisfies the condition $M_{\text{env}} > M_\star$, a characteristic of Class 0 protostars, which is also consistent with its low bolometric temperature, T_{bol} of 36 K, and the infalling profile for the gas kinematics.

The left panel of Fig. 5.11 shows the bolometric luminosities as a function of stellar masses from Table 5.6 and values of Class 0 and I sources summarised in Aso et al. (2015) (see Table 5.8 in the Appendix). The uncertainties in $M_\star$ and L_{bol} are 20% and 15%, respectively (e.g., Yen et al. 2017) and, for the particular case of the binary systems (IRS 43 and IRS 67), their $M_\star$ and L_{bol} values were divided by 2 to account for each component. For Class I sources, the correlation between L_{bol} and $M_\star$ appears to be linear, with one outlier that corresponds to the source L1551 IRS 5. The straight line in Fig. 5.11 shows the best fit for all Class I sources, providing the following power-law relationship:

$$L_{\text{bol}} = 10^{0.4 \pm 0.1} M_\star^{1.1 \pm 0.5}. \tag{5.2}$$

Assuming that L_{bol} results from the gravitational energy released by the material accreted onto

the surface of the protostar, the mass accretion rate ($\dot{M}_{\text{acc}}$) can be estimated from

$$\dot{M}_{\text{acc}} = \frac{L_{\text{bol}}R_{\star}}{GM_{\star}} \, , \tag{5.3}$$

where $R_{\star}$ is the protostellar radius and G the gravitational constant. Assuming $R_{\star} = 3R_{\odot}$ (Stahler et al. 1980), the calculated accretion rates are shown in the right panel of Fig. 5.11 as a function of T_{bol}. Combining Eqs. 5.2 and 5.3, a value of $(2.4 \pm 0.6) \times 10^{-7}$ M$_{\odot}$ year^{-1} is obtained for $\dot{M}_{\text{acc}}$ for the Class I sources, with a minimum and maximum value of 7.5×10^{-8} and 7.6×10^{-7} M$_{\odot}$ year^{-1}, respectively. The mean value is consistent with the mass accretion rates from Yen et al. (2017), where they found $\dot{M}_{\text{acc}}$ from $\sim 1 \times 10^{-7}$ to 4.4×10^{-6} M$_{\odot}$ yr^{-1} for a sample of Class I sources. The right panel of Fig. 5.11 shows $\dot{M}_{\text{acc}}$ as a function of T_{bol}. Myers & Ladd (1993) define T_{bol} as the temperature of a blackbody having the same mean frequency as the observed continuum spectrum and it is often taken as an indicator of the evolutionary stage of the source (e.g., Dunham et al. 2014a; Frimann et al. 2016a; Fischer et al. 2017). A tentative decrease of $\dot{M}_{\text{acc}}$ as the systems evolve is seen in Fig. 5.11. Nevertheless, the trend is not clear and the sample of Class 0 sources is still small.

If the accretion rate is assumed to be constant (2.4×10^{-7} M$_{\odot}$ year^{-1}), a typical Class I protostar will reach 1 M$_{\odot}$ in $\sim$4 Myr, which is inconsistent with the derived lifetime for the embedded Class 0/I phase (from 0.13 to 0.78 Myr; Dunham et al. 2015; Kristensen & Dunham 2018). This inconsistency is know as the *luminosity problem* (Kenyon & Hartmann 1995), where a constant accretion rate cannot explain the low luminosities of embedded protostars. With interferometric facilities, the stellar masses are better constrained from molecular line emission, and the only way to reconcile theory with observations is to assume a time-variable accretion rate onto the protostar (Kenyon & Hartmann 1995; White et al. 2007; Evans et al. 2009; Vorobyov & Basu 2010; Dunham & Vorobyov 2012; Audard et al. 2014; Dunham et al. 2014a). The time-variable or burst model of accretion operates in the embedded phase of protostellar evolution and the disk spends practically all of its time in a low state (low $\dot{M}_{\text{acc}}$) and accretes significant mass in relatively short bursts, which would account for the low average L_{bol} of protostars (Vorobyov & Basu 2010; Dunham et al. 2014a).

From Fig. 5.11, L1551 IRS 5 is the only Class I source with high L_{bol} and high $\dot{M}_{\text{acc}}$ that stands out over the others. This source has been proposed to be a young star experiencing a FU Ori like outburst (Hartmann & Kenyon 1996; Osorio et al. 2003). With the exception of L1551 IRS 5, the rest of the Class I sources in this sample appear to be in a low state of accretion (see Table 5.8 in the
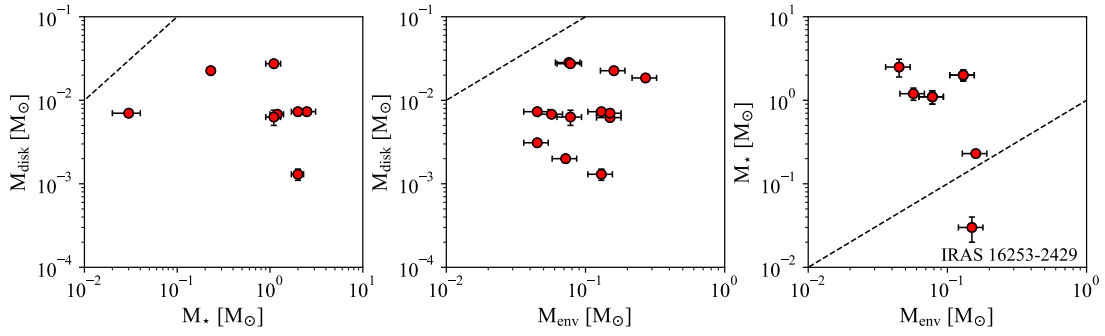
Figure 5.10: Comparison between disk mass and stellar mass (*left*), disk mass and envelope mass (*centre*), and stellar mass and envelope mass (*right*). The dashed black line is for $M_i = M_j$.
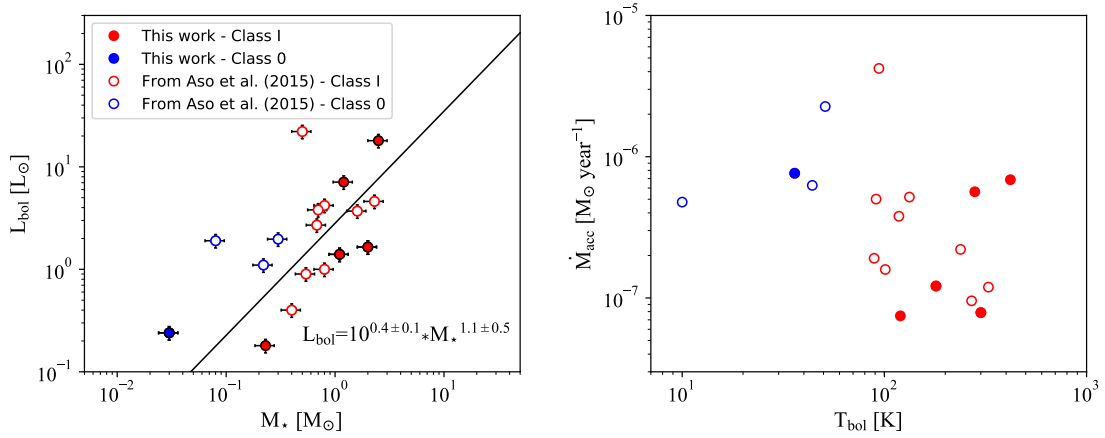
Figure 5.11:
smalltextitLeft: bolometric luminosity as a function of stellar mass with data points from this work and from Aso et al. (2015). The black straight line shows the best fit for all Class I sources. *Right:* mass accretion rate as a function of the bolometric temperature.

Appendix).

If the accretion onto the central star is episodic, the accretion bursts may have important effects on the chemistry. In consequence, observable chemical effects (such as the $C^{18}O$ spatial distribution) can provide clues to the luminosity history (e.g., Jørgensen et al. 2013, 2015; Frimann et al. 2016b). In our sample, the lack of significantly extended $C^{17}O$ emission contrasts with the $C^{18}O$ emission observed by Jørgensen et al. (2015) and Frimann et al. (2016b) towards a different sample of Class 0/I sources, which suggests a relatively quiescent phase for our sources or a low $C^{17}O$ column density at larger distances from the source.

Table 5.7: Line intensity towards the source position calculated from a Gaussian fit.

Source	Intensity [Jy beam^{-1} km s^{-1}]			
	C^{17}O	C$_2$H	H^{13}CO$^+$	SO$_2$
GSS30-IRS1	-	-	-	0.439
[GY92] 30	0.081	-	-	-
WL 12	-	-	-	-
[GY92] 197	0.226	0.073	-	-
Elias 29	-	-	-	1.036 [b]
IRS 43 VLA 1	0.049	-	0.133	0.389 [b]
IRS 43 VLA 2	0.053	-	0.051	-
IRS 44	-	-	0.124	1.478 [b]
IRAS 16253-2429	0.213	0.206	-	-
ISO-Oph 203	-	-	-	-
IRS 67 A	0.134	-	0.187	-
IRS 67 B	0.488 [a]	0.077	0.396 [a]	0.221 [b]

[a] Line profile with 3 components. [b] Line profile with 2 components.

5.6 Chemical evolution

5.6.1 Line emission as a function of L_{bol} and T_{bol}

The differences in the molecular emission signatures for the sources in the sample, may be an indication that the chemistry does depend on the physical evolution of the sources, i.e., that the molecular column densities vary as a function of the source bolometric luminosities and temperatures. For the molecular transitions detected towards the source position, the spectrum was extracted from the pixel that corresponds to the peak of the continuum emission (see Table 5.3), and a Gaussian fit was applied to the line profile (see Fig. 5.16 in the Appendix). The resulting values are listed in Table 5.7 and these are estimates of the line intensities towards the peak, and not the full integrated emission over the maps. Most of the line profiles show a single central component centered at V_{source}. When more than one component is observed, the intensity listed in Table 5.7 is the sum of all the individual components. For the sources without on-source detection, the 3σ upper limit per 1 km s^{-1}, i.e., 0.013 Jy beam^{-1} km s^{-1}, is used in the comparison.

Figure 5.12 shows the line intensities from Table 5.7 as a function of L_{bol} and T_{bol}. The binary systems are represented by non-filled bars in order to differentiate them from the single systems, since the former are particularly rich in molecular lines. The binary systems show emission of almost all the transitions presented in Table 6.1, with the exception of CH$_3$OH. This chemical richness appears to be related to the mass content and extent of the circumbinary disks, in agreement with the results of Murillo et al. (2018).
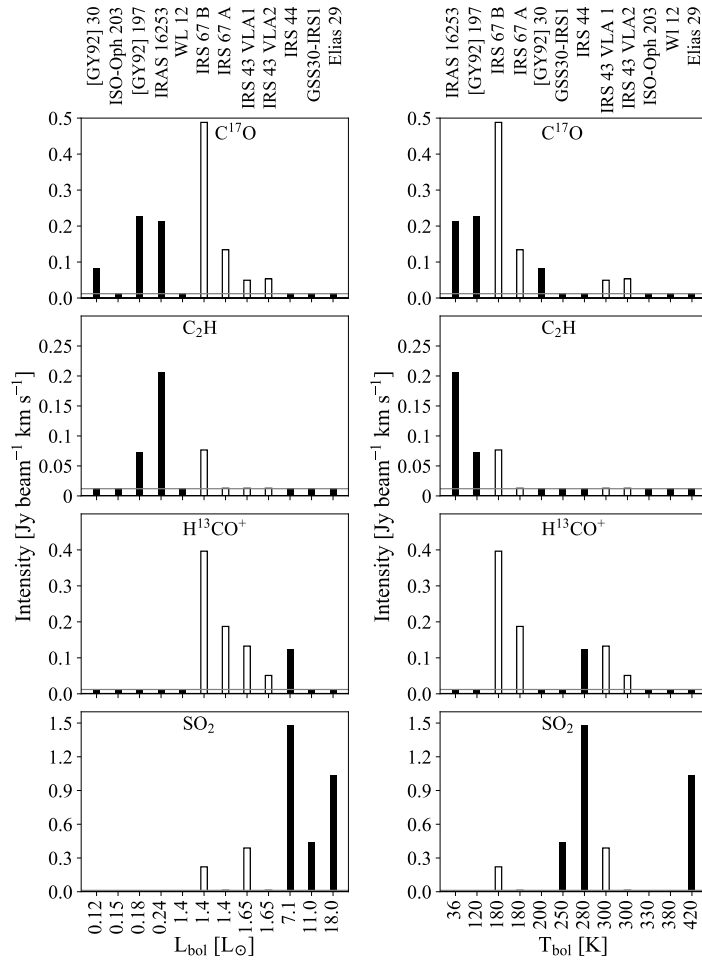
Figure 5.12: Line intensity as a function of the bolometric luminosity *(left)* and bolometric temperature *(right)* towards the source position. The non-filled bars represent the binary systems and the grey horizontal line indicates a value of 3σ.

Considering only the single sources, $C^{17}O$ is seen mostly towards the least luminous ones (see upper-left panel of Fig. 5.12), while the opposite situation is the case for SO_2 (lower-left panel of Fig. 5.12). The sources with high bolometric luminosity are associated with high temperatures close to the protostar. Therefore, for the same continuum flux, the dust mass will be lower for sources with high L_{bol}, and thus, a lower column density of $C^{17}O$ is expected. On the other hand, SO_2 traces a different physical process than $C^{17}O$ and may be related with more energetic processes that are linked to the bolometric luminosity, and thus, the accretion history. If T_{bol} is taken as an evolutionary indicator, $C^{17}O$ and C_2H emission are associated with the less evolved sources. In particular, from Figs. 5.2, 5.7 and 5.12, there is a trend between the extent of the $C^{17}O$ and C_2H emission and the evolutionary stage of the source. On the other hand, there is no clear correlation between the sources with detected $H^{13}CO^+$ emission and L_{bol} or T_{bol}.

Figure 5.13 shows the chemical signatures in a plot of L_{bol} as a function of T_{bol}, for the sources observed as part of this study with additional points from the literature: Class 0 sources from Dunham et al. (2015) and Class I sources from Harsono et al. (2014)[3]. Three groups of sources can be identified based on on-source detections. The least evolved and luminous sources show $C^{17}O$ emission towards the source position, while the more evolved and luminous sources are associated with SO_2 emission. In addition, the more evolved sources associated with low luminosities do not show any line detection. As the system evolves from Class 0 to Class I, and later to Class II, the envelope mass decreases, leading to a lower gas column density and lines may be harder to detect. This is reflected in the emission of a high-density tracer, such as $C^{17}O$: the extent of the emission decreases with the evolutionary stage of the source, followed by a non-detection towards the more evolved ones. For the latter, emission of more abundant isotopologues, such as $C^{18}O$ and ^{13}CO, is expected to be seen, as in Class II sources. On the other hand, there is a chemical differentiation between $C^{17}O$ and SO_2, where the latter may be tracing a more energetic process probably linked to higher accretion rates, which is mostly determined by inner disk properties. Future observations of CO isotopologues and SO_2 transitions with different E_u values towards a larger sample of Class I sources will provide a more statistical perspective.

5.6.2 The absence of warm CH₃OH emission

One of the important chemical results of this study is the absence of compact CH_3OH emission towards all of the sources. At large scales CH_3OH is found to be in solid form with typical abundances with respect to water, $CH_3OH:H_2O$, of about 5% (Bottinelli et al. 2010; **?**; Boogert et al. 2015). CH_3OH is expected to sublimate off dust grains in the inner envelopes and in the protostellar disks in regions where the temperature increases above ∼90 K (Brown & Bolina 2007). Such warm CH_3OH has been inferred for some Class 0 sources based on single-dish observations (e.g., van Dishoeck et al. 1995; Schöier et al. 2002; Maret et al. 2005; Jørgensen et al. 2005b; Kristensen et al. 2010) and also imaged with interferometers (e.g., Jørgensen et al. 2005a; Maury et al. 2014; Jørgensen et al. 2016; Higuchi et al. 2018).

The absence of CH_3OH line emission provides strict upper limits to the column densities of the warm gas-phase CH_3OH. The upper limit to the column density is estimated using the predictions

---

[3]Of the sources from the Harsono et al. (2014) study, two Class I sources (TMC1A and TMCR1) show SO_2 $11_{1,11}-10_{0,10}$ emission towards the source position, but this transition is from a lower level with E_u of 60 K and does not show a broad line profile. Therefore, this cold SO_2 emission appears to be tracing a different component than the warm SO_2 seen in Fig. 5.6
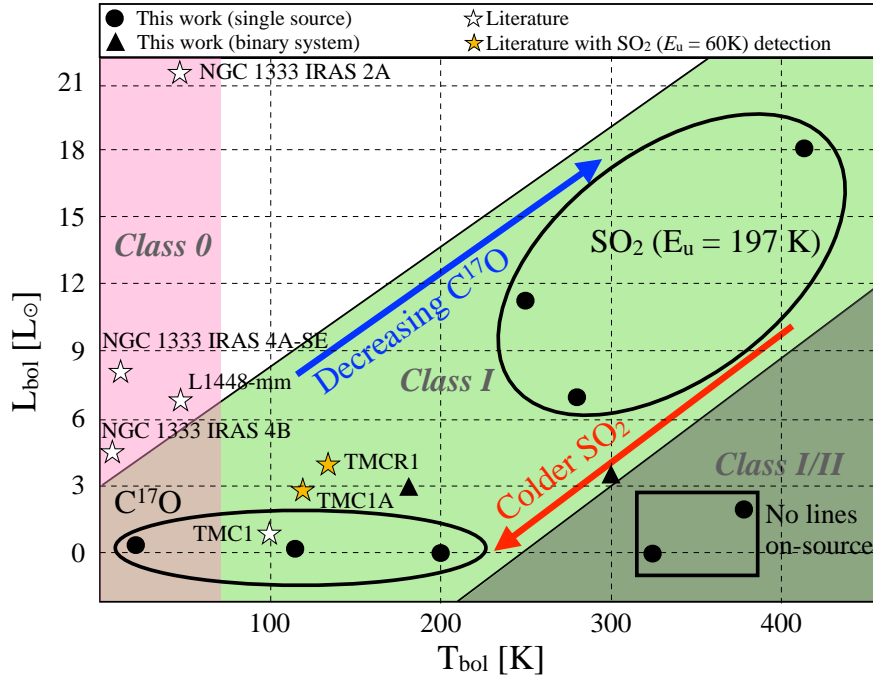
Figure 5.13: Bolometric luminosity as a function of the bolometric temperature, highlighting the regions where specific molecular transitions are detected towards the source position, and well-known Class 0 and I sources from Dunham et al. (2015) and Harsono et al. (2014), respectively. This plot only covers the lines listed in Table 6.1 plus SO_2 $11_{1,11}-10_{0,10}$ from Harsono et al. (2014). The Class 0 covers $T_{bol} \leq 70$ K (Dunham et al. 2014b) and the Class I/II region includes the sources where no line emission is detected.

for a synthetic spectrum for methanol calculated under the assumption of LTE and adopting a kinetic temperature of 100 K and a typical line width of 5 km s^{-1}. For the 3σ *rms* noise in the spectra of 13 mJy beam^{-1} km s^{-1}, this corresponds to an upper limit for the column density of 5×10^{14} cm^{-2} (assuming that the emission fills the beam uniformly), more than four orders of magnitude below that of the Class 0 protostar IRAS 16293-2422 (Jørgensen et al. 2016). As an illustration Fig. 5.5 shows the calculated synthetic spectrum for a column density a factor of five above this value (i.e., 2.5×10^{15} cm^{-2}).

The low upper limit for the CH_3OH column density implies that *(i)* there is no hot-core like region in the inner envelope close to the protostar if its envelope density profile can be extrapolated to the smallest scales and *(ii)* the gas-phase CH_3OH averaged over the entire disk is low. For the warm gas in the inner envelope, the column density can be translated to a constraint on the abundance by comparing to the results from Lindberg et al. (2014) for the Class 0/I protostar R CrA IRS 7B: through line radiative transfer modelling of ALMA detections of the same CH_3OH lines, Lindberg et al. (2014) found a CH_3OH abundance of 10^{-10} in the inner region of the 2.2 M$_\odot$ envelope. The

average envelope mass for our sample is 0.11 $M_\odot$, an order of magnitude below that from R CrA IRS 7B, and since our beam size and distance are similar to those of R CrA IRS 7B and our upper limits comparable to the brightest lines in the spectra from Lindberg et al. (2014), the upper limit to the CH_3OH abundance for our sources should be about an order of magnitude higher than the inferred abundance for R CrA IRS 7B, i.e., $\sim 10^{-9}$. Conversely, ignoring the envelope, an upper limit to the CH_3OH abundance for the disk can be estimated by comparing the inferred disk mass from the ALMA dust continuum measurements to the upper limit of the CH_3OH column density assuming that both fill the beam uniformly. Adopting an average disk mass of 0.0085 $M_\odot$ for our sample and the upper limit to the CH_3OH column density of 5×10^{14} cm^{-2}, the corresponding upper limit for the CH_3OH abundance is 10^{-10}, averaged over the entire disk.

These numbers may seem at odds with the results from ice measurements mentioned above, with CH_3OH at least of order 1% relative to water, which in turn has a typically quoted abundance ($[H_2O]/[H_2]$) of 10^{-4} (Boogert et al. 2015). However, in both cases the assumptions of the physical structures are critical: for example, for the protostellar envelope Lindberg et al. (2014) showed that the CH_3OH abundance would increase by two orders of magnitude if a constant density profile is used at scales smaller than the disk size (corresponding to the flattening of the inner envelope in rotating collapse), rather than a centrally peaked, power-law, envelope density profile as expected from free-fall. Since a number of sources in our sample show evidence for resolved disks, applying the same argument is reasonable, i.e., the upper limit to the CH_3OH abundance would be 10^{-7} (rather than 10^{-9}), comparable to the estimates for hot cores towards Class 0 protostars (e.g., Schöier et al. 2002; Maret et al. 2005; Jørgensen et al. 2005b). Likewise for the disk argument, Persson et al. (2016) showed that in simple parametrised disk models, only a small fraction, as low as 1%, of the total disk mass may have temperatures above 100 K where water could sublimate. These are the regions where CH_3OH would also be in the gas-phase, thus the upper limit for the CH_3OH abundance in the warm parts of the disks would likewise be less stringent, $\sim 10^{-8}$. Further, by analysing the $H_2^{18}O$ emission towards 4 Class 0 sources, Persson et al. (2016) showed that the H_2O abundance in the warm regions of the disks could be as low as 10^{-7}–10^{-6}, which would be consistent with the CH_3OH abundance limit derived above for typical $CH_3OH:H_2O$ ice abundance ratios of $\sim 1\%$.

Obviously, there are still a number of caveats in this analysis, in particular, what is the physical structure of the material towards protostars at these small scales, e.g., what is the density profiles of the envelopes and the temperature structures of the embedded disks. It can therefore not be ruled out

that the absence of CH_3OH is still to some degree caused by chemical effects such as the suppression of methanol formation due to higher temperatures in the precursor environments, as also discussed for the case of Corona Australis by Lindberg et al. (2014). Future modelling efforts and observation of lower-excited CH_3OH transitions at large and small scales may provide further insights.

5.6.3   Is SO_2 tracing accretion shocks?

The combination of compact ($r < 0.''5$ or 70 au; see Fig.5.6), high velocity emission (up to ± 10 km s^{-1}; see Fig.5.16), and velocity gradient perpendicular to the outflow direction, suggests that the warm SO_2 emission may be tracing warm shocked material, in particular, accretion shocks. Material from the inner envelope falls on the circumstellar disk and produces accretion shocks at the envelope-disk interface, releasing molecules from the dust grains and altering the chemistry. Miura et al. (2017) investigated the thermal desorption of molecules from the dust-grain surface by accretion shocks and found that the enhancement of some species (such as SO) can be explained by the accretion shock scenario, where the most important parameters are the grain size, the pre-shock gas number density, and the shock velocity. Taking a shock velocity of 10 km s^{-1}, Miura et al. (2017) predicted that SO_2 can be released from the dust-grain surface for a pre-shock gas number density of $\sim 10^7$ cm^{-3}.

Another formation path for SO_2 is by oxidation of SO in the gas phase (Charnley 1997):

$$SO + OH \rightarrow SO_2 + H, \tag{5.4}$$

which is very efficient for T between 100 and 200 K. In this scenario, the SO_2 abundance depends strongly on the presence of SO and OH in the gas-phase. SO can be released from dust grains at lower velocities and densities than SO_2, since SO has a lower desorption energy (E_{d0}) than SO_2 (2600 K and 3400 K for SO and SO_2, respectively; Wakelam et al. 2015; Miura et al. 2017). In addition, OH is seen towards Class I sources and has been associated with shocked regions in the inner envelope close to the protostar (Wampfler et al. 2013). In order to test both scenarios, oxidation of SO or desorption from dust grains, transitions from warm SO ($E_u \sim 200$ K) need to be observed.

Apart from SO and SO_2, CH_3OH has also been related with shocked regions (e.g., Avery & Chiao 1996; Jørgensen et al. 2007), therefore, if SO_2 (or SO) is being released from the grain surface by accretion shocks, why is there no CH_3OH detection? There are two possibilities, *(i)* CH_3OH is not being released from the grain surface because it has a higher desorption energy ($E_{d0} = 5000$

K), therefore, a higher pre-shock gas number density is needed ($\sim 10^8$ cm^{-3}; Miura et al. 2017), or *(ii)* CH$_3$OH is being released but later destroyed by the high velocities. Suutarinen et al. (2014) demonstrated that CH$_3$OH is sputtered from ices in shocks with $v \geq 3$ km s^{-1}, survives at moderate velocities, but is later dissociated for $v \geq 10$ km s^{-1}.

A Keplerian disk or disk winds are less plausible scenarios for explaining the SO$_2$ emission. For a Keplerian profile, high velocities (≥ 5 km s^{-1}) would be reached at scales smaller than 0.″2 (see Fig.5.8), therefore, the high velocity SO$_2$ component seen at $\sim$0.″5 (see Fig.5.6) is not consistent with a Keplerian profile. For disk winds towards Class I sources, it has been shown that species such as SO do not survive beyond $\sim$1 au (Panoglou et al. 2012). In contrast, towards Class 0 sources, a disk wind driven by SO survives between 10 and 100 au (Panoglou et al. 2012), in agreement with what was found towards the Class 0 source HH212: Tabone et al. (2017) proposed that SO and SO$_2$ are tracing a disk wind and the emission is observed between $\sim$50 and $\sim$150 au. In any case, neither option can be completely ruled out and higher spatial resolution is needed in order to create a PV diagram and obtain a velocity profile for SO$_2$.

5.7 Summary

This work presents high-angular-resolution (0.″4, $\sim$60 au) ALMA observations of 12 Class I sources in the Ophiuchus star forming region. The continuum emission at 0.87 mm is analysed, together with C^{17}O, C^{34}S, H^{13}CO$^+$, SO$_2$, C$_2$H and CH$_3$OH, and the main results are provided below.

Of the 12 sources, 2 do not show continuum emission nor molecular line emission, whereas another 2 show continuum emission but no line detection. Two sources are proto-binary systems with very rich line emission, and the remaining 6 show continuum emission plus some of the molecular transitions. C^{17}O is seen towards the less evolved sources and the binary systems, tracing high gas column gas densities. Keplerian profiles are found for three sources, while an infalling profile is seen for one of them. More abundant isotopologues, such as C^{18}O and ^{13}CO, may be better disk tracers for the more evolved sources.

The non-detection of warm CH$_3$OH implies that there in no hot-core like region in the inner envelope close to the protostar (that follows a power-law density profile) and that the averaged CH$_3$OH column density over the entire disk is low. This suggest that *(i)* the presence of a disk is flattening the envelope density profile at small scales, thus, leading to a low column density of warm material, *(ii)*

only a small fraction (1%) of the disk may have temperatures above 100 K, or *(iii)* chemical effects may be suppressing the formation of methanol. Clearly, future modelling efforts and observations of colder CH_3OH at envelope and disk scales are needed in order to provide stronger conclusions.

Warm (E_u = 197 K) and compact ($r <$ 70 au) SO_2 emission is detected towards 5 of the sources, with particularly large line widths (between -10 and 10 km s^{-1}) towards Elias 29 and IRS 44. This emission may be related with accretion shocks. The shocks would also liberate CH_3OH from dust mantles, but later it would be destroyed by the high velocities (> 10 km s^{-1}).

The fact that $C^{17}O$ is detected towards the less evolved and less luminous sources agrees with a decrease of the gas column density, a consequence of the evolution of the system, and with the low column density of material due to high temperatures. The envelope mass decreases as the system evolves, therefore, the gas column density related to quiescent material decreases and lines are hardly detected. However, a similar trend is not observed for SO_2 and, instead, a chemical differentiation between $C^{17}O$ and SO_2 is seen. SO_2 is detected towards the most evolved sources with high L_{bol}, and thus, related with higher accretion rates and a different physical process.

The comparison between disk, envelope, and stellar masses shows a trend between $M_\star$ and M_{env}: the most massive stars are related with less envelope material, as expected. In addition, L_{bol} shows a linear dependence with $M_\star$ for Class I sources, where the best fit gives $L_{bol} = 10^{0.4\pm0.1}M_\star{}^{1.1\pm0.5}$. Assuming that L_{bol} is a consequence of accretion onto the protostar, a mean $\dot{M}_{acc}$ of $(2.4 \pm 0.6) \times 10^{-7}$ M$_\odot$ year^{-1} is calculated, with values ranging from 7.5×10^{-8} to 7.6×10^{-7} M$_\odot$ year^{-1}. If $\dot{M}_{acc}$ is constant, the time required to accrete enough mass will be greater that the mean life-time of the embedded stage, supporting the scenario of episodic accretion bursts and a variable accretion rate. Within this scenario, the Class I sources discussed in this work may be in a quiescent phase, with the exception of L1551 IRS 5.

This work shows the importance of a representative sample for exploring the physical and chemical structure of Class I sources, by comparing not only the continuum emission, but also the emission of specific molecules and the protostellar masses obtained from the velocity profiles. The observation of disk and warm gas tracers is crucial in order to interpret the physical and chemical processes and evolution at disk scales. Future observations will provide more statistical results and the study of other species will contribute to a better understanding of the chemical evolution of low mass protostars.

Acknowledgements

5.8   Appendix

5.8.1   CH$_3$OH emission towards [GY92] 30

Two CH$_3$OH transitions are detected towards [GY92] 30, where the emission peaks beyond the 25σ continuum contour and no emission is seen towards the source position (Fig. 5.14). These transitions are associated with the lowest E_u (65 and 70 K) and the emission is related with low velocities, between -0.5 and 0.5 km s^{-1} from the source velocity. In addition, they present different morphologies and the spectra taken towards different positions show a variation in the intensity of both lines. The integrated spectrum towards a region of $\sim 300 \times 600$ au is shown in Fig. 5.15, where both CH$_3$OH transitions are detected. This emission may be related with quiescent envelope material, since [GY92] 30 has the more massive envelope from the sample (see Table 5.1).

5.8.2   Mass accretion rates

The values of L_{bol}, T_{bol}, $M_\star$, and $\dot{M}_{acc}$, plotted in Fig. 5.11, are listed in Table 5.8. L_{bol}, T_{bol}, and $M_\star$ are taken from this work and from the literature (see Tables 5.1 and 5.6), while $\dot{M}_{acc}$ is calculated from Eq. 5.3.

5.8.3   Gaussian fits

The spectra extracted from the source position (see Table 5.3) is fitted by a Gaussian profile with 1, 2, or 3 components (see Fig. 5.16). The resulting intensities from the fit are listed in Table 5.7 and plotted

Table 5.8: Bolometric luminosity, bolometric temperature, and stellar masses of Class 0 and I sources, from this work and from the literature, with the calculated mass accretion rates.

Source	L_{bol} [$L_\odot$]	T_{bol} [K]	$M_\star$ [$M_\odot$]	$\dot{M}_{acc}$ [10^{-6} $M_\odot$ yr^{-1}]	References
				Class 0	
NGC 1333 IRAS 4A2	1.9	51	0.08	2.27	Choi et al. (2010)
VLA 1623A	1.1	10	0.22	0.48	Murillo et al. (2013)
L1527 IRS	1.97	44	0.30	0.63	Ohashi et al. (2014)
IRAS 16253-2429	0.24	36	0.03	0.76	This work
				Class I	
R CrA IRS 7B	4.6	89	2.3	0.19	Lindberg et al. (2014)
L1551 NE	4.2	91	0.8	0.50	Froebrich (2005); Takakuwa et al. (2014)
L1551 IRS 5	22.1	94	0.5	4.22	Kristensen et al. (2012); Chou et al. (2014)
TMC1	0.9	101	0.54	0.16	Harsono et al. (2014)
TMC-1A	2.7	118	0.68	0.38	Aso et al. (2015)
TMR1	3.8	133	0.7	0.52	Harsono et al. (2014)
L1489 IRS	3.7	238	1.6	0.22	Yen et al. (2014)
L1536	0.4	270	0.4	0.09	Harsono et al. (2014)
IRS 63	1.0	327	0.8	0.12	Kristensen et al. (2012); Brinch & Jørgensen (2013)
[GY92] 197	0.18	120	0.23	0.07	This work
Elias 29	18.0	420	2.5	0.69	This work
IRS 43 VLA 1	1.65	300	0.9	0.17	This work
IRS 43 VLA 2	1.65	300	0.9	0.17	This work
IRS 44	7.1	280	1.2	0.56	This work
IRS 67 A	1.4	180	1.1	0.12	This work
IRS 67 B	1.4	180	1.1	0.12	This work

in Fig. 5.12. Most of the line profiles show a single central component centered at V_{source}, with the exception of the source IRS 67 B and the SO_2 transition, that show more than one component. $C^{17}O$ and $H^{13}CO^+$ emission towards IRS 67 B show 3 components associated with blue-shifted, red-shifted and a central component associated with more quiescent material, while the SO_2 emission shows 2 components related with blue-shifted and red-shifted material (with the exception of GSS30-IRS1, where only blue-shifted emission is seen.
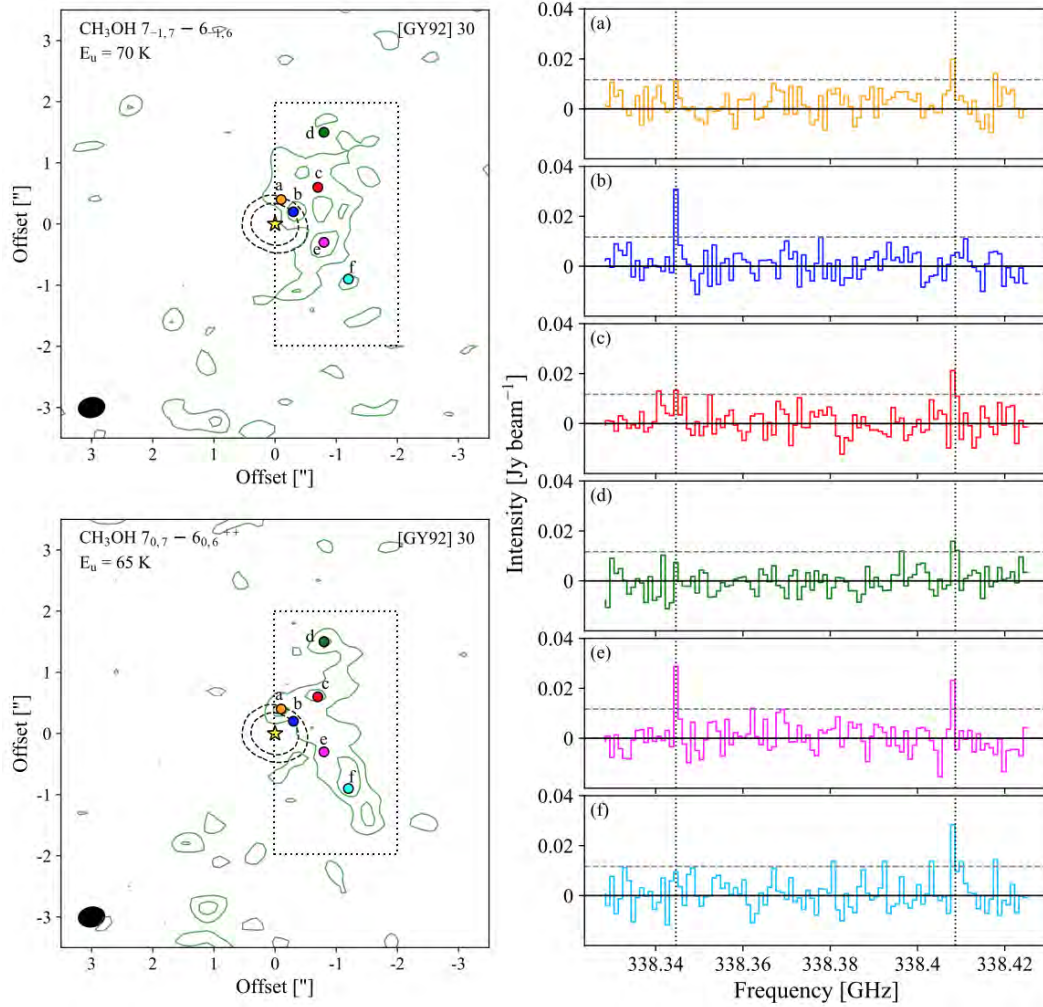
Figure 5.14: *Left*: contour maps of CH$_3$OH 7_{-1}–6_{-1} E and CH$_3$OH 7_0–6_0 A$^+$ towards [GY92] 30. The contours start at 3σ and follow a step of 3σ (σ = 4 mJy beam^{-1} km s^{-1}), representing velocities from -0.5 to 0.5 km s^{-1}. The dashed-black contours show the continuum emission for values of 4 and 25σ. The yellow star indicates the position of the 2D Gaussian fit and the synthesized beam is represented by the black filled ellipse. The dotted box represents the region from which the spectrum of Fig. 5.15 is integrated. *Right*: Spectra towards different positions marked on the contour maps. The grey dashed horizontal line represent a value of 3σ and all the spectra are rebinned by a factor of 4. The dotted black vertical lines indicate the rest frequency of both CH$_3$OH transitions.
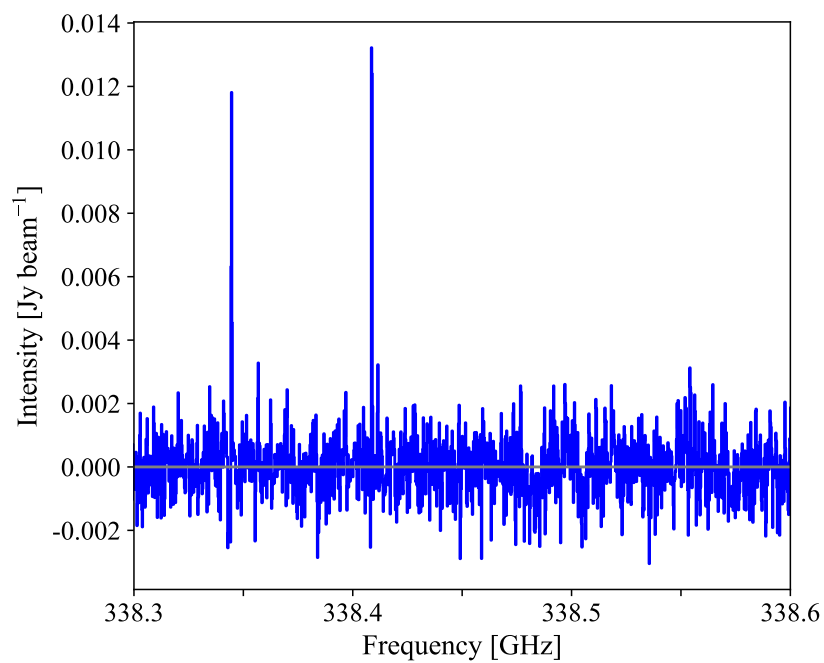
Figure 5.15: Integrated spectrum towards the squared region highlighted in the left panels of Fig. 5.14.
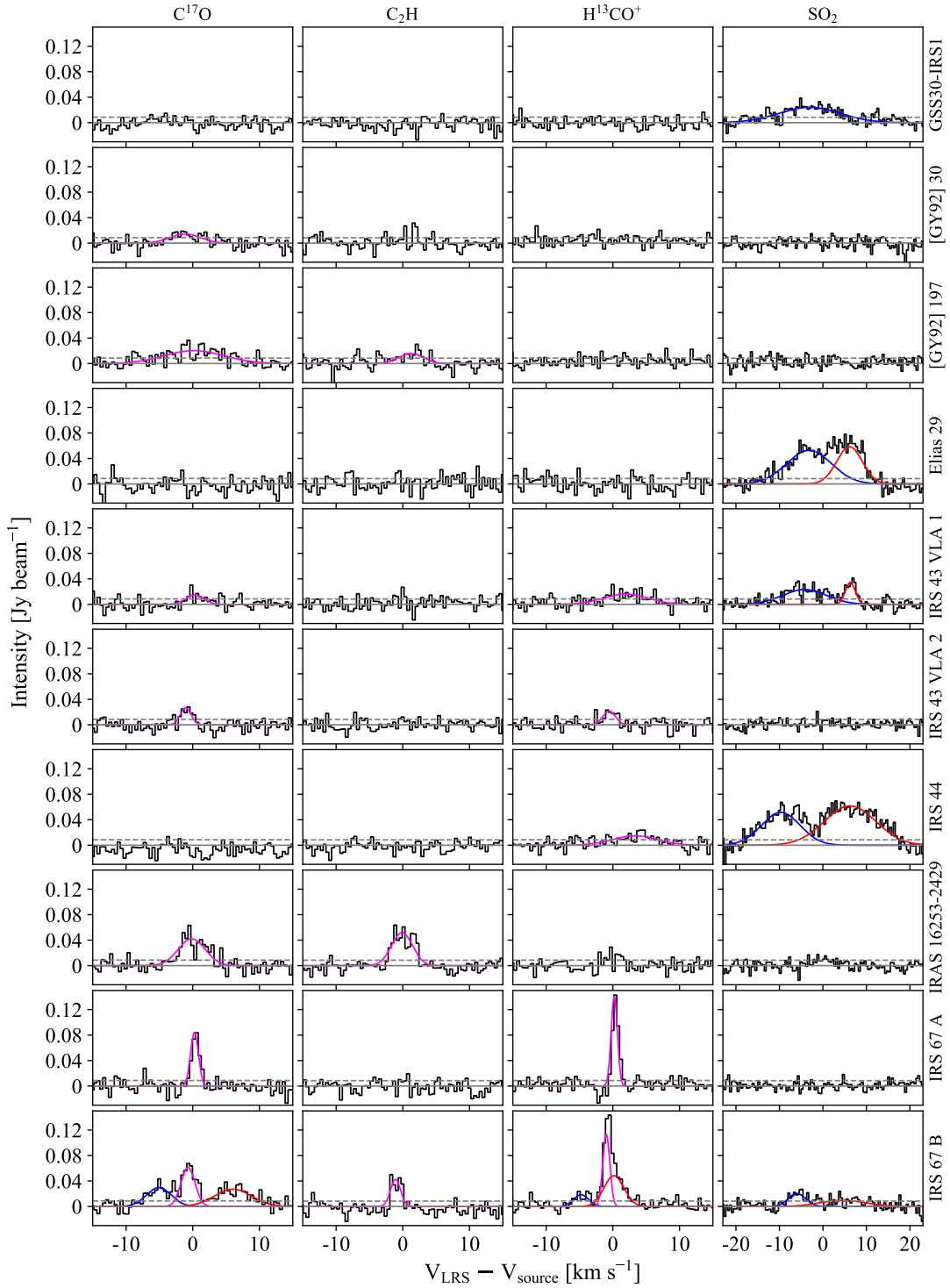
Figure 5.16: Spectra towards the source positions, overlapped with a Gaussian fit (see Table 5.7). The blue, magenta, and red curves represent blue-shifted, quiescent, and red-shifted material, respectively. The dashed grey horizontal line shows the value of 3σ. All spectra have been shifted to the source velocity (see Table 5.4).

6   PAPER III: Revealing the chemical structure of the Class I disk Oph-IRS 67

Elizabeth Artur de la Villarmois[1], Lars E. Kristensen[1] & Jes K. Jørgensen[1]

[1] Centre for Star and Planet Formation, Niels Bohr Institute and Natural History Museum of Denmark, University of Copenhagen, Øster Voldgade 5-7, DK-1350 Copenhagen K, Denmark

6.1   Abstract

Context: Recent results suggest that the first steps towards planet formation may already take place in protoplanetary disks during the first 100,000 years after stars form. Therefore, it is crucial to unravel the physical and chemical structures of such disks in their earliest stages while they are still embedded in their natal envelopes and compare them with more evolved systems.

Aims: The purpose of this paper is to explore the structure of a line-rich Class I proto-binary source, Oph-IRS 67, and analyse the differences and similarities with Class 0 and Class II sources.

Methods: We present a systematic molecular line study of IRS 67 with the Submillimeter Array (SMA) on $1-2''$ ($150-300$ AU) scales. The wide instantaneous band-width of the SMA observations (~ 30 GHz) provide detections of a range of molecular transitions that trace different physics, such as CO isotopologues, sulphur-bearing species, deuterated species, and carbon-chain molecules.

Results: Significant differences are seen for different groups of species. For example, the CO isotopologues and sulphur-bearing species show a rotational profile and are tracing the larger-scale circumbinary disk structure, while CN, DCN, and carbon-chain molecules peak at the southern edge of the disk at blue-shifted velocities. The cold gas tracer DCO^+ is seen beyond the extent of the circumbinary disk.

Conclusions: The detected molecular transitions can be grouped into three main components: cold regions far from the system, the circumbinary disk, and a UV-irradiated region likely associated with the surface layers of the disk that are reached by the UV radiation from the sources. The different

components are consistent with the temperature structure derived from the ratio of two H$_2$CO transitions, i.e., warm temperatures are seen towards the outflow direction, lukewarm temperatures are associated with the UV-radiated region, and cold temperatures are related with the circumbinary disk structure. The chemistry towards IRS 67 shares similarities with both Class 0 and Class II sources, possibly due to the high gas column density and the strong UV radiation arising from the binary system. IRS 67 is, therefore, highlighting the intermediate chemistry between deeply embedded sources and T Tauri disks.

6.2   Introduction

Protoplanetary disks are a crucial stage between warm cores and the formation of planetesimals and planets, and the final composition of planets likely depends on the chemical processing within the disk. The chemical complexity of the disk is established by the material that is incorporated from the inner envelope and by physical processes that promotes a chemical reset (e.g., outflows, accretion shocks, UV radiation field; Bergin et al. 2003; Ceccarelli 2004; Herbst & van Dishoeck 2009; Sakai & Yamamoto 2013; Miura et al. 2017). The details of how and when the disk forms are still not well understood. In particular, the physics and chemistry of the innermost regions are still challenging to observe and study due to the large amounts of gas and dust they are embedded within. It is, therefore, essential to study and understand the first stages of disks formation. This paper presents an extensive Submillimeter Array (SMA) survey of the molecular line emission on a few hundred AU scales towards the Class I proto-binary system Oph-IRS 67, and investigates the physical and chemical signatures associated with the system.

The complex structure of embedded disks is associated with a huge range of temperatures ($\sim$10−1000 K) and densities (10^5−10^{13} cm^{-3}; Herbst & van Dishoeck 2009; van Dishoeck 2018), making molecules excellent diagnostics of the physical conditions and processes. Chemical surveys towards deeply embedded sources have shown the potential of the chemistry to shed light on the physical structure of these regions (e.g., Jørgensen et al. 2016; Lefloch et al. 2018; Yoshida et al. 2019). Also, the chemical inventories and initial conditions of young disks can then be compared with disks around more evolved (Class II/T Tauri) young stars (e.g., ?Kastner et al. 2018).

Class I disks represent the bridge between deeply embedded Class 0 sources and the emergence of planet-forming disks, i.e., Class II sources. Recent high sensitivity and spatial resolution observations

suggest that planet formation starts at early stages (Class I), based on the evidence of considerable grain growth (e.g., ALMA Partnership et al. 2015; Harsono et al. 2018). The study of Class I disks is, therefore, essential in order to constrain the first steps of planet formation and to analyse the chemical evolution of disks at different stages. The observations of Class I disks are challenging since they are small in size (~100 AU; Harsono et al. 2014; Yen et al. 2015) and other components, such as inner envelope and outflow material, can contribute to the emission on small scales.

IRS 67 is a Class I proto-binary system located in the Ophiuchus star forming region, and belongs to the L1689 cloud. It has been associated with a large-scale outflow structure ($\gtrsim$1000 AU; Bontemps et al. 1996), bolometric temperature (T_{bol}) of 130 K, and bolometric luminosity (L_{bol}) of 4.0 L$_\odot$ (Dunham et al. 2015). The binarity of the system was proven by McClure et al. (2010) at infrared wavelengths, where a separation of 0.″6 (~90 AU for a distance of 151.2 pc; Ortiz-León et al. 2017) was found between the sources. More recently, a Keplerian circumbinary disk was associated to IRS 67 with an extent of ~620 AU (Artur de la Villarmois et al. 2018). In comparison with other Class I sources, IRS 67 shows a particular rich chemistry and bright emission of c-C$_3$H$_2$ (Artur de la Villarmois et al. 2018, 2019), a molecule commonly associated with photon-dominated regions (PDRs; Guzmán et al. 2015; Murillo et al. 2018).

This paper presents a SMA chemical survey towards the Class I proto-binary system IRS 67 and is laid out as follows. Section 2 presents the observational details, data calibration, and spectral coverage. The continuum emission, detected molecular transitions, contour maps, moment 0 maps, and spectral features are described in Sect. 3. We discuss the chemical and physical structure of IRS 67 in Sect. 4, together with an analysis of the non-detected molecular lines, and a comparison with other stages of low-mass star formation. Finally, the main results are summarised in Sect. 5.

6.3 Observations

IRS 67 was observed using the Submillimeter Array (SMA), in the extended and compact configurations on 2017 February 24 and 2017 April 21, respectively (program code: 2016B-S0004; PI: Elizabeth Artur de la Villarmois). The antenna configuration provided projected baselines between 10 and 188 metres. A pointing centre of $\alpha = 16^h32^m00^s98$, $\delta = -24°56'43.″4$ (J2000) was used, corresponding to the peak of the continuum emission at 0.87 mm (Artur de la Villarmois et al. 2018). The observations covered a frequency range of ~30 GHz, between 214.3 and 245.6 GHz (Table 6.1)

Table 6.1: Summary of the observations.

Receiver	Sideband	Frequency range [GHz]	Continuum *rms* [Jy beam^{-1}]	Spectral *rms* [Jy beam^{-1} channel] [a]
230	lower	214.3 - 222.3	0.001	0.08
240	lower	221.6 - 229.6	0.003	0.15
230	upper	230.3 - 238.3	0.001	0.10
240	upper	237.6 - 245.6	0.004	0.17

[a] The channel width is 0.18 km s^{-1}.

Table 6.2: Results of 2D Gaussian fits towards the continuum peaks.

Receiver	Sideband	Size [a] [″]	PA [°]	Integrated flux [Jy]	Intensity peak [Jy beam^{-1}]
230	lower	$1.4 \pm 0.1 \times 0.7 \pm 0.2$	38 ± 9	0.087 ± 0.004	0.056 ± 0.002
240	lower	$1.4 \pm 0.2 \times 1.0 \pm 0.4$	3 ± 44	0.097 ± 0.007	0.064 ± 0.003
230	upper	$1.2 \pm 0.1 \times 0.6 \pm 0.1$	41 ± 6	0.105 ± 0.003	0.071 ± 0.002
240	upper	$1.6 \pm 0.3 \times 1.3 \pm 0.5$	24 ± 81	0.130 ± 0.012	0.068 ± 0.005

[a] Deconvolved Size (FWHM).

with a spectral resolution of 139.64 kHz (0.18 km s^{-1}).

The calibration and imaging were done in CASA[1] (McMullin et al. 2007). For the extended track, the complex gains were calibrated through observations of the quasar 1626-298, passband calibration on 3c273, and flux calibration on Ganymede. For the compact track, the gain, passband, and flux calibrations were implemented by observing the quasar 1626-298, 3c454.3, and Callisto, respectively. The extended and compact observations were combined and a Briggs weighting with robustness parameter of 1 was applied to the visibilities. The resulting dataset has a typical beam size of 1.″7 ×1.″4 (~260 × 210 AU) and a maximum angular scale of ~25″. The continuum and line *rms* are given in Table 6.1.

6.4 Results

6.4.1 Continuum

The continuum emission for each receiver and sideband is fitted with two-dimensional (2D) Gaussians in the image plane, and the resulting deconvolved size, position angle, integrated flux, and intensity peak are listed in Table 6.2. The continuum emission at 0.87 mm, previously detected with ALMA (Artur de la Villarmois et al. 2018), showed the contribution of both protostellar sources and a circumbinary disk, associated with a position angle of 54°, an extent of ~620 AU, and a total integrated flux (both sources and disk) of 0.30 Jy.

---

[1] http://casa.nrao.edu/

Table 6.3: Parameters of the detected molecular transitions.

Species	Transition	Frequency [a] [GHz]	A_{ij} [a] [s^{-1}]	E_u [a] [K]	n_crit [b] [cm^{-3}]
		CO- species			
CO	$J=2-1$	230.53800	6.92×10^{-7}	17	2.2×10^4
^{13}CO	$J=2-1$	220.39868	6.07×10^{-7}	16	2.0×10^4
C^{18}O	$J=2-1$	219.56035	6.01×10^{-7}	16	1.9×10^4
C^{17}O	$J=2-1$	224.71439	6.42×10^{-7}	16	2.1×10^4
H$_2$CO	$3_{0,3}-2_{0,2}$ (para)	218.22219	2.82×10^{-4}	21	3.4×10^6
H$_2$CO	$3_{2,2}-2_{2,1}$ (para)	218.47563	1.58×10^{-4}	68	1.4×10^6
H$_2$CO	$3_{2,1}-2_{2,0}$ (para)	218.76007	1.58×10^{-4}	68	3.2×10^6
H$_2$CO	$3_{1,2}-2_{1,1}$ (ortho)	225.69778	2.75×10^{-4}	33	5.7×10^6
		Deuterated species			
DCO$^+$	$J=3-2$	216.11258	2.38×10^{-3}	21	7.0×10^6
DCN	$3-2$	217.23854	4.57×10^{-4}	21	2.5×10^7
DNC	$3-2$	228.91049	5.62×10^{-4}	22	4.9×10^6
		S- species			
CS	$5-4$	244.93556	2.95×10^{-4}	35	8.7×10^6
C^{34}S	$5-4$	241.01609	2.75×10^{-4}	28	8.0×10^6
^{13}CS	$5-4$	231.22069	2.51×10^{-4}	33	7.4×10^6
SO	5_5-4_4	215.22065	1.20×10^{-4}	44	1.8×10^{8} [c]
SO	6_5-5_4	219.94944	1.35×10^{-4}	35	2.5×10^{8} [c]
		N- species			
CN [d]	$N=2-1, J=3/2-3/2, F=1/2-1/2$	226.28742	1.02×10^{-5}	16	6.1×10^4
CN	$N=2-1, J=3/2-3/2, F=5/2-5/2$	226.35987	1.62×10^{-5}	16	5.8×10^5
CN	$N=2-1, J=3/2-1/2, F=1/2-3/2$	226.61657	1.07×10^{-5}	16	1.8×10^5
CN	$N=2-1, J=3/2-1/2, F=3/2-3/2$	226.63219	4.27×10^{-5}	16	2.6×10^5
CN	$N=2-1, J=3/2-1/2, F=5/2-3/2$	226.65956	9.55×10^{-5}	16	7.0×10^5
CN	$N=2-1, J=3/2-1/2, F=1/2-1/2$	226.66369	8.51×10^{-5}	16	6.0×10^5
CN	$N=2-1, J=3/2-1/2, F=3/2-1/2$	226.67931	5.25×10^{-5}	16	3.8×10^5
CN	$N=2-1, J=5/2-3/2, F=5/2-3/2$	226.87419	9.55×10^{-5}	16	2.4×10^6
CN	$N=2-1, J=5/2-3/2, F=7/2-5/2$	226.87478	1.15×10^{-4}	16	5.1×10^7
CN	$N=2-1, J=5/2-3/2, F=3/2-1/2$	226.87590	8.51×10^{-5}	16	1.2×10^6
CN	$N=2-1, J=5/2-3/2, F=3/2-3/2$	226.88742	2.75×10^{-5}	16	9.5×10^5
CN	$N=2-1, J=5/2-3/2, F=5/2-5/2$	226.89213	1.82×10^{-5}	16	5.4×10^5
^{13}CN	$N=2-1, J=5/2-3/2, F=4-3$	217.46715	1.01×10^{-4}	16	
		Carbon-chain species			
c-C$_3$H$_2$	$3_{3,0}-2_{2,1}$ (ortho)	216.27876	2.57×10^{-4}	19	2.0×10^8
c-C$_3$H$_2$	$6_{0,6}-5_{1,5}$ (para)	217.82215	5.37×10^{-4}	39	8.7×10^7
c-C$_3$H$_2$	$5_{1,4}-4_{2,3}$ (ortho)	217.94005	3.98×10^{-4}	35	6.3×10^7
c-C$_3$H$_2$	$5_{2,4}-4_{1,3}$ (para)	218.16046	4.07×10^{-4}	35	9.0×10^7
c-C$_3$H$_2$	$7_{2,6}-7_{1,7}$ (para)	218.73273	8.91×10^{-5}	61	2.9×10^7
c-C$_3$H$_2$	$4_{3,2}-3_{2,1}$ (ortho)	227.16914	3.09×10^{-4}	29	2.8×10^7
HC$_3$N	$J=24-23$	218.32472	8.32×10^{-4}	131	4.7×10^7
HC$_3$N	$J=25-24$	227.41891	9.33×10^{-4}	142	1.2×10^7
HC$_3$N	$J=26-25$	236.51279	1.05×10^{-3}	153	3.2×10^7

[a] Values from the CDMS database (Müller et al. 2001). [b] Calculated values for a collisional temperature of 30 K and collisional rates from the Leiden Atomic and Molecular Database (LAMDA; Schöier et al. 2005). [c] For a collisional temperature of 60 K. [d] CN transitions with A_{ij} higher than 1×10^{-5} s^{-1}. The references for collisional rates of specific species are presented in the Appendix.

In the Rayleigh-Jeans limit of the spectrum, the sub-millimeter flux (F_ν) has a power-law dependence with the frequency, i.e., $F_\nu \propto \nu^\alpha$, where α is the slope of the sub-mm spectral energy distribution (SED) and is related with the dust opacity spectral index (β) by $\alpha = \beta + 2$ (e.g., Beckwith & Sargent 1991; Testi et al. 2014). By fitting a power law distribution to the integrated fluxes from Table 6.2 and the 0.87 mm value from Artur de la Villarmois et al. (2018), an α index of 2.8 ± 0.3 is found, and $\beta = 0.8 \pm 0.3$. The typical β-value of the interstellar medium (ISM) is ∼1.7 (Natta et al. 2007), therefore, a lower value suggests grain growth or optically thick dust emission. This is consistent with the results from Jørgensen et al. (2007), where they found an α index between 2 and 3 for a sample of Class 0 protostars.

6.4.2 Molecular transitions

The observations covered multiple molecular transitions, such as CO isotopologues, S-bearing species, deuterated species, and carbon-chain molecules. The detected transitions are listed in Table 6.3 with their spectroscopic parameters, while the lines without detection above a 3σ level are listed in Table 6.4 in the Appendix.

6.4.2.1 CO isotopologues

The CO emission is shown in Fig. 6.1 for different ranges of velocities. Most of the CO emission is expected to be extended and thus, filtered out by the interferometer due to the lack of short spacings. By comparing APEX data (Lindberg et al. 2017) with convolved SMA $C^{18}O$ emission (see Fig. 6.12 and Table 6.5 in the Appendix), the recovered $C^{18}O$ flux with the SMA is less than 1%. Since CO is the more abundant isotopologue, and its emission is expected to be more extended than $C^{18}O$, the filtering out of emission is more significant for CO and thus, the recovered CO flux is expected to be much lower than 1%. This implies that the SMA observations are probing the deepest and denser regions, and the detected CO emission in Fig. 6.1 is tracing the more compact structures. The emission is centred at the position of the system, probing outer-envelope material, and knot-like structures are detected in red-shifted emission between 1 and 2 km s^{-1} and blue-shifted emission between 3 and 4 km s^{-1}, which are consistent with the outflow direction found by Bontemps et al. (1996) (see upper-left panel of Fig. 6.1).

Emission from ^{13}CO, $C^{18}O$ and $C^{17}O$ is shown in Fig. 6.2. ^{13}CO presents a flatted shape that follows the circumbinary disk structure and extends beyond it. $C^{18}O$ follows a similar distribution as
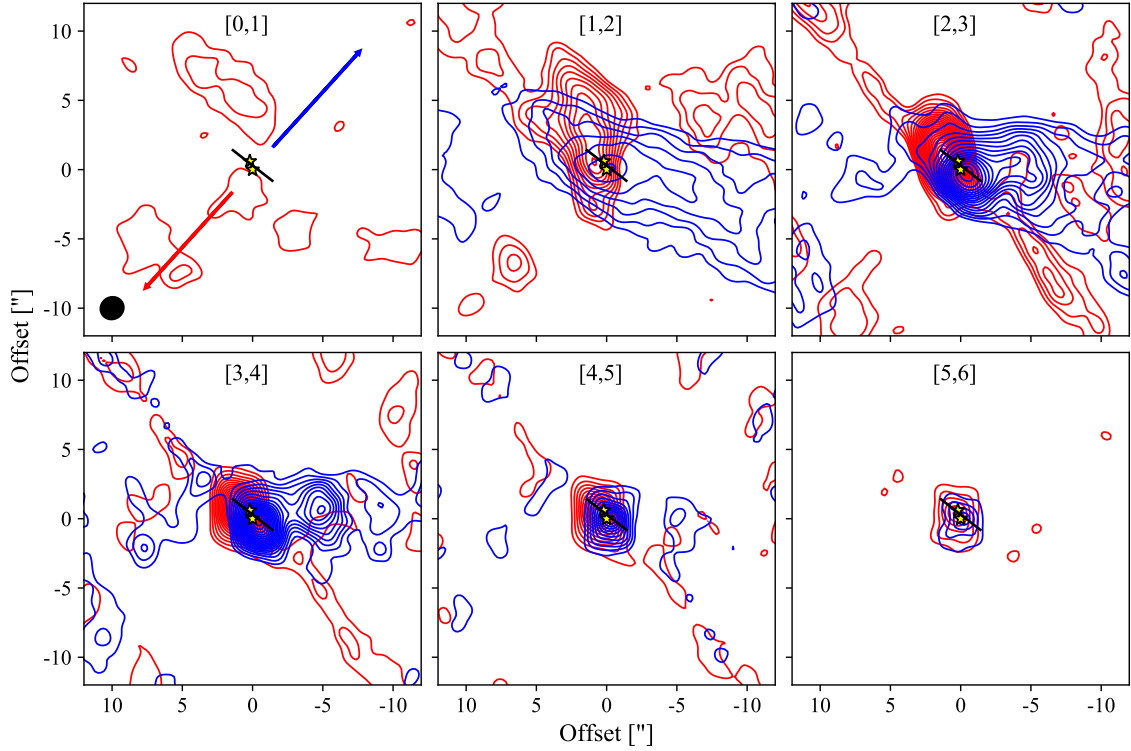
Figure 6.1: CO emission above 5σ (σ = 0.04 Jy beam^{-1} km s^{-1}). The contours start at 5σ and follow a step of 5σ. The numbers in brackets indicate the velocity interval in units of km s^{-1} and the extent of the circumbinary disk is represented by the black solid segment. The yellow stars show the position of the sources. The synthesised beam and the outflow direction from Bontemps et al. (1996) are represented in the upper-left panel with a black filled ellipse and blue and red arrows, respectively.

^{13}CO, and C^{17}O stands out towards the southern part of the disk. Another C^{17}O transition (J=3−2) was analysed by Artur de la Villarmois et al. (2018), where the emission traces the Keplerian circumbinary disk, therefore, the differences seen between C^{17}O J=3−2 and C^{17}O J=2−1 may be related with the sensitivity of the observations. A rotational profile perpendicular to the outflow direction is clearly seen for ^{13}CO and C^{18}O for velocities beyond ±2 km s^{-1}.

6.4.2.2 Sulphur-bearing species

Emission of CS and the brightest SO transition ($6_5−5_4$) is also shown in Fig. 6.2. The high dipole moment of CS makes this molecule a very good high-density tracer (e.g., van der Tak et al. 2000). Its emission shows a large extent ($\sim 10''$) and peaks at the edges of the circumbinary disk, showing a rotational profile around the binary system. SO shows a more compact distribution than CS, tracing the circumbinay disk material. SO $6_5−5_4$ is slightly brighter than SO $5_5−4_4$ (see Fig. 6.8 in the Appendix) and a third SO transition ($1_2−2_1$) was also targeted, however, no emission is detected

above a 3σ level. This may be related with its low A_{ij}, which is two orders of magnitude lower than the value from the detected SO transitions (see Tables 6.3 and 6.4 in the Appendix).

Less abundant CS isotopologues, such as $C^{34}S$ and ^{13}CS, are shown in Fig. 6.9 in the Appendix, where $C^{34}S$ is more than a factor of two brighter than ^{13}CS, in agreement with their relative abundances with respect to CS ($^{32}S/^{34}S=22$ and $^{12}C/^{13}C=69$; Wilson 1999). $C^{34}S$ follows the CS emission, where both species peak at the edges of the circumbinary disk. ^{13}CS, on the other hand, presents isolated peaks without a clear correlation with the main isotopologue, however, the emission has a low signal-to-noise level ($\leq 4\sigma$).

6.4.2.3 H_2CO

The observations include six H_2CO transitions, associated with E_u values from 21 to 280 K. The transitions with the highest E_u (174 and 280 K) are not detected (see Table 6.4) and the strongest lines are o-H_2CO $3_{1,2}-2_{1,1}$ ($E_u = 33$ K) and p-H_2CO $3_{0,3}-2_{0,2}$ ($E_u = 21$ K), shown in Fig. 6.2. The emission extends beyond the circumbinary disk structure, peaks towards the edges of the disk, and the intensity decreases towards the positions of the protostars. This is similar to what is seen for CS, however, the H_2CO emission stands out towards the southern part of the circumbinary disk and the peak is slightly south from the disk. It is interesting to notice that the southern part of the disk is related with blue-shifted emission, while the blue component of the outflow is seen towards the north-west.

Two H_2CO transitions ($3_{2,2}-2_{2,1}$ and $3_{2,1}-2_{2,0}$) show weak emission and are presented in Fig. 6.9 in the Appendix. Their emission do not follow the distribution from the brightest H_2CO transition ($3_{1,2}-2_{1,1}$), however, both of them are associated with higher E_u values of 68 K. As previously shown (e.g., Mangum & Wootten 1993), and further discussed in Section 4.1, the intensity ratios of these specific H_2CO transitions are sensitive tracers of the gas kinetic temperature and density.

6.4.2.4 Carbon-chain molecules

The C_3H_2 molecule has two isomeric forms: cyclic (c-C_3H_2) and linear (l-C_3H_2). Although standard astrochemical models predict a cyclic-to-linear C_3H_2 ratio of ~1, observations show higher values ranging from 3 to 70 (Sipilä et al. 2016). Our observations targeted nine c-C_3H_2 transitions, with E_u between 19 and 87 K, and three l-C_3H_2 transitions, with E_u between 66 and 80 K (see Tables 6.3 and 6.4). However, the linear isomer is not detected. Figure 6.2 shows the brightest c-C_3H_2 transition,
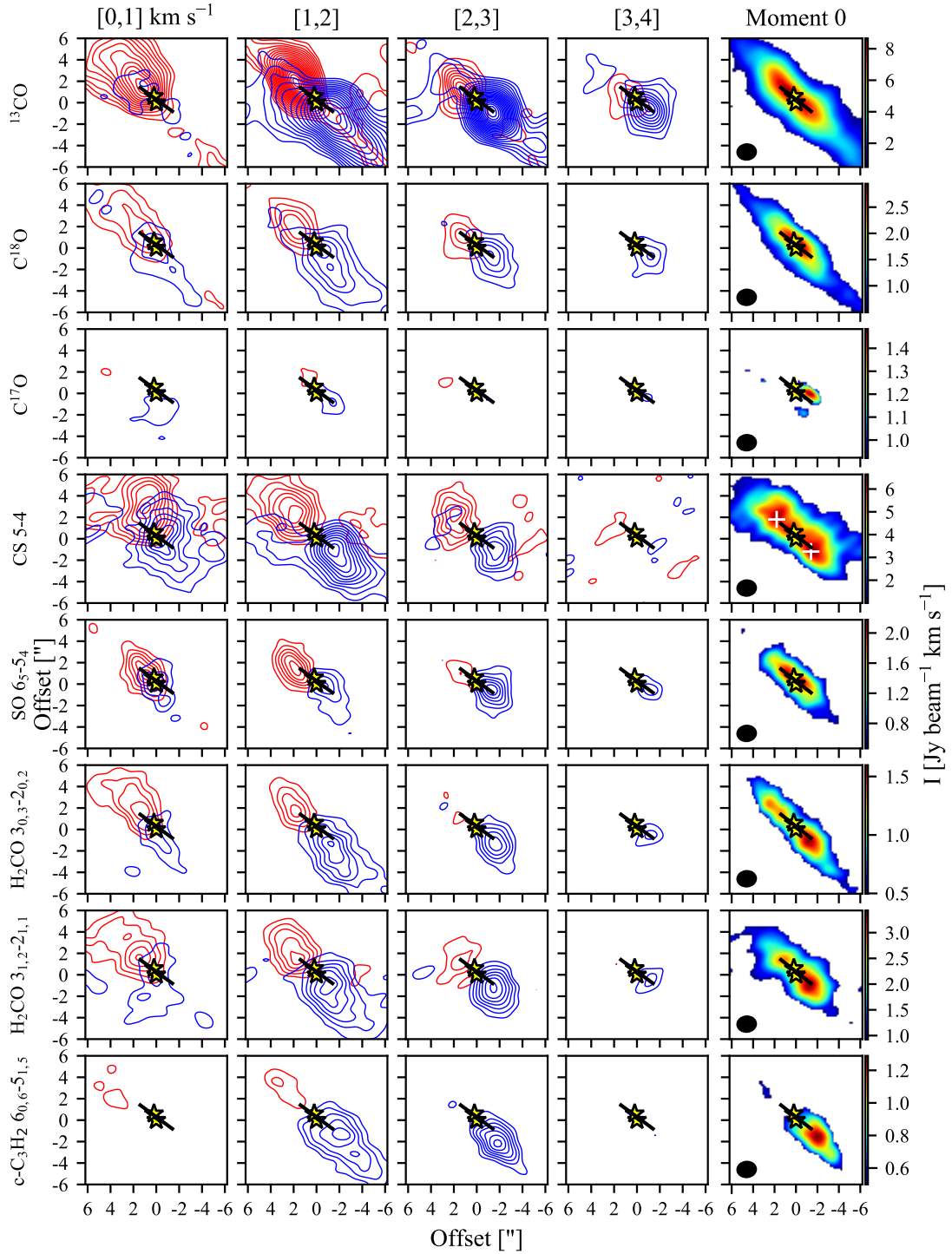
Figure 6.2: Emission of CO isotopologues and other bright molecular transitions. Channel maps consist of velocity ranges of 1 km s^{-1} and moment 0 maps are integrated over a velocity range of 8 km s^{-1}. The contours start at 5σ and follow a step of 5σ for ^{13}CO, C^{18}O, and CS (the remaining follow a step of 3σ). The two white crosses in the CS moment 0 map indicate the position from which the spectra from Figs. 6.4 and 6.5 are extracted. The yellow stars show the position of the sources and the solid segment represents the extension of the circumbinary disk. The synthesised beam is represented by a black filled ellipse in the right panels.

where the emission stands out between -3 and -1 km s^{-1} and peaks south from the circumbinary disk. Other three c-C$_3$H$_2$ lines present weaker emission and are shown in Fig. 6.10 in the Appendix.

The brightest c-C$_3$H$_2$ transition ($6_{0,6}-5_{1,5}$) was also detected with APEX by Lindberg et al. (2017) (see Appendix), and more than 92% of the flux is filtered out by the interferometer, suggesting that the c-C$_3$H$_2$ distribution is much more extended than what is seen in Fig. 6.2. In addition, c-C$_3$H$_2$ is the only transition in the APEX data that peaks at 2.9 km s^{-1}, and not at 4.2 km s^{-1} like the rest of the detected molecular transitions (DCO$^+$, H$_2$CO, C^{18}O, and SO). The velocity of 2.9 km s^{-1} is consistent with the blue-shifted material detected in the SMA observations, where the c-C$_3$H$_2$ emission stands out between -3 and -1 km s^{-1} with respect to the binary system velocity.

Three HC$_3$N transitions are detected and shown in Fig. 6.10 in the Appendix. The emission peaks south of the circumbinary disk, which is consistent with the c-C$_3$H$_2$ emission, suggesting that this region is rich in carbon-chain molecules. On the other hand, the HC$_3$N J=24$-$23 transition was observed with APEX, but not detected, therefore, the emission may arise from a compact component (i.e., the emission is suffering from beam dilution).

6.4.2.5 CN

CN is know as a Photon Dominated Region (or PhotoDissociation Region, PDR) tracer, since its abundance increases when HCN photodissociates into CN due to ultraviolet (UV) radiation from the star or the interstellar radiation field (Willacy & Langer 2000; Aikawa & Herbst 2001; van Zadelhoff et al. 2003). Although gas-phase CN is expected to be abundant towards protostars, it is often challenging to observe with interferometers at millimeter wavelengths as it typically is extended and filtered out (e.g., Jørgensen et al. 2011). Toward one Class 0 source, L483-mm, CN was found to probe material in the boundary between the bulk protostellar envelope and its outflow cavity (Jørgensen 2004). CN has also been detected towards a number of protostellar disks around Class II sources (e.g., Dutrey et al. 1997; Qi 2001; Thi et al. 2004; ?), where it is found to be a good tracer of the disk surfaces (e.g., van Dishoeck 2006).

Toward IRS67, ten of twelve hyperfine transitions from CN 2$-$1 (see Table 6.3) are detected. The emission of one of these hyperfine transitions is shown in Fig. 6.3. The brightest CN lines are blended with other CN hyperfine transitions and their moment 0 maps are shown in Fig. 6.11 in the Appendix. The CN emission stands out towards the southern region and peaks slightly offset from the southern edge of the circumbinary disk, which is consistent with the H$_2$CO peak (see Fig. 6.2).
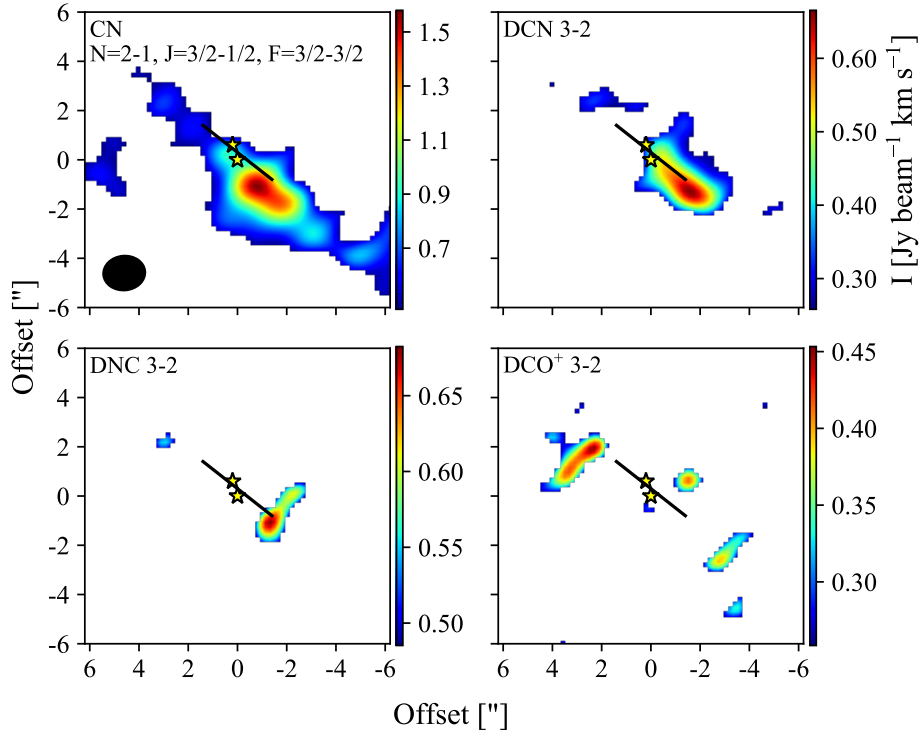
Figure 6.3: Deuterated species, DCN, DNC, and DCO⁺, moment 0 maps integrated over a velocity range of 6 km s⁻¹. The yellow stars show the position of the sources and the solid segment represents the extension of the circumbinary disk. The synthesised beam is represented by a black filled ellipse.

6.4.2.6   Deuterated species

Deuterated species are good tracers of cold regions, in particular, the outer disk midplane where the temperature is ≤ 30 K (e.g., van Dishoeck 2006; Jørgensen et al. 2011; Murillo et al. 2015; Öberg et al. 2015; Aikawa et al. 2018). The ion DCO⁺ is apparently formed in the gas phase, considering its short destruction timescale and is expected to be abundant in regions with temperature between 19 and 21 K (Aikawa et al. 2018). On the other hand, neutral species as DCN can form in interstellar ice and later desorb in the disk, thus tracing regions with higher temperatures than DCO⁺ (≥ 30 K; Jørgensen et al. 2004; Aikawa et al. 2018). Emission of DCN, DNC, and DCO⁺ is detected and shown in Fig. 6.3. Both DCN and DNC peak towards the southern edge of the protobinary disk, which is consistent with the CN peak, while DCO⁺ stands out close to the northern edge of the disk and no emission is detected where DCN and DNC peak.

6.4.2.7 Spectra

Figure 6.4 shows the spectra of the species presented in Figs. 6.2 and 6.3, towards three different positions: the geometric centre and the blue- and red-shifted peaks from the CS emission, located at 2″ and 2.4″ from the geometric center, respectively (see white crosses in the moment 0 map of CS in Fig. 6.2). CO and ^{13}CO show a clear absorption future at the system velocity (4.2 km s^{-1}), mainly due to the interferometric filtering-out of emission from large scales. $C^{18}O$, CS, SO and the two brightest H_2CO transitions present similar spectral features, with prominent emission between -3 and 3 km s^{-1} and a considerably symmetry between the blue- and red-shifted components. These components are tracing the edges of the circumbinary disk, peak around ± 2 km s^{-1} and are consistent with a rotational profile. This is in agreement with the results from Artur de la Villarmois et al. (2018), where velocities below ± 2.5 km s^{-1} are expected at a distance of 2″ from the geometric center and beyond. On the other hand, c-C_3H_2, DCN, DNC, and HC_3N show strong emission towards the southern edge of the circumstellar disk (blue spectra), with a peak around -2 km s^{-1}, tracing a different component than the CO isotopologues, CS, SO and H_2CO.

Since the observations include multiple CN hyperfine transitions, their spectra are shown in Fig. 6.5, covering a frequency range from 226.356 to 226.896 GHz. The spectra of isolated lines show an absorption feature at the system velocity, consistent with filtering-out of emission from large scales. This agrees with the results from Jørgensen et al. (2011), where the CN emission may be tracing the outer envelope towards IRAS 16293-2422 and is filtered out by the SMA. Nevertheless, towards IRS 67 the CN emission peaks at the southern edge of the circumbinary disk, with velocities around -2 km s^{-1}. The CN spectra resemble the one from c-C_3H_2 (Fig. 6.4), suggesting that both species are tracing the same material.

6.5 Discussion

6.5.1 The structure of IRS 67

The ratio between H_2CO $3_{0,3}-2_{0,2}$ and H_2CO $3_{2,2}-2_{2,1}$ has previously been shown to be a good tracer of the gas temperature (Mangum & Wootten 1993). Figure 6.6 shows the estimated gas temperature for a H_2 number density $\geq 10^8$ cm^{-3}, following those results. The highest temperatures (≥ 90 K) are seen towards the outflow direction, while the southern edge of the circumbinary disk is associated
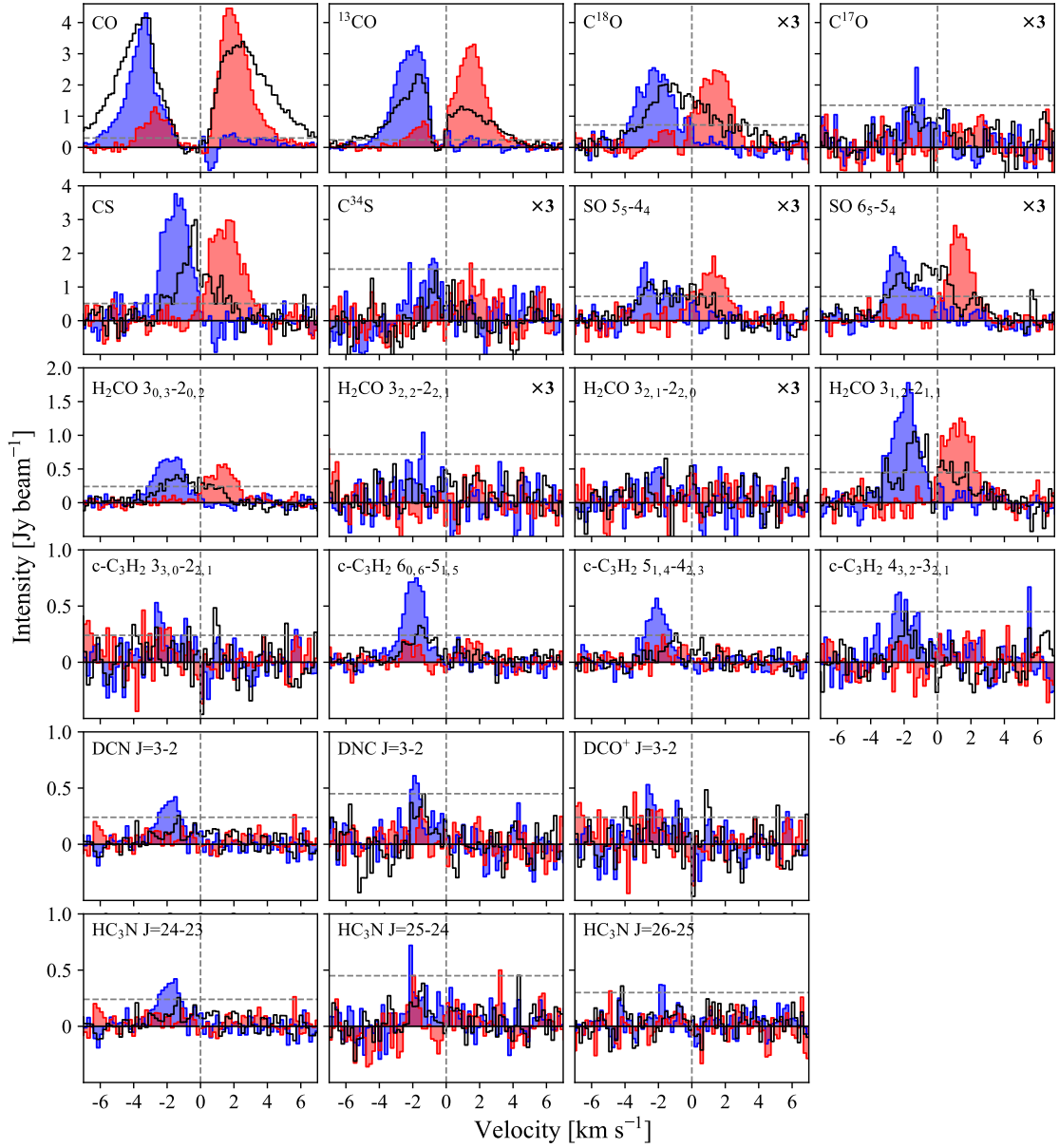
Figure 6.4: Spectra of the brightest molecular transitions (with the exception of CN) taken at three different positions: the geometric center (black), the southern edge (blue), and the northern edge of the circumbinary disk (red; see white crosses in the moment 0 map of CS in Fig. 6.2). The zero velocity value (dashed grey vertical line) corresponds to a system velocity of 4.2 km s^{-1}. The dashed grey horizontal line shows the value of 3σ (see Table 6.1). Some of the spectra are multiplied by a factor of 3, as indicated in the top right corner.
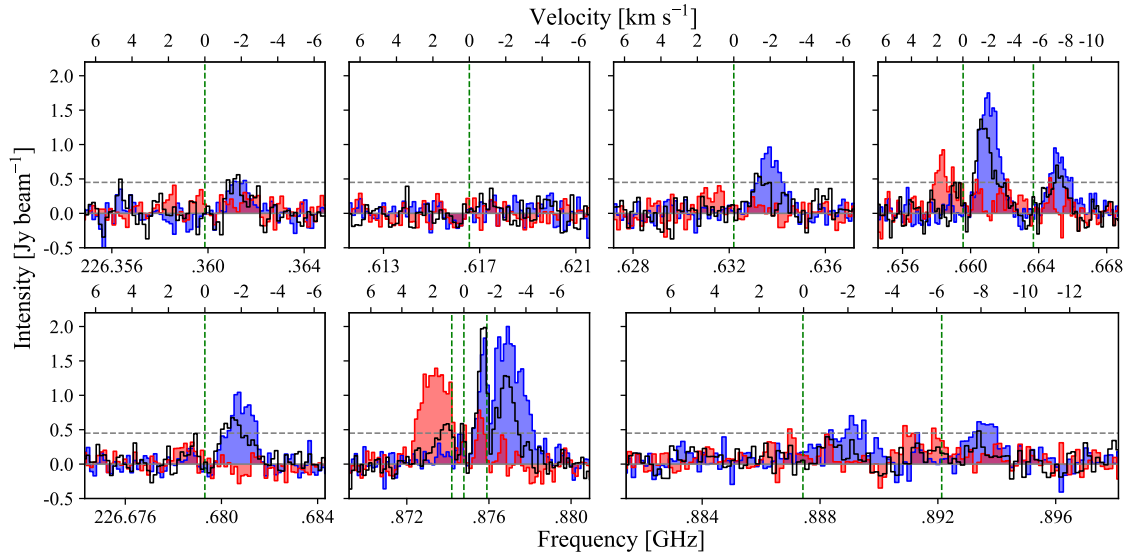
Figure 6.5: CN spectra taken at three different positions: the geometric center (black), the southern edge (blue), and the northern edge of the circumbinary disk (red; see white crosses in the moment 0 map of CS in Fig. 6.2). The dashed green vertical lines represent the rest frequency of the CN hyperfine transitions (see Table 6.3), while the dashed grey horizontal line shows the value of 3σ.

with temperatures between 50 and 60 K. This is the region where the peak of emission is seen for DCN, DNC, CN, c-C_3H_2, and HC_3N, suggesting that these species are tracing high densities ($n_{H_2} \geq 10^8$ cm^{-3}) and lukewarm temperatures (50−60 K). The non-detection of H_2CO $3_{2,2}-2_{2,1}$ where H_2CO $3_{0,3}-2_{0,2}$ is detected sets an upper limit of 50 K for the gas temperature (grey region in Fig. 6.6).

CN and c-C_3H_2 are commonly used as PDR tracers, since their emission shows a strong dependence on the UV radiation (e.g., Dutrey et al. 1997; van Dishoeck 2006; **?**; Bergin et al. 2016; Murillo et al. 2018). The circumbinary disk associated with IRS 67 may be strongly illuminated by UV radiation from the binary system and, because disks are normally flared, is it likely that the southern region of the circumbinary disk is associated with a PDR, in particular, the surface layer of the circumbinary disk. Other common PDRs originate along the outflow cavity (e.g., Murillo et al. 2018), however, this is unlikely for IRS 67 since the blue-shifted outflow component is seen towards the north-west, and blue-shifted emission from c-C_3H_2 is detected towards the south-east. The PDR originating at the surface layer of the circumbinary disk is also consistent with the temperature structure estimated from the H_2CO $3_{0,3}-2_{0,2}/3_{2,2}-2_{2,1}$ ratio (see Fig. 6.6).

The northern part of the circumbinary disk seems to be related with colder regions than the southern part (see Fig. 6.6). DCO$^+$ is expected to trace cold regions ($\leq$30 K; Jørgensen et al. 2011; Aikawa et al. 2018) and its emission peaks towards the north-east of the circumbinary disk (Fig. 6.3), showing
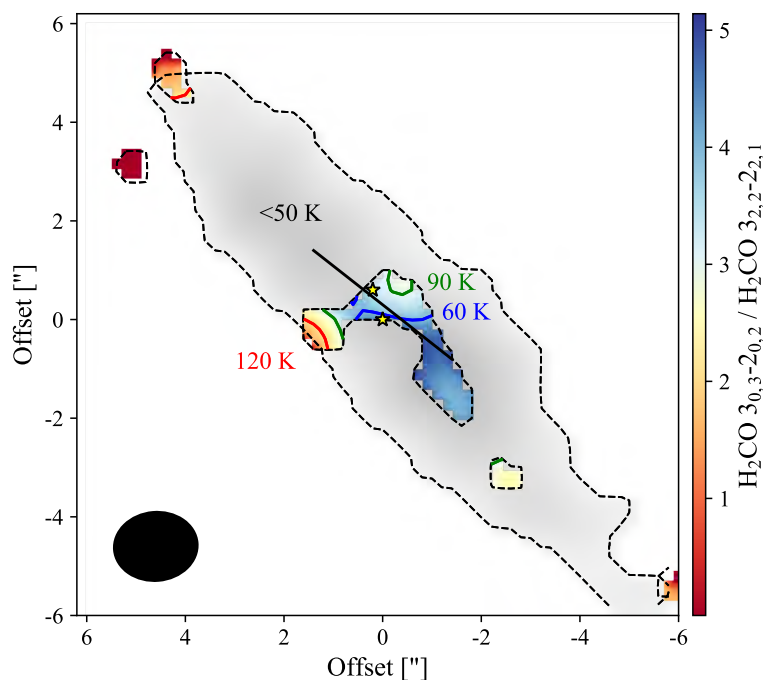
Figure 6.6: Gas temperature estimation from the ratio between o-H$_2$CO $3_{0,3}-2_{0,2}$ and o-H$_2$CO $3_{2,2}-2_{2,1}$, following the results from Mangum & Wootten (1993). Specific values of 60, 90, and 120 K are shown in blue, green, and red contours, respectively. The grey region, where o-H$_2$CO $3_{2,2}-2_{2,1}$ is not detected, indicates temperatures below 50 K. The yellow stars show the position of the sources and the solid segment represents the extension of the circumbinary disk. The synthesised beam is represented by a black filled ellipse.

an anticorrelation with the PDR tracers (mainly CN and c-C$_3$H$_2$). The DCO$^+$ emission seems to be associated with cold regions from the inner envelope at small scales ($\leq$1000 AU), however, the same DCO$^+$ transition was detected with APEX (see Fig. 6.12 in the Appendix), suggesting that more than 96% of the emission is filtered out by the interferometer. Therefore, DCO$^+$ is expected to be present also at large scales (e.g., Jørgensen et al. 2011; Murillo et al. 2018).

IRS 67 is particularly rich in molecular lines when it is compared with other single Class I sources (Artur de la Villarmois et al. 2019, subm.), possibly due to the mass content and extent of the circumbinary disk. One of the species that is only detected towards IRS 67, among other 11 Class I sources, is c-C$_3$H$_2$, where two transitions ($5_{5,1}-4_{4,0}$ and $5_{5,0}-4_{4,1}$) are seen (Artur de la Villarmois et al. 2018) and the emission is consistent with the c-C$_3$H$_2$ lines analysed in this work. c-C$_3$H$_2$ may, therefore, be related with PDRs (like outflow cavities and disk surface layers) but also with high gas column densities expected towards Class 0 sources and the binary system IRS 67. This agrees with the non-detection of c-C$_3$H$_2$ towards a sample of 12 Class II disks (Öberg et al. 2010; **?**).

6.5.2 The non-detections

Together with the detection of multiple molecular transitions, the non-detections may provide some clues about the physical parameters of the region. The main non-detections at the 3σ level are N_2D^+, the linear isomer l-C_3H_2, SiO, and CH_3OH.

N_2D^+ is a good tracer of cold regions (≤ 30 K), where CO freezes out, and usually correlates with DCO^+ (e.g., Jørgensen et al. 2011; Aikawa et al. 2018; Murillo et al. 2018). Since most of the DCO^+ is filtered out by the interferometer and its emission is expected to be present at large scales, N_2D^+ may also be present at large scales. Therefore, the non-detection of N_2D^+ may be related with the lack of short-spacings in the observations.

The non-detection of the linear C_3H_2 isomer may be related with the high cyclic-to-linear ratio or to an excitation effect, or a combination of both. The cyclic-to-linear ratio has been proven to differ from the statistical value of 1 for a variety of objects, ranging from 3 to 70 (Sipilä et al. 2016). On the other hand, the three l-C_3H_2 transitions covered in the observations have E_u values between 66 and 80 K, while the brightest c-C_3H_2 line (see Fig. 6.2) has $E_u = 39$ K. In addition, c-C_3H_2 $7_{2,6}-7_{1,7}$ ($E_u = 61$ K) shows weak emission and two c-C_3H_2 lines with $E_u = 87$ K are not detected. This sets an upper limit of 60 K for the excitation temperature of the c-C_3H_2 emitting region. Therefore, a combination of both, high cyclic-to-linear ratio and an excitation effect, may explain the non detection of the linear C_3H_2 isomer.

SiO is typically seen as a good tracers of shocks as it is present in the gas-phase when refractory grains are destroyed (e.g., Bachiller & Perez Gutierrez 1997; Codella et al. 2014; Gusdorf et al. 2008b,a). Its non-detection towards IRS 67 is consistent with other studies suggesting that Class I sources are associated with less energetic outflows.

6.5.3 Chemical differentiation around IRS 67

Figure 6.7 shows a schematic representation of the environment associated with IRS 67, where three main regions are distinguished: (*i*) a cold region ($T \leq 30$ K) beyond the extension of the circumbinary disk, traced by DCO^+, (*ii*) the circumbinary disk traced by CO isotopologues and sulphur-bearing species, and (*iii*) a PDR, likely the surface layer of the circumbinary disk reached by the UV radiation from the binary system, and traced by CN, DCN, and carbon-chain molecules.

The chemistry towards IRS 67 shows some similarities with Class 0 sources, possibly due to the
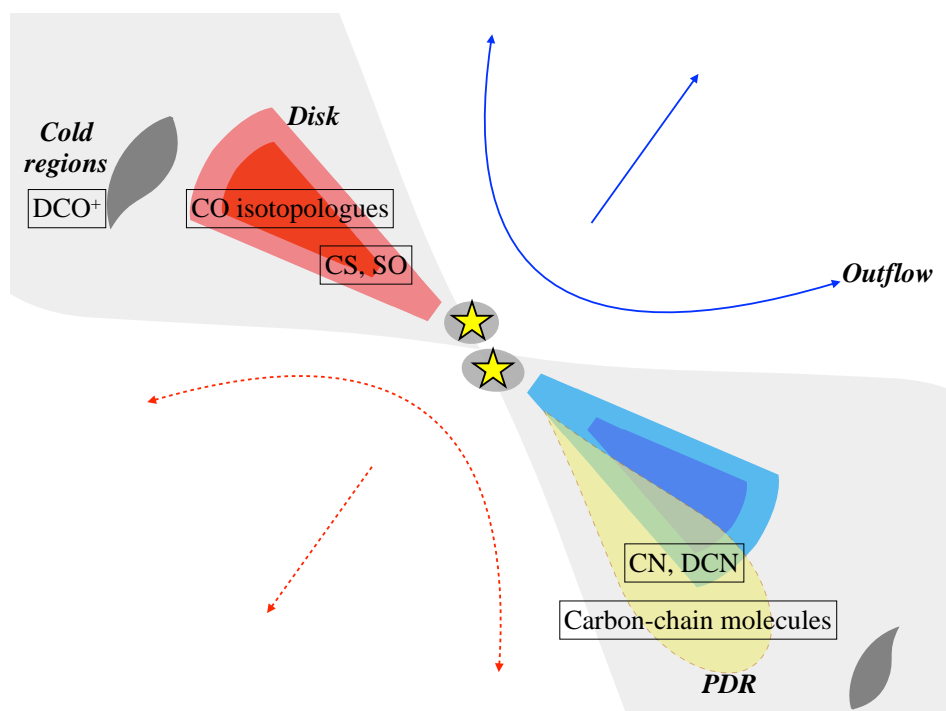
Figure 6.7: Schematic representation of the environment towards IRS 67 where three main regions are distinguished. Cold regions traced by DCO$^+$, the disk structure proben by CO isotopologues and S-bearing species, and a PDR associated with the surface layers of the disk, traced by CN, DCN and carbon-chain molecules. The outflow direction is taken from Bontemps et al. (1996).

high-gas column density, and with Class II disks, where the UV radiation from the binary system may resemble the interaction between a typical T Tauri star and the surface layers of its disk. Cold gas tracers (such as DCO$^+$ and DCN), potential grain chemistry products (such as H$_2$CO), and species associated with carbon-chain chemistry (such as c-C$_3$H$_2$ and HC$_3$N), are commonly detected towards Class 0 sources (e.g., Jørgensen et al. 2005b; Murillo et al. 2018) and are also detected towards IRS 67. However, while H$_2$CO and c-C$_3$H$_2$ are mainly seen at the outflow cavities towards Class 0 sources, towards IRS 67 they seem to be tracing the surface layers of the circumbinary disk. On the other hand, photochemistry products such as CN are abundant towards more evolved disks, associated with Class II sources (e.g., Öberg et al. 2010; **?**): CN will originate in the outer, very low density part of the disk, which is completely exposed to UV radiation. The binary system IRS 67 may be associated with a stronger UV radiation field than single Class I sources, therefore, the CN emission towards IRS 67 appears to be tracing the same physical component as in Class II sources, i.e., the surface layers of the disk exposed to UV radiation. Future observations of other Class I binary sources will verify if the chemical richness of IRS 67 is common towards these stages, and higher angular resolutions will constrain the velocity profile and the dynamics of the detected transitions.

6.6   Summary

This work presents SMA observations of the Class I binary system IRS 67 in the Ophiuchus star forming region, with an angular resolution of $1.''7 \times 1.''4$ ($\sim 260 \times 210$ AU). The continuum emission between 1.2 and 1.4 mm is analysed, together with multiple molecular transitions that trace different physics. The main results are summarised below.

- The continuum emission is consistent with previous studies (Artur de la Villarmois et al. 2018) and a power-law fitting results in a β-value of 0.8 ± 0.3, suggesting that dust grains have grown to larger sizes than the ISM dust particles, or that the dust is optically thick.

- The detected molecular transitions are tracing three main regions: cold regions beyond the circumbinary disk extension, the circumbinary disk, and a PDR likely related with the surface layers of the disk. DCO^+ is tracing the cold regions, while the CO isotopologues and the sulphur-bearing species are probing the disk structure. In addition, CN, DCN, and carbon-chain molecules are tracing the PDR.

- A particular case is seen for H_2CO, which traces both the circumbinary disk and the PDR. The ratio between o-H_2CO $3_{0,3}-2_{0,2}$ and o-H_2CO $3_{2,2}-2_{2,1}$ has been shown to be a good indicator of the gas temperature, where the temperature map is consistent with the physical structure of IRS 67, i.e., the warmer gas follows the outflow direction, lukewarm temperatures are associated with the PDR, and colder gas is related to the circumbinary disk.

- IRS 67 shows chemical similarities with Class 0 sources, such as the detection of sulphur-bearing species and carbon-chain molecules, while PDR tracers, such as CN, are associated with Class II disks, where the UV radiation can reach the surface layers of the disk. IRS 67 is, therefore, a chemical link between these two stages.

This work shows the potential of the broad spectral coverage of the SMA, allowing us to detect and analyse multiple molecules and transitions from the same species. Similar observations of other Class I sources will provide more statistical results and highlight if IRS 67 is a particular chemically-rich system or it represents a general trend. In addition, higher angular resolution observations will constrain the dynamics of the gas and possibly resolve the individual circumstellar disks around each source, constraining the link between circumstellar and circumbinary disks.

Acknowledgements

6.7   Appendix

6.7.1   Other molecular transitions

Other transitions and less abundant isotopologues of the species discussed in Sect. 3.2 show weaker emission and are presented in Figs. 6.9, 6.8, and 6.10. In addition, the brightest CN hyperfine transitions are blended with other CN lines (see Fig. 6.5) and their emission is shown in Fig. 6.11.

6.7.2   Non-detections

Within the covered molecular transitions, the non-detected lines at the 3σ level are listed in Table 6.4 with their spectroscopic parameters. The collisional rates of specific species listed Tables 6.3 and 6.4 were taken from the following sources: CO isotopologues from Yang et al. (2010), H_2CO and H_2CS from Wiesenfeld & Faure (2013), CH_3OH from Rabli & Flower (2010), DCO^+ and N_2D^+ from Flower (1999), DCN and DNC from Dumouchel et al. (2010), CS isotopologues and SO from Lique et al. (2006), SO_2 from Balança et al. (2016), OCS from Green & Chapman (1978), H_2S from Daniel et al. (2011), CN from Kalugina & Lique (2015), C_3H_2 from Chandra & Kegel (2000), HC_3N from Faure et al. (2016), SiO from Dayou & Balança (2006), HDO from Faure et al. (2012), and HNCO from Sahnoun et al. (2018).
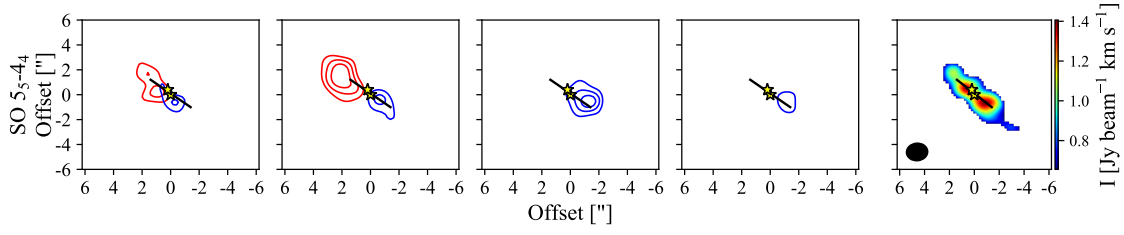
Figure 6.8: Emission of SO 5_5-4_4. Channel maps consist of velocity ranges of 1 km s^{-1} and the moment 0 map is integrated over a velocity range of 8 km s^{-1}. The contours start at 3σ and follow a step of 3σ. The yellow stars show the position of the sources and the solid segment represents the extension of the circumbinary disk. The synthesised beam is represented by a black filled ellipse in the right panel.
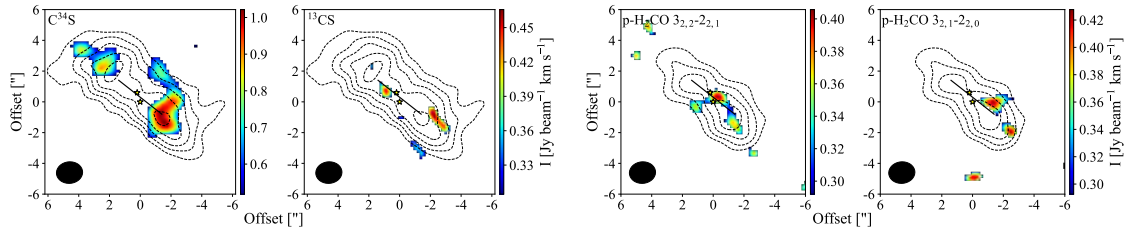
Figure 6.9: C^{34}S, ^{13}CS, and H$_2$CO ($E_u = 68$ K) moment 0 maps (colour scale) integrated over a velocity range of 6 km s^{-1}, overlapped with CS emission (contours in C^{34}S and ^{13}CS maps) and H$_2$CO $3_{1,2}-2_{1,1}$ (contours in H$_2$CO maps) from Fig. 6.2. The yellow stars show the position of the sources and the solid segment represents the extension of the circumbinary disk. The synthesised beam is represented by a black filled ellipse.

6.7.3 APEX data

IRS 67 was observed with APEX (Lindberg et al. 2017) around 220 GHz and with an angular resolution of 29″. In order to compare SMA with APEX data, the SMA observations are convolved with a 29″ beam and the intensity unit (Jy beam^{-1}) is converted into Kelvin. Figure 6.12 shows a comparison between both dataset for five transitions, highlighting the strong filtering-out of extended emission by the interferometer. The APEX and SMA intensities are presented in Table 6.5, together with the percentage of emission that is filtered-out.

Table 6.4: Parameters of the non-detected molecular transitions.

Species	Transition	Frequency [a] [GHz]	A_{ij} [a] [s^{-1}]	E_u [a] [K]	n_{crit} [b] [cm^{-3}]
		CO- species			
p-H$_2$CO	$11_{2,9}-12_{0,12}$	215.97616	3.16×10^{-7}	280	3.3×10^4
o-H$_2$CO	$9_{1,8}-9_{1,9}$	216.56865	7.24×10^{-6}	174	2.1×10^5
CH$_3$OH	$5_{0,5}-4_{0,4}$	241.70022	6.03×10^{-5}	48	1.7×10^6
CH$_3$OH	$5_{0,5}-4_{0,4}^{++}$	241.79143	6.03×10^{-5}	35	4.6×10^5
CH$_3$OH	$5_{1,4}-4_{1,3}$	241.87907	6.03×10^{-5}	56	1.5×10^7
CH$_3$OH	$5_{1,4}-4_{1,3}^{--}$	241.91583	6.03×10^{-5}	50	5.5×10^7
		S- species			
SO	1_2-2_1	236.45229	1.41×10^{-6}	16	4.0×10^4 [c]
SO$_2$	$11_{1,11}-10_{0,10}$	221.96522	1.15×10^{-4}	60	8.6×10^6 [d]
SO$_2$	$12_{3,9}-12_{2,10}$	237.06883	1.15×10^{-4}	60	1.1×10^8 [d]
SO$_2$	$5_{2,4}-4_{1,3}$	241.61580	8.51×10^{-5}	24	9.4×10^6 [d]
SO$_2$	$14_{0,14}-13_{1,13}$	244.25422	1.62×10^{-4}	94	1.2×10^7 [d]
OCS	$J=18-17$	218.90336	3.02×10^{-5}	100	8.2×10^5
OCS	$J=19-18$	231.06099	3.55×10^{-5}	111	1.3×10^6
OCS	$J=20-19$	243.21804	4.17×10^{-5}	123	3.5×10^5
p-H$_2$S	$2_{2,0}-2_{1,1}$	216.71044	4.90×10^{-5}	84	1.1×10^6
HCS	$6_{0,6}-5_{0,5}, J=13/2-11/2, F=7-6$	241.68929	1.20×10^{-5}	41	
HCS	$6_{0,6}-5_{0,5}, J=13/2-11/2, F=6-5$	241.69202	1.20×10^{-5}	41	
HCS	$6_{0,6}-5_{0,5}, J=11/2-9/2, F=6-5$	241.74108	1.17×10^{-5}	41	
HCS	$6_{0,6}-5_{0,5}, J=11/2-9/2, F=5-4$	241.74388	1.17×10^{-5}	41	
HSC	$6_{1,6}-5_{1,5}$	239.05112	4.27×10^{-4}	53	
HSC	$6_{2,5}-5_{2,4}$	243.32134	4.17×10^{-4}	94	
HSC	$6_{0,6}-5_{0,5}$	243.36604	4.68×10^{-4}	41	
HSC	$6_{2,4}-5_{2,3}$	243.52763	4.17×10^{-4}	94	
H$_2$CS	$7_{1,7}-6_{1,6}$	236.72702	1.91×10^{-4}	59	5.5×10^6
H$_2$CS	$7_{0,7}-6_{0,6}$	240.26687	2.04×10^{-4}	46	2.0×10^7
H$_2$CS	$7_{2,6}-6_{2,5}$	240.38205	1.91×10^{-4}	99	4.0×10^6
H$_2$CS	$7_{2,5}-6_{2,4}$	240.54907	1.91×10^{-4}	99	6.4×10^6
H$_2$CS	$7_{1,6}-6_{1,5}$	244.04850	2.09×10^{-4}	60	4.1×10^6
		Carbon-chain species			
N$_2$D$^+$	$3-2$	231.32186	7.08×10^{-4}	22	2.1×10^6 [e]
H$_2$CN	$3_{0,3}-2_{0,2}$	219.85186	3.39×10^{-4}	21	
H$_2$CN	$3_{1,2}-2_{1,1}$	227.43700	3.39×10^{-4}	34	
c-C$_3$H$_2$	$8_{2,6}-8_{1,7}$ (para)	218.44883	1.48×10^{-4}	87	6.7×10^7
c-C$_3$H$_2$	$8_{3,6}-8_{2,7}$ (ortho)	218.44944	1.48×10^{-4}	87	3.2×10^8
c-C$_3$H$_2$	$3_{2,1}-2_{1,2}$ (ortho)	244.22215	5.89×10^{-5}	18	1.2×10^7
l-C$_3$H$_2$	$11_{1,11}-10_{1,10}$	226.54857	1.07×10^{-3}	79	
l-C$_3$H$_2$	$11_{0,11}-10_{0,10}$	228.60835	1.12×10^{-3}	66	
l-C$_3$H$_2$	$11_{1,10}-10_{1,9}$	230.77801	1.15×10^{-3}	80	
C$_4$H	$N=23-22, J=47/2-45/2$	218.83701	4.47×10^{-5}	126	
C$_4$H	$N=23-22, J=45/2-43/2$	218.87537	4.47×10^{-5}	126	
C$_4$H	$N=24-23, J=49/2-47/2$	228.34862	5.13×10^{-5}	137	
C$_4$H	$N=24-23, J=47/2-45/2$	228.38696	5.13×10^{-5}	137	
C$_4$H	$N=25-24, J=51/2-49/2$	237.85974	5.75×10^{-5}	148	
C$_4$H	$N=25-24, J=49/2-47/2$	237.89806	5.75×10^{-5}	148	
		Others			
SiO	$J=5-4$	217.10498	5.25×10^{-4}	31	2.2×10^7
HDO	$3_{1,2}-2_{2,1}$	225.89672	1.32×10^{-5}	167	7.3×10^6
HDO	$2_{1,1}-2_{1,2}$	241.56155	1.17×10^{-5}	95	9.6×10^5
HNCO	$10_{0,10}-9_{0,9}$	219.79827	1.48×10^{-4}	58	4.4×10^8
HNCO	$11_{0,11}-10_{0,10}$	241.77403	1.95×10^{-4}	70	2.3×10^7

[a] Values from the CDMS database (Müller et al. 2001). [b] Calculated values for a collisional temperature of 30 K and collisional rates from the Leiden Atomic and Molecular Database (LAMDA; Schöier et al. 2005). [c] For a collisional temperature of 60 K. [d] For a collisional temperature of 100 K. [e] Calculated for N$_2$H$^+$.

Table 6.5: Comparison between APEX (Lindberg et al. 2017) and convolved SMA intensities.

Molecular transition	Intensity [K km s^{-1}]		Filtering [%] [a]
	APEX	SMA	
DCO$^+$ J=3−2	0.317	0.0125	96
c-C$_3$H$_2$ $6_{0,6}$−$5_{1,5}$	0.177	0.0137	92
p-H$_2$CO $3_{0,3}$−$2_{0,2}$	0.431	0.0036	99
C^{18}O J=2−1	3.198	0.0093	> 99
SO 6_5−5_4	0.316	0.0003	> 99

[a] Percentage of the emission filtered-out by the interferometer.
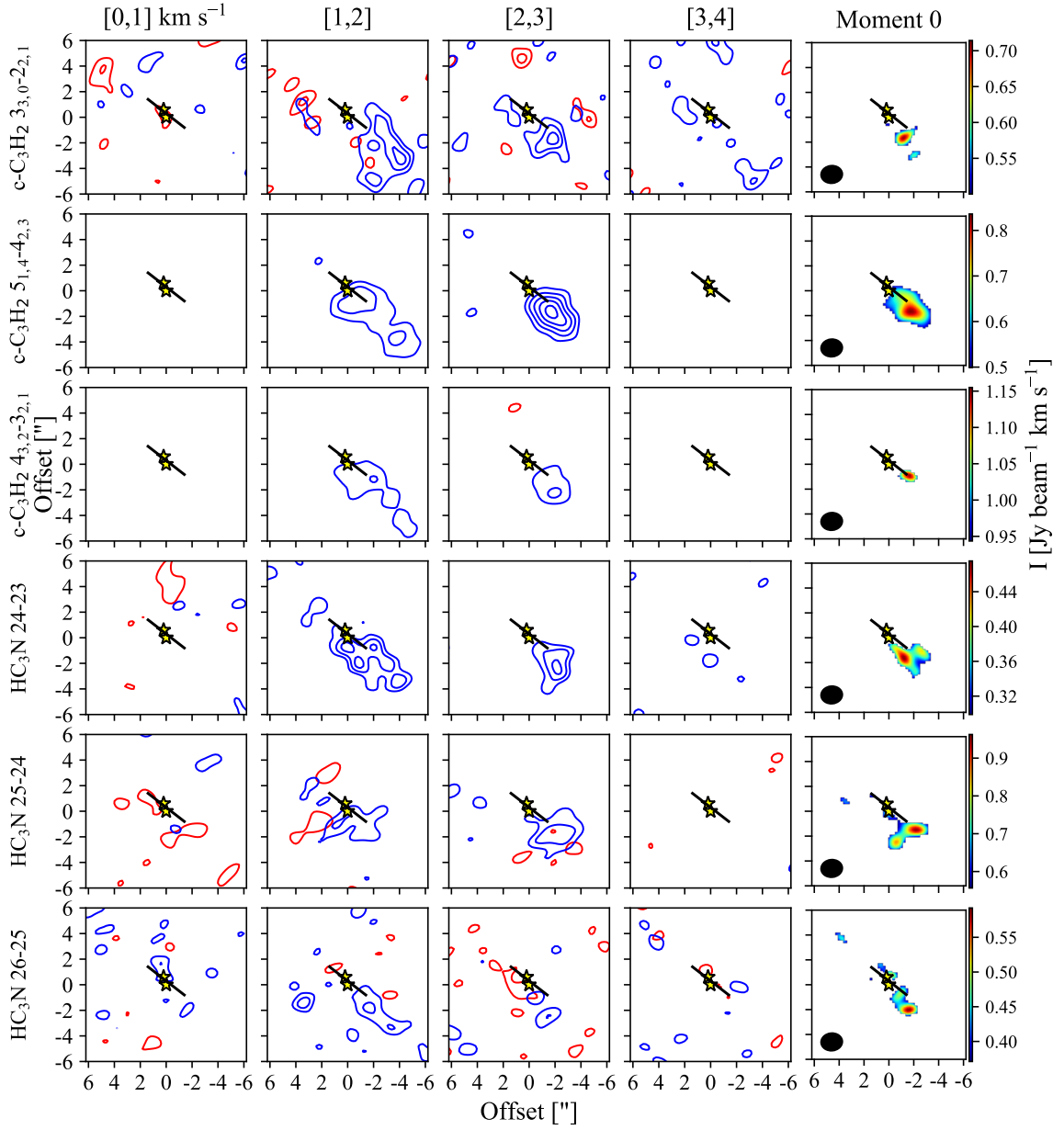
Figure 6.10: Emission of c-C$_3$H$_2$ and HC$_3$N. Channel maps consist of velocity ranges of 1 km s^{-1} and moment 0 maps are integrated over a velocity range of 8 km s^{-1}. The contours start at 3σ and follow a step of 3σ and 2σ for c-C$_3$H$_2$ and HC$_3$N, respectively. The yellow stars show the position of the sources and the solid segment represents the extension of the circumbinary disk. The synthesised beam is represented by a black filled ellipse in the right panels.
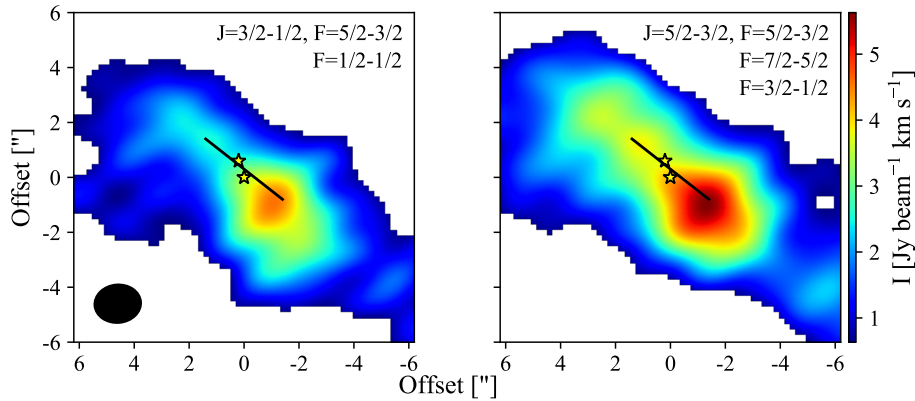
Figure 6.11: CN moment 0 maps of the brightest transitions, which are blended with other hyperfine lines. The integration is done over a velocity range of 11 and 8 km s^{-1} for the left and right panels, respectively. The yellow stars show the position of the sources and the solid segment represents the extension of the circumbinary disk. The synthesised beam is represented by a black filled ellipse in the left panel.
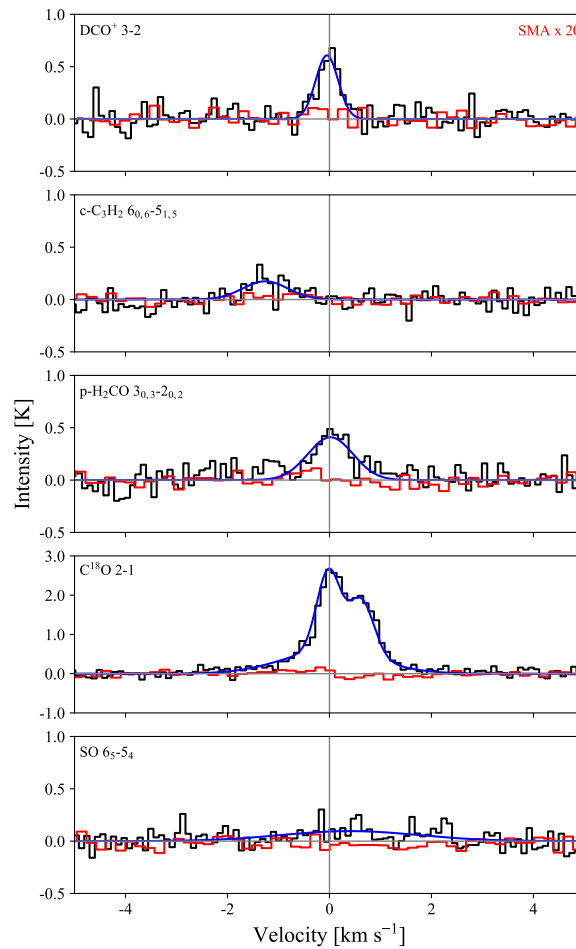
Figure 6.12: Spectra from APEX data (black) and convolved SMA data with a 29$''$ beam (red). For clarity, the SMA spectra are scaled with a factor of 20. The blue curve represents a Gaussian fit and, for C^{18}O, the curve shows the sum of three Gaussian components.

Bibliography

Aikawa, Y., Furuya, K., Hincelin, U., & Herbst, E. 2018, ApJ, 855, 119

Aikawa, Y. & Herbst, E. 2001, A&A, 371, 1107

Allen, L. E., Myers, P. C., Di Francesco, J., et al. 2002, ApJ, 566, 993

ALMA Partnership, Brogan, C. L., Pérez, L. M., et al. 2015, ApJL, 808, L3

Anderl, S., Maret, S., Cabrit, S., et al. 2016, A&A, 591, A3

André, P., Montmerle, T., & Feigelson, E. D. 1987, AJ, 93, 1182

André, P., Montmerle, T., Feigelson, E. D., & Steppe, H. 1990, A&A, 240, 321

André, P., Ward-Thompson, D., & Barsony, M. 1993, ApJ, 406, 122

Andrews, S. M., Huang, J., Pérez, L. M., et al. 2018, ApJL, 869, L41

Andrews, S. M., Wilner, D. J., Espaillat, C., et al. 2011, ApJ, 732, 42

Ansdell, M., Williams, J. P., Trapman, L., et al. 2018, ApJ, 859, 21

Ansdell, M., Williams, J. P., van der Marel, N., et al. 2016, ApJ, 828, 46

Arce, H. G., Mardones, D., Corder, S. A., et al. 2013, ApJ, 774, 39

Arce, H. G. & Sargent, A. I. 2006, ApJ, 646, 1070

Artur de la Villarmois, E., Kristensen, L. E., & Jørgensen, J. K. 2019, subm.

Artur de la Villarmois, E., Kristensen, L. E., Jørgensen, J. K., et al. 2018, A&A, 614, A26

Aso, Y., Ohashi, N., Saigo, K., et al. 2015, ApJ, 812, 27

Audard, M., Ábrahám, P., Dunham, M. M., et al. 2014, Protostars and Planets VI, 387

Avery, L. W. & Chiao, M. 1996, ApJ, 463, 642

Bachiller, R. & Perez Gutierrez, M. 1997, in IAU Symposium, Vol. 182, Herbig-Haro Flows and the Birth of Stars, ed. B. Reipurth & C. Bertout, 153–162

Bae, J., Zhu, Z., & Hartmann, L. 2017, ApJ, 850, 201

Balança, C., Spielfiedel, A., & Feautrier, N. 2016, MNRAS, 460, 3766

Bally, J., Langer, W. D., Stark, A. A., & Wilson, R. W. 1987, ApJL, 312, L45

Barsony, M. 1994, in Astronomical Society of the Pacific Conference Series, Vol. 65, Clouds, Cores, and Low Mass Stars, ed. D. P. Clemens & R. Barvainis, 197

Barsony, M., Kenyon, S. J., Lada, E. A., & Teuben, P. J. 1997, ApJS, 112, 109

Basu, S. 1998, ApJ, 509, 229

Beckwith, S. V. W. & Sargent, A. I. 1991, ApJ, 381, 250

Bergin, E., Calvet, N., D'Alessio, P., & Herczeg, G. J. 2003, ApJL, 591, L159

Bergin, E. A., Du, F., Cleeves, L. I., et al. 2016, ApJ, 831, 101

Bertout, C. 1989, ARAA, 27, 351

Birnstiel, T., Fang, M., & Johansen, A. 2016, SSR, 205, 41

Bontemps, S., André, P., Kaas, A. A., et al. 2001, A&A, 372, 173

Bontemps, S., Andre, P., Terebey, S., & Cabrit, S. 1996, A&A, 311, 858

Boogert, A. C. A., Gerakines, P. A., & Whittet, D. C. B. 2015, ARAA, 53, 541

Bottinelli, S., Boogert, A. C. A., Bouwman, J., et al. 2010, ApJ, 718, 1100

Briggs, D. S., Schwab, F. R., & Sramek, R. A. 1999, in Astronomical Society of the Pacific Conference Series, Vol. 180, Synthesis Imaging in Radio Astronomy II, ed. G. B. Taylor, C. L. Carilli, & R. A. Perley, 127

Brinch, C., Crapsi, A., Hogerheijde, M. R., & Jørgensen, J. K. 2007, A&A, 461, 1037

Brinch, C. & Jørgensen, J. K. 2013, A&A, 559, A82

Brinch, C., Jørgensen, J. K., Hogerheijde, M. R., Nelson, R. P., & Gressel, O. 2016, ApJL, 830, L16

Brown, W. A. & Bolina, A. S. 2007, MNRAS, 374, 1006

Cabrit, S., Ferreira, J., Dougados, C., & Garcia, P. 2010, Highlights of Astronomy, 15, 261

Cabrit, S., Raga, A., & Gueth, F. 1997, in IAU Symposium, Vol. 182, Herbig-Haro Flows and the
    Birth of Stars, ed. B. Reipurth & C. Bertout, 163–180

Canto, J., D'Alessio, P., & Lizano, S. 1995, in Revista Mexicana de Astronomia y Astrofisica Confer-
    ence Series, Vol. 1, Revista Mexicana de Astronomia y Astrofisica Conference Series, ed. S. Lizano
    & J. M. Torrelles, 217

Casanova, S., Montmerle, T., Feigelson, E. D., & Andre, P. 1995, ApJ, 439, 752

Ceccarelli, C. 2004, in Astronomical Society of the Pacific Conference Series, Vol. 323, Star Forma-
    tion in the Interstellar Medium: In Honor of David Hollenbach, ed. D. Johnstone, F. C. Adams,
    D. N. C. Lin, D. A. Neufeeld, & E. C. Ostriker, 195

Chandra, S. & Kegel, W. H. 2000, AA&PS, 142, 113

Charnley, S. B. 1997, ApJ, 481, 396

Charnley, S. B., Tielens, A. G. G. M., & Millar, T. J. 1992, ApJL, 399, L71

Choi, M., Tatematsu, K., & Kang, M. 2010, ApJL, 723, L34

Chou, T.-L., Takakuwa, S., Yen, H.-W., Ohashi, N., & Ho, P. T. P. 2014, ApJ, 796, 70

Chuang, K.-J., Fedoseev, G., Ioppolo, S., van Dishoeck, E. F., & Linnartz, H. 2016, MNRAS, 455,
    1702

Codella, C., Ceccarelli, C., Cabrit, S., et al. 2016, A&A, 586, L3

Codella, C., Maury, A. J., Gueth, F., et al. 2014, A&A, 563, L3

Cuppen, H. M., van Dishoeck, E. F., Herbst, E., & Tielens, A. G. G. M. 2009, A&A, 508, 275

Daniel, F., Dubernet, M.-L., & Grosjean, A. 2011, A&A, 536, A76

Dayou, F. & Balança, C. 2006, A&A, 459, 297

de Geus, E. J., Bronfman, L., & Thaddeus, P. 1990, A&A, 231, 137

Drozdovskaya, M. N., van Dishoeck, E. F., Jørgensen, J. K., et al. 2018, MNRAS, 476, 4949

Drozdovskaya, M. N., Walsh, C., Visser, R., Harsono, D., & van Dishoeck, E. F. 2015, MNRAS, 451, 3836

Dullemond, C. P. & Monnier, J. D. 2010, ARAA, 48, 205

Dumouchel, F., Faure, A., & Lique, F. 2010, MNRAS, 406, 2488

Dunham, M. M., Allen, L. E., Evans, II, N. J., et al. 2015, ApJS, 220, 11

Dunham, M. M., Stutz, A. M., Allen, L. E., et al. 2014a, Protostars and Planets VI, 195

Dunham, M. M. & Vorobyov, E. I. 2012, ApJ, 747, 52

Dunham, M. M., Vorobyov, E. I., & Arce, H. G. 2014b, MNRAS, 444, 887

Dutrey, A. 2015, in Astronomical Society of the Pacific Conference Series, Vol. 499, Revolution in Astronomy with ALMA: The Third Year, ed. D. Iono, K. Tatematsu, A. Wootten, & L. Testi, 261

Dutrey, A., Guilloteau, S., & Bachiller, R. 1997, A&A, 325, 758

Dutrey, A., Semenov, D., Chapillon, E., et al. 2014, Protostars and Planets VI, 317

Evans, II, N. J., Dunham, M. M., Jørgensen, J. K., et al. 2009, ApJS, 181, 321

Faure, A., Lique, F., & Wiesenfeld, L. 2016, MNRAS, 460, 2103

Faure, A., Wiesenfeld, L., Scribano, Y., & Ceccarelli, C. 2012, MNRAS, 420, 699

Fendt, C. & Camenzind, M. 1996, Astrophysical Letters and Communications, 34, 289

Fischer, W. J., Megeath, S. T., Furlan, E., et al. 2017, ApJ, 840, 69

Flower, D. R. 1999, MNRAS, 305, 651

Frank, J., King, A., & Raine, D. 1992, Accretion power in astrophysics.

Frimann, S., Jørgensen, J. K., & Haugbølle, T. 2016a, A&A, 587, A59

Frimann, S., Jørgensen, J. K., Padoan, P., & Haugbølle, T. 2016b, A&A, 587, A60

Froebrich, D. 2005, ApJS, 156, 169

Galli, D., Lizano, S., Shu, F. H., & Allen, A. 2006, ApJ, 647, 374

Garrod, R., Park, I. H., Caselli, P., & Herbst, E. 2006, Faraday Discussions, 133, 51

Garrod, R. T., Wakelam, V., & Herbst, E. 2007, A&A, 467, 1103

Girart, J. M., Rodríguez, L. F., & Curiel, S. 2000, ApJL, 544, L153

Green, S. & Chapman, S. 1978, ApJS, 37, 169

Greene, T. P., Wilking, B. A., Andre, P., Young, E. T., & Lada, C. J. 1994, ApJ, 434, 614

Greene, T. P. & Young, E. T. 1992, ApJ, 395, 516

Grosso, N., Montmerle, T., Bontemps, S., André, P., & Feigelson, E. D. 2000, A&A, 359, 113

Gusdorf, A., Cabrit, S., Flower, D. R., & Pineau Des Forêts, G. 2008a, A&A, 482, 809

Gusdorf, A., Pineau Des Forêts, G., Cabrit, S., & Flower, D. R. 2008b, A&A, 490, 695

Guzmán, V. V., Pety, J., Goicoechea, J. R., et al. 2015, ApJL, 800, L33

Haisch, Jr., K. E., Barsony, M., Greene, T. P., & Ressler, M. E. 2002, AJ, 124, 2841

Haro, G. 1952, ApJ, 115, 572

Harris, R. J., Andrews, S. M., Wilner, D. J., & Kraus, A. L. 2012, ApJ, 751, 115

Harsono, D., Bjerkeli, P., van der Wiel, M. H. D., et al. 2018, Nature Astronomy, 2, 646

Harsono, D., Bruderer, S., & van Dishoeck, E. F. 2015a, A&A, 582, A41

Harsono, D., Jørgensen, J. K., van Dishoeck, E. F., et al. 2014, A&A, 562, A77

Harsono, D., van Dishoeck, E. F., Bruderer, S., Li, Z.-Y., & Jørgensen, J. K. 2015b, A&A, 577, A22

Hartmann, L. 1998, Cambridge Astrophysics Series, 32

Hartmann, L. & Kenyon, S. J. 1996, ARAA, 34, 207

Henning, T. & Semenov, D. 2013, Chemical Reviews, 113, 9016

Herbig, G. H. 1950, ApJ, 111, 11

Herbst, E. & van Dishoeck, E. F. 2009, ARAA, 47, 427

Heyer, M. H., Vrba, F. J., Snell, R. L., et al. 1987, ApJ, 321, 855

Higuchi, A. E., Sakai, N., Watanabe, Y., et al. 2018, ApJS, 236, 52

Ho, P. T. P., Moran, J. M., & Lo, K. Y. 2004, ApJL, 616, L1

Högbom, J. A. 1974, AA&PS, 15, 417

Honda, M., Inoue, A. K., Fukagawa, M., et al. 2009, ApJL, 690, L110

Imanishi, K., Tsujimoto, M., & Koyama, K. 2001, ApJ, 563, 361

Jacobsen, S. K., Jørgensen, J. K., van der Wiel, M. H. D., et al. 2018, A&A, 612, A72

Jones, A. P., Tielens, A. G. G. M., & Hollenbach, D. J. 1996, ApJ, 469, 740

Joos, M., Hennebelle, P., & Ciardi, A. 2012, A&A, 543, A128

Jørgensen, J. K. 2004, A&A, 424, 589

Jørgensen, J. K., Bourke, T. L., Myers, P. C., et al. 2007, ApJ, 659, 479

Jørgensen, J. K., Bourke, T. L., Myers, P. C., et al. 2005a, ApJ, 632, 973

Jørgensen, J. K., Bourke, T. L., Nguyen Luong, Q., & Takakuwa, S. 2011, A&A, 534, A100

Jørgensen, J. K., Favre, C., Bisschop, S. E., et al. 2012, ApJL, 757, L4

Jørgensen, J. K., Harvey, P. M., Evans, II, N. J., et al. 2006, ApJ, 645, 1246

Jørgensen, J. K., Johnstone, D., Kirk, H., et al. 2008, ApJ, 683, 822

Jørgensen, J. K., Schöier, F. L., & van Dishoeck, E. F. 2004, A&A, 416, 603

Jørgensen, J. K., Schöier, F. L., & van Dishoeck, E. F. 2005b, A&A, 437, 501

Jørgensen, J. K., van der Wiel, M. H. D., Coutens, A., et al. 2016, A&A, 595, A117

Jørgensen, J. K., van Dishoeck, E. F., Visser, R., et al. 2009, A&A, 507, 861

Jørgensen, J. K., Visser, R., Sakai, N., et al. 2013, ApJL, 779, L22

Jørgensen, J. K., Visser, R., Williams, J. P., & Bergin, E. A. 2015, A&A, 579, A23

Kalugina, Y. & Lique, F. 2015, MNRAS, 446, L21

Kamp, I. 2019, arXiv e-prints [[arXiv]1901.10862]

Kastner, J. H., Qi, C., Dickson-Vandervelde, D. A., et al. 2018, ApJ, 863, 106

Kauffmann, J., Bertoldi, F., Bourke, T. L., Evans, II, N. J., & Lee, C. W. 2008, A&A, 487, 993

Kenyon, S. J. 1999, in NATO Advanced Science Institutes (ASI) Series C, Vol. 540, NATO Advanced
    Science Institutes (ASI) Series C, ed. C. J. Lada & N. D. Kylafis, 613

Kenyon, S. J. & Hartmann, L. 1995, ApJS, 101, 117

Kirk, H., Johnstone, D., & Di Francesco, J. 2006, ApJ, 646, 1009

Knauth, D. C., Andersson, B.-G., McCandliss, S. R., & Warren Moos, H. 2004, Natur, 429, 636

Kristensen, L. E. & Dunham, M. M. 2018, A&A, 618, A158

Kristensen, L. E., van Dishoeck, E. F., Bergin, E. A., et al. 2012, A&A, 542, A8

Kristensen, L. E., van Dishoeck, E. F., van Kempen, T. A., et al. 2010, A&A, 516, A57

Krumholz, M. R., Crutcher, R. M., & Hull, C. L. H. 2013, ApJL, 767, L11

Kuffmeier, M., Haugbølle, T., & Nordlund, Å. 2017, ApJ, 846, 7

Lacy, J. H., Knacke, R., Geballe, T. R., & Tokunaga, A. T. 1994, ApJL, 428, L69

Lada, C. J. 1987, in IAU Symposium, Vol. 115, Star Forming Regions, ed. M. Peimbert & J. Jugaku,
    1–17

Lada, C. J. 1999, in NATO Advanced Science Institutes (ASI) Series C, Vol. 540, NATO Advanced
    Science Institutes (ASI) Series C, ed. C. J. Lada & N. D. Kylafis, 143

Lada, C. J. & Wilking, B. A. 1984, ApJ, 287, 610

Larson, R. B. 1969, MNRAS, 145, 271

Law, C. J., Öberg, K. I., Bergner, J. B., & Graninger, D. 2018, ApJ, 863, 88

Lee, C.-F., Hirano, N., Zhang, Q., et al. 2014, ApJ, 786, 114

Lefloch, B., Bachiller, R., Ceccarelli, C., et al. 2018, MNRAS, 477, 4792

Leous, J. A., Feigelson, E. D., Andre, P., & Montmerle, T. 1991, ApJ, 379, 683

Li, Z.-Y., Banerjee, R., Pudritz, R. E., et al. 2014, Protostars and Planets VI, 173

Lin, D. N. C., Hayashi, M., Bell, K. R., & Ohashi, N. 1994, ApJ, 435, 821

Lindberg, J. E., Charnley, S. B., Jørgensen, J. K., Cordiner, M. A., & Bjerkeli, P. 2017, ApJ, 835, 3

Lindberg, J. E., Jørgensen, J. K., Brinch, C., et al. 2014, A&A, 566, A74

Lique, F., Spielfiedel, A., & Cernicharo, J. 2006, A&A, 451, 1125

Lommen, D., Jørgensen, J. K., van Dishoeck, E. F., & Crapsi, A. 2008, A&A, 481, 141

Loren, R. B. 1989, ApJ, 338, 902

Loren, R. B., Wootten, A., & Wilking, B. A. 1990, ApJ, 365, 269

Luhman, K. L. & Rieke, G. H. 1999, ApJ, 525, 440

Lynds, B. T. 1962, ApJS, 7, 1

Machida, M. N. & Matsumoto, T. 2011, MNRAS, 413, 2767

Mamajek, E. E. 2008, Astronomische Nachrichten, 329, 10

Mangum, J. G. & Wootten, A. 1993, ApJS, 89, 123

Maret, S., Ceccarelli, C., Tielens, A. G. G. M., et al. 2005, A&A, 442, 527

Maury, A. J., André, P., Hennebelle, P., et al. 2010, A&A, 512, A40

Maury, A. J., Belloche, A., André, P., et al. 2014, A&A, 563, L2

McClure, M. K., Furlan, E., Manoj, P., et al. 2010, ApJS, 188, 75

McGuire, B. A. 2018, ApJS, 239, 17

McMullin, J. P., Waters, B., Schiebel, D., Young, W., & Golap, K. 2007, in Astronomical Society of the Pacific Conference Series, Vol. 376, Astronomical Data Analysis Software and Systems XVI, ed. R. A. Shaw, F. Hill, & D. J. Bell, 127

Meru, F., Juhász, A., Ilee, J. D., et al. 2017, ApJL, 839, L24

Mezger, P. G., Sievers, A., Zylka, R., et al. 1992, A&A, 265, 743

Miura, H., Yamamoto, T., Nomura, H., et al. 2017, ApJ, 839, 47

Montmerle, T., Koch-Miramond, L., Falgarone, E., & Grindlay, J. E. 1983, ApJ, 269, 182

Mottram, J. C., van Dishoeck, E. F., Kristensen, L. E., et al. 2017, A&A, 600, A99

Müller, H. S. P., Thorwirth, S., Roth, D. A., & Winnewisser, G. 2001, A&A, 370, L49

Murillo, N. M., Bruderer, S., van Dishoeck, E. F., et al. 2015, A&A, 579, A114

Murillo, N. M., Lai, S.-P., Bruderer, S., Harsono, D., & van Dishoeck, E. F. 2013, A&A, 560, A103

Murillo, N. M., van Dishoeck, E. F., Tobin, J. J., & Fedele, D. 2016, A&A, 592, A56

Murillo, N. M., van Dishoeck, E. F., van der Wiel, M. H. D., et al. 2018, A&A, 617, A120

Muzerolle, J. 2010, Highlights of Astronomy, 15, 732

Myers, P. C. & Ladd, E. F. 1993, ApJL, 413, L47

Nagy, Z., Ossenkopf, V., Van der Tak, F. F. S., et al. 2015, A&A, 578, A124

Natta, A., Testi, L., Calvet, N., et al. 2007, Protostars and Planets V, 767

Öberg, K. I., Boogert, A. C. A., Pontoppidan, K. M., et al. 2011a, ApJ, 740, 109

Öberg, K. I., Furuya, K., Loomis, R., et al. 2015, ApJ, 810, 112

Öberg, K. I., Garrod, R. T., van Dishoeck, E. F., & Linnartz, H. 2009, A&A, 504, 891

Öberg, K. I., Qi, C., Fogel, J. K. J., et al. 2010, ApJ, 720, 480

Öberg, K. I., Qi, C., Fogel, J. K. J., et al. 2011b, ApJ, 734, 98

Ohashi, N., Saigo, K., Aso, Y., et al. 2014, ApJ, 796, 131

Ortiz-León, G. N., Loinard, L., Kounkel, M. A., et al. 2017, ApJ, 834, 141

Osorio, M., D'Alessio, P., Muzerolle, J., Calvet, N., & Hartmann, L. 2003, ApJ, 586, 1148

Ossenkopf, V. & Henning, T. 1994, A&A, 291, 943

Ouyed, R. & Pudritz, R. E. 1997, ApJ, 482, 712

Ozawa, H., Grosso, N., & Montmerle, T. 2005, A&A, 429, 963

Padgett, D. L., Rebull, L. M., Stapelfeldt, K. R., et al. 2008, ApJ, 672, 1013

Panoglou, D., Cabrit, S., Pineau Des Forêts, G., et al. 2012, A&A, 538, A2

Pattle, K., Ward-Thompson, D., Kirk, J. M., et al. 2015, MNRAS, 450, 1094

Penzias, A. A. 1981, ApJ, 249, 518

Persson, M. V., Harsono, D., Tobin, J. J., et al. 2016, A&A, 590, A33

Persson, M. V., Jørgensen, J. K., & van Dishoeck, E. F. 2012, A&A, 541, A39

Podio, L., Codella, C., Gueth, F., et al. 2015, A&A, 581, A85

Pontoppidan, K. M., Dullemond, C. P., van Dishoeck, E. F., et al. 2005, ApJ, 622, 463

Pontoppidan, K. M., Salyk, C., Bergin, E. A., et al. 2014, Protostars and Planets VI, 363

Pudritz, R. E., Ouyed, R., Fendt, C., & Brandenburg, A. 2007, Protostars and Planets V, 277

Qi, C. 2001, PhD thesis, CALIFORNIA INSTITUTE OF TECHNOLOGY

Rabli, D. & Flower, D. R. 2010, MNRAS, 406, 95

Reipurth, B. 1989, Natur, 340, 42

Reipurth, B. 1990, in IAU Symposium, Vol. 137, Flare Stars in Star Clusters, Associations and the Solar Vicinity, ed. L. V. Mirzoian, B. R. Pettersen, & M. K. Tsvetkov, 229–251

Reipurth, B. & Bally, J. 2001, ARAA, 39, 403

Robitaille, T. P., Whitney, B. A., Indebetouw, R., Wood, K., & Denzmore, P. 2006, ApJS, 167, 256

Sahnoun, E., Wiesenfeld, L., Hammami, K., & Jaidane, N. 2018, The Journal of Physical Chemistry A, 122, 3004

Sakai, N., Sakai, T., Hirota, T., Burton, M., & Yamamoto, S. 2009, ApJ, 697, 769

Sakai, N., Sakai, T., Hirota, T., et al. 2014, Natur, 507, 78

Sakai, N., Sakai, T., Hirota, T., & Yamamoto, S. 2008, ApJ, 672, 371

Sakai, N. & Yamamoto, S. 2013, Chemical Reviews, 113, 8981

Schöier, F. L., Jørgensen, J. K., van Dishoeck, E. F., & Blake, G. A. 2002, A&A, 390, 1001

Schöier, F. L., van der Tak, F. F. S., van Dishoeck, E. F., & Black, J. H. 2005, A&A, 432, 369

Seifried, D., Banerjee, R., Pudritz, R. E., & Klessen, R. S. 2013, MNRAS, 432, 3320

Sheehan, P. D. & Eisner, J. A. 2017, ApJ, 851, 45

Shirley, Y. L., Huard, T. L., Pontoppidan, K. M., et al. 2011, ApJ, 728, 143

Shu, F., Najita, J., Galli, D., Ostriker, E., & Lizano, S. 1993, in Protostars and Planets III, ed. E. H. Levy & J. I. Lunine, 3–45

Shu, F. H. 1977, ApJ, 214, 488

Sipilä, O., Spezzano, S., & Caselli, P. 2016, A&A, 591, L1

Spielfiedel, A., Feautrier, N., Najar, F., et al. 2012, MNRAS, 421, 1891

Stahler, S. W., Shu, F. H., & Taam, R. E. 1980, ApJ, 241, 637

Strom, S. E. 1972, PASP, 84, 745

Suutarinen, A. N., Kristensen, L. E., Mottram, J. C., Fraser, H. J., & van Dishoeck, E. F. 2014, MNRAS, 440, 1844

Tabone, B., Cabrit, S., Bianchi, E., et al. 2017, A&A, 607, L6

Takakuwa, S., Saigo, K., Matsumoto, T., et al. 2017, ApJ, 837, 86

Takakuwa, S., Saito, M., Saigo, K., et al. 2014, ApJ, 796, 1

Taquet, V., López-Sepulcre, A., Ceccarelli, C., et al. 2015, ApJ, 804, 81

Terebey, S., Shu, F. H., & Cassen, P. 1984, ApJ, 286, 529

Testi, L., Birnstiel, T., Ricci, L., et al. 2014, Protostars and Planets VI, 339

Thi, W.-F., van Zadelhoff, G.-J., & van Dishoeck, E. F. 2004, A&A, 425, 955

Tielens, A. G. G. M. & Hagen, W. 1982, A&A, 114, 245

Tobin, J. J., Hartmann, L., Bergin, E., et al. 2012, ApJ, 748, 16

Tobin, J. J., Kratter, K. M., Persson, M. V., et al. 2016, Natur, 538, 483

Ungerechts, H. & Thaddeus, P. 1987, ApJS, 63, 645

van der Marel, N., Kristensen, L. E., Visser, R., et al. 2013, A&A, 556, A76

van der Tak, F. F. S., Black, J. H., Schöier, F. L., Jansen, D. J., & van Dishoeck, E. F. 2007, A&A,
    468, 627

van der Tak, F. F. S., van Dishoeck, E. F., Evans, II, N. J., & Blake, G. A. 2000, ApJ, 537, 283

van Dishoeck, E. F. 2006, Proceedings of the National Academy of Science, 103, 12249

van Dishoeck, E. F. 2018, in IAU Symposium, Vol. 332, IAU Symposium, ed. M. Cunningham,
    T. Millar, & Y. Aikawa, 3–22

van Dishoeck, E. F., Blake, G. A., Jansen, D. J., & Groesbeck, T. D. 1995, ApJ, 447, 760

van Dishoeck, E. F., Glassgold, A. E., Guelin, M., et al. 1992, in IAU Symposium, Vol. 150, Astro-
    chemistry of Cosmic Phenomena, ed. P. D. Singh, 285

van 't Hoff, M. L. R., Tobin, J. J., Harsono, D., & van Dishoeck, E. F. 2018, A&A, 615, A83

van Zadelhoff, G.-J., Aikawa, Y., Hogerheijde, M. R., & van Dishoeck, E. F. 2003, A&A, 397, 789

Visser, R. 2013, in New Horizons in Astronomy (BASH 2013), 6

Vorobyov, E. I. & Basu, S. 2010, ApJ, 719, 1896

Wakelam, V., Loison, J.-C., Herbst, E., et al. 2015, ApJS, 217, 20

Walsh, C., Loomis, R. A., Öberg, K. I., et al. 2016, ApJL, 823, L10

Wampfler, S. F., Bruderer, S., Karska, A., et al. 2013, A&A, 552, A56

Ward-Thompson, D. 2005, Astronomy and Geophysics, 46, 38

Watanabe, N. & Kouchi, A. 2002, ApJL, 571, L173

White, G. J., Drabek-Maunder, E., Rosolowsky, E., et al. 2015, MNRAS, 447, 1996

White, R. J., Greene, T. P., Doppmann, G. W., Covey, K. R., & Hillenbrand, L. A. 2007, Protostars and Planets V, 117

Wiesenfeld, L. & Faure, A. 2013, MNRAS, 432, 2573

Wilking, B. A., Bontemps, S., Schuler, R. E., Greene, T. P., & André, P. 2001, ApJ, 551, 357

Wilking, B. A., Gagné, M., & Allen, L. E. 2008, Star Formation in the ρ Ophiuchi Molecular Cloud, ed. B. Reipurth, 351

Wilking, B. A., Meyer, M. R., Robinson, J. G., & Greene, T. P. 2005, AJ, 130, 1733

Wilking, B. A., Schwartz, R. D., & Blackwell, J. H. 1987, AJ, 94, 106

Wilking, B. A., Schwartz, R. D., Mundy, L. G., & Schultz, A. S. B. 1990, AJ, 99, 344

Willacy, K. & Langer, W. D. 2000, ApJ, 544, 903

Wilson, T. L. 1999, Reports on Progress in Physics, 62, 143

Yang, B., Stancil, P. C., Balakrishnan, N., & Forrey, R. C. 2010, ApJ, 718, 1062

Yen, H.-W., Koch, P. M., Takakuwa, S., et al. 2015, ApJ, 799, 193

Yen, H.-W., Koch, P. M., Takakuwa, S., et al. 2017, ApJ, 834, 178

Yen, H.-W., Takakuwa, S., Ohashi, N., et al. 2014, ApJ, 793, 1

Yoo, H., Lee, J.-E., Mairs, S., et al. 2017, ApJ, 849, 69

Yorke, H. W., Bodenheimer, P., & Laughlin, G. 1993, ApJ, 411, 274

Yoshida, K., Sakai, N., Nishimura, Y., et al. 2019, PASJ [[arXiv]1901.06546]

Young, E. T., Lada, C. J., & Wilking, B. A. 1986, ApJL, 304, L45

Zhang, M., Brandner, W., Wang, H., et al. 2013, A&A, 553, A41

Zhang, M. & Wang, H. 2009, AJ, 138, 1830